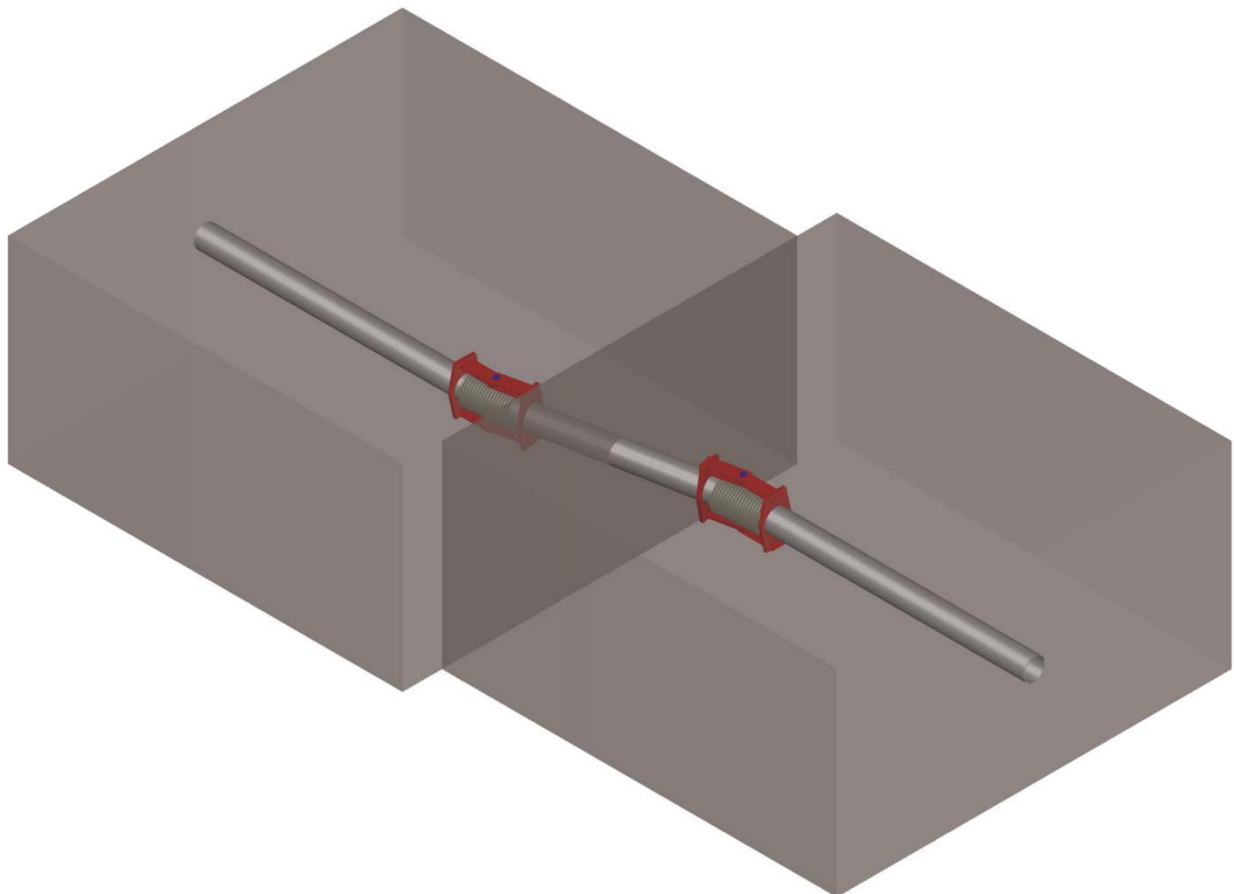




NATIONAL TECHNICAL UNIVERSITY OF ATHENS
SCHOOL OF CIVIL ENGINEERING
DEPARTMENT OF STRUCTURAL ENGINEERING
INSTITUTE OF STEEL STRUCTURES

BURIED STEEL PIPELINES WITH FLEXIBLE JOINTS UNDER FAULTING

DOCTORAL THESIS OF
VASILEIOS E. MELISSIANOS



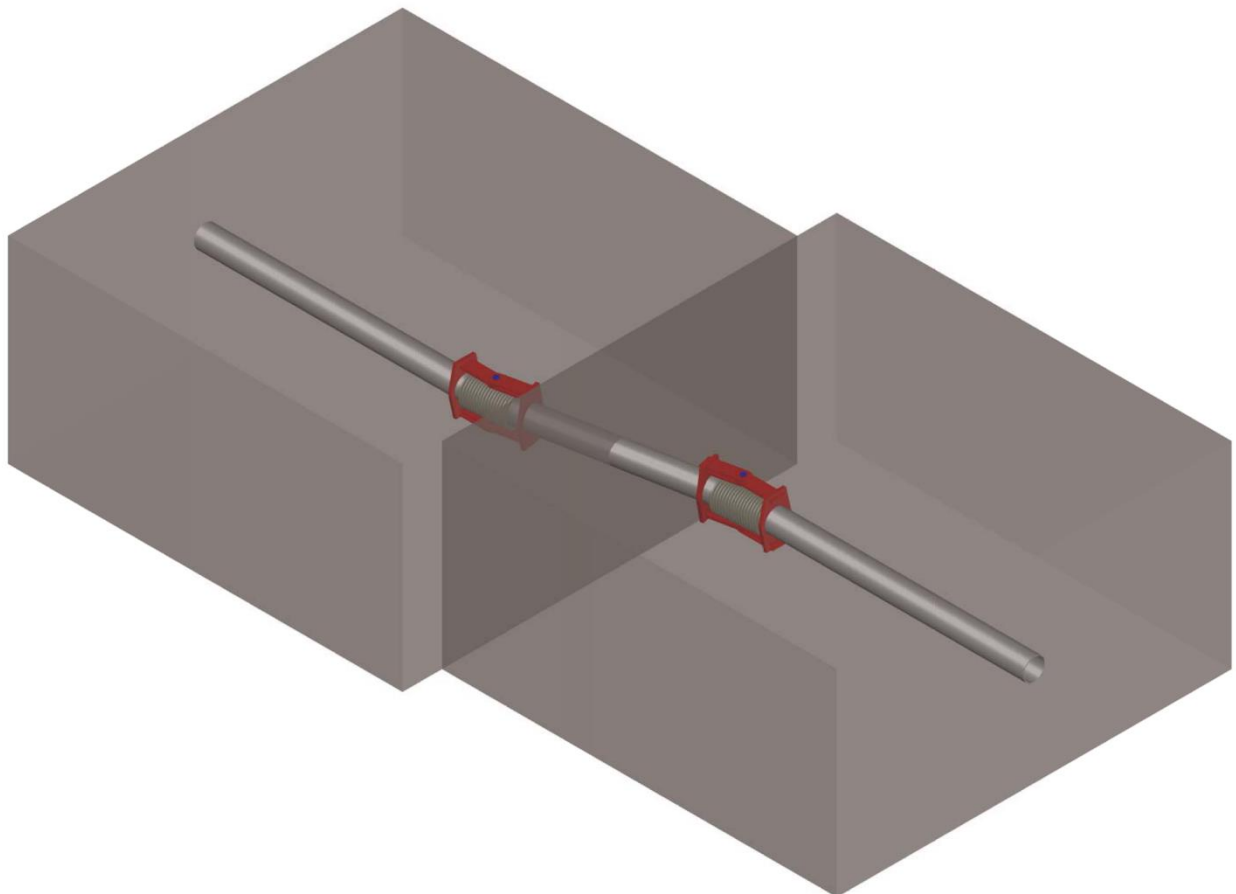
ATHENS 2016



ΕΘΝΙΚΟ ΜΕΤΣΟΒΙΟ ΠΟΛΥΤΕΧΝΕΙΟ
ΣΧΟΛΗ ΠΟΛΙΤΙΚΩΝ ΜΗΧΑΝΙΚΩΝ
ΤΟΜΕΑΣ ΔΟΜΟΣΤΑΤΙΚΗΣ
ΕΡΓΑΣΤΗΡΙΟ ΜΕΤΑΛΛΙΚΩΝ ΚΑΤΑΣΚΕΥΩΝ

ΥΠΟΓΕΙΟΙ ΧΑΛΥΒΔΙΝΟΙ ΑΓΩΓΟΙ ΜΕ ΕΥΚΑΜΠΤΟΥΣ ΚΟΜΒΟΥΣ ΥΠΟ ΔΙΑΡΡΗΞΗ ΣΕΙΣΜΙΚΟΥ ΡΗΓΜΑΤΟΣ

ΔΙΔΑΚΤΟΡΙΚΗ ΔΙΑΤΡΙΒΗ
ΒΑΣΙΛΕΙΟΥ Ε. ΜΕΛΙΣΣΙΑΝΟΥ



ΑΘΗΝΑ 2016



**NATIONAL TECHNICAL UNIVERSITY OF ATHENS
SCHOOL OF CIVIL ENGINEERING**

**BURIED STEEL PIPELINES WITH FLEXIBLE JOINTS
UNDER FAULTING**

DOCTORAL THESIS OF

VASILEIOS E. MELISSIANOS

Civil Engineering Diploma N.T.U.A. (2009)

Post-graduate Specialization Diploma N.T.U.A. (2010)

"Analysis and Design of Earthquake Resistant Structures"

The thesis is submitted to the School of Civil Engineering
of the National Technical University of Athens
in fulfilment of the requirements for the Degree of Doctor of Philosophy

ADVISORY COMMITTEE:

1. C. J. GANTES, Professor N.T.U.A. (supervisor)
2. G. D. BOUCKOVALAS, Professor N.T.U.A.
3. D. VAMVATSIKOS, Assistant Professor N.T.U.A.

EXAMINATION COMMITTEE:

1. C. J. GANTES, Professor N.T.U.A. (supervisor)
2. G. D. BOUCKOVALAS, Professor N.T.U.A.
3. D. VAMVATSIKOS, Assistant Professor N.T.U.A.
4. I. VAYAS, Professor N.T.U.A.
5. S. A. KARAMANOS, Professor University of Thessaly
6. D. G. LIGNOS, Associate Professor EPFL
7. M. FRAGIADAKIS, Assistant Professor N.T.U.A.

Athens, July 2016

© Copyright 2016 by Vasileios E. Melissianos
All Rights Reserved

Neither the whole nor any part of this doctoral thesis may be copied, stored in a retrieval system, distributed, reproduced, translated, or transmitted for commercial purposes, in any form or by any means now or hereafter known, electronic or mechanical, without the written permission from the author. Reproducing, storing and distributing this doctoral thesis for non-profitable, educational or research purposes is allowed, without prejudice to reference to its source and to inclusion of the present text. Any queries in relation to the use of the present doctoral thesis for commercial purposes must be addressed to its author.

Approval of this doctoral thesis by the School of Civil Engineering of the National Technical University of Athens (NTUA) does not constitute in any way an acceptance of the views of the author contained herein by the said academic organisation (L. 5343/1932, art. 202).



ΕΘΝΙΚΟ ΜΕΤΣΟΒΙΟ ΠΟΛΥΤΕΧΝΕΙΟ
ΣΧΟΛΗ ΠΟΛΙΤΙΚΩΝ ΜΗΧΑΝΙΚΩΝ

ΥΠΟΓΕΙΟΙ ΧΑΛΥΒΔΙΝΟΙ ΑΓΩΓΟΙ ΜΕ ΕΥΚΑΜΠΤΟΥΣ
ΚΟΜΒΟΥΣ ΥΠΟ ΔΙΑΡΡΗΞΗ ΣΕΙΣΜΙΚΟΥ ΡΗΓΜΑΤΟΣ

ΔΙΔΑΚΤΟΡΙΚΗ ΔΙΑΤΡΙΒΗ

ΒΑΣΙΛΕΙΟΥ Ε. ΜΕΛΙΣΣΙΑΝΟΥ

Δίπλωμα Πολιτικού Μηχανικού Ε.Μ.Π. (2009)

Μεταπτυχιακό Δίπλωμα Ειδίκευσης Ε.Μ.Π. (2010)

«Δομοστατικός Σχεδιασμός και Ανάλυση Κατασκευών»

Η διατριβή υποβλήθηκε στη Σχολή Πολιτικών Μηχανικών του Εθνικού Μετσοβίου Πολυτεχνείου προς εκπλήρωση των προϋποθέσεων του τίτλου του Διδάκτορος Μηχανικού

ΤΡΙΜΕΛΗΣ ΣΥΜΒΟΥΛΕΥΤΙΚΗ ΕΠΙΤΡΟΠΗ:

1. Χ. Ι. ΓΑΝΤΕΣ, Καθηγητής Ε.Μ.Π. (επιβλέπων)
2. Γ. Δ. ΜΠΟΥΚΟΒΑΛΑΣ, Καθηγητής Ε.Μ.Π.
3. Δ. ΒΑΜΒΑΤΣΙΚΟΣ, Επ. Καθηγητής Ε.Μ.Π.

ΕΠΤΑΜΕΛΗΣ ΕΞΕΤΑΣΤΙΚΗ ΕΠΙΤΡΟΠΗ:

1. Χ. Ι. ΓΑΝΤΕΣ, Καθηγητής Ε.Μ.Π. (επιβλέπων)
2. Γ. Δ. ΜΠΟΥΚΟΒΑΛΑΣ, Καθηγητής Ε.Μ.Π.
3. Δ. ΒΑΜΒΑΤΣΙΚΟΣ, Επ. Καθηγητής Ε.Μ.Π.
4. Ι. ΒΑΓΓΙΑΣ, Καθηγητής Ε.Μ.Π.
5. Σ. Α. ΚΑΡΑΜΑΝΟΣ, Καθηγητής Παν. Θεσσαλίας
6. Δ. Γ. ΛΙΓΝΟΣ, Αν. Καθηγητής ΕΡΦΛ
7. Μ. ΦΡΑΓΚΙΑΔΑΚΗΣ, Επ. Καθηγητής Ε.Μ.Π.

© Copyright 2016 by Βασίλειος Ε. Μελισσιανός
Με επιφύλαξη παντός δικαιώματος

Απαγορεύεται η αντιγραφή, αποθήκευση σε αρχείο πληροφοριών, διανομή, αναπαραγωγή, μετάφραση ή μετάδοση της παρούσας εργασίας, εξ ολοκλήρου ή τμήματος αυτής, για εμπορικό σκοπό, υπό οποιαδήποτε μορφή και με οποιοδήποτε μέσο επικοινωνίας, ηλεκτρονικό ή μηχανικό, χωρίς την προηγούμενη έγγραφη άδεια του συγγραφέα. Επιτρέπεται η αναπαραγωγή, αποθήκευση και διανομή για σκοπό μη κερδοσκοπικό, εκπαιδευτικής ή ερευνητικής φύσης, υπό την προϋπόθεση να αναφέρεται η πηγή προέλευσης και να διατηρείται το παρόν μήνυμα. Ερωτήματα που αφορούν στη χρήση της εργασίας για κερδοσκοπικό σκοπό πρέπει να απευθύνονται προς το συγγραφέα.

Η έγκριση της διδακτορικής διατριβής από την Ανώτατη Σχολή Πολιτικών Μηχανικών του Εθνικού Μετσοβίου Πολυτεχνείου δεν υποδηλώνει αποδοχή των απόψεων του συγγραφέως (Ν. 5343/1932, Άρθρο 202).

ACKNOWLEDGMENTS

The research work leading to this thesis was carried out at the Institute of Steel Structures, School of Civil Engineering, National Technical University of Athens, under the supervision of Professor Charis Gantes. It is time now to thank those who contributed more or less to the completion of my doctoral thesis.

I would like to express the deepest thanks and my wholehearted gratitude to my supervisor for his help. My cooperation with Prof. Gantes started in 2008, as he supervised my diploma thesis. Then, he supervised my postgraduate thesis and later my PhD thesis. So, his inspiring guidance, high educational level, practical experience and broad scientific interests contributed the most to my studies as a civil engineer and particularly to the successful completion of my PhD thesis. Of course, apart from the scientific guidance, his psychological support and encouragement were important.

I appreciate the guidance of Prof. Georgios Bouckovalas, and Assist. Prof. Dimitrios Vamvatsikos throughout the course of this research. I deeply appreciate the opportunity that Dr. Vamvatsikos gave me to work in the field of seismic performance assessment of structures under his inspiring guidance. It was a new research field for me and his sincere support was more than significant.

Thanks are due to the members of the Institute of Steel Structures for the nice working environment which we created. In particular, I would like to thank my friends and colleagues Dr. Konstantinos Kalochairetis, Konstantina Koulatsou, Konstantinos Bakalis, Stella Avgerinou, Maria-Eleni Dasiou, Maria Livanou, Dimitrios Billionis and Andreas Spiliopoulos. Special thanks are due to Stylianos Vernardos and Ilias Thanasoulas, as we worked together in the same office for a long time and to Dr. Xenofon Lignos, Stelios Katsatsidis, Konstantinos Bachas, Georgia Papadatou and Moris Kalderon for their invaluable help in performing the experimental tests.

I would like to thank Dr. Isabella Vassilopoulou for her help in preparing my thesis, which ensured the high quality of this work.

Also, I would like to thank Dr. Michalis Hadjioannou for providing valuable literature, whenever I asked for. Additionally, I would like to thank Dr. Alexandros Valsamis and Konstantinos Bakalis for their assistance in the literature review and Giorgos Korakitis and Aggelos Karvelis for assisting in the numerical analyses.

Last, but not least, I would like to express my deepest and wholehearted gratitude to my family for the unconditional financial, psychological support and encouragement during the last five years. It is a fact that without their help, this work would not have been possible.

This PhD thesis is the outcome of a research work that lasted five years. I would like to mention therefore that the maximum effort has been made to minimize errors and clarify that I am exclusively responsible for any of those that may still exist.

Vasileios E. Melissianos

July 2016

To my family,
for their invaluable support

Η παρούσα έρευνα έχει συγχρηματοδοτηθεί μερικώς από την Ελλάδα και την Ευρωπαϊκή Ένωση (Ευρωπαϊκό Κοινωνικό Ταμείο) μέσω του Επιχειρησιακού Προγράμματος "Ανάπτυξη Ανθρώπινου Δυναμικού" του Εθνικού Στρατηγικού Πλαισίου Αναφοράς (ΕΣΠΑ) 2007-2013 – Δράση: «Ενίσχυση της απασχόλησης ερευνητών σε επιχειρήσεις». Έργο: «Άμεση Μεθοδολογία Αντισεισμικού Σχεδιασμού με Στάθμες Επιτελεστικότητας».

This research has been partially co-financed by Greece and the European Union (European Social Funds) through the Operational Program "Human Resources Development" of the National Strategic Framework (NSRF) 2007-2013, Project: "Direct Performance-Based Seismic Design Methodology".



Ευρωπαϊκή Ένωση
Ευρωπαϊκό Κοινωνικό Ταμείο

ΥΠΟΥΡΓΕΙΟ ΕΡΓΑΣΙΑΣ, ΚΟΙΝΩΝΙΚΗΣ ΑΣΦΑΛΙΣΗΣ ΚΑΙ ΠΡΟΝΟΙΑΣ



ΕΠΙΧΕΙΡΗΣΙΑΚΟ ΠΡΟΓΡΑΜΜΑ
"ΑΝΑΠΤΥΞΗ ΑΝΘΡΩΠΙΝΟΥ ΔΥΝΑΜΙΚΟΥ"
Προσανατολισμός στον Άνθρωπο



Με τη συγχρηματοδότηση της Ελλάδας και της Ευρωπαϊκής Ένωσης

Η παρούσα έρευνα έχει συγχρηματοδοτηθεί μερικώς από την Ευρωπαϊκή Ένωση (Ευρωπαϊκό Κοινωνικό Ταμείο) και Εθνικούς Πόρους μέσω του Επιχειρησιακού Προγράμματος «Εκπαίδευση και Δια Βίου Μάθηση» (ΕΣΠΑ 2007-2013) – Ερευνητικό Πρόγραμμα «Αριστεία II», Έργο: «Πρωτότυπες Έννοιες Σχεδιασμού Μεταλλικών Κατασκευών για τον Ενεργειακό Τομέα με Χρήση Σύγχρονων Υλικών».

This research has been partially co-financed by the European Union (European Social Fund - ESF) and Hellenic National Funds through the Operational Program "Education and Lifelong Learning" (NSRF 2007-2013) – Research Funding Program "Aristeia II", Project: "Novel Design Concepts for Energy Related Steel Structures Using Advanced Materials".



Ευρωπαϊκή Ένωση
Ευρωπαϊκό Κοινωνικό Ταμείο



ΥΠΟΥΡΓΕΙΟ ΠΑΙΔΕΙΑΣ ΚΑΙ ΘΡΗΣΚΕΥΜΑΤΩΝ
ΕΙΔΙΚΗ ΥΠΗΡΕΣΙΑ ΔΙΑΧΕΙΡΙΣΗΣ



Με τη συγχρηματοδότηση της Ελλάδας και της Ευρωπαϊκής Ένωσης



National Technical University of Athens
School of Civil Engineering
Department of Structural Engineering
Institute of Steel Structures

Doctoral Thesis of Vasileios E. Melissianos
Buried Steel Pipelines with Flexible Joints under Faulting

Supervisor: Professor Charis J. Gantes
Athens, July 2016

Abstract

Objective of the present doctoral thesis is the investigation of the behavior and the formulation of practical guidelines for the design of onshore, buried steel pipelines transmitting oil and gas, subjected to seismic fault rupture and equipped with flexible joints as innovative mitigating measure against the consequences of faulting. To that effect, a combined experimental and numerical approach is adopted and a performance assessment methodology for pipelines at fault crossings is developed.

If a tectonic fault is activated, a buried pipeline crossing the fault is forced to follow the ground movement, thus developing deformations and stresses, having bending, shear and axial components, depending on the relative orientation of the pipeline with respect to the fault plane and the fault dip angle. In such cases, the most common failure modes of the pipeline are local buckling of the pipeline wall caused by high compressive strains and tensile weld fracture due to concentrated tensile strains. The pipeline design against fault rupture is carried out in strain terms, given that the problem is displacement-controlled. Hence, pertinent design codes provide expressions of allowable upper bounds for the compressive and the tensile strains. The safety evaluation of buried pipes is thus carried out by ensuring that the developing strains remain below the code-based limits, in order to avoid local buckling and/or tensile failure.

The grave financial, environmental and social impact of a pipe failure necessitate the implementation of appropriate seismic countermeasures in order to minimize the consequences of fault activation and the potential of pipe failure. The primary aim of the measures used nowadays is the reduction of the developing friction on the pipe – soil interface (e.g. trench backfilling with loose granular soil, pipe wrapping with friction-reducing geotextile, use of concrete culverts), or the increase of the pipe strength (e.g. steel grade upgrade, pipe wall thickness increase). However, the range of application of these measures is not broad (e.g. maximum allowable fault offset magnitude with respect to pipe diameter), while their efficiency has not been fully quantified.

Flexible joints are proposed as an innovative mitigating measure and are introduced in the pipeline in the fault vicinity, aiming at absorbing the developing deformation through relative rotation between adjacent pipeline parts, which then remain relatively undeformed and consequently unstressed. This concept introduces a different design approach for reducing the risk of local buckling and/or tensile failure, by transforming the pipeline structural system from continuous to segmented, thus concentrating strains at the joints, instead of reducing the soil-induced friction.

In this thesis, the design and execution of a series of experimental tests of four circular hollow section beams, three continuous and one with flexible joints are initially presented. The specimens were

clamped at their ends and subjected to transverse loading applied at their middle, in three-point bending tests. The objective was that the deformed shape of each half resembles the s-shaped deformation exhibited by a pipe subjected to fault rupture. The effect of the surrounding soil was not considered. The test results for the continuous specimens and the specimen with flexible joints are presented by means of photographs at various displacement levels, as well as load – displacement and strain – displacement curves. The continuous specimen's behavior was found to be initially elastic, up to the formation of plastic hinges at the locations of maximum bending moment. On the contrary, the response of the specimen with flexible joints was fully elastic. Based on the comparison of experimental results, the effectiveness of flexible joints in reducing the developing longitudinal strains by three orders of magnitude and thus efficiently protecting the pipe against failure is convincingly demonstrated.

Next, numerical modeling of the experimental tests with the finite element method is presented, aiming at predicting the specimens' behavior and extracting useful remarks for the subsequent stages of the research. The continuous specimens were meshed with shell elements, while their boundary conditions were assumed to be rigid, following an investigation on the effect of stiffness of the specimen – testing frame connection to the specimen's behavior. Additionally, the effect of longitudinal residual stresses due to seam-welding of the specimen at the manufacturing stage, adopting stress distributions published in the literature, was incorporated by discretizing the beam section into appropriate zones, each of which had different initial stress. It was concluded that if geometrical and material nonlinearity, as well as longitudinal residual stresses due to seam-welding, are included in the analysis, a satisfactory agreement between numerical and experimental results is observed, in terms of strength, deformation and developing strains. Then, the specimen with flexible joints was modeled with beam-type finite elements and the flexible joints with nonlinear rotational and translation springs, whose properties were evaluated by individual experimental tests. Comparison of numerical and experimental results indicated a good match.

As mentioned above, the integration of flexible joints between adjacent pipe steel parts aims at protecting the pipe against local buckling and/or tensile fracture. In case of reverse faulting the pipeline is subjected to high compressive forces, and the reduction of overall stiffness induced by the flexible joints may lead to a third possible failure mode, which is flexural buckling. The latter is also known as upheaval buckling, as the pipe may then deform heavily within the trench or even outside of it. To investigate this potential, a Winkler beam with flexible internal hinges is adopted as the appropriate model. An internal hinge modifies the beam global stiffness and consequently affects the corresponding buckling and post-buckling behavior. The extent of this effect depends on the relative pipe – joint – soil stiffness and has to be taken into account in case flexible joints are adopted to mitigate the aftereffects of faulting. In order to acquire qualitative understanding of the interaction between the hinge and the soil stiffness for different cases, the beam under investigation is considered as either simply-supported or clamped and with one or two equally spaced internal flexible joints. Firstly, elastic critical buckling loads and the corresponding eigenmodes are numerically obtained via linearized buckling analysis. Eigenmode cross-over is also investigated by considering the interaction of soil and hinge rotational stiffness. Then, geometrically nonlinear analyses with imperfections are performed, indicating for most cases descending post-buckling paths, thus unstable post-buckling behavior, with the exception of cases of very soft soil. The response sensitivity to initial geometrical imperfections is also addressed, indicating insignificant effect of the imperfection shape and on the contrary significant impact of the imperfection magnitude on the post-buckling behavior and ultimate load. Moreover, the beam is considered to be embedded in soil exhibiting different stiffness in the upward and the downward direction. Corresponding results show that such soil nonlinearity has to be considered in the analysis in order to get reliable results on the beam buckling behavior. The results are compared for each case to the corresponding ones of a continuous beam, in order to highlight the impact of internal hinges on the beam overall buckling behavior.

Next, the effectiveness of flexible joints in buried pipelines subjected to strike-slip fault rupture is numerically evaluated. Firstly, the proposed numerical model for the analysis of buried pipelines with flexible joints, based on the model of beam resting on soil springs, is described in detail. Then, the optimization of the flexible joints' configuration in terms of number and location is outlined. The behavior of pipes with flexible joints subjected to strike-slip fault rupture is presented and the essential differences to the continuous pipe in terms of deformation, developing stress-state, stress and strain distributions and surrounding soil response are highlighted. Consequently, extensive parametric studies are carried out to determine the effect of pipeline – fault crossing angle, fault offset magnitude, joint angular capacity, burial depth and diameter over thickness ratio on the joint efficiency. Crossing angle dominates the relationship of the bending and axial forces developing along the pipe, and thus affect the behavior of pipes with flexible joints, the effectiveness of which is optimized as this angle approaches 90°, particularly for high fault offset magnitude. On the contrary, burial depth and diameter over thickness ratio have insignificant influence. The effectiveness of flexible joints is eventually compared to other commonly used mitigating measures in terms of developing strains, highlighting their competitiveness.

In general, the efficiency of flexible joints in protecting the pipe against local buckling and/or tensile failure is demonstrated convincingly. The results are used to formulate preliminary design guidelines for the practical use of flexible joints in buried pipelines crossing active faults. Taking into account the uncertainty regarding the exact fault trace location, it is proposed to integrate several joints over the entire length of the pipe, in which the soil rupture is likely to appear, as is also the case for other mitigating measures. Within this length, joints are proposed to be located at constant distances, equal to the distance between the location of maximum bending moment and the fault trace in the corresponding continuous pipeline without joints.

Finally, a performance assessment methodology for buried steel pipelines at fault crossings is presented. The uncertainty associated with earthquakes and fault displacements generates the need to determine the distribution of fault displacement that has to be taken into account for the seismic risk assessment of a pipeline and thus a probabilistic approach is adopted. The proposed methodology is based on the framework of Performance-Based Earthquake Engineering and consists of three interrelated steps: seismic hazard assessment, pipe structural analysis and pipe strain hazard assessment. At first, Probabilistic Fault Displacement Hazard Analysis is performed to quantify the probabilistic nature of the fault offset, while the magnitude of the three fault displacement components in space is determined. Decomposing the fault offset in three components leads to the introduction of a vector to serve as the measure of intensity, instead of the typical scalar (e.g. peak ground acceleration or displacement). Additionally, aleatory and epistemic uncertainties are considered in the seismic hazard analysis through sampling and logic trees, respectively. Then, three-dimensional structural analysis of the pipe is performed, using the nonlinear beam-type finite element model. Finally, the convolution of seismic hazard and structural response results in joint hazard surfaces of compressive and tensile strains leads to the estimation of the mean annual rate of exceeding any limit-state of interest. Strain demand and capacity uncertainty are incorporated in the analysis and their effect on the mean annual rate of exceeding local buckling or tensile fracture is evaluated. To demonstrate also the proposed methodology as an engineering decision making tool, it is implemented to compare the failure probability of a continuous pipe and the corresponding pipe with flexible joints.

In conclusion, flexible joints are highlighted as a very promising alternative for the protection of buried steel pipelines against seismic fault activation.



Εθνικό Μετσόβιο Πολυτεχνείο
Σχολή Πολιτικών Μηχανικών
Τομέας Δομοστατικής
Εργαστήριο Μεταλλικών Κατασκευών

**Διδακτορική Διατριβή Βασιλείου Ε. Μελισσιανού
Υπόγειοι Χαλύβδινοι Αγωγοί με Εύκαμπτους Κόμβους
υπό Διάρρηξη Σεισμικού Ρήγματος**

Επιβλέπων: Καθηγητής Χάρης Ι. Γαντές
Αθήνα, Ιούλιος 2016

Περίληψη

Αντικείμενο της παρούσας διατριβής είναι η μελέτη της συμπεριφοράς χερσαίων υπόγειων χαλύβδινων αγωγών με εύκαμπτους κόμβους υπό διάρρηξη σεισμικού ρήγματος και η διατύπωση πρακτικών οδηγιών για τη χρήση των εύκαμπτων κόμβων ως καινοτόμων μέτρων προστασίας έναντι των επιπτώσεων της διάρρηξης ρήγματος σε αγωγούς μεταφοράς υδρογονανθράκων. Για την επίτευξη των στόχων αυτών υιοθετείται μία συνδυασμένη πειραματική και αριθμητική προσέγγιση, ενώ παρουσιάζεται και μία ολοκληρωμένη μεθοδολογία για την αποτίμηση της επιτελεστικότητας αγωγών σε διασταύρωση με σεισμικά ρήγματα.

Στην περίπτωση διάρρηξης τεκτονικού ρήγματος, ο τεμνόμενος εκ του ρήγματος αγωγός είναι αναγκασμένος να ακολουθήσει τις εδαφικές μετακινήσεις, αναπτύσσοντας έντονες παραμορφώσεις και εντάσεις, οι οποίες έχουν καμπτική, διατμητική και αξονική συνιστώσα, ανάλογα με τη γωνία διασταύρωσης αγωγού – ρήγματος και τη γωνία βύθισης του ρήγματος. Οι κύριες μορφές αστοχίας σε αυτήν την περίπτωση είναι ο τοπικός λυγισμός του κελύφους, λόγω ανάπτυξης έντονων θλιπτικών παραμορφώσεων και η εφελκυστική αστοχία των συγκολλήσεων, λόγω συγκέντρωσης εφελκυστικών παραμορφώσεων. Ο σχεδιασμός των υπόγειων αγωγών έναντι διάρρηξης ρήγματος πραγματοποιείται σε όρους παραμορφώσεων αντί τάσεων, καθώς το υπό εξέταση πρόβλημα είναι επιβαλλόμενης μετακίνησης. Ως εκ τούτου, οι σχετικοί κανονισμοί παρέχουν σχέσεις για τον προσδιορισμό ενός άνω ορίου για τις θλιπτικές και εφελκυστικές παραμορφώσεις. Έτσι, ο έλεγχος ασφαλείας του αγωγού υλοποιείται διασφαλίζοντας πως οι αναπτυσσόμενες παραμορφώσεις θα είναι μικρότερες από τα κανονιστικά όρια, προκειμένου να αποφευχθεί ο τοπικός λυγισμός ή/και η εφελκυστική αστοχία των συγκολλήσεων.

Οι σημαντικές οικονομικές, περιβαλλοντικές και κοινωνικές επιπτώσεις μίας ενδεχόμενης αστοχίας επιβάλλουν τη λήψη κατάλληλων μέτρων προστασίας του αγωγού, προκειμένου να ελαχιστοποιηθούν οι συνέπειες της διάρρηξης ρήγματος στον αγωγό και το ενδεχόμενο αστοχίας του. Τα μέτρα που χρησιμοποιούνται σήμερα για το σκοπό αυτό στοχεύουν κυρίως στη μείωση της αναπτυσσόμενης τριβής στη διεπιφάνεια αγωγού – εδάφους (π.χ. επίχωση ορύγματος με χαλαρό μη-συνεκτικό εδαφικό υλικό, περιτύλιξη αγωγού με γεωύφασμα μειωμένου συντελεστή τριβής, χρήση οχητών από οπλισμένο σκυρόδεμα), ή στην αύξηση της αντοχής του αγωγού (π.χ. βελτίωση ποιότητας χάλυβα, αύξηση πάχους τοιχώματος). Παρ' όλα αυτά, το εύρος εφαρμογής των μέτρων αυτών δεν είναι ευρύ (π.χ. μέγιστη επιτρεπόμενη μετακίνηση ρήγματος σε σχέση με τη διάμετρο του αγωγού), ενώ η αποτελεσματικότητά τους δεν έχει διερευνηθεί πλήρως.

Οι εύκαμπτοι κόμβοι προτείνονται ως ένα καινοτόμο μέτρο προστασίας και εισάγονται στον αγωγό στην εγγύς περιοχή του ρήγματος, στοχεύοντας στην απορρόφηση της αναπτυσσόμενης παραμόρφωσης του αγωγού μέσω σχετικής στροφής των συνδεδεμένων τμημάτων, τα οποία παραμένουν σχεδόν απαραμόρφωτα και συνεπώς άτονα. Αυτή η προσέγγιση εισάγει μία διαφορετική φιλοσοφία σχεδιασμού για τον περιορισμό του κινδύνου τοπικού λυγισμού ή/και εφελκυστικής αστοχίας, καθώς το στατικό σύστημα του αγωγού μετατρέπεται από συνεχές σε σπονδυλωτό, προκειμένου να συγκεντρώνονται οι αναπτυσσόμενες παραμορφώσεις στους κόμβους, αντί να επιδιώκεται η μείωση της τριβής.

Στην παρούσα διατριβή παρουσιάζεται αρχικά ο σχεδιασμός και η εκτέλεση μίας σειράς πειραματικών δοκιμών τεσσάρων δοκών κοίλης κυκλικής διατομής, ήτοι τριών συνεχών και μίας με εύκαμπτους κόμβους. Τα δοκίμια ήταν πακτωμένα στα άκρα τους και υποβλήθηκαν σε εγκάρσια μετακίνηση στο μέσον τους, υλοποιώντας δοκιμές κάμψης τριών σημείων. Σκοπός αυτής της διαμόρφωσης ήταν η παραμόρφωση του κάθε ημι-δοκιμίου να μοιάζει με την παραμόρφωση ενός αγωγού υποκείμενου σε διάρρηξη ρήγματος. Η επιρροή του περιβάλλοντος εδάφους δε λήφθηκε υπόψη. Τα πειραματικά αποτελέσματα των συνεχών δοκιμών και του δοκιμίου με κόμβους παρουσιάζονται μέσω φωτογραφιών των παραμορφωμένων φορέων σε διάφορα επίπεδα επιβαλλόμενης μετακίνησης, καθώς και μέσω διαγραμμάτων φορτίου – μετατόπισης και εφελκυστικής/θλιπτικής παραμόρφωσης – μετατόπισης. Η συμπεριφορά των συνεχών δοκιμών ήταν ελαστική έως το σχηματισμό των πλαστικών αρθρώσεων στις θέσεις ανάπτυξης μέγιστης καμπτικής ροπής. Αντιθέτως, η απόκριση του δοκιμίου με εύκαμπτους κόμβους ήταν εξ ολοκλήρου ελαστική. Η σύγκριση των πειραματικών αποτελεσμάτων αναδεικνύει με πειστικό τρόπο την αποτελεσματικότητα των εύκαμπτων κόμβων στη μείωση των αναπτυσσόμενων παραμορφώσεων και συνεπώς στην προστασία του αγωγού έναντι των συνεπειών της σεισμικής διάρρηξης, καθώς οι αναπτυχθείσες παραμορφώσεις στο δοκίμιο με τους κόμβους ήταν κατά τρεις τάξεις μεγέθους μικρότερες συγκριτικά με τα συνεχή δοκίμια.

Ακολούθως, παρουσιάζεται η αριθμητική προσομοίωση των πειραματικών δοκιμών με χρήση της μεθόδου των πεπερασμένων στοιχείων, στοχεύοντας στην πρόβλεψη της συμπεριφοράς των δοκιμών και στην εξαγωγή χρήσιμων συμπερασμάτων για τα επόμενα στάδια της έρευνας. Τα συνεχή δοκίμια διακριτοποιήθηκαν με πεπερασμένα στοιχεία κελύφους, ενώ οι συνοριακές συνθήκες τους προσομοιώθηκαν με πακτώσεις, βάσει της διερεύνησης που πραγματοποιήθηκε για τον προσδιορισμό της επιρροής της δυσκαμψίας της σύνδεσης δοκιμίου – πλαισίου δοκιμών στη συμπεριφορά του δοκιμίου. Επιπροσθέτως, η επιρροή των διαμήκων παραμενουσών τάσεων, λόγω της ραφής συγκόλλησης του δοκιμίου κατά το στάδιο της κατασκευής του, ελήφθη υπόψη μέσω αποπλοημένων κατανομών που υιοθετήθηκαν από τη βιβλιογραφία. Η επιρροή των παραμενουσών τάσεων προσομοιώθηκε αριθμητικά μέσω διακριτοποίησης του δοκιμίου σε επαρκώς μικρές ζώνες, κάθε μία εκ των οποίων είχε διαφορετική παραμένουσα τάση. Από τις αριθμητικές αναλύσεις προκύπτει πως εφόσον ληφθούν υπόψη στην ανάλυση η μη-γραμμικότητα υλικού και γεωμετρίας, καθώς και η επιρροή των παραμενουσών τάσεων, διαπιστώνεται ικανοποιητική σύγκλιση μεταξύ των αριθμητικών και των πειραματικών αποτελεσμάτων σε όρους αντοχής, μετατοπίσεων και αναπτυσσόμενων παραμορφώσεων. Έπειτα, το δοκίμιο με εύκαμπτους κόμβους προσομοιώθηκε με γραμμικά πεπερασμένα στοιχεία δοκού και οι εύκαμπτοι κόμβοι με μη-γραμμικά στροφικά ελατήρια και ελατήρια μετάθεσης, των οποίων οι ιδιότητες προσδιορίστηκαν από ξεχωριστές πειραματικές δοκιμές σε εύκαμπτους κόμβους. Και σε αυτήν την περίπτωση, η σύγκριση πειραματικών και αριθμητικών αποτελεσμάτων δείχνει μια ικανοποιητική προσέγγιση.

Όπως προαναφέρθηκε, η εισαγωγή εύκαμπτων κόμβων μεταξύ των διαδοχικών χαλύβδινων τμημάτων του αγωγού στοχεύει στην προστασία του έναντι τοπικού λυγισμού ή/και εφελκυστικής αστοχίας. Στην περίπτωση αναστροφής διάρρηξης, ο αγωγός υπόκειται σε έντονη θλίψη και η μείωση της καθολικής δυσκαμψίας της κατασκευής, λόγω της εισαγωγής των εύκαμπτων κόμβων, ενδέχεται να αναδείξει τον καμπτικό λυγισμό ως μία τρίτη πιθανή μορφή αστοχίας. Ο καμπτικός λυγισμός αγωγών είναι επίσης γνωστός ως καθολικός λυγισμός, όπου ο αγωγός μπορεί να παραμορφωθεί έντονα ως δοκός εντός του

ορύγματος ή ακόμα και εκτός αυτού. Για να διερευνηθεί αυτό το ενδεχόμενο μορφώνεται το μοντέλο της δοκού Winkler με εσωτερικές εύκαμπτες αρθρώσεις. Η εσωτερική άρθρωση μεταβάλλει την καθολική δυσκαμψία της δοκού και συνεπακόλουθα την προλυγισμική και μεταλυγισμική της συμπεριφορά. Η έκταση αυτής της επιρροής εξαρτάται από τη σχετική δυσκαμψία αγωγού – άρθρωσης – εδάφους και πρέπει να λαμβάνεται υπόψη στην περίπτωση που οι εύκαμπτοι κόμβοι εφαρμόζονται ως μέτρο προστασίας αγωγών υποκειμένων σε σεισμική διάρρηξη. Έτσι, προκειμένου να αποκτηθεί ποιοτική κατανόηση της αλληλεπίδρασης μεταξύ της στροφικής δυσκαμψίας του κόμβου και της εδαφικής δυσκαμψίας για διάφορες περιπτώσεις, η υπό μελέτη δοκός θεωρείται ως αμφιέριστη ή αμφίπακτη και με έναν ή δύο ισοκατανεμημένους εσωτερικούς εύκαμπτους κόμβους. Αρχικά, προσδιορίζεται το ελαστικό κρίσιμο φορτίο λυγισμού και οι αντίστοιχες ιδιομορφές λυγισμού μέσω αριθμητικών γραμμικοποιημένων αναλύσεων λυγισμού. Διερευνάται, επίσης, η μετάθεση της κρίσιμης ιδιομορφής συναρτήσει της αλληλεπίδρασης της στροφικής και της εδαφικής δυσκαμψίας. Έπειτα, πραγματοποιούνται μη-γραμμικές αναλύσεις γεωμετρίας με αρχικές ατέλειες, οι οποίες αναδεικνύουν στην πλειονότητα των περιπτώσεων πως η μεταλυγισμική συμπεριφορά του φορέα είναι ασταθής, εκτός των περιπτώσεων που η δοκός εδράζεται επί εδάφους πολύ χαμηλής δυσκαμψίας. Η διερεύνηση της ευαισθησίας της απόκρισης στις αρχικές γεωμετρικές ατέλειες εν συνεχεία υποδεικνύει πως η επιρροή του σχήματος των ατελειών είναι σχεδόν αμελητέα, εν αντιθέσει με το μέγεθος των ατελειών, του οποίου η επιρροή είναι πολύ σημαντική. Επιπλέον, η δοκός θεωρείται εγκιβωτισμένη εντός εδαφικού υλικού με διαφορετική δυσκαμψία στην προς τα άνω και την προς τα κάτω διεύθυνση. Τα σχετικά αποτελέσματα δείχνουν πως αυτή η μη-γραμμικότητα του εδαφικού υλικού θα πρέπει να λαμβάνεται υπόψη κατά την ανάλυση, προκειμένου τα αποτελέσματα να είναι αξιόπιστα. Τέλος, τα αποτελέσματα της κάθε υπό εξέταση περίπτωσης συγκρίνονται με τα αντίστοιχα της συνεχούς δοκού, ώστε να δοθεί έμφαση στην επιρροή των εσωτερικών αρθρώσεων στην συνολική λυγισμική συμπεριφορά της δοκού.

Έπειτα, η αποτελεσματικότητα των εύκαμπτων κόμβων σε υπόγειους αγωγούς υποκειμένους σε διάρρηξη οριζόντιας ολίσθησης διερευνάται αριθμητικά. Αρχικά, παρουσιάζεται το αριθμητικό μοντέλο που μορφώνεται για την προσομοίωση των αγωγών με εύκαμπτους κόμβους, βασιζόμενο στο μοντέλο της δοκού επί ελατηριωτού εδάφους. Έπειτα, περιγράφεται η διαδικασία βελτιστοποίησης της διάταξης των εύκαμπτων κόμβων στον αγωγό αναφορικά με το πλήθος και τη χωροθέτηση αυτών. Η συμπεριφορά των αγωγών με εύκαμπτους κόμβους υπό διάρρηξη οριζόντιας ολίσθησης εξετάζεται ακολούθως, δίνοντας έμφαση στις διαφορές μεταξύ των συνεχών και των αγωγών με κόμβους σε όρους παραμόρφωσης, αναπτυσσόμενης έντασης, κατανομών τάσεων και παραμορφώσεων, καθώς και απόκρισης του περιβάλλοντος εδάφους. Εν συνεχεία, πραγματοποιούνται εκτεταμένες παραμετρικές αναλύσεις για τον προσδιορισμό της επιρροής της γωνίας διασταύρωσης αγωγού – ρήγματος, του μεγέθους της σεισμικής διάρρηξης, της στροφικής ικανότητας του κόμβου, του βάθους ταφής και του λόγου διαμέτρου προς πάχος στην αποτελεσματικότητα των κόμβων. Η γωνία διασταύρωσης αγωγού – ρήγματος καθορίζει τη σχέση της αναπτυσσόμενης καμπτικής και αξονικής έντασης στον αγωγό και επομένως επηρεάζει τη συμπεριφορά των αγωγών με κόμβους, των οποίων η αποτελεσματικότητα αυξάνεται όσο η γωνία αυτή προσεγγίζει τις 90°, ιδιαίτερος για μεγάλο μέγεθος διάρρηξης. Αντιθέτως, το βάθος ταφής και ο λόγος διαμέτρου προς πάχος έχουν αμελητέα επίδραση. Ακολούθως, παρουσιάζεται συγκριτική μελέτη της αποδοτικότητας των εύκαμπτων κόμβων σε σχέση με τα συνήθη μέτρα προστασίας σε όρους αναπτυσσόμενων παραμορφώσεων, που αναδεικνύει την ανταγωνιστικότητά τους.

Συμπερασματικά, η αποτελεσματικότητα των εύκαμπτων κόμβων στην προστασία του αγωγού έναντι τοπικού λυγισμού ή/και εφελκυστικής αστοχίας αποδεικνύεται με πειστικό τρόπο. Τα αποτελέσματα της αριθμητικής διερεύνησης χρησιμοποιούνται για τη διατύπωση προκαταρκτικών οδηγιών σχεδιασμού για τη χρήση των εύκαμπτων κόμβων στην πράξη ως μέτρου προστασίας αγωγών σε διασταύρωση με ενεργά σεισμικά ρήγματα. Λαμβάνοντας υπόψη και την αβεβαιότητα ως προς την ακριβή θέση εκδήλωσης της εδαφικής διάρρηξης, προτείνεται οι κόμβοι να τοποθετούνται σε όλο το μήκος του

αγωγού, στο οποίο είναι ενδεχόμενη η εμφάνιση του ίχνους του ρήγματος, όπως άλλωστε συμβαίνει και σε άλλα μέτρα προστασίας. Εντός αυτού του μήκους οι κόμβοι προτείνεται να διατάσσονται ανά σταθερές αποστάσεις, ίσες με την απόσταση της θέσης μέγιστης καμπτικής ροπής από τη θεωρητική θέση του ρήγματος, για τον αντίστοιχο συνεχή αγωγό χωρίς κόμβους.

Τέλος, διατυπώνεται μία ολοκληρωμένη μεθοδολογία για την αποτίμηση επιτελεστικότητας υπόγειων χαλύβδινων αγωγών υπό διάρρηξη ρήγματος. Η τυχαιότητα εμφάνισης ενός σεισμικού γεγονότος και της διάρρηξης ρήγματος που το προκαλεί δημιουργεί την ανάγκη για τον προσδιορισμό της κατάλληλης τιμής μετακίνησης ρήγματος που θα πρέπει να ληφθεί υπόψη κατά το σχεδιασμό και τη σεισμική αποτίμηση αγωγών υπό διάρρηξη ρήγματος. Για το λόγο αυτό υιοθετείται μία πιθανοτική προσέγγιση που βασίζεται στο πλαίσιο της Σεισμικής Μηχανικής Βάσει Επιτελεστικότητας και συνίσταται από τρία αλληλένδετα βήματα: αποτίμηση σεισμικού κινδύνου, δομική ανάλυση αγωγού και αποτίμηση κινδύνου παραμορφώσεων. Αρχικά, εφαρμόζεται η Πιθανοτική Ανάλυση Κινδύνου Μετακίνησης Ρήγματος για την ποσοτικοποίηση της πιθανοτικής φύσης της μετακίνησης ρήγματος, ενώ προσδιορίζεται το μέγεθος της κάθε συνιστώσας της μετακίνησης ρήγματος στο χώρο. Η ανάλυση της μετακίνησης ρήγματος σε χωρικές συνιστώσες κρίνεται απαραίτητη, λόγω της επιρροής των συνιστωστών στην απόκριση ρήγματος, ενώ οδηγεί στην υιοθέτηση ενός διανυσματικού μέτρου έντασης για τη σύνδεση της ανάλυσης σεισμικού κινδύνου με τη δομική ανάλυση του αγωγού. Παράλληλα, οι φυσικές αβεβαιότητες αντιμετωπίζονται μέσω δειγματοληψίας, ενώ οι επιστημικές μέσω λογικών δένδρων. Έπειτα, πραγματοποιείται τρισδιάστατη δομική ανάλυση του αγωγού με χρήση του αριθμητικού μοντέλου της δοκού επί ελατηριωτού εδάφους. Τέλος, ο συνδυασμός των αποτελεσμάτων της ανάλυσης σεισμικού κινδύνου και της δομικής ανάλυσης του αγωγού οδηγεί στη δημιουργία συνδυαστικών καμπυλών και επιφανειών κινδύνου για τις εφελκυστικές και θλιπτικές παραμορφώσεις, προκειμένου να προσδιοριστεί ο μέσος ετήσιος ρυθμός υπέρβασης οποιασδήποτε οριακής κατάστασης ενδιαφέροντος. Η αβεβαιότητα της απαίτησης και της ικανότητας σε όρους παραμορφώσεων λαμβάνεται υπόψη, ώστε να προσδιοριστεί η επιρροή τους στο μέσο ετήσιο ρυθμό υπέρβασης του τοπικού λυγισμού και της εφελκυστικής αστοχίας. Επιπροσθέτως, η προτεινόμενη μεθοδολογία χρησιμοποιείται για την αποτίμηση του κινδύνου αστοχίας ενός συνεχούς αγωγού και του αντίστοιχου με εύκαμπτους κόμβους, ώστε να αναδειχθεί η εφαρμοσιμότητά της ως εργαλείο λήψης αποφάσεων.

Εν κατακλείδι, οι εύκαμπτοι κόμβοι αναδεικνύονται ως μία υποσχόμενη εναλλακτική πρόταση για την προστασία των υπόγειων χαλύβδινων αγωγών έναντι ενδεχόμενης διάρρηξης σεισμικού ρήγματος από το οποίο διέρχονται.

CONTENTS

1	INTRODUCTION	1
1.1	HISTORICAL BACKGROUND AND PREFACE	1
1.2	ACTIONS ON PIPELINES.....	4
1.3	REVIEW OF PIPELINE DAMAGES DUE TO EARTHQUAKE EFFECTS.....	5
1.3.1	Historical pipeline damage due to earthquake effects	5
1.3.2	Pipeline subjected to faulting	6
1.3.3	Pipeline failure modes due to faulting	7
1.3.4	Preventive measures against the consequences of faulting on pipelines	9
1.4	OBJECTIVE AND STRUCTURE OF THE THESIS	10
2	THEORETICAL BACKGROUND AND LITERATURE REVIEW	11
2.1	INTRODUCTION	11
2.2	PIPELINE STRAIN-BASED DESIGN AGAINST FAULTING.....	12
2.2.1	Strain-based versus stress-based design	12
2.2.2	Code-based strain limits.....	13
2.2.2.1	Compressive strain	13
2.2.2.2	Tensile strain	14
2.3	ANALYSIS OF CONTINUOUS PIPELINE AT FAULT CROSSINGS	15
2.4	EXPERIMENTAL STUDIES OF PIPES.....	20
2.4.1	Experiments of members with circular hollow section	20
2.4.2	Experiments of pipes	21
2.4.2.1	Experiments of pipes without surrounding soil	21
2.4.2.2	Experiments of pipes with surrounding soil	23
2.4.3	Experiments of pipe mitigating measures	24
2.4.4	Framework of experimental investigation	24
2.5	CURRENT SEISMIC COUNTERMEASURES IN FAULT CROSSINGS.....	24
2.6	FLEXIBLE JOINTS	28
2.6.1	Slip expansion joints.....	29
2.6.2	Ball joints	30
2.6.3	Bellows	30
2.6.3.1	Introduction to bellows	30
2.6.3.2	Types of bellow joints	31
2.6.4	Composite type.....	32
2.7	SEGMENTED PIPELINES UNDER PERMANENT GROUND DISPLACEMENTS.....	33
2.7.1	Review on flexible joints in segmented pipes subjected to ground movement.....	33
2.7.2	Experimental investigation	36
2.7.3	Analytical methodologies	37
2.7.4	Criteria for flexible joint selection.....	40

2.8	CONCLUSIONS.....	40
3	EXPERIMENTAL INVESTIGATION	43
3.1	INTRODUCTION	43
3.2	DESCRIPTION OF EXPERIMENTS AND EXPERIMENTAL SET-UP	43
3.2.1	Specimens	43
3.2.2	Testing frame	46
3.2.3	Testing procedure and measuring devices	47
3.3	STEEL PROPERTIES	49
3.4	FLEXIBLE JOINT PROPERTIES.....	51
3.5	EXPERIMENTAL RESULTS	55
3.5.1	Continuous specimens	55
3.5.2	Specimen with flexible joints	60
3.6	COMPARISON OF EXPERIMENTAL RESULTS	63
3.7	CONCLUSIONS.....	64
4	NUMERICAL MODELING OF EXPERIMENTS.....	65
4.1	INTRODUCTION	65
4.2	DESCRIPTION OF NUMERICAL MODELS AND ANALYSES	65
4.2.1	Continuous specimens	65
4.2.2	Specimen with flexible joints	68
4.2.3	Analysis method	69
4.3	EXPERIMENTAL AND NUMERICAL RESULTS	70
4.3.1	Continuous specimen.....	70
4.3.2	Specimen with flexible joints	74
4.4	CONCLUSIONS.....	75
5	BUCKLING OF BEAMS WITH INTERNAL FLEXIBLE JOINTS RESTING ON FOUNDATION MODELING BURIED PIPELINES.....	77
5.1	INTRODUCTION	77
5.2	LITERATURE REVIEW AND RESEARCH OBJECTIVES.....	77
5.3	ANALYSIS MODEL	79
5.4	LINEARIZED BUCKLING ANALYSIS	81
5.4.1	General aspects.....	81
5.4.2	Continuous beam	82
5.4.3	Simply-supported beam with one internal hinge	86
5.4.4	Simply-supported beam with two internal hinges.....	87
5.4.5	Critical buckling loads of simply-supported beams	88
5.4.6	Clamped beam with one internal hinge.....	89
5.4.7	Clamped beam with two internal hinges	89
5.4.8	Critical buckling loads of clamped beams.....	90

5.5	GEOMETRICALLY NONLINEAR ANALYSIS	91
5.5.1	Analysis methodology and imperfections	91
5.5.2	Simply-supported beam with one hinge.....	92
5.5.2.1	Low soil stiffness $K_s=180$	92
5.5.2.2	Medium soil stiffness $K_s=10000$	93
5.5.2.3	High soil stiffness $K_s=20000$	94
5.5.2.4	Discussion of results	94
5.5.2.5	Considerations on eigenmode cross-over	95
5.5.3	Simply-supported beam with two hinges	96
5.5.3.1	Low soil stiffness $K_s=180$	96
5.5.3.2	Medium soil stiffness $K_s=10000$	97
5.5.3.3	High soil stiffness $K_s=20000$	98
5.5.3.4	Discussion of results	98
5.5.4	Comparison of simply-supported beam ultimate loads	99
5.5.5	Clamped beam with one hinge	100
5.5.5.1	Low soil stiffness $K_s=180$	100
5.5.5.2	Medium soil stiffness $K_s=10000$	100
5.5.5.3	High soil stiffness $K_s=20000$	101
5.5.5.4	Discussion of results	102
5.5.6	Clamped beam with two hinges.....	102
5.5.6.1	Low soil stiffness $K_s=180$	102
5.5.6.2	Medium soil stiffness $K_s=10000$	103
5.5.6.3	High soil stiffness $K_s=20000$	104
5.5.6.4	Discussion of results	104
5.5.7	Comparison of clamped beam ultimate loads	105
5.5.8	Imperfection magnitude sensitivity	106
5.5.9	Effect of soil nonlinearity.....	107
5.6	SUMMARY AND CONCLUSIONS	110
6	NUMERICAL INVESTIGATION OF PIPELINES WITH FLEXIBLE JOINTS	113
6.1	INTRODUCTION	113
6.2	PIPELINE – FAULT CROSSING NUMERICAL MODELING	114
6.3	INTRODUCTION OF FLEXIBLE JOINTS.....	117
6.3.1	Investigation of optimum number and locations of flexible joints.....	117
6.3.2	Response features of pipeline with flexible joints.....	118
6.4	EFFECT OF PIPELINE – FAULT CROSSING ANGLE.....	120
6.4.1	Pipeline under bending and tension	120
6.4.2	Pipeline under bending and compression.....	127
6.5	EFFECT OF D/t RATIO.....	133
6.6	EFFECT OF BURIAL DEPTH.....	134

6.7	UNCERTAINTY REGARDING FAULT TRACE	135
6.7.1	Origins of fault trace uncertainty	135
6.7.2	Effects of different fault location	136
6.7.3	Optimum distance between flexible joints	137
6.8	COMPARISON AMONG MITIGATING MEASURES	138
6.9	CONCLUSIONS.....	141
7	PERFORMANCE ASSESSMENT OF BURIED PIPELINES AT FAULT CROSSINGS	143
7.1	INTRODUCTION	143
7.2	SEISMIC HAZARD ANALYSIS	144
7.2.1	Probabilistic fault displacement hazard analysis framework.....	144
7.2.2	PFDHA aspects.....	148
7.2.2.1	PFDHA application concerns and advances.....	148
7.2.2.2	Earthquake magnitude	148
7.2.2.3	Poisson model	149
7.2.2.4	Gutenberg – Richter Bounded Recurrence Law	150
7.2.3	PFDHA implementation for pipeline – fault crossing	150
7.2.4	Fault displacement components.....	152
7.2.5	Seismic hazard uncertainty.....	154
7.3	PIPELINE STRUCTURAL ANALYSIS.....	155
7.4	PIPELINE STRAIN HAZARD ANALYSIS.....	155
7.4.1	Framework of failure limit states.....	155
7.4.2	Estimation of limit states	157
7.4.2.1	Limit states with deterministic demand and capacity	157
7.4.2.2	Limit states with deterministic demand and uncertain capacity	157
7.4.2.3	Limit states with uncertain demand and capacity	158
7.5	CASE STUDY 1.....	158
7.5.1	Seismic hazard analysis.....	158
7.5.2	Pipeline structural analysis	160
7.5.3	Pipeline strain hazard analysis	161
7.5.4	Deterministic versus probabilistic approach.....	163
7.6	CASE STUDY 2.....	164
7.6.1	Seismic hazard analysis.....	165
7.6.2	Pipeline structural analysis	165
7.6.3	Strain hazard analysis	166
7.7	CONCLUSIONS	167
8	SUMMARY AND CONCLUSIONS.....	169
8.1	EXTENDED SUMMARY	169
8.2	CONCLUDING REMARKS	172

8.3 RESEARCH CONTRIBUTION AND INNOVATION	174
8.3.1 Contribution to the advancement of engineering science	175
8.3.2 Contribution to the advancement of engineering practice.....	176
8.4 SUGGESTIONS FOR FUTURE RESEARCH.....	176
9 REFERENCES	179
10 APPENDIX – BASIC ASPECTS OF STATISTICS AND PROBABILITY THEORY.....	193
10.1 PROBABILITY DENSITY FUNCTION	193
10.2 CUMMULATIVE DISTRIBUTION FUNCTION	194
10.3 UNIFORM DISTRIBUTION.....	195
10.4 NORMAL DISTRIBUTION	195
10.5 LOGNORMAL DISTRIBUTION.....	197
10.6 GAMMA DISTRIBUTION.....	198
10.7 WEIBULL DISTRIBUTION	198
10.8 BETA DISTRIBUTION	199
10.9 TOTAL PROBABILITY THEOREM.....	200

List of Figures

Figure 1-1:	Existing and new natural gas transmission pipeline network of Europe ("European Commission, Energy - Infrastructure" 2008).....	2
Figure 1-2:	Above ground section of Alaska Pipeline ("National Snow & Ice Data Center" 2016).....	2
Figure 1-3:	Buried pipeline construction ("ConstructionWeekOnline.com" 2016).....	3
Figure 1-4:	Cross-section of a typical trench for buried pipelines ("Georg Fischer Harvel LLC" 2016) 3	
Figure 1-5:	Stages of onshore buried pipeline construction (Constitution Pipeline 2016)	4
Figure 1-6:	Fault types: (a) normal, (b) reverse and (c) strike-slip	6
Figure 1-7:	Regression of average fault displacement on magnitude (Wells and Coppersmith 1994) 7	
Figure 1-8:	Schematic illustration of two successive stages of pipeline deformation due to (a) strike-slip, (b) normal and (c) reverse faulting	7
Figure 1-9:	Pipe girth weld tensile fracture ("Impact Solutions" 2016).....	8
Figure 1-10:	Wrinkling of a 2.2m diameter steel water pipe at a fault crossing in Kullar, Izmit in the 1999 Kocaeli Earthquake (Uckan et al. 2015).....	8
Figure 1-11:	Upheaval buckling of onshore buried steel pipeline due to faulting (Yun and Kyriakides 1990)	8
Figure 1-12:	Pipe cross-section ovalization due to external loading (AISI 2007)	9
Figure 1-13:	Schematic illustration of the introduction of flexible joints in a pipe.....	9
Figure 2-1:	Geometry of pipeline – fault crossing	12
Figure 2-2:	Transverse and frictional forces on a buried pipeline due to strike-slip faulting.....	12
Figure 2-3:	Pipeline – fault crossing analytical model proposed by Wang and Yeh (1985)	16
Figure 2-4:	Pipeline partitioning into four segments proposed by Karamitros et al. (2007)	17
Figure 2-5:	Geometry of FEM model for a buried pipeline under reverse faulting proposed by Joshi et al. (2011)	18
Figure 2-6:	Continuum model proposed by Vazouras et al. (2010, 2012, 2015) for the analysis of buried pipelines at strike-slip fault crossings	19
Figure 2-7:	3D finite element model employed by Karamitros et al. (2007), detail of the connection between the shell and the beam part of the model.....	20
Figure 2-8:	Trench backfilling with graded soil	25
Figure 2-9:	Pipeline wrapping with friction-reducing geotextile (Gantes and Bouckovalas 2013)	25
Figure 2-10:	Use of concrete culverts to protect buried pipelines in case of strike-slip fault movement by retaining the pipe undeformed	26
Figure 2-11:	Construction of the dog-leg structure at the pipeline – fault crossing at Sakhalin (Besstrashnov and Strom 2011).....	26
Figure 2-12:	Trans-Alaska pipeline undeformed shape and deformed shape after the Denali fault rupture in November 3, 2002 following a M=7.9 earthquake (Hall et al. 2003).....	27
Figure 2-13:	Pipe deformation due to faulting within a typical and a wider trench.....	27
Figure 2-14:	Schematic illustration of flexible joints' behavior in pipes under fault rupture	28
Figure 2-15:	72in tied universal thick-wall flexible joint for a sulfuric acid industrial plant ("U.S. Bellows" 2016)	29
Figure 2-16:	Construction of segmented pipe with ball joints (Xinxing Pipes International Development Co. Ltd. 2016).....	29

Figure 2-17: Typical configuration of a slip expansion joint (Lee 2013).....	29
Figure 2-18: Typical configuration of a ball joint with expansion capability (“EBBA Iron Sales, Inc.” 2016)	30
Figure 2-19: Bellow (a) axial, (b) lateral and (c) angular deformation capability	30
Figure 2-20: Alternative profiles of bellow convolutions (Wilson 1984)	31
Figure 2-21: Bellow types: (a) single, (b) tied and (c) hinged	31
Figure 2-22: Universal (a) single, (b) tied and (c) hinged bellow.....	32
Figure 2-23: Gimbal-type hinged bellow: (a) single and (b) universal	32
Figure 2-24: Flexible joint that combines the properties of ball joints and expansion joints (Ford 1983)	33
Figure 2-25: Flexible joints proposed by Isenberg and Richardson (1989)	34
Figure 2-26: Potential beneficial contribution of expansion joints (O’Rourke and Liu 2012).....	35
Figure 2-27: Potential harmful contribution of expansion joints (O’Rourke and Liu 2012)	35
Figure 2-28: Flexible joints investigated by Cheng (2001)	35
Figure 2-29: Segmented pipe joint with external coupling (Klamflex Pipe Couplings Ltd 2016).....	36
Figure 2-30: Experimental set-up and results from Takada (1984).....	37
Figure 2-31: Maximum allowable fault displacement relatively to the pipe – fault crossing angle and the segmented pipe joint type according to O’Rourke and Trautmann (1981)	38
Figure 2-32: Analytical model of segmented pipeline by Takada (1984).....	38
Figure 2-33: Analytical model of segmented pipeline by Elhmadi and O’Rourke (1990)	38
Figure 2-34: Analytical model of segmented pipeline by O’Rourke (2009)	39
Figure 3-1: Schematic illustration of pipeline deformation subjected to strike-slip fault offset	44
Figure 3-2: Schematic illustration of the experimental concept.....	44
Figure 3-3: Specimen types: (a) continuous (CP) and (b) with flexible joints (PFJ)	45
Figure 3-4: Detailing of specimen connection to an end-plate: (a) view and (b) side view	46
Figure 3-5: View of a CP specimen at the testing frame	46
Figure 3-6: View of PFJ specimen at the testing frame.....	47
Figure 3-7: Configuration of measuring devices.....	47
Figure 3-8: LVDTs placed on a flexible joint’s edges.....	48
Figure 3-9: Components of Deformation Plotter.....	48
Figure 3-10: Strain gauge (SG) placed on specimen crown.....	49
Figure 3-11: Typical tensile coupon.....	49
Figure 3-12: Coupon during tensile test.....	50
Figure 3-13: (a) Engineering and (b) true stress – strain curves for steel of specimen N=1 with bilinearized approximation.....	50
Figure 3-14: (a) Engineering and (b) true stress – strain curves for steel of specimen N=2 with bilinearized approximation.....	51
Figure 3-15: (a) Engineering and (b) true stress – strain curves for steel of specimen N=3 with bilinearized approximation.....	51
Figure 3-16: (a) Engineering and (b) true stress – strain curves for steel of specimen N=4 with bilinearized approximation.....	51

Figure 3-17: Flexible joint (single bellow-type) used in the experimental investigation.....	52
Figure 3-18: Flexible joint tensile test experimental set-up and measuring devices.....	53
Figure 3-19: (a) Experimental equilibrium path of joint tensile test and (b) joint failure in expansion through local deformation of the convolutions.....	54
Figure 3-20: Flexible joint bending test experimental set-up and measuring devices	54
Figure 3-21: Experiment equilibrium path of joint bending test in terms of (a) force – displacement and (b) moment – angle curves	55
Figure 3-22: Geometry of flexible joint failure in bending through contact of consecutively convolutions	55
Figure 3-23: Load – displacement experimental equilibrium paths of CP specimens.....	56
Figure 3-24: Analytical approach of CP specimen’s behavior in the elastic range: static model and bending moment distribution.....	56
Figure 3-25: Experimental and analytical equilibrium paths of CP specimens	56
Figure 3-26: (a) Tensile and (b) compressive strain measurements from strain gauges of specimen CP N=1	57
Figure 3-27: (a) Tensile and (b) compressive strain measurements from strain gauges of specimen CP N=2	57
Figure 3-28: (a) Tensile and (b) compressive strain measurements from strain gauges of specimen CP N=3	57
Figure 3-29: N=3 CP specimen experimental deformation for imposed displacement ranging from 0mm to 115mm.....	58
Figure 3-30: Experimental deformation of CP N=1 specimen at various levels of imposed displacement	59
Figure 3-31: Experimentally obtained tensile and compressive strains of CP specimens from side A.	59
Figure 3-32: Experimentally obtained tensile and compressive strains of CP specimens from side B.	60
Figure 3-33: Load – displacement experimental equilibrium path of PFJ specimen	60
Figure 3-34: PFJ specimen experimental deformation at level of imposed displacement ranging from 0mm to 115mm (photos from different angles).....	61
Figure 3-35: Experimental deformation of specimen PFJ at various levels of imposed displacement.	62
Figure 3-36: Experimentally obtained tensile and compressive strains of PFJ specimen from side A.	62
Figure 3-37: Experimentally obtained tensile and compressive strains of PFJ specimen from side B.	63
Figure 3-38: Comparison of (a) CP and (b) PFJ specimen’s experimental deformations at the end of the tests.....	64
Figure 4-1: CP specimen at the testing frame and corresponding numerical models	66
Figure 4-2: Numerical model of CP specimen with detailed modeling specimen – testing frame connection.....	66
Figure 4-3: Modeling details of the CP specimen – testing frame bolted connection.....	67
Figure 4-4: Longitudinal residual stresses on circular hollow section due to seam-weld (Gao et al. 1998)	67
Figure 4-5: Modeling of longitudinal residual stresses through different element groups	68
Figure 4-6: Seam-weld location on the cross-sectional circumference of CP specimens.....	68
Figure 4-7: Numerical modeling of CP specimen.....	68

Figure 4-8:	PFJ specimen at the testing frame and corresponding numerical model.....	69
Figure 4-9:	Experimental and numerical equilibrium paths of CP specimens considering different finite element type and fixed boundary conditions	70
Figure 4-10:	Experimental and numerical equilibrium paths of CP specimens (FEM-shell) considering different numerical boundary conditions	71
Figure 4-11:	Comparison of experimental and numerical load – displacement equilibrium paths of CP specimens by considering or not longitudinal residual stresses.....	71
Figure 4-12:	Experimental and numerical deformation of CP N=1 specimen at various levels of imposed displacement.....	72
Figure 4-13:	Experimental and numerical displacement – strain curves of N=3 CP specimen at measuring locations	73
Figure 4-14:	Elastic and plastic regions at failure of N=3 CP specimen	74
Figure 4-15:	Distribution of von-Mises stresses of N=3 CP specimen.....	74
Figure 4-16:	Distribution of longitudinal strains of N=3 CP specimen.....	74
Figure 4-17:	Summary of experimental and numerical results of PFJ specimen including: (a) load – displacement equilibrium path and (b) specimen deformation at various imposed displacement levels.....	75
Figure 5-1:	Simply-supported beam resting on foundation with one internal hinge	80
Figure 5-2:	Simply-supported beam resting on foundation with two internal hinges.....	81
Figure 5-3:	Clamped beam resting on foundation with one internal hinge	81
Figure 5-4:	Clamped beam resting on foundation with two internal hinges.....	81
Figure 5-5:	Continuous simply-supported beam resting on foundation.....	82
Figure 5-6:	First four eigenmode shapes of continuous simply-supported beam resting on foundation	83
Figure 5-7:	Elastic critical buckling load of the lower four eigenmodes of simply-supported continuous beam with respect to normalized soil stiffness.....	84
Figure 5-8:	Continuous clamped beam resting on foundation.....	84
Figure 5-9:	First four eigenmode shapes of clamped continuous beam resting on foundation	85
Figure 5-10:	Eigenmode shapes of clamped continuous beam resting on foundation	85
Figure 5-11:	Minimum buckling load vs. soil stiffness of clamped continuous beam with respect to normalized soil stiffness	86
Figure 5-12:	Normalized critical buckling load of simply-supported beam with one internal hinge with respect to soil stiffness for varying hinge rotational stiffness.....	86
Figure 5-13:	Critical eigenmodes of simply-supported beam with one internal hinge with respect to soil stiffness and for varying hinge rotational stiffness	87
Figure 5-14:	Normalized critical buckling load of simply-supported beam with two internal hinges with respect to soil stiffness for varying hinge rotational stiffness.....	87
Figure 5-15:	Critical eigenmodes of simply-supported beam with two internal hinges with respect to soil stiffness and for varying hinge rotational stiffness.....	88
Figure 5-16:	Critical buckling loads of simply-supported beams with respect to soil stiffness and for varying rotational stiffness.....	88
Figure 5-17:	Normalized critical buckling load of clamped beam with one internal hinge with respect to soil stiffness for varying hinge rotational stiffness	89

Figure 5-18:	Critical eigenmodes of clamped beam with one internal hinge with respect to soil stiffness and for varying hinge rotational stiffness	89
Figure 5-19:	Normalized critical buckling load of clamped beam with two internal hinges with respect to soil stiffness for variable hinge rotational stiffness	90
Figure 5-20:	Critical eigenmodes of clamped beam with two internal hinges with respect to soil stiffness and for variable hinge rotational stiffness	90
Figure 5-21:	Critical buckling loads of clamped beams with respect to soil stiffness and for varying rotational stiffness.....	91
Figure 5-22:	(a) Eigenmode shapes and (b) imperfection shapes considered in GNIA for simply-supported beam with one internal hinge for $K_s=180$ and rotational stiffness $K_r=5$	93
Figure 5-23:	(a) Equilibrium paths and (b) beam deformed shapes obtained from GNIA of simply-supported beam with one internal hinge for $K_s=180$ and rotational stiffness $K_r=5$	93
Figure 5-24:	(a) Eigenmode shapes and (b) imperfection shapes considered in GNIA for simply-supported beam with one internal hinge for $K_s=10000$ and rotational stiffness $K_r=5$	93
Figure 5-25:	(a) Equilibrium paths and (b) beam deformed shapes obtained from GNIA of simply-supported beam with one internal hinge for $K_s=10000$ and rotational stiffness $K_r=5$	94
Figure 5-26:	(a) Eigenmode shapes and (b) imperfection shapes considered in GNIA for simply-supported beam with one internal hinge for $K_s=20000$ and rotational stiffness $K_r=5$	94
Figure 5-27:	(a) Equilibrium paths and (b) beam deformed shapes obtained from GNIA of simply-supported beam with one internal hinge for $K_s=20000$ and rotational stiffness $K_r=5$	94
Figure 5-28:	(a) Equilibrium paths from GNIA of simply-supported beam with one internal hinge for $K_s=2$ and rotational stiffness $K_r=5$ and (b) soil range regarding the post-buckling behavior of simply-supported beam with one internal hinge with respect to soil stiffness and rotational stiffness $K_r=5$	95
Figure 5-29:	Eigenmode shapes obtained from LBA for simply-supported beam with one internal hinge for (a) $K_s=426$ (before cross-over) and (b) $K_s=540$ (after cross-over) and rotational stiffness $K_r=5$	96
Figure 5-30:	(a) Equilibrium paths and (b) beam deformed shapes obtained from GNIA of simply-supported beam with one internal hinge for $K_r=5$ before ($K_s=526$) and after ($K_s=540$) the cross-over point	96
Figure 5-31:	(a) Eigenmode shapes and (b) imperfection shapes considered in GNIA for simply-supported beam with two internal hinges for $K_s=180$ and rotational stiffness $K_r=5$	97
Figure 5-32:	(a) Equilibrium paths and (b) beam deformed shapes obtained from GNIA of simply-supported beam with two internal hinges for $K_s=180$ and rotational stiffness $K_r=5$	97
Figure 5-33:	(a) Eigenmode shapes and (b) imperfection shapes considered in GNIA for simply-supported beam with two internal hinges for $K_s=10000$ and rotational stiffness $K_r=5$..	97
Figure 5-34:	(a) Equilibrium paths and (b) beam deformed shapes obtained from GNIA of simply-supported beam with two internal hinges for $K_s=10000$ and rotational stiffness $K_r=5$..	98
Figure 5-35:	(a) Eigenmode shapes and (b) imperfection shapes considered in GNIA for simply-supported beam with two internal hinges for $K_s=20000$ and rotational stiffness $K_r=5$..	98
Figure 5-36:	(a) Equilibrium paths and (b) beam deformed shapes obtained from GNIA of simply-supported beam with two internal hinges for $K_s=20000$ and rotational stiffness $K_r=5$..	98
Figure 5-37:	Soil range regarding the post-buckling behavior of simply-supported beam with two internal hinges with respect to soil stiffness and rotational stiffness $K_r=5$	99

Figure 5-38: Ultimate loads comparison of simply-supported beams (continuous (C), with one internal hinge (1H) and with two internal hinges (2H)) with respect to soil stiffness and for hinge rotational stiffness $K_r=5$	99
Figure 5-39: (a) Eigenmode shapes and (b) imperfection shapes considered in GNIA of clamped beam with one internal hinge for $K_s=180$ and rotational stiffness $K_r=5$	100
Figure 5-40: (a) Equilibrium paths and (b) beam deformed shapes obtained from GNIA of clamped beam with one internal hinge for $K_s=180$ and rotational stiffness $K_r=5$	100
Figure 5-41: (a) Eigenmode shapes and (b) imperfection shapes considered in GNIA of clamped beam with one internal hinge for $K_s=10000$ and rotational stiffness $K_r=5$	101
Figure 5-42: (a) Equilibrium paths and (b) beam deformed shapes obtained from GNIA of clamped beam with one internal hinge for $K_s=10000$ and rotational stiffness $K_r=5$	101
Figure 5-43: (a) Eigenmode shapes and (b) imperfection shapes considered in GNIA of clamped beam with one internal hinge for $K_s=20000$ and rotational stiffness $K_r=5$	101
Figure 5-44: (a) Equilibrium paths and (b) beam deformed shapes obtained from GNIA of clamped beam with one internal hinge for $K_s=20000$ and rotational stiffness $K_r=5$	102
Figure 5-45: Soil range regarding the post-buckling behavior of clamped beam with one internal hinge with respect to soil stiffness and rotational stiffness $K_r=5$	102
Figure 5-46: (a) Eigenmode shapes and (b) imperfection shapes considered in GNIA of clamped beam with two internal hinges for $K_s=180$ and rotational stiffness $K_r=5$	103
Figure 5-47: (a) Equilibrium paths and (b) beam deformed shapes obtained from GNIA of clamped beam with two internal hinges for $K_s=180$ and rotational stiffness $K_r=5$	103
Figure 5-48: (a) Eigenmode shapes and (b) imperfection shapes considered in GNIA of clamped beam with two internal hinges for $K_s=10000$ and rotational stiffness $K_r=5$	103
Figure 5-49: (a) Equilibrium paths and (b) beam deformed shapes obtained from GNIA of clamped beam with two internal hinges for $K_s=10000$ and rotational stiffness $K_r=5$	104
Figure 5-50: (a) Eigenmode shapes and (b) imperfection shapes considered in GNIA of clamped beam with two internal hinges for $K_s=20000$ and rotational stiffness $K_r=5$	104
Figure 5-51: (a) Equilibrium paths and (b) beam deformed shapes obtained from GNIA of clamped beam with two internal hinges for $K_s=20000$ and rotational stiffness $K_r=5$	104
Figure 5-52: Soil range regarding the post-buckling behavior of clamped beam with two internal hinges with respect to soil stiffness and rotational stiffness $K_r=5$	105
Figure 5-53: Ultimate loads comparison of clamped beams (continuous (C), with one internal hinge (1H) and with two internal hinges (2H)) with respect to soil stiffness and for hinge rotational stiffness $K_r=5$	105
Figure 5-54: Equilibrium paths for varying imperfection magnitude of clamped beam with two internal hinges for (a) $K_s=180$ and (b) $K_s=20000$ and rotational stiffness $K_r=5$, considering the first linear combination of eigenmodes as the imperfection shape	106
Figure 5-55: Equilibrium paths for varying imperfection magnitude and shape of clamped beam with two internal hinges for $K_s=20000$ and rotational stiffness $K_r=5$	107
Figure 5-56: Beam deformed shapes for varying imperfection magnitude and shape of clamped beam with two internal hinges for $K_s=20000$ and hinge rotational stiffness $K_r=5$	107
Figure 5-57: Ultimate loads comparison of simply-supported beams resting on elastic vs. tensionless soil for hinge rotational stiffness $K_r=5$	108

Figure 5-58:	Deformation shapes obtained from GNIA of continuous beam and beam with one or two internal hinges resting on elastic and tensionless soil for hinge rotational stiffness $K_r=5$	108
Figure 5-59:	Elastic loose and stiff and nonlinear soil considered for the investigation of the effect of soil nonlinearity.....	109
Figure 5-60:	(a) Equilibrium paths and (b) deformed shapes of clamped beam with two internal hinges for $K_s=10000$ and considering either uniform or nonlinear soil with rotational stiffness $K_r=5$	109
Figure 6-1:	Schematic illustration of a pipeline with hinged bellow-type flexible joints subjected to strike-slip fault rupture	113
Figure 6-2:	Beam-type finite element model for pipeline – fault crossing numerical modeling.....	114
Figure 6-3:	API5L-X65 pipeline steel bilinear stress – strain relationship.....	115
Figure 6-4:	Soil springs’ force – displacement relations.....	116
Figure 6-5:	Definition of length L_j in bending moment distribution of a continuous pipeline.....	117
Figure 6-6:	Bending moment distributions of continuous pipeline and pipelines with flexible joints subjected to strike-slip faulting	118
Figure 6-7:	Optimum configuration of flexible joints for a pipe subjected to strike-slip fault rupture, without considering fault trace uncertainty	118
Figure 6-8:	CP and PFJ displacements.....	119
Figure 6-9:	(a) Axial force and (b) bending moment distributions of CP and PFJ	119
Figure 6-10:	Maximum effective stress distributions along CP and PFJ	119
Figure 6-11:	Longitudinal (a) tensile and (b) compressive strain distributions along CP and PFJ	120
Figure 6-12:	(a) Frictional soil force and (b) lateral soil force distributions along CP and PFJ.....	120
Figure 6-13:	Effect of pipe –fault crossing angle β in pipe elongation.....	121
Figure 6-14:	CP and PFJ displacements for $\beta=50^\circ$, $\beta=70^\circ$ and $\beta=90^\circ$ at various levels of fault offset magnitude	122
Figure 6-15:	Distributions of axial force on CP and PFJ pipelines with respect to fault offset (Δ/D) for $\beta=50^\circ$	122
Figure 6-16:	Distributions of axial force on CP and PFJ pipelines with respect to fault offset (Δ/D) for $\beta=70^\circ$ and $\beta=90^\circ$	123
Figure 6-17:	Maximum axial force (N_{max}) of CP and PFJ with respect to fault offset (Δ/D) for $\beta=50^\circ$, $\beta=70^\circ$ and $\beta=90^\circ$	123
Figure 6-18:	Distributions of bending moment on CP and PFJ pipelines with respect to fault offset (Δ/D) for $\beta=50^\circ$, $\beta=70^\circ$ and $\beta=90^\circ$	124
Figure 6-19:	Maximum bending moment (M_{max}) of CP and PFJ with respect to fault offset (Δ/D) for $\beta=50^\circ$, $\beta=70^\circ$ and $\beta=90^\circ$	124
Figure 6-20:	Distributions of longitudinal tensile strains on CP and PFJ pipelines with respect to fault offset (Δ/D) for $\beta=50^\circ$, $\beta=70^\circ$ and $\beta=90^\circ$	125
Figure 6-21:	Maximum longitudinal tensile strain ($\epsilon_{t,max}$) of CP and PFJ with respect to fault offset (Δ/D) for $\beta=50^\circ$, $\beta=70^\circ$ and $\beta=90^\circ$	126
Figure 6-22:	Distributions of longitudinal compressive strains on CP and PFJ pipelines with respect to fault offset (Δ/D) for $\beta=50^\circ$, $\beta=70^\circ$ and $\beta=90^\circ$	126

Figure 6-23: Maximum longitudinal compressive strain ($\epsilon_{c,max}$) of CP and PFJ with respect to fault offset (Δ/D) for $\beta=50^\circ$, $\beta=70^\circ$ and $\beta=90^\circ$	127
Figure 6-24: CP and PFJ displacements for crossing angles $\beta=100^\circ$, $\beta=110^\circ$ $\beta=120^\circ$ and at various levels of fault offset magnitude	128
Figure 6-25: Distributions of axial force on CP and PFJ pipelines with respect to fault offset (Δ/D) for $\beta=100^\circ$, $\beta=110^\circ$ and $\beta=120^\circ$	129
Figure 6-26: Maximum axial force (N_{max}) of PFJ with respect to fault offset (Δ/D) for various crossing angles	129
Figure 6-27: PFJ displacements for $\beta=100^\circ$ and $\beta=110^\circ$ at various levels of fault offset magnitude	130
Figure 6-28: Maximum axial force (N_{max}) of CP and PFJ with respect to fault offset (Δ/D) for $\beta=100^\circ$, $\beta=110^\circ$ and $\beta=120^\circ$	130
Figure 6-29: Distributions of bending moment on CP and PFJ pipelines with respect to fault offset (Δ/D) for $\beta=100^\circ$, $\beta=110^\circ$ and $\beta=120^\circ$	131
Figure 6-30: Maximum bending moment (M_{max}) of CP and PFJ with respect to fault offset (Δ/D) for $\beta=100^\circ$, $\beta=110^\circ$ and $\beta=120^\circ$	131
Figure 6-31: Distributions of longitudinal tensile strains on CP and PFJ pipelines with respect to fault offset (Δ/D) for $\beta=100^\circ$, $\beta=110^\circ$ and $\beta=120^\circ$	132
Figure 6-32: Maximum longitudinal tensile strain ($\epsilon_{t,max}$) of CP and PFJ with respect to fault offset (Δ/D) for $\beta=100^\circ$, $\beta=110^\circ$ and $\beta=120^\circ$	132
Figure 6-33: Distributions of longitudinal compressive strains on CP and PFJ pipelines with respect to fault offset (Δ/D) for $\beta=100^\circ$, $\beta=110^\circ$ and $\beta=120^\circ$	133
Figure 6-34: Maximum longitudinal compressive strain ($\epsilon_{c,max}$) of CP and PFJ with respect to fault offset (Δ/D) for $\beta=100^\circ$, $\beta=110^\circ$ and $\beta=120^\circ$	133
Figure 6-35: (a) Tensile and (b) compressive strains distributions of CP and PFJ for various D/t ratios	134
Figure 6-36: (a) Tensile and (b) compressive strain distributions of CP and PFJ for various burial depths (H/D)	135
Figure 6-37: Schematic illustration of fault rupture propagation being affected by the soil stratigraphy (Plate tectonic & northern Pacific 2016)	135
Figure 6-38: Assumed alternative fault trace locations along the pipeline	136
Figure 6-39: Tensile strain distributions for varying fault trace location and crossing angle $\beta=70^\circ$..	137
Figure 6-40: Configuration of equally-spaced flexible joints over the length of fault trace uncertainty	137
Figure 6-41: Tensile strain distributions for crossing angle (a) $\beta=70^\circ$ and (b) $\beta=90^\circ$ considering different configuration of flexible joints and fault trace being located either between two adjacent joints or on a joint	138
Figure 6-42: Maximum tensile and compressive strains with respect to fault offset for crossing angles $\beta=70^\circ$, $\beta=90^\circ$ and $\beta=100^\circ$ considering alternative mitigating measures	140
Figure 7-1: Schematic illustration of fault displacement components	153
Figure 7-2: Hazard uncertainty logic tree for determining the fault displacement Δ hazard by considering seismic rate ν , maximum earthquake magnitude M_{max} and the AD or MD referring to the two different approaches of PFDHA	155
Figure 7-3: (a) Mean fault displacement hazard curve on pipeline crossing site, (b) mean fault displacement hazard curve and its dispersion	159

Figure 7-4:	Mean annual rate of equaling surface for the independent fault displacement components Δ_1 - Δ_3	159
Figure 7-5:	Mean annual rate of equaling surface for the dependent fault displacement components (a) Δ_1 - Δ_2 and (b) Δ_2 - Δ_3	159
Figure 7-6:	Mean fault displacement hazard curve adopting the AD versus the MD approach	160
Figure 7-7:	Disaggregation results on earthquake magnitude regarding the Eurocode 8 limit states.....	160
Figure 7-8:	Pipeline structural response – (a) tensile strain demand and (b) compressive strain demand.....	161
Figure 7-9:	Contours of tensile and compressive strain mean annual rate of equaling (deterministic demand and capacity)	162
Figure 7-10:	Tensile and compressive strains mean annual rate of equaling (deterministic demand and capacity)	162
Figure 7-11:	Tensile and compressive strains hazard curves (deterministic demand and capacity) .	163
Figure 7-12:	Cumulative probability of tensile fracture (random demand and capacity) for (a) operable limits and (b) pressure integrity limits, the crosses indicate the physical possible combinations for given pipeline – fault geometry	163
Figure 7-13:	Continuous pipeline (CP), pipeline with two (2PFJ) and pipeline with four flexible joints (4PFJ) considered in case study 2	164
Figure 7-14:	Mean fault displacement hazard curve on pipeline crossing site	165
Figure 7-15:	Deformation of continuous pipeline (CP) and pipelines with two (2PFJ) or four (4PFJ) flexible joints subjected to 1.83m fault offset.....	166
Figure 7-16:	(a) Bending moment and (b) axial force distributions of continuous pipeline (CP) and pipelines with two (2PFJ) or four (4PFJ) flexible joints subjected to 1.83m fault offset	166
Figure 7-17:	Longitudinal (a) tensile and (b) compressive strain distributions of continuous pipeline (CP) and pipelines with two (2PFJ) or four (4PFJ) flexible joints subjected to 1.83m fault offset	166
Figure 7-18:	(a) Tensile and (b) compressive strain hazard curves for the three pipeline models (CP: continuous pipe, 2PFJ and 4PFJ: pipes with flexible joints).....	167
Figure 10-1:	Example of a probability density function (standard normal distribution)	194
Figure 10-2:	Example of a cumulative distribution function (standard normal distribution)	194
Figure 10-3:	Examples of uniform distribution (a) PDF and (b) CDF with parameters $\alpha=1$ and $b=5$	195
Figure 10-4:	Examples of normal distribution (a) PDF and (b) CDF with constant mean value	196
Figure 10-5:	Examples of normal distribution (a) PDF and (b) CDF with constant standard deviation	196
Figure 10-6:	Examples of lognormal distribution (a) PDF and (b) CDF with constant mean value...	197
Figure 10-7:	Examples of lognormal distribution (a) PDF and (b) CDF with constant standard deviation	197
Figure 10-8:	Examples of gamma distribution (a) PDF and (b) CDF	198
Figure 10-9:	Examples of Weibull distribution (a) PDF and (b) CDF with constant scale parameter ($\lambda=1$).....	199
Figure 10-10:	Examples of beta distribution (a) PDF and (b) CDF.....	200

List of Tables

Table 1-1:	Injuries resulting from petroleum incidents: pipelines vs. road and railway from 2005 to 2009 (Furchtgott-Roth 2013).....	1
Table 2-1:	Compressive strain limits for a typical API X65 unpressurized pipe.....	14
Table 3-1:	Specimens.....	44
Table 3-2:	Mean true yield stresses of specimens.....	50
Table 3-3:	Comparison of CP and PFJ experimental results.....	64
Table 5-1:	Clamped beam eigenmodes.....	85
Table 5-2:	Imperfection combinations of global eigenmode shapes for geometrically nonlinear analysis.....	92
Table 5-3:	Buckling loads of eigenmodes for soil stiffness $K_s=526$ and $K_s=540$	96
Table 5-4:	Soil stiffness for elastic and nonlinear soil properties.....	109
Table 6-1:	API5L-X65 steel properties.....	115
Table 6-2:	Soil spring properties.....	116
Table 6-3:	Cases of pipelines with flexible joints under investigation.....	117
Table 6-4:	Maximum bending moment reduction and joint rotation in all cases of pipelines with flexible joints.....	118
Table 6-5:	Cases under investigation to compare mitigating measures.....	139
Table 7-1:	Empirical equation coefficients for $\log SRL=a+bM$ (Wells and Coppersmith 1994).....	152
Table 7-2:	Empirical equation coefficients for $\log FD=a+bM$ (Wells and Coppersmith 1994).....	152
Table 7-3:	Empirical equation coefficients for $\log FD=a+bM$ (Moss and Ross 2011).....	152
Table 7-4:	Empirical Equation coefficients for $\log SRL=a+b\log FD$ (Wells and Coppersmith 1994).....	152
Table 7-5:	Uniform and normal distribution parameters of the principal fault displacement component.....	153
Table 7-6:	Seismological parameters and uncertainty weight factors considered in case study 1.....	158
Table 7-7:	Probabilistic strain capacity uncertainty parameters.....	161
Table 7-8:	Mean annual rate of exceeding tensile fracture and local buckling limit states by considering demand and capacity being either non-random or random.....	162
Table 7-9:	Seismological and seismic hazard uncertainty parameters considered in case study 2.....	165
Table 10-1:	Uniform distribution parameters.....	195
Table 10-2:	Normal distribution parameters.....	196
Table 10-3:	Lognormal distribution parameters.....	197
Table 10-4:	Gamma distribution parameters.....	198
Table 10-5:	Weibull distribution parameters.....	199
Table 10-6:	Beta distribution parameters.....	199

Notation

AD	average fault displacement approach of PFDHA
A_r	area of rupture along the geologic fault
c	soil cohesion
D	pipeline nominal diameter
d_{joint}	flexible joint axial displacement
D_{min}	pipe minimum inside diameter
DV	decision variable
$d\lambda_{\Delta}$	mean annual rate differential of fault offset magnitude
$d\lambda_{\Delta_1, \Delta_3}$	mean annual rate differential of fault displacement components Δ_1 and Δ_3
E	steel modulus of elasticity
EDP	engineering demand parameter
F_{LS}	fragility function
f_u	steel ultimate strength
f_y	steel yield stress
H	pipe burial depth
I	cross-section moment of inertia
IM	intensity measure
k_r	rotational stiffness of hinge
K_r	normalized rotational stiffness of hinge
k_s	soil stiffness
K_s	normalized soil stiffness
K_{sd}	normalized downward soil stiffness
K_{su}	normalized upward soil stiffness
L	beam or pipe length
L_1, L_2	distance from head or toe of PGD zone to location of expansion joint
L_3	distance along pipe
L_f	distance between two adjacent flexible joints in a pipeline
LF	fault trace length
L_j	distance between the fault trace location and the maximum bending moment location
L_p	pipe crossing site distance from the fault closest edge
L_{pz}	pipe length in which plastic strain develops
LS	limit state
M (m)	bending moment, earthquake magnitude (lower case letter denotes the value of the variable)
M_{max}	maximum earthquake magnitude seismic source can produce
M_{min}	minimum earthquake magnitude of engineering significance
MD	maximum fault displacement approach of PFDHA
p	pipe internal pressure
P	applied external load
P_{cr}	elastic critical buckling load
$P_{cr,cs,cl}$	elastic critical buckling load of continuous clamped beam resting on foundation
$P_{cr,cs,ss}$	elastic critical buckling load of continuous simply-supported beam resting on foundation
p_e	maximum external hydrostatic pressure
$P_{E,cl}$	elastic critical buckling load of clamped beam without lateral support
$P_{E,ss}$	elastic critical buckling load of simply-supported beam without lateral support
Pos	position of rupture on fault trace
p_u	transverse horizontal soil force
R (r)	distance of site of interest from fault rupture location (lower case letter denotes the value of the variable)
Slip	fault slip occurrence
SRL	surface rupture length
t	pipeline wall thickness
t_u	maximum longitudinal force per unit length at pipe – soil interface
v	rate of all earthquakes above a minimum earthquake magnitude of engineering significance

V	shear force
wD	uncertainty logic weight factor of AD or MD approach of Probabilistic Fault Displacement Hazard Analysis
wM	uncertainty logic weight factor for maximum earthquake magnitude
wv	uncertainty logic weight factor for seismic rate
x	beam longitudinal displacement
y	beam transverse displacement
β	pipeline - fault crossing angle
γ	soil unit weight
γ_{joint}	flexible joint rotation
γ_{pipe}	rotation of pipe segment between two adjacent joints
Δ (δ)	fault displacement (lower case letter denotes the value of the variable)
Δ_1 (δ_1)	fault-trace-parallel horizontal displacement component (lower case letter denotes the value of the variable)
Δ_2 (δ_2)	fault-trace-perpendicular displacement component (lower case letter denotes the value of the variable)
Δ_3 (δ_3)	vertical fault displacement component (lower case letter denotes the value of the variable)
Δ_x	pipeline imposed longitudinal displacement with respect to its axis
Δ_y	pipeline imposed transverse displacement with respect to the its axis
Δ_z	pipeline imposed vertical displacement
$\Delta\lambda_{\Delta}$	mean annual rate of equaling of fault offset magnitude
$\Delta\lambda_{\Delta_1, \Delta_3}$	mean annual rate of equaling of fault displacement components Δ_1 and Δ_3
$\Delta\lambda_{\epsilon}$	mean annual rate of equaling of strains
ϵ_c	compressive strain
ϵ_{cap}	strain capacity
ϵ_{dam}	strain demand
ϵ_e	engineering strain
ϵ_t	tensile strain
ϵ_{true}	true strain
ζ	crack-tip opening displacement toughness
η	ratio of pipe wall defect height over pipe wall thickness
κ	ratio of yield stress to ultimate strength
λ_{LS}	mean annual rate of exceeding limit state
λ_{Δ}	mean annual rate of exceeding fault offset magnitude on pipeline crossing site
μ	shear modulus of the rocks involved in an earthquake
N	axial force
ξ	ratio of pipe wall defect length over pipe wall thickness
σ_e	engineering stress
σ_{true}	true stress
ϕ	soil internal friction angle
ψ	fault dip angle

1 INTRODUCTION

1.1 HISTORICAL BACKGROUND AND PREFACE

Consumption of natural resources for energy production has been rising worldwide since the Industrial Revolution in the 19th century and with greater intensity after the middle of the 20th century. The main energy source used today is oil and natural gas that are drilled from onshore and offshore reservoirs. Even though there is a trend to minimize the use of fossil fuel due to global warming, industry and transportation means still need significant amounts of fuel. However, oil wells are usually located hundreds of kilometers away from the oil end users, namely refineries, tank farms and customers and thus the need to transport oil and oil products over long distances has emerged from the beginning of massive oil production in the 19th century. Nowadays, oil is transported via sea by offshore pipelines and tanker ships or by onshore pipelines, tanker cars or trains. The accumulated experience and collected data after several decades of oil and gas pipelines operation indicate that pipelines remain the safest way for onshore oil transportation. The advantages of pipelines versus truck and train tankers in terms of injuries per billion ton-miles are listed in Table 1-1, for example. These data reveal that oil and gas pipelines outbalance road and railway tankers in terms of safety per billion ton-miles.

Table 1-1: Injuries resulting from petroleum incidents: pipelines vs. road and railway from 2005 to 2009 (Furchtgott-Roth 2013)

		2005	2006	2007	2008	2009	Total	Per Year	Injuries per Billion Ton-Miles
Road	Hospitalization	9	10	10	6	9	44	8.8	0.2526
	Total	38	37	38	17	41	171	34.2	0.9816
Railway	Hospitalization	20	2	1	0	0	23	4.6	0.1925
	Total	24	2	4	0	1	31	6.2	0.2594
Hazardous Liquid Pipeline	Hospitalization	2	2	10	2	4	20	4.0	0.0068
Hazardous Gas Pipeline	Hospitalization	45	32	37	53	58	225	45.0	0.1130

The first pipelines for oil transportation were constructed in the U.S.A. in the 1850s and were made of cast iron with oxyacetylene welds. Later, the introduction of steel in construction engineering and the application of stricter safety regulations contributed to the construction of pipes with larger diameter and capable of transporting oil under high pressure and temperature. Additionally, oxyacetylene welds have been proven during the past decades as insufficient for pipeline applications after many and severe pipe failures were attributed to them. Modern onshore and offshore pipelines are now constructed

mainly by carbon steel and pipe parts are jointed with girth butt welds. The major advantages of steel pipes are strength, ease of installation, high flow capacity, leak resistance, long service life, reliability, versatility and economy (AISI 2007).

Onshore pipelines are divided into four categories with respect to their role in the oil supply chain: (i) gathering, (ii) feeder, (iii) transmission and (iv) distribution lines. The present dissertation focuses on transmission pipelines, also referred as energy-highways, which transport oil, natural gas and fuel products within a province and across international boundaries. The diameter of such pipelines ranges usually from 101.6mm (4in) to 1219.2mm (48in). Fuel products are transported under high pressure that can range up to 70bars or more (Canadian Energy Pipeline Association 2016). As an example, the major transmission natural gas pipeline network of Europe is illustrated in Figure 1-1. More pipelines are under construction or design to transport oil and natural gas from the Arabian Peninsula, the Caucasus area, North Africa etc. Transmission pipelines can be either above ground (Figure 1-2) or buried (Figure 1-3), depending on local geological conditions, safety restrictions, environmental issues, etc. Buried pipelines are investigated in this thesis, which are placed a few meters below the ground surface for protection against corrosion and external or third party damage. The surrounding soil provides support to the pipe cross-section against the internal pressure. Buried pipelines, also referred as underground pipelines, are embedded inside a trench, which is then backfilled with soil material. A typical trench cross-section is depicted in Figure 1-4.



Figure 1-1: Existing and new natural gas transmission pipeline network of Europe ("European Commission, Energy - Infrastructure" 2008)



Figure 1-2: Above ground section of Alaska Pipeline ("National Snow & Ice Data Center" 2016)



Figure 1-3: Buried pipeline construction ("ConstructionWeekOnline.com" 2016)

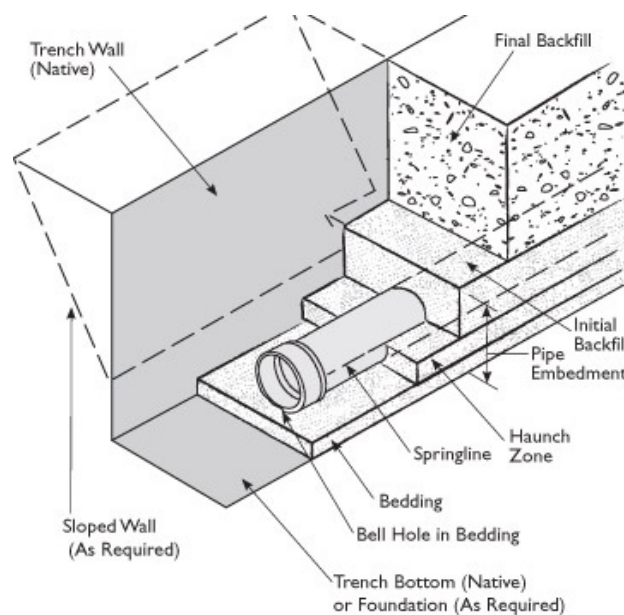


Figure 1-4: Cross-section of a typical trench for buried pipelines ("Georg Fischer Harvel LLC" 2016)

The construction of an onshore buried pipeline includes eight major stages (Figure 1-5):

- Stage 1 – Pre-construction survey: The construction area is surveyed and marked in order to locate any utility lines and agricultural drainages and to prevent accidental damage during the pipeline construction.
- Stage 2 – Cleaning and grading: The pipeline route is cleared of vegetation, while temporary erosion control measures are taken to prevent ground moving prior to any excavation.
- Stage 3 – Trenching: The trench is excavated using trenching machines. The excavated soil is temporarily stockpiled near to the trench.
- Stage 4 – Pipe stringing and bending: Pipeline parts are transported to the construction site and are strung along the route, near to the trench. A pipe-bending machine bends individual pipe parts for advancement to any route change or at locations where there is significant change in the natural ground contours.
- Stage 5 – Welding, x-ray inspection and pipe coating: The pipe sections are aligned along the trench, welded together and placed on temporary supports. Welding inspection is carried out using x-ray machines. Welded joints are then coated and electronically inspected.

- Stage 6 – Lowering pipe in and backfilling: The pipe assembly is lowered into the trench by sideboom tractors and then the trench is backfilled.
- Stage 7 – Testing: Hydraulic test of the pipe is carried out under pressure using water.
- Stage 8 – Restoration: The construction area is restored as nearly as possible to its original form.



Figure 1-5: Stages of onshore buried pipeline construction (Constitution Pipeline 2016)

1.2 ACTIONS ON PIPELINES

The design and construction of a buried transmission pipeline is a complex procedure that employs different engineering disciplines (e.g. hydraulic, mechanical, civil, geotechnical, material engineers). The design procedure of a pipeline system can be divided into three major phases:

- Process design: specification of material, flow capacity, operational internal pressure and temperature;
- Design in operational conditions: pipe strength analysis against non-accidental/operational actions, design of corrosion protection, specification of pipeline components (e.g. pump stations and valves);
- Design against accidental actions: pipe strength analysis against accidental actions, such as third party damage, explosion, unaccepted flow interruption and seismic-induced actions.

The main design loads in operational conditions are the internal pressure, vertical earth pressure, thermal expansion, live surface loads (wheel loads from vehicles, trains, etc.), stresses due to route change, impact of a surface load, etc. Design in operational conditions is carried out in stress terms, where the developing stresses should not exceed the pertinent code-based limits (e.g. material yield limit). Special attention is also given to weld design in order to avoid any leak or fracture in the weld areas. The major potential non-seismic failure modes are corrosion, fatigue, buckling, corrosion fatigue, ring deflection, flotation, dynamic fracture and stress corrosion cracking. To prevent these failures specific preventing measures are applied, such as coatings for external corrosion, linings for internal corrosion, crack arrestors for dynamic fracture and cathodic protection for corrosion. Relevant structural design codes and provisions for buried pipeline design against non-seismic actions are ASME B31.4 and ASME B31.8 (American Society of Mechanical Engineers 2012), Eurocode 3 – Part 4-3 (European Committee for Standardization 2007), API 5L (American Petroleum Institute 2012), API 1102 (American Petroleum Institute 2002), API 1104 (American Petroleum Institute 2005), DNV-OSS-300 (Det Norske Veritas 2012a), DNV-RP-B401 (Det Norske Veritas 2011), DNV-RD-C204 (Det Norske Veritas 2010a), DNV-RP-D101 (Det Norske Veritas 2008), DNV-RP-F101 (Det Norske Veritas 2010b), DNV-RP-F106 (Det Norske Veritas 2006), DNV-RP-F110 (Det Norske Veritas 2007).

Design of buried pipelines against earthquake-induced actions is a crucial aspect given that any pipe fracture, leakage or failure may have devastating consequences in the environment (soil, water and air pollution), nearby populated areas (injuries or fatalities due to explosion), as well as economic losses (flow interruption, repair cost, insurance cost). The response of buried pipelines to earthquake effects differs from that of common civil engineering structures (e.g. buildings, bridges, towers, etc.). The latter are founded in the soil and in case of an earthquake event, their foundation is forced to follow the ground motion and the superstructure is excited due to its inertia. On the other hand, in case of buried pipelines, the foundation soil surrounds the pipeline/structure, which is forced to follow the soil movement by developing excessive deformation. In other words, the seismic performance of buried pipelines depends on the response of the coupled pipe – soil interacting system. Earthquake-induced actions on pipelines are divided into two distinct categories: (i) transient ground displacements (TGD) and (ii) permanent ground displacements (PGD). Ground shaking caused by seismic wave propagation is related to TGD. Permanent ground displacements are associated to ground failure during an earthquake event. The major PGDs are landslide, slope failure, tectonic fault rupture and liquefaction-induced lateral spreading. Relevant structural design codes and provisions for buried pipeline design against seismic actions are Eurocode 8 – Part 4 (European Committee for Standardization 2006), CSA-Z662-07 (Canadian Standards Association 2007), ALA (American Lifelines Alliance 2005), IITK – GSDMA (Indian Institute of Technology Kanpur and Gujarat State Disaster Management Authority 2007) and Seismic Design for Gas Pipelines (Japan Gas Association 2000).

1.3 REVIEW OF PIPELINE DAMAGES DUE TO EARTHQUAKE EFFECTS

1.3.1 Historical pipeline damage due to earthquake effects

Pipelines are vulnerable to earthquake effects and pipe failures in the 20th century have been reported after the 1906 San Fernando (Manson 1908), 1933 Long Beach (Wood 1933), 1952 Kern County (Steinbrugge and Moran 1954), 1964 Alaska (Hansen 1971), 1964 Niigata (Hamada and O'Rourke 1992), 1971 San Fernando (McCaffrey and O'Rourke 1983), 1976 Guatemala (O'Rourke and Liu 1999), 1976 Tangshan (Sun and Shien 1983), 1979 Imperial Valley (Waller and Ramanathan 1980), 1983 Coalinga (Isenber and Escalante 1984), 1983 Nihonkai-Chunbu (Hamada and O'Rourke 1992), 1987 Whittier Narrows (Wang 1990), 1989 Loma Prieta (Hamada and O'Rourke 1992), 1991 Costa Rica (O'Rourke and Ballantyne 1992), 1993 Kushiro-Oki (Wakamatsu and Yoshida 1994), 1994 Northridge (O'Rourke and Palmer 1994), 1995 Kobe (Nakata and Hasuda 1995), 1999 Kocaeli (Earthquake Engineering Research Institute 1999) and 1999 Chi-Chi (Takada et al. 1999). Pipelines may suffer minor or even severe damages during earthquake events. Some indicative pipeline damage cases caused by recent earthquakes were reported by O'Rourke and Liu (1999):

- The 1964 earthquake in Anchorage, Alaska, caused over 200 fractures in gas pipelines and 100 fractures in water distribution lines. The majority of pipe fractures was caused by landslides, ground cracking and faulting.
- The 1971 San Fernando earthquake resulted in 1400 fractures in various pipeline systems, which led to temporal lack of water, sewage and gas supply in the city of San Fernando. Research carried out after the earthquake revealed that liquefaction-induced lateral spreading was the cause of damage in water and oil transmission lines.
- The largest reported pipeline loss in history was the destruction of the trans-Ecuadorian 660mm diameter pipeline, reported after the 1987 Ecuador earthquake. The pipeline loss cost about \$850 million in sales and reconstruction.

1.3.2 Pipeline subjected to faulting

Seismic fault rupture has been identified as the dominant cause of pipeline catastrophic failure after past major earthquake events (O'Rourke and Liu 1999). Fault movement is a significant geohazard and is applied on the pipeline in a quasi-static manner, which is not necessarily associated with severe seismic shaking. A seismic fault is defined as a discontinuity between two blocks of the earth crust, where relative movement can occur to release the concentrated energy below the crust. The fault movement is usually concentrated in relatively narrow zones, referred as fault planes. The two "sides" of the fault zone are called blocks. The moving block is called hanging wall, while the other block is referred as footwall of the fault. A fault can be identified in a geological map by the interruption and the transfer of geological formations. The fault trace, thus, appears as a line where the geological formations are interrupted. The rupture surface is usually assumed to be planar. In nature, however, a single planar fault can be hardly found. More than one faults, instead, are located "side-by-side" and a fault zone is created, where the prevailing tectonic stresses are defused. Tectonic faults are categorized in general as:

- normal, where the soil rupture incline is downwards (Figure 1-6a);
- reverse, where the soil rupture incline is upwards and both soil blocks are heavily compressed and consequently the hanging wall is forced to move upwards (Figure 1-6b);
- strike-slip, where the rupture plane is almost vertical and relative fault block slip takes place along the rupture plane (Figure 1-6c).

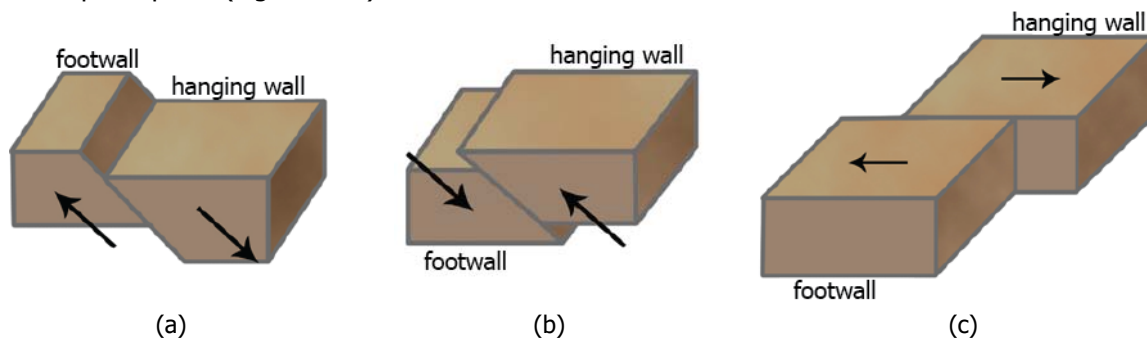


Figure 1-6: Fault types: (a) normal, (b) reverse and (c) strike-slip

Fault activation is related to soil movement that sometimes can reach the order of meters. The estimation of the expected fault offset magnitude is based on the geological, geotechnical and seismological surveys carried out for the fault under investigation. However, estimating the characteristic fault offset during the pipe lifetime is in fact quite difficult due to limited data and the inherent uncertainty of earthquake events. In practice, thus, empirical relations are used for this estimation. Such equations among fault characteristics (fault length, earthquake magnitude, fault width, average and maximum offset, surface rupture length) were proposed by Wells and Coppersmith (1994) for every fault type. The average fault displacement is related to the earthquake magnitude, for example, in Figure 1-7 where regression curves are presented for strike-slip, normal and reverse fault type. The single lines (solid lines) in Figure 1-7a represent a combined model, while the curves in Figure 1-7b correspond every fault type separately (Wells and Coppersmith 1994).

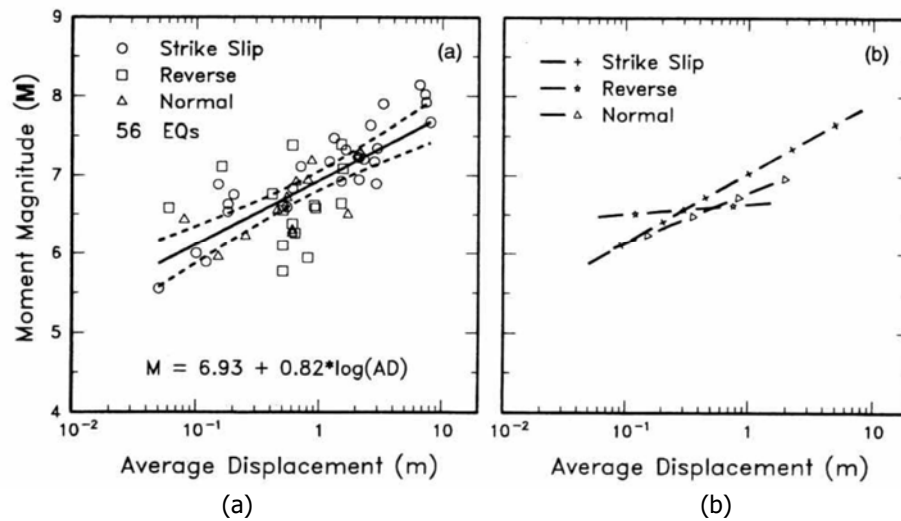


Figure 1-7: Regression of average fault displacement on magnitude (Wells and Coppersmith 1994)

When a buried pipeline is subjected to faulting, it is forced to follow the soil displacement by developing excessive deformation and consequently complex stress-state. Such pipe deformation due to normal, reverse and strike-slip faulting is schematically illustrated in Figure 1-8, where for every fault type two stages of soil movement are depicted with smaller and larger corresponding pipe deformation, respectively. In every case, the pipe deformation is a smooth curved line.

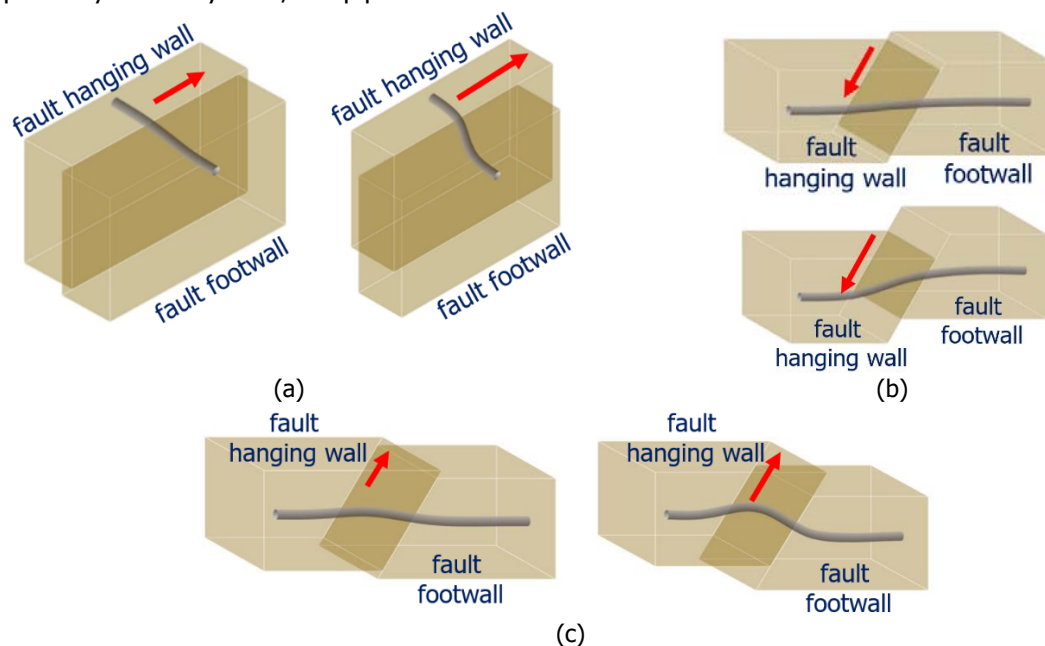


Figure 1-8: Schematic illustration of two successive stages of pipeline deformation due to (a) strike-slip, (b) normal and (c) reverse faulting

1.3.3 Pipeline failure modes due to faulting

The integrity of buried pipelines subjected to faulting is heavily endangered by the development of high stresses and strains in critical locations. The potential major failure modes in such case are:

- Tensile fracture: The excessive tensile strains may rupture the pipeline wall at areas of strain concentration or defected locations. Areas of great concern are the girth welds between the adjacent pipeline parts, assuming that the pipeline is corrosion- and defect-free. An example of girth weld tensile failure is illustrated in Figure 1-9.



Figure 1-9: Pipe girth weld tensile fracture ("Impact Solutions" 2016)

- Buckling: Compression may cause local (Figure 1-10) or global (Figure 1-11) instability of the pipe. Regarding the local phenomenon, strain concentration leads to the formation of a wrinkle that extends over a short pipe length. The wrinkle then evolves to a local buckle as compression increases. The dominant parameters affecting the pipe instability are the diameter over thickness ratio (D/t) and the burial depth. Pipelines being relatively shallowly buried with low ratio D/t tend to buckle globally ("beam-mode" or upheaval buckling), while deeply buried pipes with high ratio D/t tend to buckle locally (Yun and Kyriakides 1990).



Figure 1-10: Wrinkling of a 2.2m diameter steel water pipe at a fault crossing in Kullar, Izmit in the 1999 Kocaeli Earthquake (Uckan et al. 2015)



Figure 1-11: Upheaval buckling of onshore buried steel pipeline due to faulting (Yun and Kyriakides 1990)

- Cross-section ovalization: External loading, such as ground movement, may cause flattening or ovalization of the pipe cross-section, which directly affects the strength of the pipe and its operability (Figure 1-12).

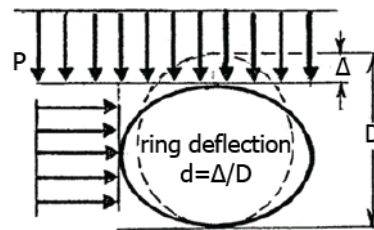


Figure 1-12: Pipe cross-section ovalization due to external loading (AISI 2007)

1.3.4 Preventive measures against the consequences of faulting on pipelines

Avoiding pipeline failure and associated leakage is the major priority in pipeline design against faulting and remains a top research objective for both academia and industry. A set of different seismic countermeasures is thus employed in engineering and constructional practice to minimize the developing strains on pipe wall, mainly by reducing pipe – soil frictional forces. The commonly adopted measures are pipe embedment in a shallow sloped-wall trench, pipe wrapping with friction reducing geotextile, construction of a wider trench, use of culverts and backfilling with pumice. Further details on the mitigating measures are presented in section 2.5.

In the present dissertation, the effectiveness of a new mitigating measure against the consequences of faulting on onshore buried steel pipelines is evaluated, namely integrating flexible joints between the pipe adjacent parts in the fault crossing area, an idea initially proposed by Bekki et al. (2002). This concept introduces a different design approach for reducing the risk of failure instead of reducing the developing pipe – soil friction, by transforming the pipeline structural system from continuous to segmented, to concentrate strains at the joints and retain steel parts barely undeformed and consequently unstressed. Flexible joints are widely used in the piping industry to absorb thermal expansion and thrust. A major advantage is that flexible joints are commercial products and can thus be customized upon diameter, internal pressure and allowable deformations. The introduction of flexible joints between the adjacent pipe parts is schematically illustrated in Figure 1-13.



Figure 1-13: Schematic illustration of the introduction of flexible joints in a pipe

1.4 OBJECTIVE AND STRUCTURE OF THE THESIS

This thesis focuses on onshore buried steel pipelines with flexible joints that cross an active tectonic fault. The main purpose of this research is to investigate the effectiveness of flexible joints in buried pipelines – fault crossings in terms of mitigating the consequences of faulting on pipes. To that effect, a combined experimental and numerical approach has been followed. Additionally, acknowledging the importance of pipelines and motivated by the fact that the estimation of fault offset is highly uncertain, a comprehensive methodology for the performance assessment of buried pipelines at fault crossings is presented. The research is thus based on three aspects that include on the one hand experimental tests and numerical calculations to estimate the seismic performance of pipelines with flexible joints and on the other hand performance-based earthquake engineering to formulate the performance assessment of pipelines at fault crossings.

A brief introduction to buried pipeline – fault crossing and the statement of the problem under investigation are presented in this first chapter. Then, Chapter 2 contains a literature review regarding the behavior of continuous and segmented pipelines at fault crossings, presenting analytical, numerical and experimental research that has been carried out until now, as well as relevant structural provisions and guidelines. The seismic countermeasures used in engineering practice and proposed in the literature for pipeline protection are also discussed.

In Chapter 3, the set-up and the results of the experimental investigation that was carried out in the Institute of Steel Structures at the School of Civil Engineering of the National Technical University of Athens, in the context of the present doctoral thesis are described in detail. The experimental work aimed at investigating the strain reduction caused by the integration of flexible joints in beam specimens modeling pipes without the effect of surrounding soil subjected to imposed displacement. The specimens' deformation models the pipe deformation caused by fault rupture. In Chapter 4, the experimental results are utilized to calibrate the numerical models. The numerical and the experimental results are compared in terms of deformation and developing strains.

Then, in Chapter 5, a numerical effort is presented to investigate the buckling and post-buckling response of beams with internal hinges under compression resting on foundation. The aim is with the use of a simplified model to investigate the likelihood of upheaval buckling emerging as a potential failure mode in case of reverse fault rupture, where high compression is developed. Then, in Chapter 6, a thorough numerical investigation of buried pipelines with flexible joints subjected to strike-slip faulting is presented. The optimum number and position of joints in buried pipelines is addressed and all parameters affecting the pipe behavior are examined through extensive parametric studies. Preliminary design guidelines regarding the integration of joints in buried pipes are provided.

In Chapter 7, the performance assessment of buried pipelines at fault crossing is presented, which includes the seismic hazard assessment of fault offset, the pipeline structural analysis and the pipe performance assessment. Finally, in Chapter 8, the findings and the outcomes of the doctoral thesis are summarized. The main intellectual contributions are highlighted and some issues for future research are suggested.

2 THEORETICAL BACKGROUND AND LITERATURE REVIEW

2.1 INTRODUCTION

Aim of the doctoral thesis is to investigate the mechanical behavior of buried pipelines with flexible joints that are subjected to fault rupture. The investigated pipelines are assumed to be corrosion- and defect-free. According to pertinent seismic provisions and the engineering practice, the pipeline is assumed to intersect a planar fault with zero thickness, i.e. disturbance of geological formulations and distributed faulting issues are neglected. The pipeline segment crossing a seismic tectonic fault is assumed to be straight without bends, as changes in pipe route may impose undesirable forces on the pipe due to fault movement.

The pipeline – fault crossing geometry is schematically illustrated in Figure 2-1, where the fault dip angle is denoted by ψ , the pipe – fault crossing angle by β , the fault trace length by LF and the pipe crossing site distance from the fault closest edge by L_p . The fault displacement magnitude Δ can be represented in three dimensions with three components: Δ_1 and Δ_2 are the fault-trace-parallel and fault-trace-perpendicular horizontal components, while Δ_3 represents the vertical component:

$$\Delta = \sqrt{\Delta_1^2 + \Delta_2^2 + \Delta_3^2} \quad (2-1)$$

$$\Delta_2 = \begin{cases} \Delta_3 / \tan \psi & 0^\circ < \psi < 90^\circ \\ 0 & \psi = 90^\circ \end{cases} \quad (2-2)$$

It is noted that the fault dip angle ψ ranges from 0° (theoretical value) to 90° (vertical fault plane). When $\psi=90^\circ$ the Δ_2 fault-perpendicular component yields $\Delta_2=0$, as defined by the fault geometry.

The spatial fault offset is defined on the fault (global) coordinate system (1,2,3), while the local coordinate system of the pipeline (x,y,z) is also specified by considering the global coordinate system being rotated in the horizontal plane by the pipeline – fault crossing angle β . The pipeline imposed displacements can be also expressed in the local system: Δ_x is the longitudinal displacement with respect to the pipeline axis, Δ_y is the transverse displacement with respect to the pipeline axis and Δ_z is the pipeline vertical displacement, which are evaluated via the expressions:

$$\begin{aligned} \Delta_x &= \Delta_1 \cos \beta + \Delta_2 \sin \beta \\ \Delta_y &= -\Delta_1 \sin \beta + \Delta_2 \cos \beta \\ \Delta_z &= \Delta_3 \end{aligned} \tag{2-3}$$

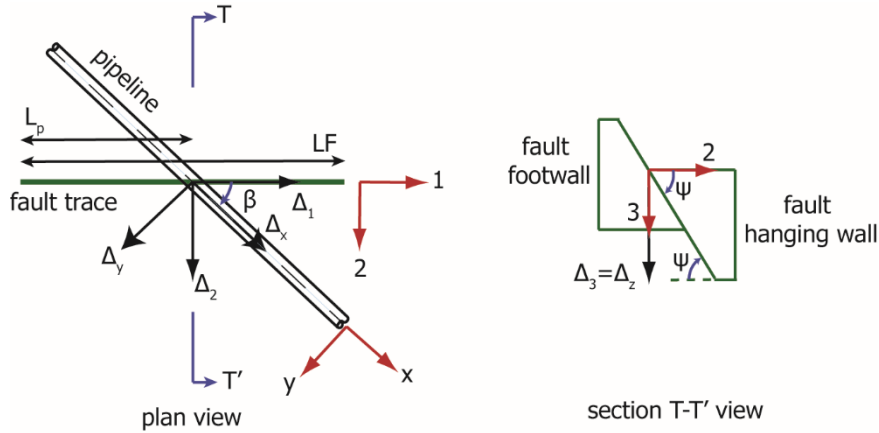


Figure 2-1: Geometry of pipeline – fault crossing

2.2 PIPELINE STRAIN-BASED DESIGN AGAINST FAULTING

2.2.1 Strain-based versus stress-based design

The activation of a tectonic fault is associated with large ground displacements that are imposed on the buried pipeline. The pipe is curved due to faulting and consequently lateral forces are imposed from the surrounding backfill soil on the curved pipe length. The pipe also experiences elongation resisted by the frictional forces (pipeline – soil interaction) that are activated along the so-called anchor length (Figure 2-2). The combination of lateral and frictional forces results in the development of tensile and compressive stresses on the pipe wall.

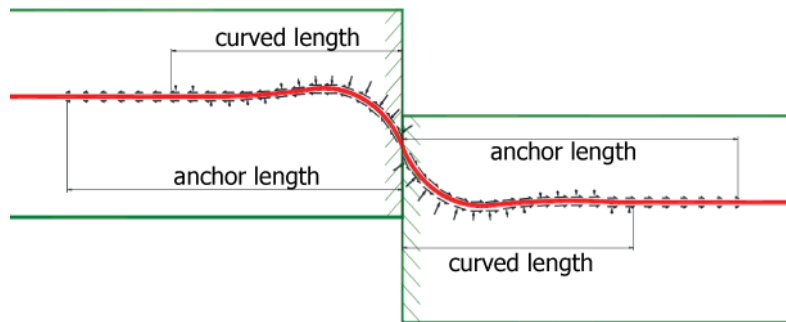


Figure 2-2: Transverse and frictional forces on a buried pipeline due to strike-slip faulting

The problem under investigation is displacement-controlled and consequently strain-controlled rather than stress-controlled. Large stresses are expected to develop on the pipeline wall due to faulting that will probably exceed the yield limit, while the corresponding strains may remain below a limit that is associated to failure, i.e. concentration of tensile strains may cause tensile rupture, while concentration of compressive strains may induce local buckling. The pipeline design against permanent ground displacements is thus carried out in strain terms (Strain Based Design) rather than in stress terms, exploiting the steel's ductility. Mohr (2003) provides a characteristic example to demonstrate that the strain-based design is appropriate when the performance limits for the design, in at least one direction, are better described in strain-terms than in stress-terms: when a pipeline is fitted to a curved surface

(e.g. over a hill), then the curve of the ground surface determines the pipe curve and consequently its strain. Thus, the pipe strain is obtained directly from the surface curvature instead of going through the pipe stress and then back to the strain. Furthermore, if the surface curve is sharp enough to cause pipe yielding due to bending as the pipe fits the curve, then the strain-based design becomes more important. Considering then in the same case two pipes made of different steel grade (different stress-strain relations) fitted to the same surface curve, they will exhibit the same strains but different stresses. In such case, a stress upper limit would lead to different evaluation of the pipe's response. On the other hand, if the upper limit is strain-based, then the two pipes would be evaluated as the same in relation to that limit.

2.2.2 Code-based strain limits

Strain-based design of pipelines has been incorporated in codes, standards and provisions for both the construction and operation of pipes. The provision A842.23 in code B31.8 (American Society of Mechanical Engineers 2012) indicatively defines that when the support of a pipeline (e.g. foundation soil) is subjected to a predictable non-cyclic displacement (e.g. fault movement), the stress limits need not be used, unless steel yielding threatens the pipe integrity. Instead, if plastic strains are expected, then the pipe eccentricity, pipe out of roundness and the ability of welds to undergo such strains without failure should be considered. The longitudinal strain limit depends upon the steel ductility, the pipe buckling behavior and the previously experienced plastic strains.

2.2.2.1 Compressive strain

Compressive strains may lead to local or global buckling of the pipeline (section 1.3.3). Local buckling is not directly associated with failure. Strain concentration leads to the initiation of a wrinkle that neither interrupts fuel flow, nor allows a leak. However, the increase of compression leads to the evolution of the wrinkle to a local buckle and consequently the pipe may reach a predefined limit state. Additionally, local buckling can also be recognized as a sign of the pipe degrading capacity to resist other loadings. Thus, pertinent codes suggest upper compressive strain limits to avoid local buckling of the pipe wall.

The compressive strain capacity of a pipe is affected by three main parameters:

- Girth welds: It has been demonstrated by several researchers through experimental studies that girth welds tend to attract the buckle to a nearby region of the pipe wall within a distance of approximately constant moment loading (e.g. B31.8 (ASME) 2012; Dorey et al. 2000; Prion and Birkemoe 1992; Sherman 1983). This attraction is influenced by welding residual stresses, pipe steel inhomogeneous properties along the pipe and misalignment of the pipe parts on either sides of a weld.
- Internal pressure: The pipe internal pressure increases the resistance to local buckling because it creates tensile hoop stresses that assist the pipe to resist the diametrical changes caused by the local buckling, tends to suppress some shapes of buckles and, in particular, it favors the outward buckle against the diamond-shape buckle.
- External pressure: The external pressure reduces the resistance to local buckling and may be potentially responsible for a propagating buckle.

The compressive strain limits used nowadays are provided by the following standards:

- Guidelines for the Design of Buried Steel Pipe (American Lifelines Alliance 2005)

The compressive strain limit in the operable limit state is given by the expression:

$$\epsilon_c = 0.5 \left(\frac{t}{D'} \right) - 0.0025 + 3000 \left(\frac{pD}{2Et} \right)^2, \quad D' = \frac{D}{1 - 3 \frac{(D - D_{min})}{D}} \quad (2-4)$$

The compressive strain limit in pressure integrity limit state is given by the expression:

$$\varepsilon_c = 1.76 \frac{t}{D} \quad (2-5)$$

- Eurocode 8 – Part 4 Silos, Tanks and Pipelines (European Committee for Standardization 2006)

The compressive strain limit is provided by the expression:

$$\varepsilon_c = \min \left\{ 1\%; 40 \frac{t}{D} (\%) \right\} \quad (2-6)$$

- Z622-07 Oil and Gas Pipeline Systems (Canadian Standards Association 2007)

The compressive strain limit is given by the expression:

$$\varepsilon_c = \begin{cases} 0.50 \left(\frac{t}{D} \right) - 0.0025 + 3000 \left(\frac{(p - p_e) D}{2E_s t} \right)^2, & \text{for } \frac{(p - p_e) D}{2t f_y} < 0.4 \\ 0.50 \left(\frac{t}{D} \right) - 0.0025 + 3000 \left(\frac{0.4 f_y}{E_s} \right)^2, & \text{for } \frac{(p - p_e) D}{2t f_y} < 0.4 \end{cases} \quad (2-7)$$

where t is the pipe wall thickness, D is the external diameter, D_{\min} is the minimum inside diameter, E is the steel modulus of elasticity, f_y is the effective specified minimum yield strength, $E_s=207\text{GPa}$, p_e is the maximum external hydrostatic pressure and p is the internal pressure.

Finally, to acquire a better perspective regarding the different compressive strain limits provided by codes and standards, a typical API X65 unpressurized ($p=0\text{kPa}$) pipe is considered, featuring a diameter of $D=914\text{mm}$ and wall thickness of $t=12.7\text{mm}$. The different compressive strain limits are listed in Table 2-1, indicating variation between the proposed compressive strain limits.

Table 2-1: Compressive strain limits for a typical API X65 unpressurized pipe

Standard	Expression	Compressive strain limit
American Lifelines Alliance (2005) – Operable limit	Eq. (2-4)	0.39%
American Lifelines Alliance (2005) – Pressure integrity	Eq. (2-5)	2.45%
Eurocode 8 – Part 4 (European Committee for Standardization 2006)	Eq. (2-6)	0.56%
Z622-07 Oil (Canadian Standards Association 2007)	Eq. (2-7)	0.44%

2.2.2.2 Tensile strain

Tensile strains may rupture the pipeline wall at areas of strain concentration or defected locations. Areas of great concern are the girth welds between the adjacent pipeline parts due to the reduced ductility of steel in these regions and the imperfections associated with the welding process. Tension tests on strip specimens and in wide plates are usually carried out to experimentally investigate the tensile strain limit, e.g. Wang et al. (2010). The tensile strain limits used nowadays are recommended by the following standards/codes:

- Guidelines for the Design of Buried Steel Pipe (American Lifelines Alliance 2005)

The tensile strain limit in the operable limit state is proposed as:

$$\varepsilon_t = 2\% \quad (2-8)$$

The recommended tensile strain limit in the pressure integrity limit state is:

$$\varepsilon_t = 4\% \quad (2-9)$$

- Eurocode 8 – Part 4 Silos, Tanks and Pipelines (European Committee for Standardization 2006)

The recommended tensile strain limit is:

$$\varepsilon_t = 3\% \quad (2-10)$$

- Z622-07 Oil and Gas Pipeline Systems (Canadian Standards Association 2007)

The tensile strain limit is given by the following expression, where surface-breaking defects are considered:

$$\varepsilon_t = \zeta^{(2.36-1.583\lambda-0.101\xi\eta)} (1 + 16.1\kappa^{-4.45}) (-0.157 + 0.239\xi^{-0.241}\eta^{-0.315}) \% \quad (2-11)$$

where ζ is the apparent CTOD (mm) toughness ($0.1 \leq \zeta \leq 1$), CTOD is the Crack-Tip Opening Displacement from fracture mechanics tests, κ is the ratio of yield strength to tensile strength (f_y/f_u), ξ is the ratio of defect length over pipe wall thickness ($2c/t$) with $1 \leq \xi \leq 10$, η is the ratio of defect height over pipe wall thickness with $\eta \leq 0.5$. Further information on the background of Eq. (2-11) is provided by Wang et al. (2007). Considering for example a pipe with a minor defect and with $\xi=1.0$, $\eta=0.1$, $\zeta=0.7$ and $\kappa=0.775$, the tensile strain limit after Eq. (2-11) is 4.5%.

- FEMA 233 (Yokel and Mathey 1992)

The recommended tensile strain limit for steel pipelines is:

$$\varepsilon_t = 0.3\% \quad (2-12)$$

- DNV-OS-F101 (Det Norske Veritas 2012b)

According to DNV-OS-F101, if the accumulated plastic strain exceeds 0.3%, then Engineering Critical Assessment (ECA) acceptance criteria are needed for both girth- and seam-welds. This statement leads to the application of fracture mechanics analysis or fitness-for-purpose criteria in order to gain thorough understanding of brittle and ductile failure, as well as plastic collapse of the area of interest.

- EN 1594 (European Committee for Standardization 2013)

In EN 1594 it is stated that in case design strain exceeds 0.5%, following a Strain-Based Design procedure, the allowable yield over-strength ratio should not exceed 0.85%.

- Tensile strain limits provided by codes and standards range from 0.3% up to 4%. However, there is concern regarding the integrity of girth welds and their capability to develop such high strains due to the metallurgical alterations induced by the steel heat-affected zone during the welding procedure. For this reason DNV-OS-F101 (Det Norske Veritas 2012b), EN 1594 (European Committee for Standardization 2013) and FEMA 233 (Yokel and Mathey 1992), as well as engineering practice (Gantes and Bouckovalas 2013) suggest the adoption of conservatively lower tensile limit equal to 0.5%. Additionally, higher tensile strain limits suggested by codes are based on the assumption of a defect-free homogeneous pipe material (Liu et al. 2009).

In the present thesis, the operable limits proposed by the American Lifelines Alliance (2005) are adopted, namely the compressive limit of Eq. (2-4) and the tensile limit of Eq. (2-8). The considered strain limits in this study constitute a conservative approach, but are nevertheless considered as appropriate in light of demonstrating that the proposed flexible joints can ensure both the integrity and the operability of the pipe after its severe deformation due to faulting. It is noted that the internal pressure will not be considered hereinafter, as a less favorable situation, and thus the corresponding term of compressive limit in Eq. (2-4) is neglected.

2.3 ANALYSIS OF CONTINUOUS PIPELINE AT FAULT CROSSINGS

Analytical or numerical approaches have been applied to assess the pipe stress-state due to faulting. Newmark and Hall (1975) were the pioneers of such work and analytically calculated the pipeline wall stress-state, considering the pipeline as a long cable undergoing small displacements and being

intercepted by a planar fault. The analysis did not account for the pipe flexural rigidity and faults causing pipe compression could not be analyzed. Kennedy et al. (1977) extended the work of Newmark and Hall (1975). The authors considered a non-uniform friction interface between the pipe and the surrounding soil with the latter assumed to be cohesionless. The methodology was limited to pipe – fault crossing angles that cause only pipe tension and not compression. Later, Kennedy and Kincaid (1983) extended the work of Kennedy et al. (1977) by accounting for the lateral and the vertical soil pressure on the pipe. Wang and Yeh (1985) integrated the pipe bending stiffness in the established analytical models. The pipe was divided into four segments, namely two segments in the fault vicinity with constant curvature and two outer segments, modeled as beams on elastic foundation (Figure 2-3). The axial force and the bending moment at point B of the pipeline were obtained through an iterative procedure.

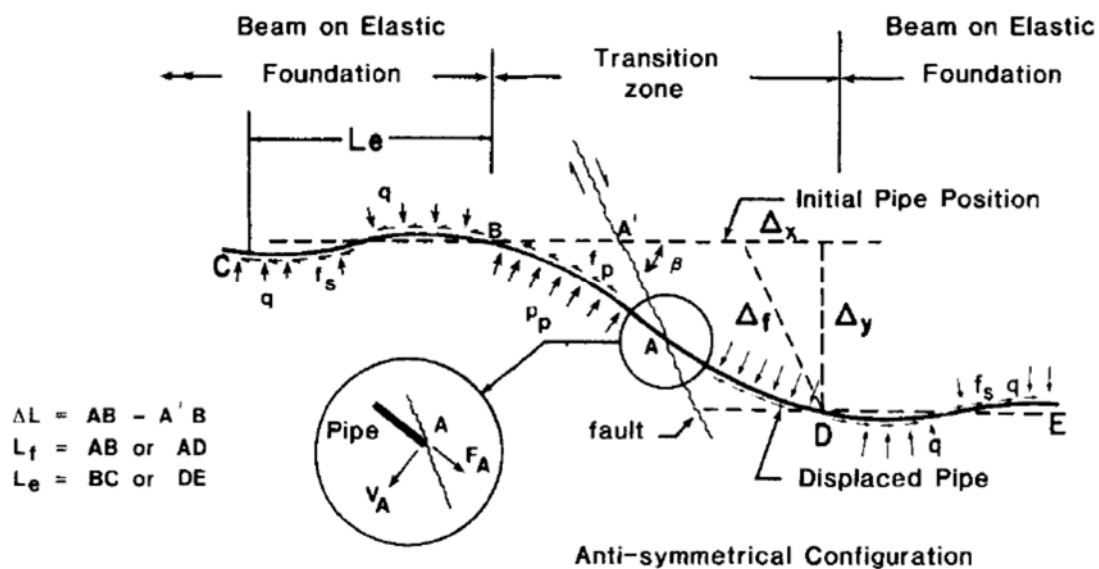


Figure 2-3: Pipeline – fault crossing analytical model proposed by Wang and Yeh (1985)

The pipe model of elastic beam was adopted by Vougioukas et al. (1979) to account for the vertical and horizontal fault movements. McCaffrey and O'Rourke (1983) and Desmod et al. (1995) took advantage of field observations in gas and water pipelines after the 1971 San Fernando earthquake and examined the developed strains. Wang and Wang (1995) modeled the pipe as a beam on elastic foundation, while Takada et al. (2001) proposed a more accurate model by relating the cross-sectional deformation and the pipe bending angle to calculate the maximum strain. Recently, Karamitros et al. (2007, 2011) improved the previous analytical approaches for strike-slip and normal fault crossings by combining the model of a beam on elastic foundation (segments AA' and CC') and the elastic beam theory to estimate the maximum strains and the relation between bending moment, shear force and rotation angle at points A and C (Figure 2-4).

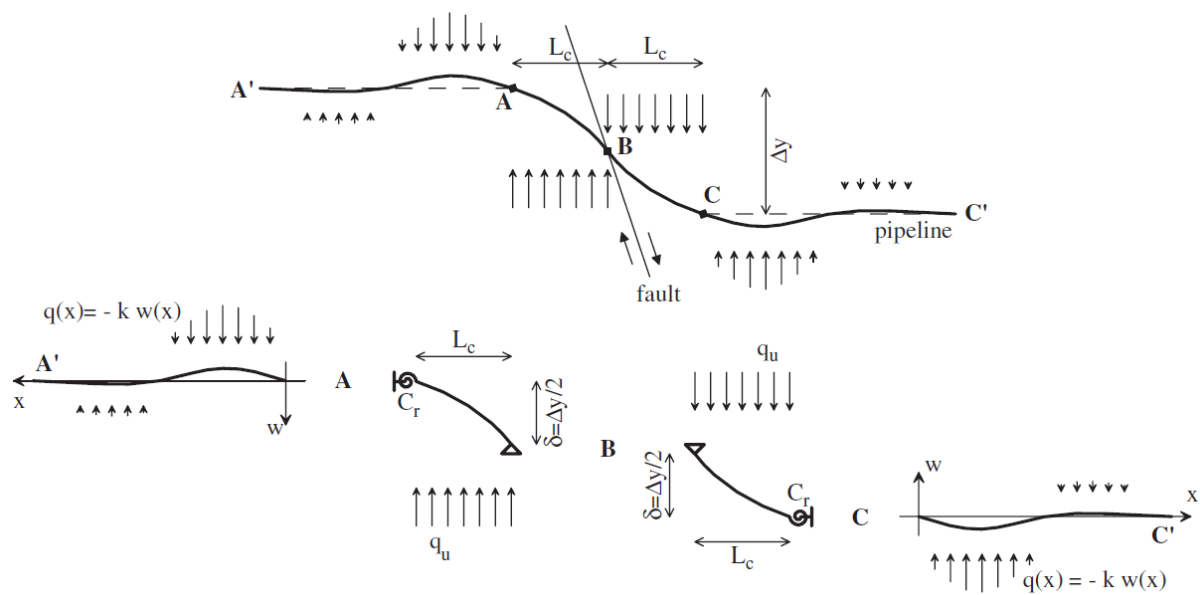


Figure 2-4: Pipeline partitioning into four segments proposed by Karamitros et al. (2007)

Trifonov and Cherniy (2010, 2012) presented a semi-analytical methodology for pipeline stress – strain analysis by considering the contribution of transverse displacements to the axial elongation and the effects of temperature and internal pressure, while a two-dimensional stress-state was adopted with constant hoop stress.

The analytical approach remains a helpful tool during the preliminary design stage of a pipeline – fault crossing. The pipeline – soil interaction complexity, however, requires the implementation of advanced numerical models that are capable of considering all pertinent parameters, such as geometrical and material nonlinearity, cross-section ovalization and complex soil properties. The finite element method was initially introduced by Ariman and Lee (1992) to evaluate the developing strains of buried pipelines subjected to fault rupture. Nowadays two categories of numerical models are available:

- The first is the so-called beam-type model, where the pipeline is meshed into beam-type finite elements that can model the axial, shear and bending deformation and can provide stresses and strains at cross-sectional integration points along the pipe. The surrounding soil is modeled using a series of nonlinear translational springs in four directions (axial, transverse horizontal, transverse vertical upward and downward), based on the Winkler soil approach (Figure 2-5). However, trench dimensions and native soil properties cannot be directly encountered in the analysis. Additionally, the use of beam-type finite elements does not allow the direct estimation of local buckling, cross-section ovalization and detailed stress-strain distributions around the circumference of the pipe. Thus, checks on failure modes are carried out by comparing the maximum developing tensile and compressive strains obtained from the integration points to the corresponding strain limits provided by pertinent standards.

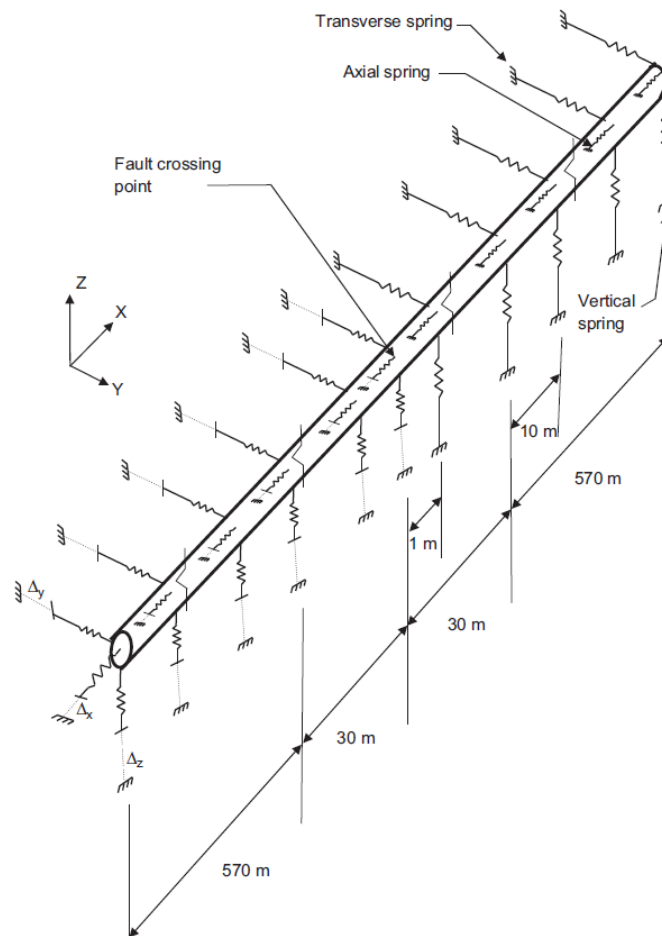


Figure 2-5: Geometry of FEM model for a buried pipeline under reverse faulting proposed by Joshi et al. (2011)

The beam-type model is extensively used by researchers to evaluate the pipeline integrity at active fault crossings. Ogawa et al. (2004) adopted the beam-type model and compared the obtained numerical results to those reported in pipelines after the Chi-Chi earthquake. Joshi et al. (2011) employed this model to investigate the pipe behavior due to reverse faulting. Chaudhary et al. (2013) developed a nonlinear solution algorithm accounting for the geometrical and material nonlinearity of the problem to employ the beam-type FE model and investigate continuous pipes under strike-slip faulting and presented numerical considerations on the FE model. Uckan et al. (2015) presented a simplified beam-type model as a useful tool to calculate the pipe critical length and established a methodology for the formulation of pipe fragility curves. Very recently, Liu et al. (2016) employed the beam-type model, due to its simplicity, in order to carry out a very large number of analyses with different parameters and then performed regression on the results to conclude with a semi-analytical expression for the prediction of maximum compressive strain in X80 pipes subjected to strike-slip faulting. The beam-type model is also proposed by pertinent Standards and Regulations such as Eurocode 8 – Part 4 (European Committee for Standardization 2006), American Lifelines Alliance (2005) and ASCE (1984) as a reliable and computationally efficient numerical modeling approach.

- The second approach is the so-called continuum model that is implemented to overcome the shortcomings of the beam-type model. The pipeline is discretized into shell finite elements and the surrounding soil into 3D solid elements. The pipe – soil interaction is modeled with contact finite elements. This approach severely increases modeling complexity due to the introduction of contact elements, nonlinearity and computational effort in terms of solution time requirements, boundary conditions, resulting degrees of freedom and convergence difficulties. The initial attempts to employ

the continuum model by considering pipe – soil contact issues were presented by Kokavessis and Anagnostidis (2006) and Odina and Tan (2009). Recently, Vazouras et al. (2010, 2012, 2015) presented in a series of papers a rigorous finite element model for pipeline – strike-slip fault crossing by considering soil parameters, pipe – fault crossing angle and pipeline mechanical characteristics to come up with a simplified expression for critical buckling strain and investigated the proper boundary conditions of the model using experimental results. This model was then adopted by other researchers to consider the effects of trench dimensions, native soil properties and fault motion simulation (Trifonov 2015; Zhang et al. 2014, 2015b). Rahman and Taniyama (2015) compared the continuum model to an analysis method with 3D discrete elements in order to account for the soil sedimentation and focus on the force – displacement relation between pipes and soil particles.

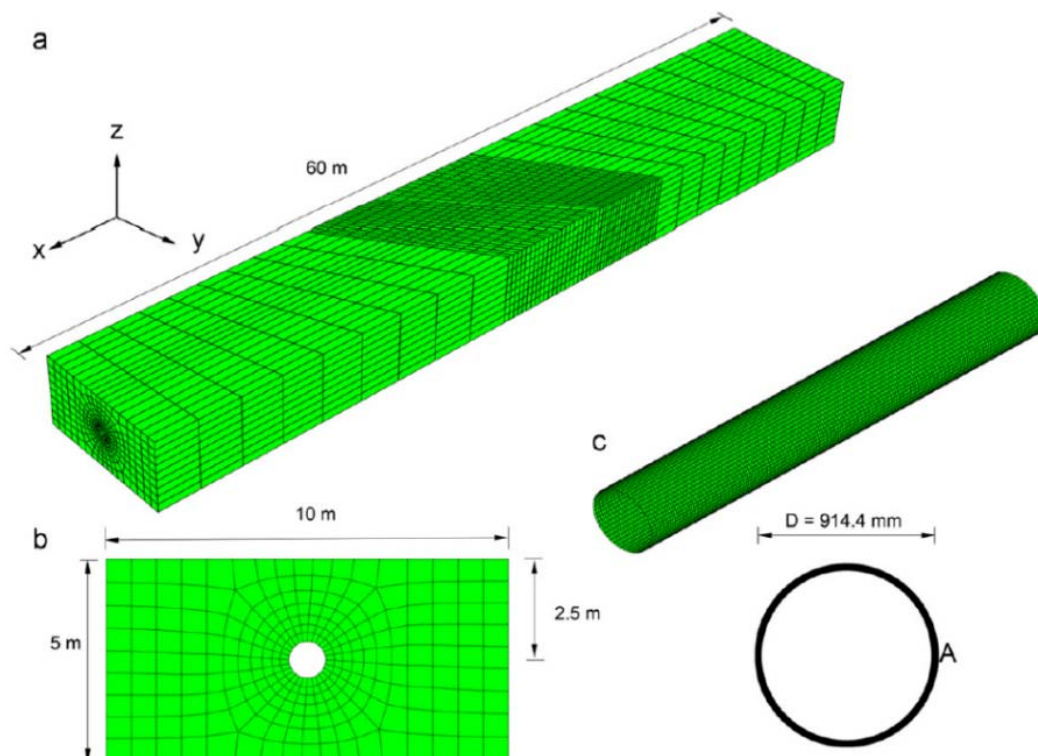


Figure 2-6: Continuum model proposed by Vazouras et al. (2010, 2012, 2015) for the analysis of buried pipelines at strike-slip fault crossings

As an alternative, nonlinear translation springs can be used for soil modeling instead of 3D-solid elements to avoid the numerical difficulties related to the use of contact elements between the pipeline and the soil (Gantes and Bouckovalas 2013; Karamitros et al. 2007, 2011; Takada et al. 1998). However, soil modeling with springs in combination with pipe meshing into shell elements may lead to the introduction of local forces on shell elements that, especially in case of a coarse mesh, do not represent accurately the physical problem, as they alter the distribution of stresses and strain on the pipeline wall, hence local buckling considerations may be inaccurate.

- Additionally, buried pipeline – fault numerical modeling can be carried out by employing a hybrid model than combines the beam-type and the continuum model (Figure 2-7). In such case, the pipeline around the fault zone, where higher strains are anticipated and there is increased potential of local buckling, is modeled using the continuum model, while the rest of the pipe length is modeled using the beam-type model (e.g. Karamitros et al. 2007, 2011). This approach aims at reducing the computational cost and exploiting the advantages of both numerical approaches, even though the above mentioned disadvantages of both models cannot be really avoided.

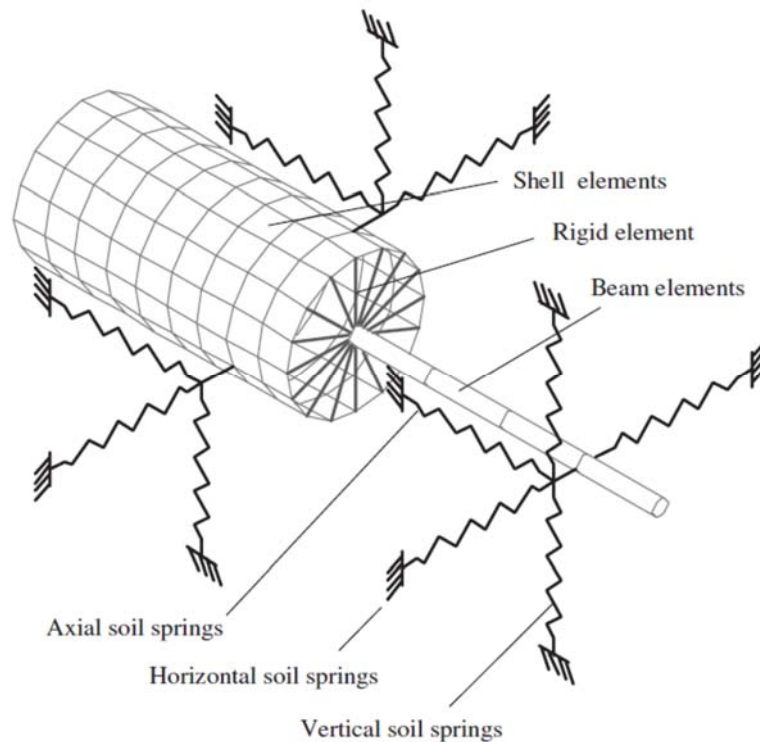


Figure 2-7: 3D finite element model employed by Karamitros et al. (2007), detail of the connection between the shell and the beam part of the model

Among the two alternative pipeline modeling techniques presented, i.e. beam-type and continuum model, the beam-type model is considered as more appropriate for practical applications, taking also into account the fact that several fault crossings will be encountered by a single pipeline traversing a seismic area, hence a large number of analyses will be required. Time and computational cost requirements can be significant parameters determining the acceptability of the continuum model by design engineers. The beam-type model is selected in the present thesis to investigate the mechanical behavior of continuous pipelines and pipelines with flexible joints to demonstrate the effectiveness of flexible joints in protecting buried pipelines against PGD. Aspects of the application of the beam-type model have been presented by the author in Gantes and Melissianos (2013) and Melissianos and Gantes (2015b).

2.4 EXPERIMENTAL STUDIES OF PIPES

2.4.1 Experiments of members with circular hollow section

Members of circular hollow section are widely used in piping networks and in a wide range of structural applications and thus their experimental investigation has been extensive since the 1950s. The first experiments were carried out for sections with low diameter over thickness ratio (D/t) that are mainly used in buildings and bridges. Experiments of cylindrical members under pure bending were presented by Moore and Clark (1952), Reddy (1979), Tugcu (1979), Gresnigt (1986), Kyriakides and Shaw (1987), Fowler (1990), Ju and Kyriakides (1992), Gresnigt and van Foeken (2001). Researchers in these studies tested thick cylinders with $D/t < 100$ in order to examine the elastic or elastoplastic buckling of pipes for onshore and offshore applications.

Sherman (1976) was motivated by the need for safe design of offshore truss structures and presented a series of experimental tests of circular hollow sections (D/t ranging from 35 to 102) under bending with cantilever and simply-supported boundary conditions. The author's experimental investigation focused on the members' capacity to undergo plastic deformations prior to failure. Later, an important

experimental program was carried out within the CBI – SwRI project (Marlow 1988; Steinman and Vojta 1989) to investigate the local buckling of 36 circular cross-section beams (D/t ranging from 42 to 60) under bending and axial force in order to contribute to the design of offshore deep-water platforms. The major objective was to examine the effect of the external pressure to the bending capacity, while more specimens without external pressure were tested. Then, Foeken and Gresnigt (1988) carried out experiments on a relatively thin cylinder under bending and internal pressure in order to investigate the effect of internal pressure and experimental results from cylinders with ratio D/t from 102 to 107 were also presented. Finally, Elchalakani et al. (2002) experimentally investigated cold-formed thin cylinders with ratio D/t ranging from 36 to 110 and manufactured with very high strength steel (grade C350L0 according to AS/NZS 1163) to estimate the deformability of such members.

2.4.2 Experiments of pipes

The increasing energy demands during the last decades led to the expansion of pipeline networks and consequently highlighted the need for safe pipe design against earthquake-induced actions and mainly against permanent ground displacements. From the beginning of the 1980s, the scientific community began to investigate the capacity of buried pipes through experimental programs. However, the behavior of buried pipes subjected to PGDs is governed by the pipe – soil interaction. When the surrounding soil is incorporated in the test, many constructional, cost and time consuming issues emerge. Thus, the experimental investigation of pipes can be roughly divided into two categories:

- Pipes without surrounding soil: The experiments are usually three- or four-point bending tests with or without accounting for any axial force and/or internal pressure. The specimens' boundary conditions may be simply-supported, clamped or cantilever. The main objective of these experiments is the estimation of the pipe bending capacity, the pre- and post-buckling behavior and mainly the critical compressive buckling strain.
- Pipes with surrounding soil: The experimental set-up is usually a shear-box or a centrifuge. The objectives of these experiments is to study the pipeline behavior subjected to faulting, soil liquefaction or settlement and at the same time identify the effects of soil properties, burial depth and fault offset rate on the pipe response.

2.4.2.1 Experiments of pipes without surrounding soil

Experiments of pipes without surrounding soil are carried out to assess aspects of the pipe behavior under simple loading, such as bending, axial force and internal pressure. This type of experiment is performed more often due to less emerging practical difficulties and consequently lower cost than those with surrounding soil.

Murray (1997) tested X52 and X65 pipes with external diameter 508mm and 324mm to examine the strain localization at areas where local buckling appears. The experimental set-up consisted of eccentric braces that imposed bending and compressive axial force. Results showed that the local buckling of unpressurized pipes was diamond shaped and of pressurized pipes was outward. Moreover, the evolution of local buckling in pressurized pipes revealed that a periodical waveform was initially formed on the shell surface where the maximum compression is developed. Then, after yielding took place and when the pipe steel was softening, one of the waveforms developed to local buckling, while the rest of them disappeared.

Dama et al. (2007) studied the structural behavior of pipes under bending and internal pressure through full-scale four-point bending tests of API5L Grade B pipes with external diameter of 610mm (24in) and length of 12m. The obtained experimental results revealed that locally buckled pipes, due to strain concentration, might fail due to fatigue or fracture in the buckled area. Quasi-static cyclic load was applied after the buckled pipes were pressurized. The maximum internal pressure capacity might also not be affected by the formation of local buckles or the cyclic loading, as long as the pipe material is

sufficiently ductile to withstand the developing strains at the buckled area during loading and unloading. Thinvongpituk et al. (2008) experimentally investigated steel pipes with D/t ratio ranging from 21.16 to 42.57. The specimens were subjected to pure bending in order to validate the analytical methodology, proposed by the authors, for the estimation of the pipe cross-section ovalization.

Gresnigt and Karamanos (2009), then, presented an additional study on the results obtained from an extensive program of experiments carried out in the late 1990's at the Technical University of Delft in the Netherlands. The experimental investigation focused on the elastoplastic local buckling of pipes and the effect of the manufacturing process on the pipe ultimate capacity and the local buckling. Full scale four-point bending tests of pipes with D/t ranging from 20 to 50 were performed. The processing of the experimental results revealed that the critical compressive strain of local buckling had to be measured at the maximum bending moment. Comparison of test results with available analytical expression for critical buckling strains showed that results fit better with the expressions proposed by Murphy and Langner (1985) and Gresnigt (1986), rather than those by BS 8010 (British Standards Institution 1993) and DNV-OS-F101 (Det Norske Veritas 2007). Furthermore, it was found for pipelines with low D/t ratio that the steel strain hardening properties had greater impact on the gradient of the moment – curvature relation in the post-yielding area than on the strain value at the maximum moment. Finally, the experimental results for UOE pipes were on the safe side compared to the analytical expressions of Murphy and Langner (1985) and Gresnigt (1986), rather than those for seamless pipes.

Mason et al. (2010) were the first to perform tensile tests of full-scale pipes with welded slip joints (WSJ). Two API5L Grade B pipe specimens were used of external diameter 320mm and wall thickness 6.4mm with a WSJ in the middle. The pipes were subjected to cyclic axial loading. External full circumferential fillet welds of the joints were made following the AISC (1994) procedures. The experimental results showed that the pipes with WSJ had post-buckling strength provided that the pertinent requirement and specifications had been implemented. The authors concluded that the maximum allowable tensile strain that should be considered in the design depends on engineering judgment of the pipeline operator with reference to the on-site construction quality. Thus, in case the construction quality is poor, then the allowable strains should be lowered.

Chen et al. (2012) performed full-scale experiments of X70 pipes with diameter of 40in in order to assess their strength prior to their installation in a project. Pipes were subjected to bending, compression and internal pressure. The experimental results revealed that the distributions of tensile strains were quite uniform along the top of the pipe, while concentration of compressive strains was reported on the bottom of the pipes, indicating the potential of local buckling if the applied bending moment was further increased.

Later, Ferino et al. (2013) carried out experiments on full-scale X80 pipes to examine the critical buckling strain of high-strength steel pipes. Unpressurized pipes with D/t ratio between 50 and 65 were subjected to pure bending (four-point bending test). The authors used the experimental results to validate their numerical models and concluded to an analytical expression for the estimation of the critical buckling compressive strain. The considered parameters of this analytical expression were the D/t ratio, the yield stress over modulus of elasticity ratio, the level of steel hardening, as well as safety factors regarding the pipe geometrical imperfections and the potential misalignment of the pipe adjacent parts due to the welds.

Recently, Kristoffersen et al. (2015) presented experimental results of in-scale offshore X65 pressurized pipelines. The authors carried out three-point bending tests, while a lateral load was applied in the middle of the specimens. It was found that: (i) the increase of axial load led to the increase of the bending capacity, (ii) the increase of the internal pressure reduced the cross-section distortion and increased the pipe strength, (iii) the local deformation of the cross-section was quite unaffected by the

axial load and (iv) the deformation of the pressurized specimen compared to the unpressurized was smoother at the end of the test.

2.4.2.2 Experiments of pipes with surrounding soil

Yoshizaki et al. (2003) carried out full-scale tests on 100mm diameter steel pipe with 4.1mm thickness. The pipes were subjected to permanent ground deformation and the effects of elbows were investigated by considering different soil water contents. Results revealed different response of pipes embedded in dry and partially saturated sand.

Wijewickreme et al. (2009) carried out full-scale pullout tests of pipes in a soil chamber. Results in terms of strains were compared to those predicted in design guidelines and recommendations were extracted regarding the use of code expressions for pipes buried in soils that might experience significant shear-induced dilation.

Abdoun et al. (2009) used a centrifuge to investigate in-scale HDPE pipes subjected to strike-slip faulting. The parameters under examination were the fault offset rate, the backfill soil moisture content, the burial depth and the pipe diameter. The experimental results showed that the offset rate did not affect the maximum axial strain, while low offset rate led to the increase of the maximum bending strains. Also, regardless the moisture content of the backfill soil, surface soil disturbance was located in a narrow zone in the fault vicinity, while for moist sand backfill additional soil cracks were reported downstream of the pipe, where passive soil pressure was developed. Then, for large burial depth over diameter ratio (H/D) no soil failure was reported, while for intermediate H/D ratio values typical soil failure was observed. The effect of H/D ratio is related to the fact that burial depth increase leads to stiffer soil springs that restrict the pipe bending deformation around the fault zone. Finally, the pipe diameter did not alter the location of the maximum bending strains, while the diameter increase contributed to the significant increase of developing bending moment.

A year later, Ha et al. (2010) used the same centrifuge to experimentally investigate HDPE pipes in order to compare the obtained results to failures reported on a major water pipeline in Izmir (Turkey), after the 1999 Kocaeli (Earthquake Engineering Research Institute 1999) earthquake. The authors concluded that: (i) the pipeline – fault crossing angle should be as close to 90° as possible, (ii) the pipeline – fault crossing angle has to be selected in such a way that pipe compression is avoided and (iii) in case the pipe internal pressure is not very high, HDPE is more suitable as pipe material in the vicinity of fault crossings, compared to carbon steel. Furthermore, it was found that the locations where local buckling has occurred, acted as “flexible joints” in case of increasing fault offset.

Sim et al. (2012) performed experiments of in-scale acrylic pipelines (diameter 20mm, thickness 4mm and length 800mm) on a shake table (gravity conditions 1g) to examine the shear failure of pipes due to faulting or landslide. The pipe – fault crossing angles under investigation were 30°, 45°, 60° and 90°. The authors concluded that the developing bending moment depended almost exclusively on the fault offset magnitude, while the seismic shaking did not play a role. The efficiency of tyre derived aggregate backfill in terms of reducing the pipe developing bending moments was proven.

Rofooei et al. (2012) utilized a shear box to in-scale model in a rigorous manner the behavior of buried pipes subjected to reverse fault rupture. API5L Grade B pipes with 4in diameter were subjected to reverse faulting of dip angle $\psi=61^\circ$. Results revealed that inelastic local buckling occurred at the pipe in both the fault hanging wall and footwall parts. Experimental results were verified through numerical modeling.

Recently, Moradi et al. (2013) used a centrifuge to experimentally investigate the behavior of in-scale stainless steel pipes subjected to normal fault rupture. The main parameters of the experiment were pipe – fault crossing angle $\beta=90^\circ$, fault dip angle $\psi=60^\circ$, D/t ratio ranging from 20 to 50, while the specimens were hinged at the shear box walls. The major findings of this investigation were that axial

strains were larger than bending strains and larger on the fault hanging wall. Increase of burial depth caused decrease of the failure fault offset magnitude. Increase of pipe diameter caused: (i) larger strains for lower fault offset, (ii) improvement of bending and degradation of axial pipe behavior and (iii) pipe stiffness increase and consequently vertical pipe displacement was reported for lower fault offset magnitude.

2.4.3 Experiments of pipe mitigating measures

Choo et al. (2007) experimentally investigated HDPE pipes using a centrifuge to examine the strain reduction due to reduced pipe – soil friction through the implementation of expanded polystyrene geofoam blocks as low-density backfill. Sim et al. (2012) performed shaking table tests of small diameter pipes crossing a vertical fault to investigate the performance of tyre derived aggregate (TDA) backfill in terms of protecting buried pipelines against vertical faulting and shaking. The obtained experimental results showed that TDA backfill contributed to pipe bending moment reduction. Monroy-Concha (2013) carried out tests of pulling pipes embedded in sand backfill to examine the effect of trench cover with geotextiles on the buried pipe protection. Hegde and Sitharam (2015) tested small diameter PVC pipes embedded in geocell reinforced sand beds in order to investigate the efficiency of geocells in terms of protecting buried pipelines. The experimental set-up consisted of a test tank filled with sand, where the pipeline was placed at the bottom and force was applied on the top soil surface through a hydraulic jack. Finally, experimental investigation of flexible joints as individual components, i.e. without considering them as part of a piping network, are primarily conducted to determine the mechanical properties of the joint (e.g. Medeiros et al. 2009, Veiga et al. 2016).

2.4.4 Framework of experimental investigation

The presented literature review reveals that the major research objective of the experimental investigation of pipes, with or without considering the effects of the surrounding soil, is the assessment of pipe behavior due to faulting. Additionally, researchers aim at extracting qualitative and quantitative results regarding the effect of various parameters influencing the pipe behavior. Investigation of the efficiency of alternative mitigating measures against the consequences of faulting on pipelines is however very limited until now. Towards this research gap, the experimental investigation of pipes with flexible joints carried out within this study (chapter 3) aims at demonstrating the efficiency of flexible joints as components that can be introduced in buried pipe – fault crossings and prevent pipe failure. The experimental investigation of pipes with flexible joints complies with the experiment practice, as published in the literature, regarding the testing procedure, specimen boundary conditions, specimen static model, etc.

2.5 CURRENT SEISMIC COUNTERMEASURES IN FAULT CROSSINGS

In pipeline design against faulting, alternative seismic countermeasures are employed to minimize the developing strains on pipe walls, mainly by reducing pipe – soil interacting forces. The commonly applied measures are:

- Pipeline embedment in a shallow, sloped-wall trench with loose backfill (Figure 2-8) aiming at reducing soil resistance and allowing pipeline deformation to take place over a longer length. Development of large strains and permanent deformations is allowed if pipe failure is prevented (Gantes and Bouckovalas 2013; Karamanos et al. 2014).



Figure 2-8: Trench backfilling with graded soil

- Increase of pipe wall thickness or steel grade upgrade to reduce developing strains and pipe curvature by increasing pipe stiffness (Gantes and Bouckovalas 2013; Karamanos et al. 2014).
- Avoidance of sharp bends that increase constraints to axial displacements and may impose additional forces on the pipeline (American Lifelines Alliance 2005; European Committee for Standardization 2006; Gantes and Bouckovalas 2013).
- Pipeline wrapping with friction-reducing geotextile (Figure 2-9) to reduce pipe – soil friction and increase the anchor length aiming at reducing the developing longitudinal strains (Gantes and Bouckovalas 2013).



Figure 2-9: Pipeline wrapping with friction-reducing geotextile (Gantes and Bouckovalas 2013)

- Pipeline wrapping with composite FRP wraps to increase strength and consequently the critical fault movement that causes failure (Mokhtari and Alavi Nia 2015).
- Pipeline placement within buried concrete culverts, which are sacrificed during the fault movement to retain pipeline undeformed and unstressed. The lack of backfill contributed to the reduction of the friction-induced strains on the pipeline (Figure 2-10). This approach is practically the only applicable in case the fault offset magnitude is expected as high as 1.5D to 2.0D.

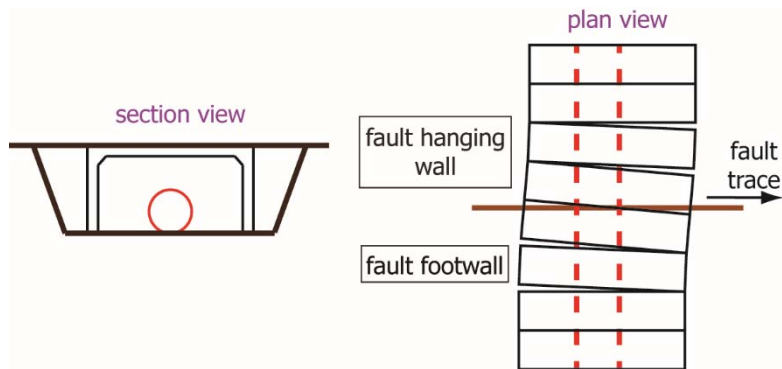


Figure 2-10: Use of concrete culverts to protect buried pipelines in case of strike-slip fault movement by retaining the pipe undeformed

- Use of geocells and geogrids in the trench above the pipeline to reduce pipe deformation (Hegde and Sitharam 2015).
- Backfill pipe trench with tyre derived aggregate surrounded by sand to reduce pipe bending moments (Sim et al. 2012).
- Change of pipeline route by constructing a dog-leg structure to allow pipeline deformation take place within a larger area in case there is great uncertainty on the fault trace location, as illustrated in (Besstrashnov and Strom 2011).



Figure 2-11: Construction of the dog-leg structure at the pipeline – fault crossing at Sakhalin (Besstrashnov and Strom 2011)

- Creation of a buckling pattern section in order to control the location and mode of pipe local deformation and increase the fault displacement that can be absorbed (Nobuhiro et al. 2013).
- Creation of an offset section of the pipeline at well-known strike-slip fault crossings by installing four cold bends to favor the development of tension on the pipeline (Hart et al. 2004).
- Construction of the pipe – fault crossing segment above ground on embankment or supports. The efficiency of this design approach has been clearly demonstrated in case of the Alaska pipeline – Denali fault crossing (Figure 2-12).

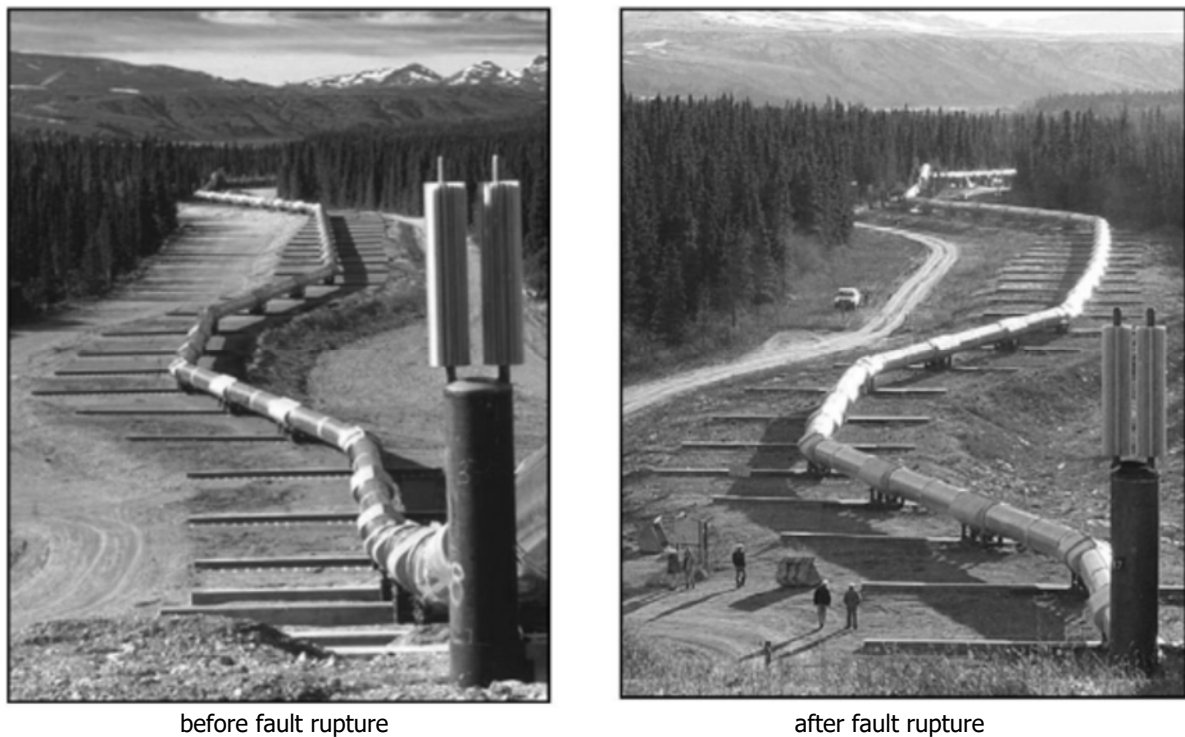


Figure 2-12: Trans-Alaska pipeline undeformed shape and deformed shape after the Denali fault rupture in November 3, 2002 following a M=7.9 earthquake (Hall et al. 2003)

- Construction of a wider trench in order to allow pipeline deformation take place over a longer distance and therefore avoid strain concentration (Figure 2-13).

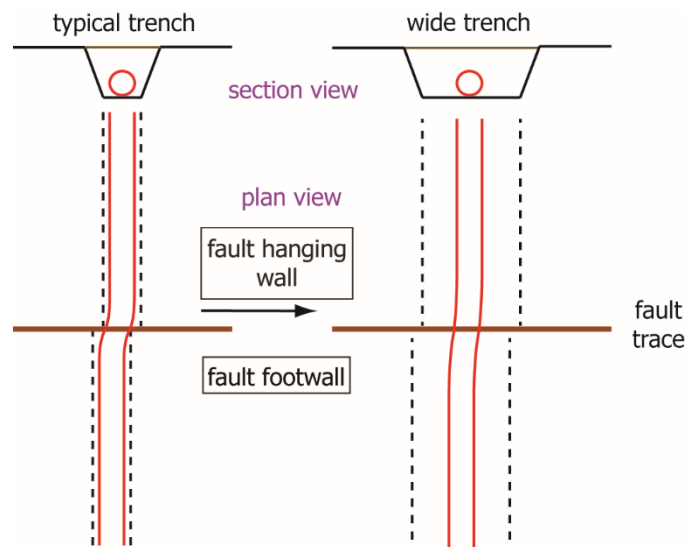


Figure 2-13: Pipe deformation due to faulting within a typical and a wider trench

Engineering practice and limited research results have demonstrated that various parameters, such as the maximum allowable fault offset magnitude and constructional issues, can limit the efficiency of the conventional measures. Monroy-Concha (2013), for example, suggested that wrapping the pipeline with a double layer geotextile is effective only if the distance between pipeline and trench wall is less than half the pipeline diameter. In general, it has to be noted that all preventive measures have to be applied or installed along a significant pipeline length, in order to confront the uncertainty regarding the exact fault trace location.

A new design concept for the protection of buried pipelines and consequently reducing the risk of local buckling or tensile fracture is proposed within this study, which relies on the modification of the structural system of the pipeline from continuous to segmented by introducing flexible joints between the adjacent pipeline parts in the fault crossing area, following the suggestions of Bekki et al. (2002). The principal objective is to concentrate strains at the joints through joint rotation and expansion and retain the steel parts barely undeformed (Melissianos and Gantes 2015b; Melissianos et al. 2015a), as schematically illustrated in Figure 2-14, instead of reducing the soil friction.

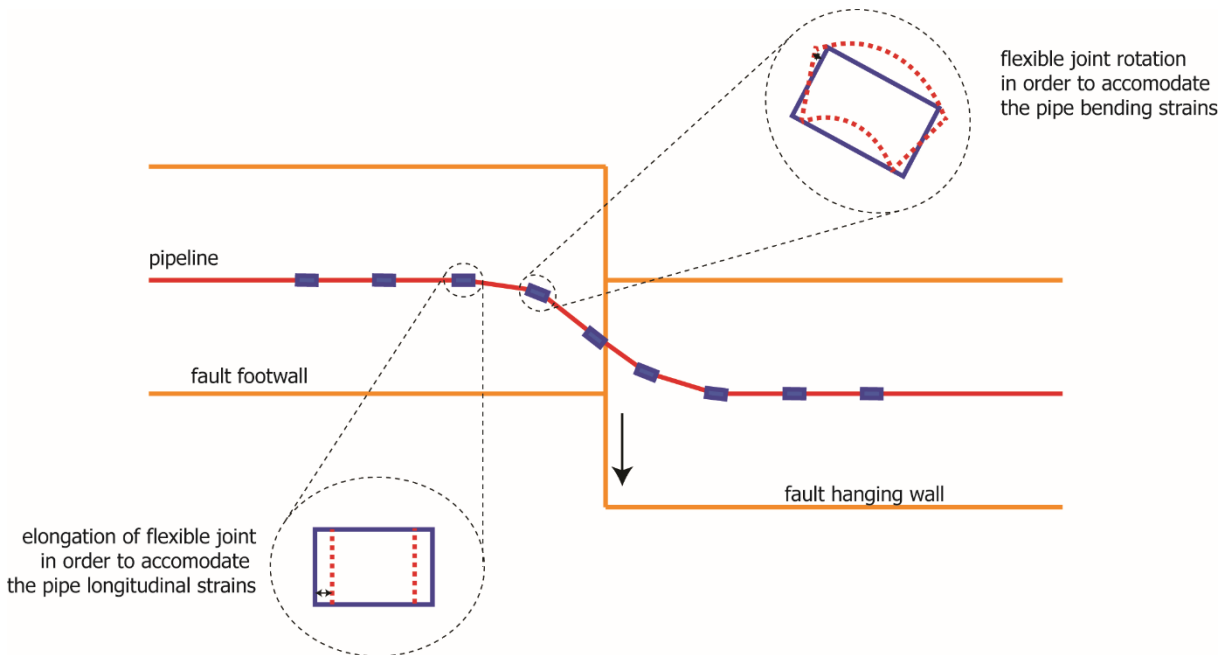


Figure 2-14: Schematic illustration of flexible joints' behavior in pipes under fault rupture

2.6 FLEXIBLE JOINTS

The term flexible joints refers to mechanical products that have been available in the market for many decades and have two major applications in the piping industry. The first application is in industrial piping systems, to absorb thermal expansion, machinery vibration and thrust (Figure 2-15). The second one is the use as connecting layouts between the adjacent parts of segmented pipes (Figure 2-16). In general, flexible joints are capable of undergoing relative displacement and rotations. Commercial flexible joints, which are also called expansion joints in the market, are made either of steel (metallic joints) or rubber (rubber joints). For buried pipeline applications, the metallic joints are selected, which are made of carbon or stainless steel. This selection is based upon the specifications of metallic flexible joints that meet the requirements regarding among others the resistance to external damage, corrosion and internal pressure. Finally, it has to be noted that flexible joints are prone to fatigue. Estimation of the maximum allowed fatigue life is crucial for the selection of a flexible joint in a piping system, but is not related to earthquake-induced actions and therefore it will not be examined hereinafter.



Figure 2-15: 72in tied universal thick-wall flexible joint for a sulfuric acid industrial plant ("U.S. Bellows" 2016)



Figure 2-16: Construction of segmented pipe with ball joints (Xinxing Pipes International Development Co. Ltd. 2016)

The commercially available flexible joints today can be divided into the following categories with respect to the way in which the imposed displacements are accommodated:

- slip expansion joints;
- ball joints;
- bellows;
- composite type.

2.6.1 Slip expansion joints

Slip expansion joints consist of two parts with flush mounting of one part into the other. The parts are not welded and thus relative axial deformation is allowed, while rotation is very limited (Figure 2-17). The main properties that characterize the behavior of this joint are: (i) the maximum allowable slip, (ii) the slip overstrength and (iii) the sealing method. Joints of this type are available in the market for internal pressure up to 6.9MPa (≈ 1000 psi) and can thus be used in high-pressure oil and gas pipelines.

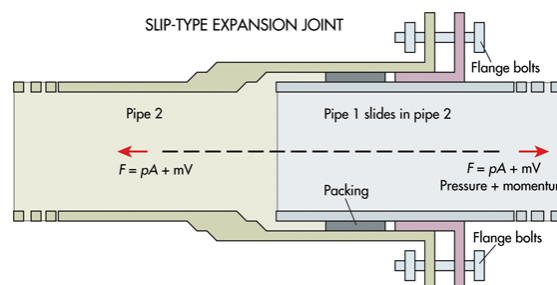


Figure 2-17: Typical configuration of a slip expansion joint (Lee 2013)

The application of this joint type in buried pipelines has to meet the restrictions and follow the recommendations stated by O'Rourke and Liu (1994, 2012). However, due to the potential uncertainty regarding the fault trace location on buried pipeline – fault crossing, these joints could be a costly solution, without ensuring that their contribution to pipe strain reduction would be beneficial.

2.6.2 Ball joints

The configuration of ball joints, is determined by the ball-shape of the one edge that is inserted in the other edge (Figure 2-18). The spherical configuration allows the relative rotation of joint's edges. If the joint is capable of undergoing slip, then relative axial displacement (expansion) can also be accommodated. In such case, a robust restriction layout has to be developed in order to prevent slip exceeding the maximum allowable corresponding value. Ball joints are available in the market but their pressure integrity is limited to 2.4MPa (≈ 350 psi) and therefore they cannot be used in high-pressure (e.g. 7MPa) transmission pipelines.

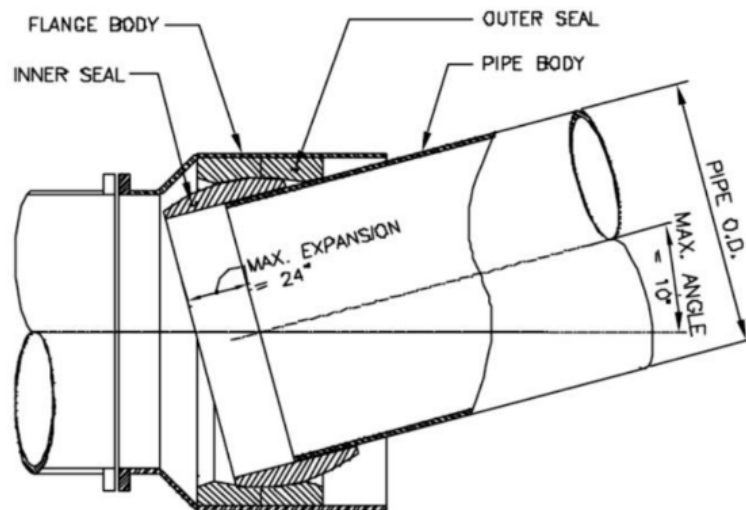


Figure 2-18: Typical configuration of a ball joint with expansion capability ("EBBA Iron Sales, Inc." 2016)

2.6.3 Bellows

2.6.3.1 Introduction to bellows

Bellows are flexible joints manufactured by the expansion of lightweight thin metal sheets, usually stainless steel. Bellows are designed to accommodate significant axial and transverse deformation and rotation and to withstand high internal pressure. The deformation capabilities of a bellow are schematically presented in Figure 2-19.

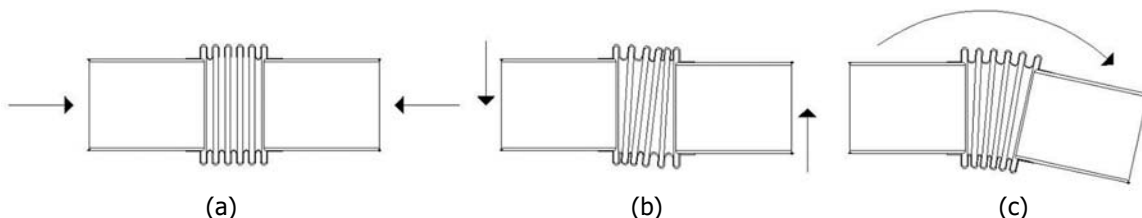


Figure 2-19: Bellow (a) axial, (b) lateral and (c) angular deformation capability

The deformation capability of a bellow is primarily determined by the cross-section and the width of each convolution, while the bellow's axial, lateral and angular stiffness is determined by the total number of convolutions. According to Wilson (1984), there are 10 different types of convolution's cross-section (Figure 2-20). The most common convolution type is the "S-Shaped" (Figure 2-20f). Bellow-type flexible

joints can be produced upon request with reference to the specifications of the pipeline system. Indicatively, manufacturers can produce bellows featuring a diameter up to 1830mm (72in) and resistance to internal pressure up to 8.3MPa ($\approx 1200\text{psi}$).

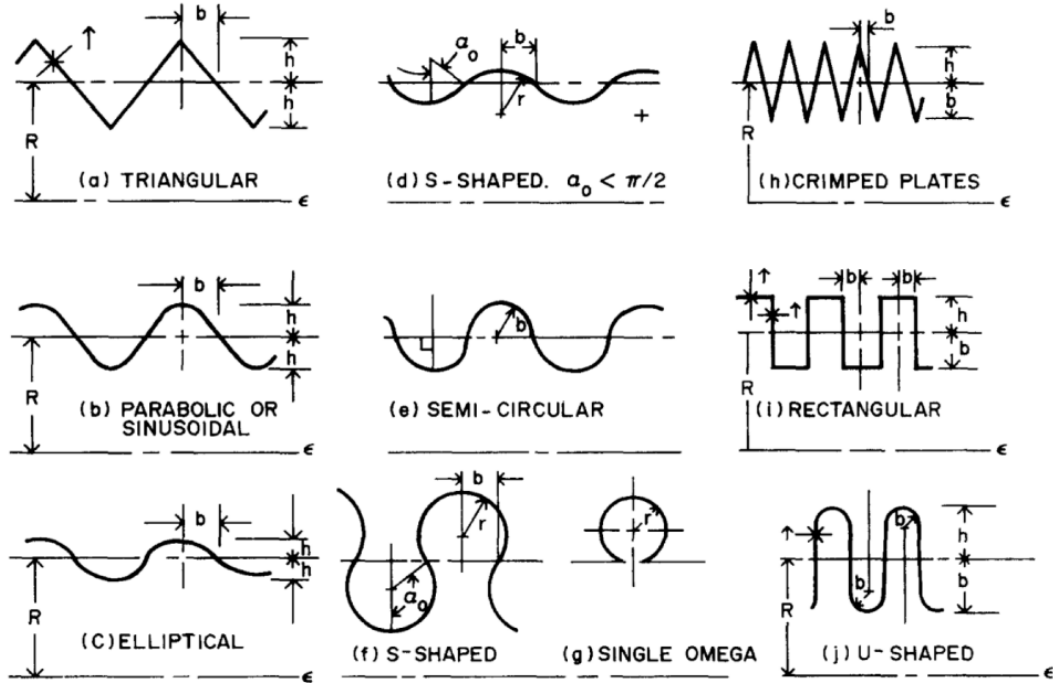


Figure 2-20: Alternative profiles of bellow convolutions (Wilson 1984)

2.6.3.2 Types of bellow joints

The basic type of bellow is the single (Figure 2-21a), which can accommodate axial, lateral and angular movement (Figure 2-19), but it is mainly used for axial differential movements. Additionally, when rods are added only lateral deformation is allowed (tied bellow – Figure 2-21a) or when a uniaxial hinge is introduced, only rotation is available (hinged bellow – Figure 2-21b).

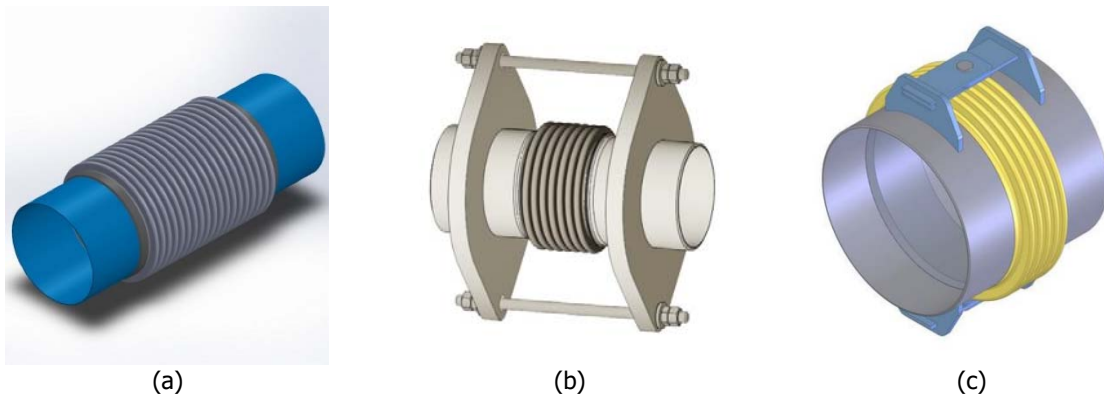


Figure 2-21: Bellow types: (a) single, (b) tied and (c) hinged

Furthermore, a considerable advantage of bellow-type joints is that the deformation capability can be increased through the increase of the number of convolutions. In case the required deformation capability cannot be accommodated through the increase of the number of convolutions, then the universal type is also available. A single universal bellow is presented in Figure 2-22a, a tied universal bellow is shown in Figure 2-22b and finally a universal hinged bellow in Figure 2-22c.

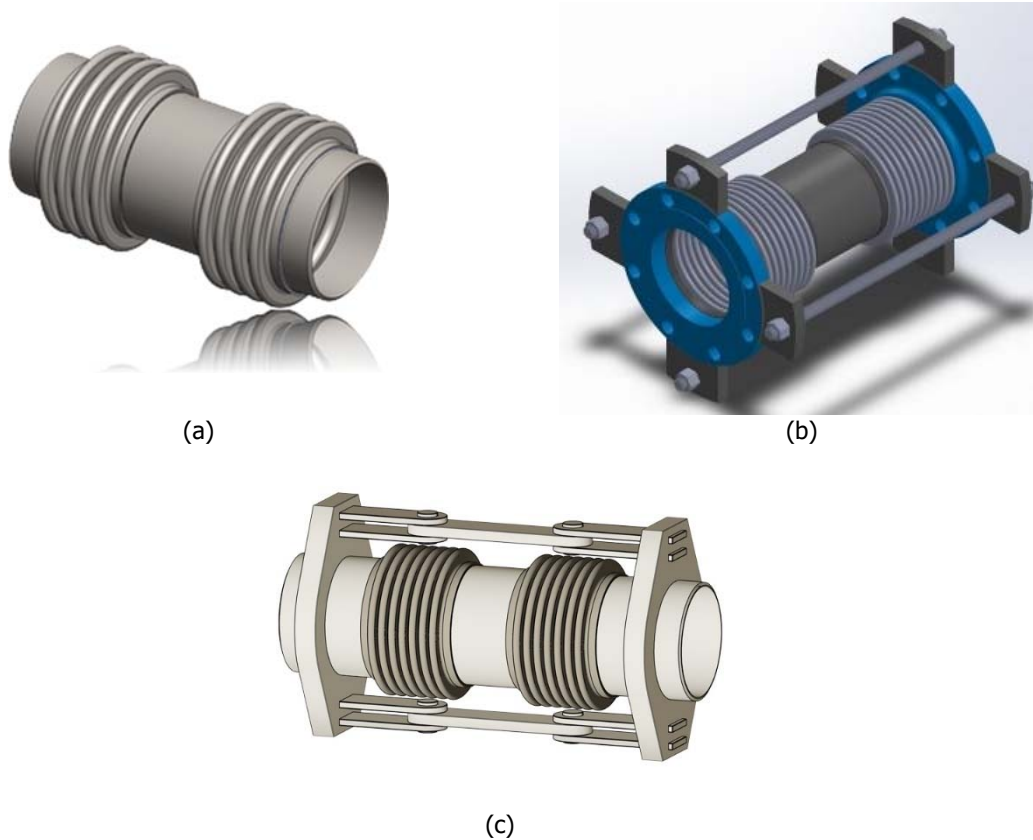


Figure 2-22: Universal (a) single, (b) tied and (c) hinged bellow

The hinged bellow presented above can accommodate only in-plane angular movement. In case the expected rotation is biaxial, there are also available in the market hinged bellows that can accommodate such movement (Figure 2-23).



Figure 2-23: Gimbal-type hinged bellow: (a) single and (b) universal

2.6.4 Composite type

Manufacturers of flexible joints and researchers (e.g. Ford 1983; Isenberg and Richardson 1989) provide various configurations of joints that are usually a combination of slip expansion joints (section 2.6.1) and ball joints (section 2.6.2), whose properties are a combination of the properties of the individual joint types and further discussion on these is out of the scope of this thesis.

2.7 SEGMENTED PIPELINES UNDER PERMANENT GROUND DISPLACEMENTS

Segmented pipelines are constructed by successive pipeline parts that are connected via flexible joints in a manner that does not ensure the structural continuity of the structure, namely pull-out of the joint is a potential failure mode at the joint area. To make this task clearer, continuous pipes are constructed by joining pipe segments with girth butt welds that ensure the structural continuity of the pipe. Segmented pipelines has been used for decades, mainly for water and sewer transmission. The potential of imposed ground displacement due to ground settlement, landslide and fault rupture led to the analytical, experimental and numerical investigation of the behavior of segmented pipes subjected to ground movement, while specific configurations of flexible joints have been studied as mitigating measures in case of ground movement.

The present thesis deals with mechanical behavior of buried oil and gas pipelines under faulting. The introduction of flexible joints along a pipeline in the fault vicinity transforms its structural system from continuous to segmented. It is then essential to review the behavior of segmented pipelines under PGDs and also examine the type of flexible joints that have been studied in such cases.

2.7.1 Review on flexible joints in segmented pipes subjected to ground movement

Research on the integration of expansion and ball-type flexible joints in segmented pipes subjected to PGDs is relatively confined and limited to water or sewer pipes under low internal pressure applications. Ford (1983) was the first to propose the application of flexible joints for pipeline applications against PGDs. The suggested configuration is illustrated in Figure 2-24 and consisted of two successive rotational joints (ball joints) and an intermediate expansion joint. The author suggested the application of these joints to areas where significant settlement is expected (e.g. pipeline crossing beneath building foundation).

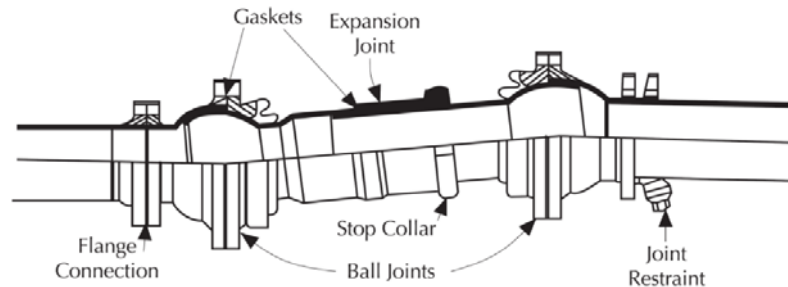


Figure 2-24: Flexible joint that combines the properties of ball joints and expansion joints (Ford 1983)

Isenberg and Richardson (1989) examined commercially available flexible joints of that time and investigated cases of water and sewer pipelines equipped with such joints, concluding that the available joints in the market (Figure 2-25) could be used in practice. However, the limited knowledge of the expected ground movement was a significant drawback towards the successful application of these devices.

Ballantyne (1992) investigated the behavior of water and sewer pipes subjected to PGDs ranging from 2.5cm up to 100cm and suggested the integration of flexible joints. The author noted that these joints should be custom-designed in order to be capable of undergoing larger deflection, extension or compression than the usual joints used in segmented pipes. Additionally, the necessary criteria for the proper operation of such joints were established. Finally, the author concluded that the commercially available joints at that time could not satisfy the basic specifications.

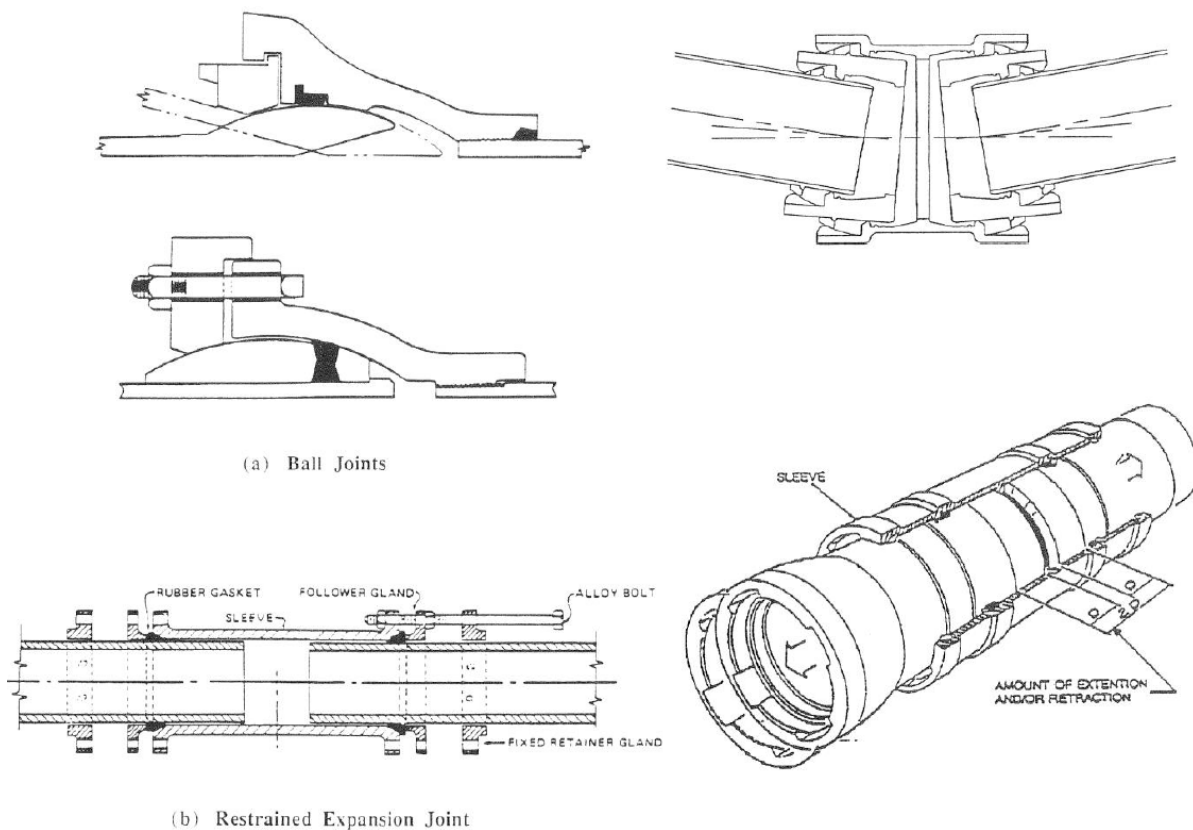


Figure 2-25: Flexible joints proposed by Isenberg and Richardson (1989)

O'Rourke and Liu (1994, 2012) investigated the use of Dresser type expansion joints (Figure 2-17) in pipes undergoing transverse PGD, with respect to the pipeline axis. The authors' results revealed that these joints could have beneficial as well as harmful contribution on the pipe developing stresses and strains, as illustrated in Figure 2-26 and Figure 2-27, respectively.

Namely, joints have beneficial contribution (Figure 2-26) when the pipe developing tensile and compressive stresses are limited to $t_u L_1$ and $t_u L_2$, respectively, compared to the initial value of $t_u L/2$. Joints have harmful contribution (Figure 2-27) when the tensile stresses are limited to $t_u L_1$, but compressive stresses increase to $t_u L_3$. It is noted that t_u is the maximum longitudinal force per unit length at pipe – soil interface, L_1 and L_2 are the distances from head or toe of PGD zone to location of expansion joint and L_3 is the distance along pipe. These outcomes suggest, according to O'Rourke and Liu (2012), that at least two joints have to be introduced in the pipe close to the margins of the PGD (head and toe). The design procedure by O'Rourke and Liu (1994) was adopted by Indian Institute of Technology Kanpur and Gujarat State Disaster Management Authority (2007). Later, Wang (1996) aiming at strengthening existing pipeline networks, suggested the replacement of rigid joints with flexible and/or restrained joints at segmented pipelines. These suggestions, however, were qualitative and did not include specific recommendations and suggestions on the joints' properties.

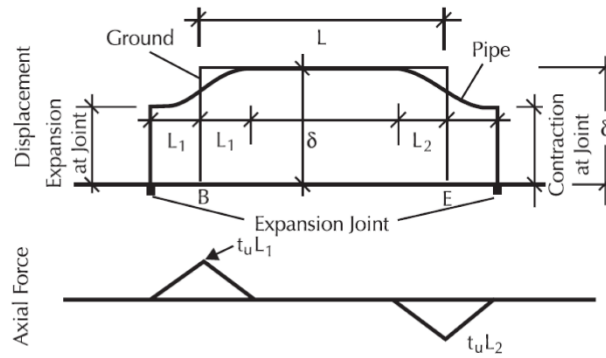


Figure 2-26: Potential beneficial contribution of expansion joints (O'Rourke and Liu 2012)

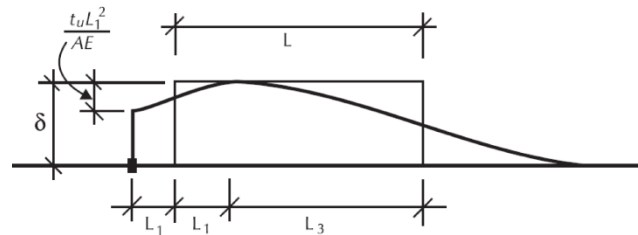


Figure 2-27: Potential harmful contribution of expansion joints (O'Rourke and Liu 2012)

Cheng (2001) investigated alternative configurations for pipelines to accommodate PGDs and among others studied an expansion joint (Figure 2-28a) and a ball-type joint (Figure 2-28b). Both joints could undergo displacement and rotation but only the ball-type could undergo large rotations, as those caused by fault rupture. The author concluded to a design procedure for pipes at areas of PGDs without considering either of these two joints. This conclusion was based on the fact that the usual design procedures at that time were not sufficient for the design of pipes with joints.

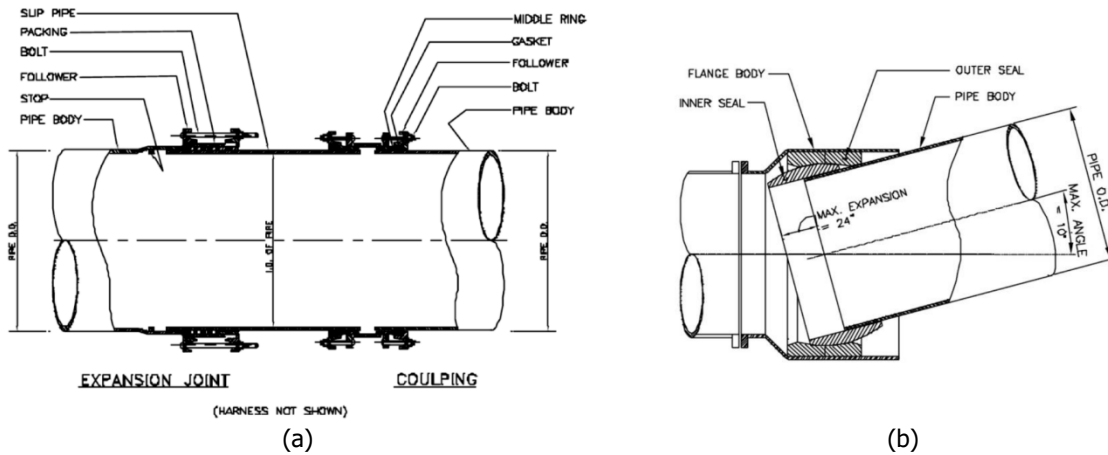


Figure 2-28: Flexible joints investigated by Cheng (2001)

Segmented pipeline failures reported after past earthquake events (e.g. O'Rourke and Ballantyne 1992; Sun and Shien 1983) have indicated that the connections between the adjacent parts of segmented pipelines were the most vulnerable components of the pipes and were associated with operational or structural failures. Even though the configuration of these joints depends on the design of the pipe manufacturer, the most common type of joint is the ball (Figure 2-18) or with external coupling (Figure 2-29).

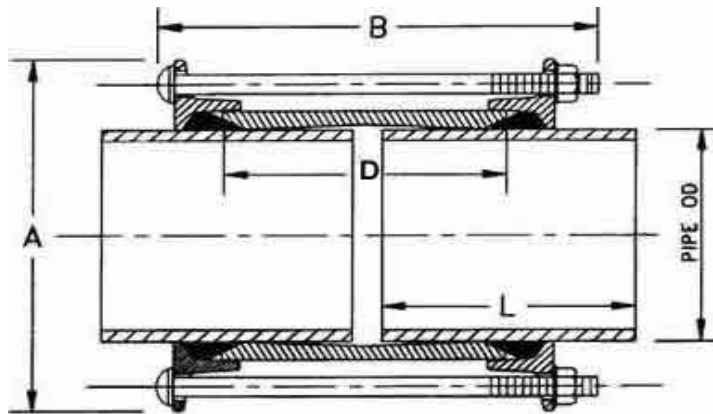


Figure 2-29: Segmented pipe joint with external coupling (Klamflex Pipe Couplings Ltd 2016)

O'Rourke and Ballantyne (1992) and O'Rourke and Liu (2012) have identified the main failure modes of segmented pipes: (i) axial pull-out of pipe at the joint area, (ii) joint rupture and (iii) development of pipe cyclic cracks at a long distance from the joint. The behavior of segmented pipes subjected to PGDs, such as fault rupture, depends on: (i) ground movement type (e.g. longitudinal or transverse with respect to pipe axis), (ii) the rupture magnitude and (iii) the pipe length over which the PGD is applied and the PGD distribution. Joints are the weaker components of the system and therefore if PGD is distributed over a longer distance, then the imposed displacements on the joints are lower, which reduces the potential of joint failure. Additionally, Suzuki (1988) studied the failures of pipes after the Niigata 1964 earthquake and concluded that segmented pipes are more vulnerable to longitudinal than to transverse PGDs. These observations have been adopted also by American Lifelines Alliance (2005) guidelines.

The use of segmented pipelines is very broad and thus a lot of effort has been devoted to the analysis methodologies of such structures. There have been attempts to analytically model distributed and local PGDs on segmented pipes both in longitudinal (e.g. American Lifelines Alliance 2005; O'Rourke and Liu 2012; O'Rourke et al. 1995) and transverse (e.g. O'Rourke and Norberg 1991) direction with respect to pipe axis. The main assumption in such studies was that the pipe segments are rigid bodies (infinite axial and flexural stiffness) and remain unstressed, while deformations are concentrated at the joints. This assumption is based on the disproportionately lower stiffness of the joints, compared to that of the pipe segments.

2.7.2 Experimental investigation

The main application of segmented pipes is in water distribution systems and therefore experimental investigation of such pipes dates back to the 1980s. Takada (1984) experimentally investigated two segmented pipes under normal faulting with crossing angle $\beta=90^\circ$. The first pipe (Case A) consisted of three parts and the second (Case B) of five parts. The experimental set-up and the results are illustrated in Figure 2-30. It is observed that the developed stresses were lower in Case B, in which the pipeline consisted of more intermediate parts. This indicates that joints with angular capability contribute to the distribution of bending moments on adjacent pipe parts proportionally to the parts' length.

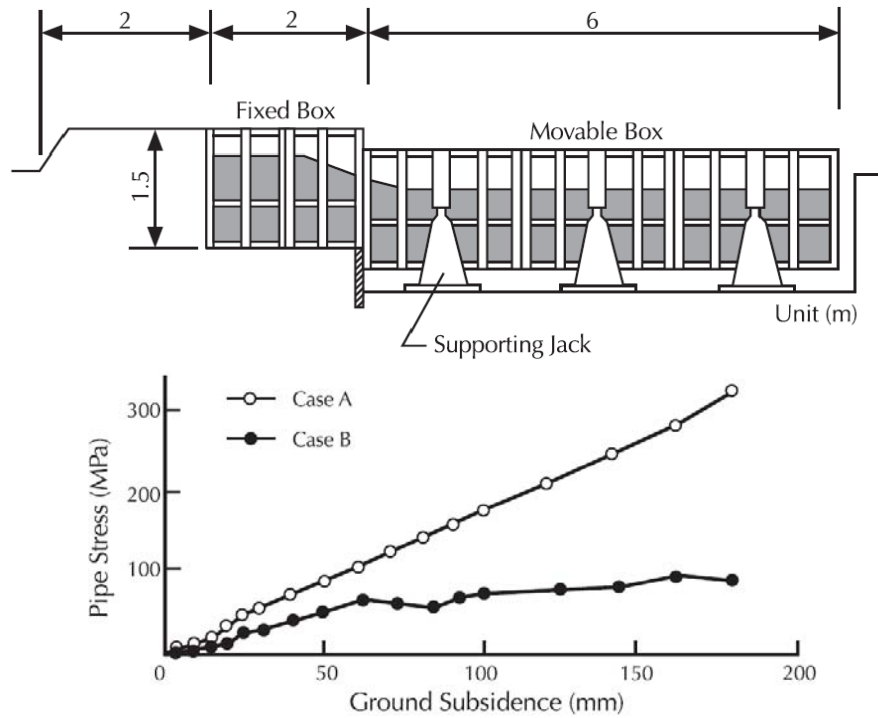


Figure 2-30: Experimental set-up and results from Takada (1984)

Later, Kim et al. (2009) carried out in-scale experiments on segmented concrete pipes. The joints were filled with cementitious mortar resulting in increased joint stiffness in comparison to common connections. However, results revealed that deformations were concentrated at the joints and therefore verified the assumption that the adjacent pipe parts between the joints behave in practice as rigid bodies.

Kaneko et al. (2013) performed experiments on buried ductile iron pipes with earthquake resistant joints (ball joints) to evaluate their behavior, as these pipes are widely used in Japan for water transportation. A shear-box was used to model normal fault rupture. Results revealed the sequence in which the joints are “activated” during the fault movement and were used by the authors to validate numerical models for further analysis of these pipes.

2.7.3 Analytical methodologies

Analysis of segmented pipelines subjected to PGDs is based on the same framework as for continuous pipes, namely every pipe part is modelled as an elastic beam resting on elastoplastic foundation (American Lifelines Alliance 2005). The major difference is that pipe segments are coupled with connections capable of undergoing angular, axial and lateral movement.

O’Rourke and Trautmann (1981) presented an analytical methodology to evaluate the behavior of segmented pipe, considering every pipe part as an elastic beam resting on elastoplastic foundation and additionally assuming that strains are concentrated at the connections and the pipe segments are undeformed. The authors concluded that the optimum pipe – fault crossing angle (β_{optimal}) is that for which the joint fails both in axial pull-out and shear due to rotation. This angle is estimated via the expression:

$$\beta_{\text{optimal}} = \arctan\left(\frac{\Delta_3}{\Delta_2}\right) \quad (2-13)$$

Depending on the joint properties, the authors concluded to a fault displacement – crossing angle relation and created the diagram of Figure 2-31. It is noted that the outcomes of this research do not set restrictions regarding the use of flexible joints in buried pipes.

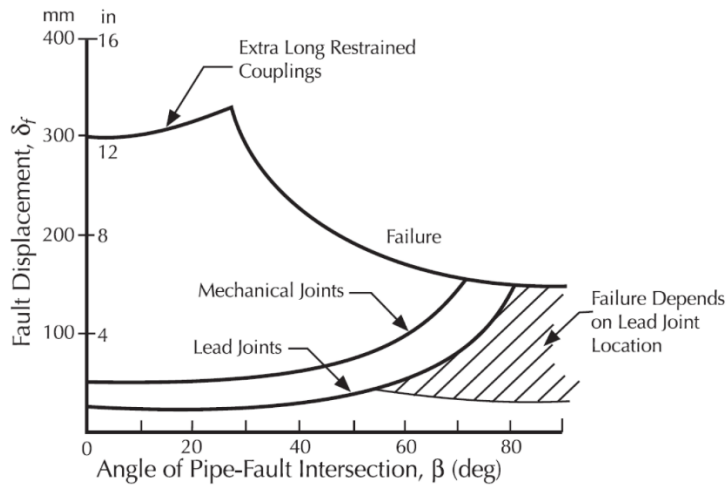


Figure 2-31: Maximum allowable fault displacement relatively to the pipe – fault crossing angle and the segmented pipe joint type according to O'Rourke and Trautmann (1981)

Adopting the same analysis approach, Takada (1984) used the analysis model shown in Figure 2-32 and consequently Elhmadi and O'Rourke (1990) the model presented in Figure 2-33 and finally O'Rourke (2009) the one depicted in Figure 2-34.

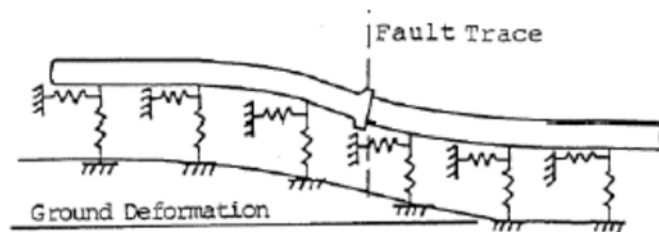


Figure 2-32: Analytical model of segmented pipeline by Takada (1984)

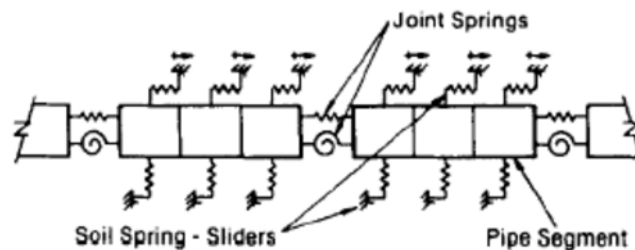


Figure 2-33: Analytical model of segmented pipeline by Elhmadi and O'Rourke (1990)

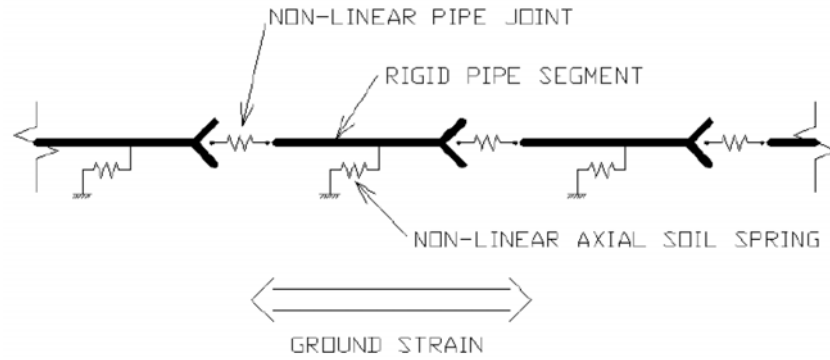


Figure 2-34: Analytical model of segmented pipeline by O'Rourke (2009)

American Lifelines Alliance (2005) guidelines suggest an analytical methodology for the analysis of segmented pipelines subjected to strike-slip fault rupture. The fault is assumed to intercept the pipe in the middle of a pipe segment, while the joint is treated as a hinge, where only shear is transferred from one part to the other. The joints on either side exhibit axial displacement (d_{joint}) and rotation (γ_{joint}):

$$d_{\text{joint}} = \frac{2}{3} \cos \beta \quad (2-14)$$

$$\gamma_{\text{joint}} = \arcsin \left(\frac{\Delta}{L_f} \sin \beta \right) \quad (2-15)$$

where δ is the fault displacement, β is the pipe – fault crossing angle and L_f is the pipe segment length between two adjacent joints.

Then, assuming that the transverse horizontal (lateral) soil forces have reached their maximum value p_u , i.e. soil plastification, the developing bending moment (M_{max}) and shear (V_{max}) are estimated via the expressions:

$$V_{\text{max}} = \frac{p_u L_f}{4} \quad (2-16)$$

$$M_{\text{max}} = \frac{p_u L_f^2}{32} \quad (2-17)$$

However, O'Rourke and Liu (2012) have pointed out that this analysis approach neglects the imposed axial deformation on the joint due to the rotation of the pipe segment between two adjacent joints (γ_{pipe}), which is estimated as:

$$\gamma_{\text{pipe}} = \frac{L_f}{2} - \sqrt{\left(\frac{L_f}{2}\right)^2 - \left(\frac{\Delta}{2} \sin \beta\right)^2} \quad (2-18)$$

The rotation of Eq. (2-18) is added to or deducted from the rotation of Eq. (2-14) depending on whether the pipe is subjected to extension or shortening.

In case the pipe is intercepted by the fault on a joint, which is the worst case scenario, the bending moment increases to:

$$M_{\text{max}} = \frac{p_u L_f^2}{8} \quad (2-19)$$

The axial displacement by neglecting the rotations increases to:

$$d_{\text{joint}} = \Delta \cos \beta \quad (2-20)$$

and the relative rotation of the joints before and after the one that is intercepted by the fault trace are increased to:

$$\gamma_{\text{joint}} = \arcsin \left(\frac{\Delta}{2L_{pz}} \sin \beta \right) \quad (2-21)$$

O'Rourke and Liu (2012) concluded that the abovementioned equations are rather conservative compared to the experimental results of Kim et al. (2009). Thus, they can be treated as upper limits of expected displacements and rotations, depending on the fault trace location.

2.7.4 Criteria for flexible joint selection

Flexible joints have been used in segmented pipes for many years and have also been proposed as mitigating measure for buried pipes subjected to PGDs (sections 2.7.1 through 2.7.3). However, within these studies, oil and gas high-pressure pipes were not examined. It is therefore important to establish the proper criteria for the selection of the appropriate flexible joint type for buried pipe applications that transmit oil and gas. The pertinent suggested criteria take into account the structural, constructional and operational demands of buried pipes:

- Availability in the market and manufacturing upon request regarding the internal pressure, diameter and wall thickness.
- Reduction of pipe developing longitudinal tensile and compressive strains through significant relative rotation of the joint.
- Avoidance of failure at the joint area (e.g. pipe pull-out).
- Continuity of the structure and full mechanical cooperation between the pipe and the flexible joint through rigid connection (e.g. butt welding).
- Compliance with the pipe flow process without obstruction of normal pipeline inspection procedures (e.g. in-line inspection with pigs).
- Ease of construction in the field.

Based on the aforementioned criteria, the appropriate type of flexible joint is considered to be the bellow. It is important to note that bellows have not been used or studied before for this particular application. Moreover, if bellows are due to be introduced in a buried pipeline operating in very high pressure (e.g. 8MPa), then the capability of the joint to withstand such high pressure has to be examined. In such case, the hinged bellow (Figure 2-21b) is likely to be the most appropriate choice, rather than the single bellow (Figure 2-19), while the tied bellow-type (Figure 2-21a) is not appropriate, as it cannot accommodate angular movement.

2.8 CONCLUSIONS

The literature review presented in sections 2.7.1 through 2.7.3 indicates that the bellow-type flexible joints are the appropriate type for buried pipeline under faulting applications. Therefore, in the following chapters of the present doctoral thesis the term flexible joint will refer to bellow-type joints, either single or hinged. Bellows are connected to the adjacent pipe segments through girth butt welds. Additionally, it has to be noted that the structural system of pipes with bellow-type flexible joints are referred as segmented in order to make the distinction against the continuous pipe, even though strictly speaking the term segmented refers to pipes, where the joints do not ensure the structural continuity in terms that may fail due to pull-out, in contrast to pipes with bellow-type joints.

Then, the available analytical methodologies for the analysis of segmented pipes cannot be implemented for the evaluation of the behavior of pipelines with bellow-type flexible joints because: (i) in these methodologies various simplifying assumptions are used, which are suitable for preliminary design and not final design, (ii) they deal with flexible joints (not of bellow-type) that cause pipe discontinuity in terms that pipe pull-out is a potential failure mode at the joint area, contrary to the bellow-type joints that are welded to the adjacent pipe parts and (iii) the pipe adjacent parts are assumed to be rigid bodies. Consequently, the analytical methodologies aim at estimating both the axial and rotational deformation capacity of the joint with respect to fault offset magnitude and pipe – fault crossing angle. In the present thesis, therefore, in order to acquire qualitative and quantitative understanding of the behavior of buried pipelines with bellow-type joints under faulting a numerical approach will be selected, taking advantage of the established FEM models for continuous pipes under faulting and the suggestions of pertinent codes for the numerical modeling of bellow-type joints.

3 EXPERIMENTAL INVESTIGATION

3.1 INTRODUCTION

In this chapter, the experiments of continuous pipes and pipes with flexible joints that took place in the context of the present doctoral thesis will be presented. The main purpose of this experimental work was the evaluation of flexible joints in terms of reducing the developing tensile and compressive strains on the pipe. Thus, a set of continuous pipe specimens and a pipe specimen with flexible joints were experimentally investigated. The measurements performed during the tests can be divided into two categories: (i) evaluation of the developing stress-state by using strain gauges to measure the developing strains and (ii) evaluation of the effect of flexible joints in terms of transforming the continuous pipe structural system to segmented by monitoring the pipe deformation in various steps of the displacement application by using LVDTs and Deformation Plotters. In general bellow-type flexible joints have not been previously used in buried pipes for strain reduction and thus there is no relevant literature on this topic, as presented in section 2.4. Apart from the assessment of the structural behavior of continuous pipes and pipes with flexible joints, the present experimental investigation was also used as the basis for the calibration of the numerical models.

3.2 DESCRIPTION OF EXPERIMENTS AND EXPERIMENTAL SET-UP

3.2.1 Specimens

A total number of four pipe specimens, namely three continuous and one with flexible joints, have been tested at the Institute of Steel Structures in the School of Civil Engineering of the National Technical University of Athens. The specimens were constructed by the Greek company Afoi Valasi & Sons O.E. (2015) that is active in the field of fabrication and erection of many kinds of steel structures. The flexible joints were produced by the Greek company J. Bellos & Co (2015), which is a producer of pipe accessories products. The selection of the geometry and cross-section of specimens was based on achieving a balance between the desirable research objectives and the limitations imposed by the existing testing and measuring equipment in the laboratory and the dimensions of the testing frame. The total available length of the specimens in the testing frame was approximately equal to 5.6m. Fixed end conditions were selected at both specimens' ends aiming at proper modeling of the pipeline deformation due to faulting. Namely, the deformation of a buried pipeline subjected to strike-slip fault rupture is a smooth s-shaped curved line (Figure 3-1), where two anchor points represent the pipeline locations beyond which the structure is assumed to be unstressed. In the experimental set-up, the specimens were fixed at the ends, while the offset (transverse imposed displacement) was applied in

the middle-span. Thus, the deformation of each half of the specimen was expected to model the s-shaped deformation of a pipe (Figure 3-2), considering the fixed ends and the middle-span locations as virtual anchor points.

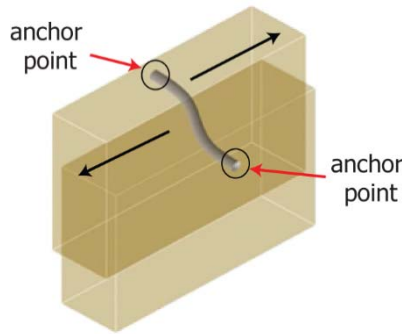


Figure 3-1: Schematic illustration of pipeline deformation subjected to strike-slip fault offset

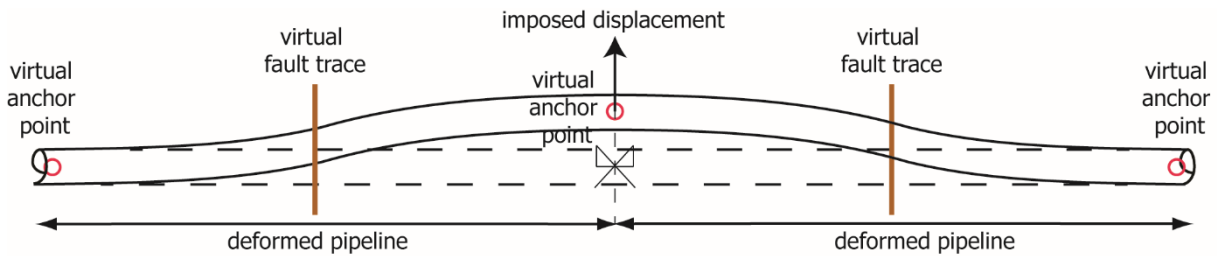


Figure 3-2: Schematic illustration of the experimental concept

Two types of tubes were tested, as listed in Table 3-1, where the continuous specimens were abbreviated as CP and the specimen with flexible joints as PFJ. Indicative sketches of the continuous specimens and the specimen with flexible joints are provided in Figure 3-3. The tubes were of cross-section CHS 114.3x3, which was selected on the basis of the geometrical restrictions of the testing frame, in order to have a realistic length over diameter ratio for each s-shaped deformed configuration. It should be noted that the diameter over thickness ratio (D/t) of the CHS 114.3x3 cross-section is equal to 38.1. The value was considered to be relatively low and in combination with the imposed displacement magnitude no local buckling was expected in the elastic range. The actual length of the specimens was equal to 5568mm and they were connected to 30mm thick end-plates with tube socket joint fillet welds (Figure 3-4).

Table 3-1: Specimens

	CP		PFJ	
Specimen number	N=1	N=2	N=3	N=4

The structural system of the specimens was that of a beam with fixed ends, subjected to imposed displacement at the middle. The maximum bending moment was thus expected at the fixed ends and the middle. The introduction of flexible joints aimed at reducing the developing strains and thus their location was selected as close as possible to the maximum moments' locations, based on preliminary numerical analysis results and the restrictions of the measuring instruments. The maximum imposed displacement by the actuator was equal to one specimen diameter, i.e. about 115mm. It is noted that the magnitude of the imposed displacement was selected based on: (i) the research objective of the experimental tests, i.e. strain reduction due to the integration of flexible joints, (ii) preliminary numerical results revealing that higher displacement would not modify the expected behavior of the specimens and (iii) the mechanical properties of the flexible joints.

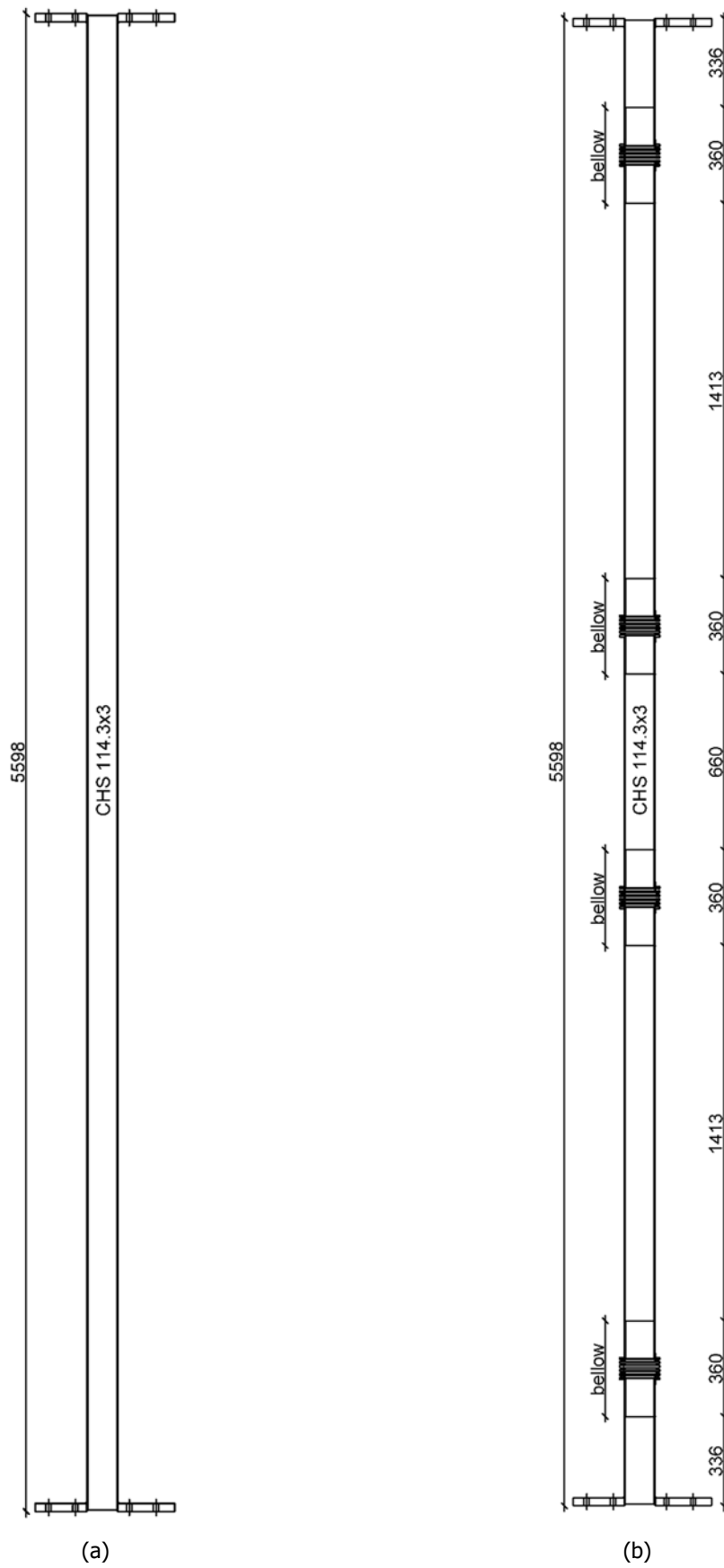


Figure 3-3: Specimen types: (a) continuous (CP) and (b) with flexible joints (PFJ)

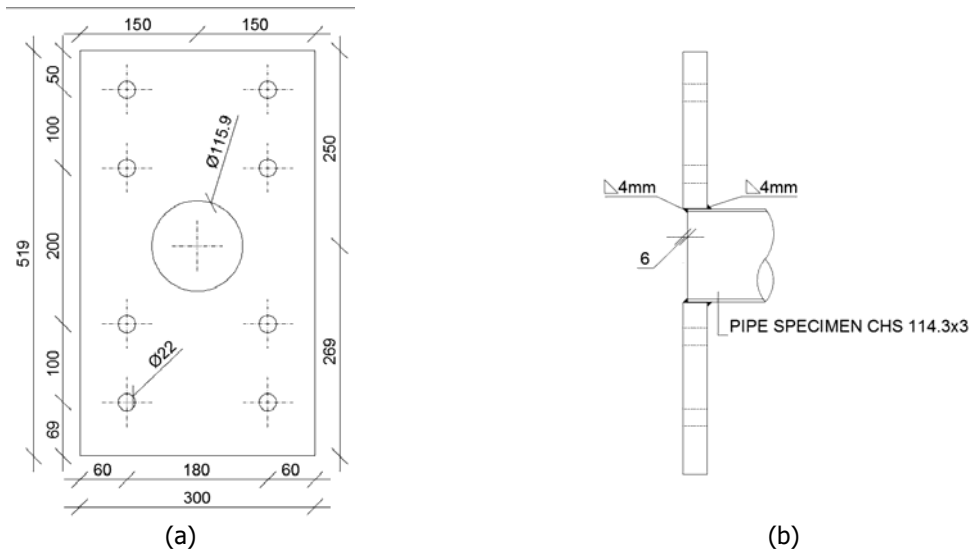


Figure 3-4: Detailing of specimen connection to an end-plate: (a) view and (b) side view

3.2.2 Testing frame

A typical CP specimen and the PFJ specimen placed in the testing frame are depicted in Figure 3-5 and Figure 3-6, respectively. The specimens were connected to the testing frame through the aforementioned end-plates that were bolted with eight M20 8.8 bolts. The design of the specimen – testing frame connection was found to be adequate for the expected magnitude and deflection of the connection to prevent yielding and to ensure that the connection would be sufficiently rigid.

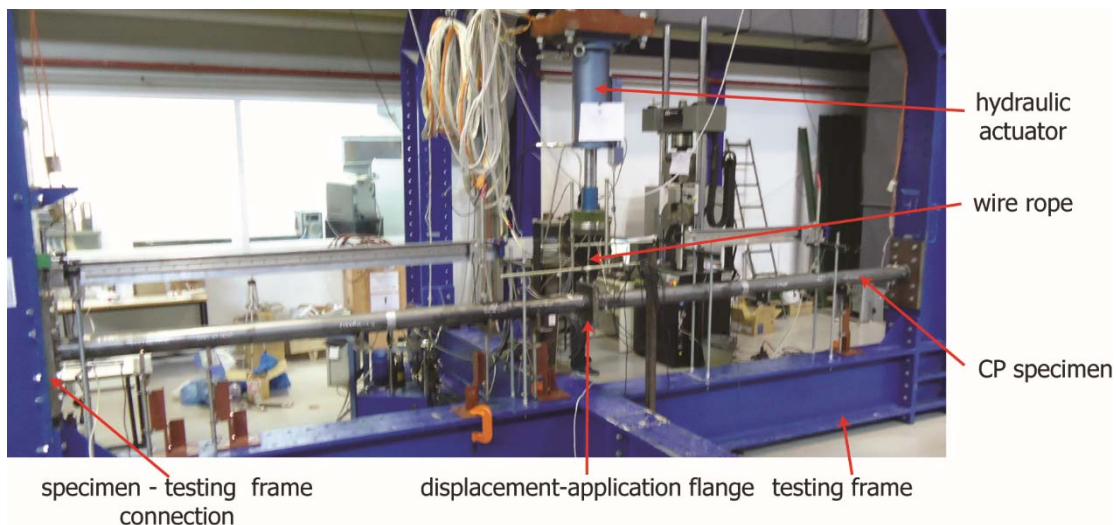


Figure 3-5: View of a CP specimen at the testing frame

The specimen installation in the testing frame was carried out in two steps: (i) the bolts on one side were pretensioned (level of pretension was 55% of bolt yield strength) and (ii) on the other side, shim plates were inserted between the end-plate and the frame column flange to fill any potential gap, and then the bolts were pretensioned. Developing strains on the specimen during bolt pretensioning were measured by strain gauges and the recorded strains were found to be very low compared to those recorded during the experiments, thus they were not considered thereafter. The imposed displacement was applied through a flange (referred thereafter as displacement-application flange) that was connected to the actuator via a wire rope. The displacement-application flange was designed to be sufficiently thick (40mm) to ensure uniform load application on the specimen and consequently avoid

any undesirable local failure of the specimen. Hence, the structural system of the PFJ specimen was that of a beam with fixed ends and four internal “hinges”. Thus, temporary support was necessary before the test to avoid sagging. It is noted that initial imperfection measurements for the pipe itself and the out-of-straightness of the pipe prior to testing were not conducted.

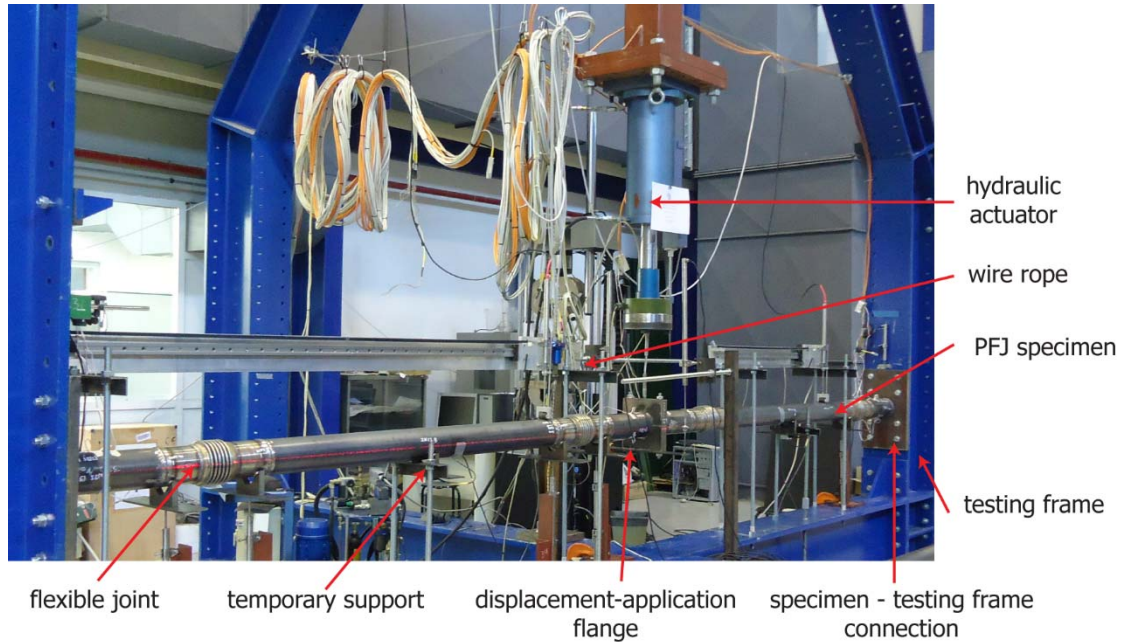


Figure 3-6: View of PFJ specimen at the testing frame

3.2.3 Testing procedure and measuring devices

The tests were performed using a 300kN hydraulic actuator of maximum pressure equal to 125bar, operating in displacement control. The rate of the imposed displacement was in all cases equal to 0.032mm/s. The reaction force was measured by a load-cell mounted at the actuator’s head. The measuring devices’ configuration was nominally identical in all specimens and it is indicatively illustrated in Figure 3-7 for specimen N=4.

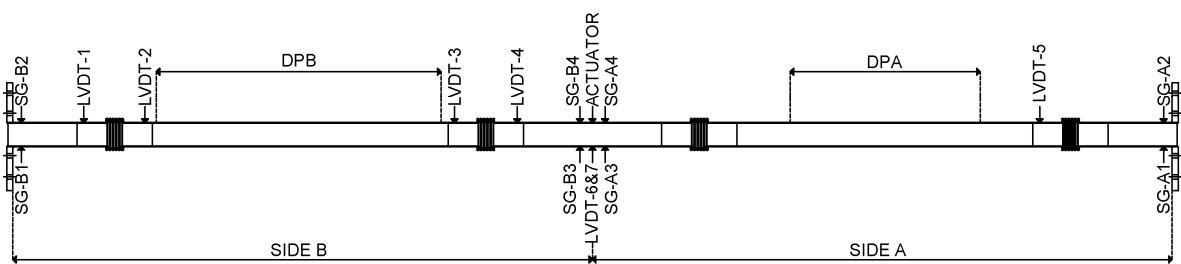


Figure 3-7: Configuration of measuring devices

A set of distance and strain measuring devices was used. Individual Linear Variable Differential Transformers (LVDTs) were installed to measure the specimen’s deflection (vertical displacement in-plane with applied load) at bellow edges (Figure 3-8) in order to identify the differences between the CP and PFJ deformation. Two additional LVDTs were installed on the displacement-application flange (ACTUATOR in Figure 3-7) to record the true specimen displacement, since the displacement recorded by the load-cell could be affected by the electromagnetic noise of the actuator operation, the wire rope expansion and other relevant parameters.

Furthermore, a 2D Deformation Plotter (DP) was designed and manufactured in the Institute of Steel Structures in order to plot the specimen's deformed shape (Figure 3-9). The main transducers of DP were a LVDT monitoring the vertical displacement and a wire-type displacement transducer, monitoring the longitudinal coordinate. Thus, DP was capable of scanning the specimen's deformation, i.e. monitoring simultaneously the vertical and the longitudinal coordinate at predefined time steps. The LVDT was attached to the movable part of the system, namely the linear table, which was sliding along an aluminum linear guide. Motion of the system was provided by an electric stepper motion and was transmitted via a timing belt. Then, in order to provide uninterrupted sliding of the LVDT's rod on the specimen's surface, an appropriately constructed roller system was mounted on the LVDT's rod edge. The system (DP) was assembled on a thick aluminum base, which was installed on supporters at a sufficient distance above the specimen, determined by the maximum LVDT stroke and the maximum expected vertical displacement of the specimen. The system was controlled by an in-house built computer-driver, controlling the micro-steps of the stepper motor rotation (each full rotation of the motor consisted of 200steps and every step of 128micro-steps), the velocity and the acceleration. Two DPs were constructed with maximum longitudinal plotting length capacity equal to 920mm (DPA) and 1920mm (DPB), respectively (Figure 3-7).

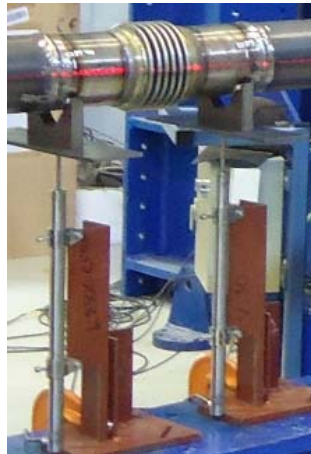


Figure 3-8: LVDTs placed on a flexible joint's edges

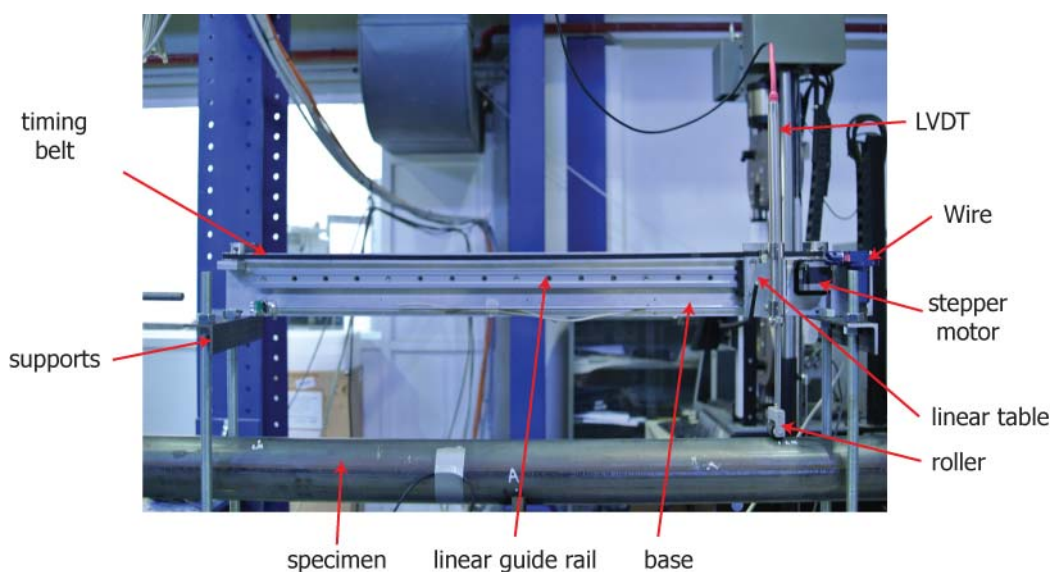


Figure 3-9: Components of Deformation Plotter

Strains were measured with the use of sensing elements that electrically detected micromechanical changes through a change of their resistance. The utilized strain gauges (gauge length was 10mm) had a nominal resistance of 120 Ω and were placed at locations detailed in Figure 3-7, which were selected based on the maximum expected stress-state which entered into plasticity (Figure 3-10). The locations of the strain gauges were outside the heat-affected zone of the specimen – end-plate weld. Strain gauges measured the longitudinal tensile and compressive strains. Special care was given for the correct placement of the strain gauges by polishing the desirable locations in order to ensure a satisfactory contact between the strain gauge and the specimen surface.



Figure 3-10: Strain gauge (SG) placed on specimen crown

3.3 STEEL PROPERTIES

Tensile tests were carried out to extract the material properties of the steel used for manufacturing of the specimens. Appropriately designed coupons cut from specimens during their construction were subjected to displacement controlled tests. The geometry of the coupons and the testing procedure were based on the guidance provided by EN ISO 6892-1:2009 (International Organization for Standardization 2010). The tensile test results were provided in terms of the applied load and the corresponding displacement of the coupon's edges, from which the engineering stress (σ_e) and engineering strain (ϵ_e) could be calculated based on the coupons cross-section area. Then, in order to take into account the change of coupon's width during the loading process, the true stress (σ_{true}) and true strain (ϵ_{true}) were calculated according to the expressions:

$$\sigma_{true} = \sigma_e (1 + \epsilon_e) \quad (3-1)$$

$$\epsilon_{true} = \ln(1 + \epsilon_e) \quad (3-2)$$

A view of a typical coupon at its final shape before testing is illustrated in Figure 3-11 and during testing in Figure 3-12. From each specimen (N=1 to N=4) three coupons were cut, named for example N=1.1 to N=1.3 for specimen N=1. An INSTRON 300kN tensile testing machine was used and the elongation of the tensile test coupon was measured by an extensometer mounted on the coupons over a gauge length of 50mm.



Figure 3-11: Typical tensile coupon



Figure 3-12: Coupon during tensile test

The average modulus of elasticity for all specimens was found equal to 210GPa, which is in accordance with the value provided in pertinent structural textbooks for steel. The yield stress for each coupon was taken as the 0.2% proof stress found in the plateau following the elastic branch. The obtained engineering stress – strain curves from the tensile tests are illustrated in Figure 3-13a through Figure 3-16a for all specimens. Furthermore, the true stress – strain curves and the assumed bilinearized material law for all specimens are depicted in Figure 3-13b through Figure 3-16b. Finally, the mean yield stresses for each specimen is listed in Table 3-2.

Table 3-2: Mean true yield stresses of specimens

	N=1	N=2	N=3	N=4
Yield stress (MPa)	355	354	344	345

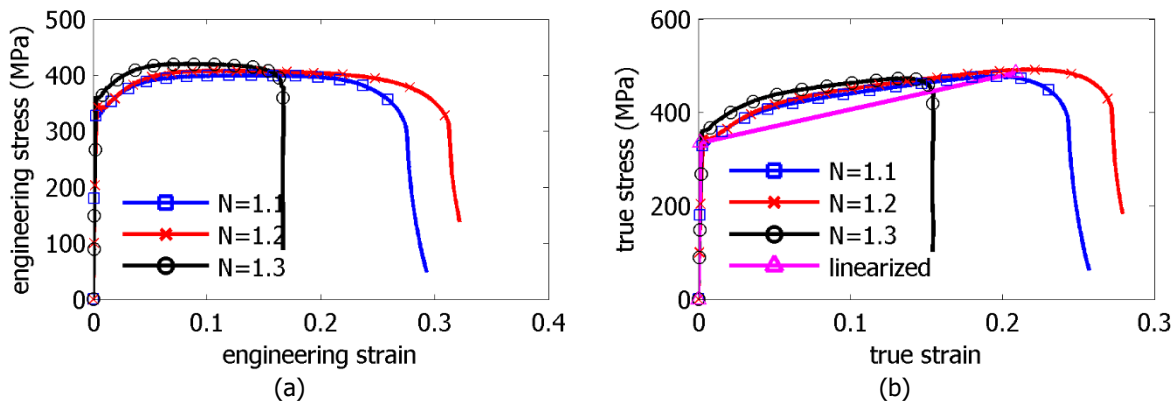


Figure 3-13: (a) Engineering and (b) true stress – strain curves for steel of specimen N=1 with bilinearized approximation

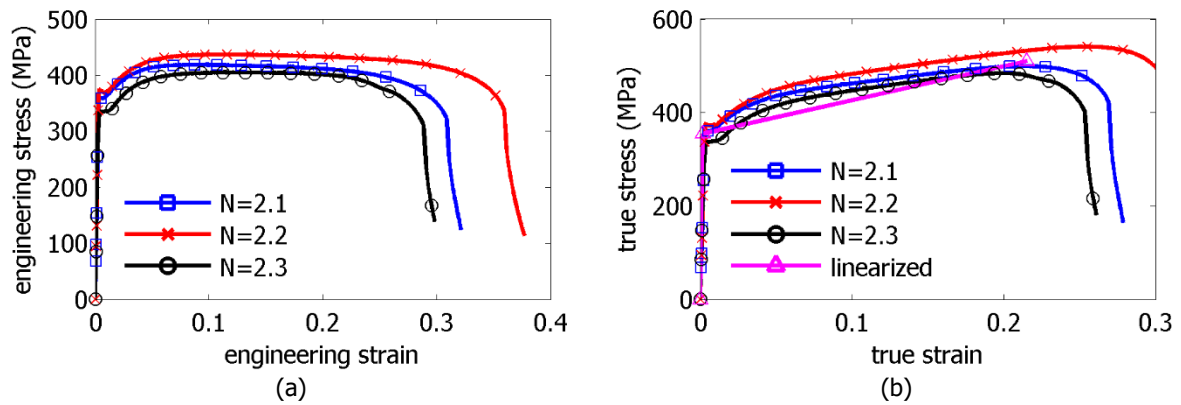


Figure 3-14: (a) Engineering and (b) true stress – strain curves for steel of specimen N=2 with bilinearized approximation

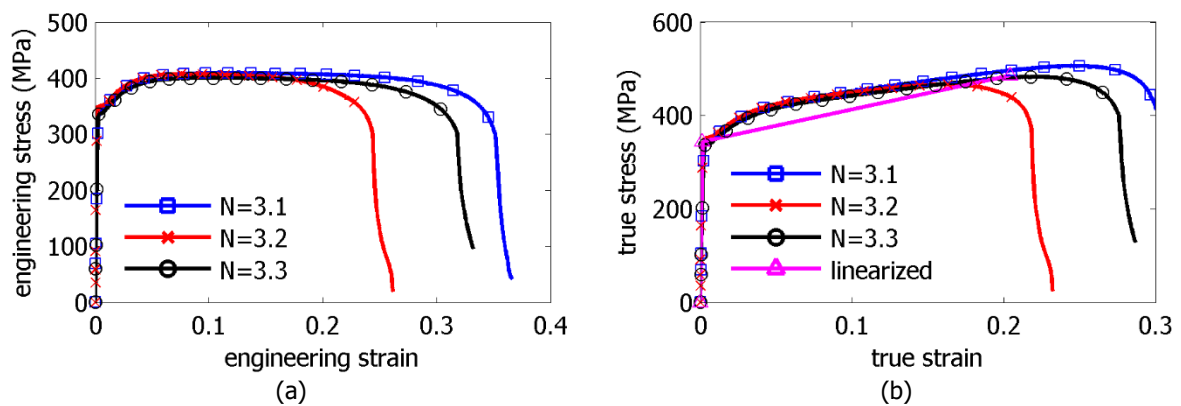


Figure 3-15: (a) Engineering and (b) true stress – strain curves for steel of specimen N=3 with bilinearized approximation

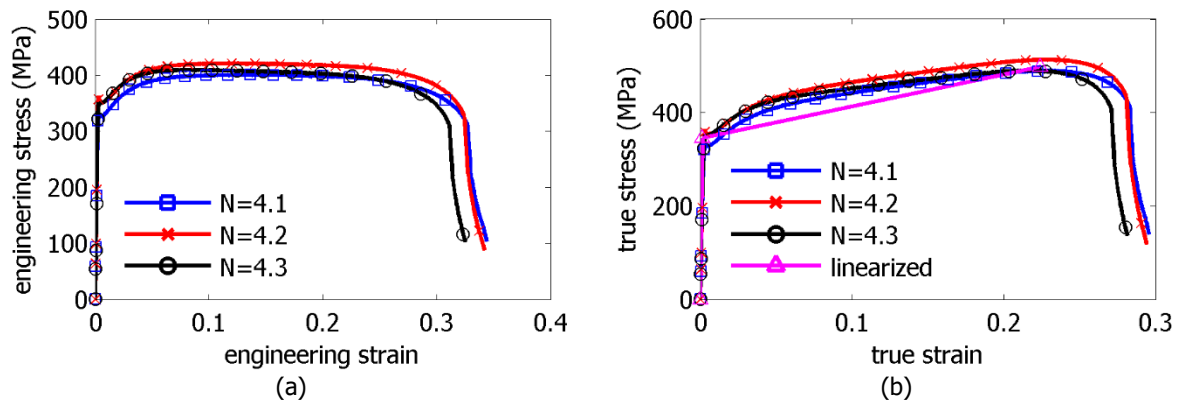


Figure 3-16: (a) Engineering and (b) true stress – strain curves for steel of specimen N=4 with bilinearized approximation

3.4 FLEXIBLE JOINT PROPERTIES

The flexible joints used in the experimental investigation were commercial metallic single bellows. The joint and its geometry are depicted in Figure 3-17. The material of the convolutions was stainless steel AISI 321L, while the pipe edges were made of carbon steel ST 37-2. Bellows were connected to the segmented parts of specimen N=4 through full-penetration butt welds. Bellow edges were chamfered, while tube segment edges were not. The single bellow used in the experimental study could

accommodate axial compression and extension, lateral and angular movement (Figure 2-19). The flexible joint type was selected based on its availability in the market and budget limitations, taking into account also that internal pressure was not considered in the investigation.



Figure 3-17: Flexible joint (single bellow-type) used in the experimental investigation

The purpose of the presented experimental investigation was to quantify the contribution of flexible joints in strain reduction when integrated in pipes subjected to imposed displacement. It was thus necessary to measure their axial, lateral and angular stiffness. For that purpose, two individual experiments were performed to estimate the axial and angular stiffness of the joint, respectively. It is noted that due to the inherent difficulty to experimentally decouple shear and bending, an individual experiment for measuring lateral stiffness was not carried out. This lack of data was decided to be handled using joint properties published on data sheets by joints manufacturers. Commercial joint specifications indicate that for similar low pressure single joints, the ratio of axial over lateral stiffness can range from 0.25 to 0.75.

Firstly, an experiment was conducted to investigate the axial stiffness of the joint. The experimental set-up and the measuring devices are shown in Figure 3-18. The joint was welded between two CHS 114.3x3 segments, while two flanges were attached at their edges. On the top flange a wire rope was mounted through a hinge formulation and properly connected to the actuator head. The test was performed with the use of a 300kN hydraulic actuator operating in displacement control. The rate control of the imposed displacement was equal to 0.032mm/s and the applied load was measured by a load-cell attached to the actuator. Four vertical LVDTs (V.LVDT) were installed to record the joint's extension, while two horizontal LVDTs (H.LVDT) were placed horizontally to measure any deflection of the specimen from verticality. The number of LVDTs was selected in order to increase the accuracy of the measurements and to provide sufficient amount of experimental data in order to exclude any out-of-plane movement. Additionally, two SGs were mounted at the bottom of the specimen to record any extension of the support segment, to verify that the applied extension was absorbed by the joint. It is noted that preliminary numerical results of the PFJ experiment disclosed that joint's axial movement would be tensile. Thus, a tensile test was decided to be performed, rather than a compressive one.

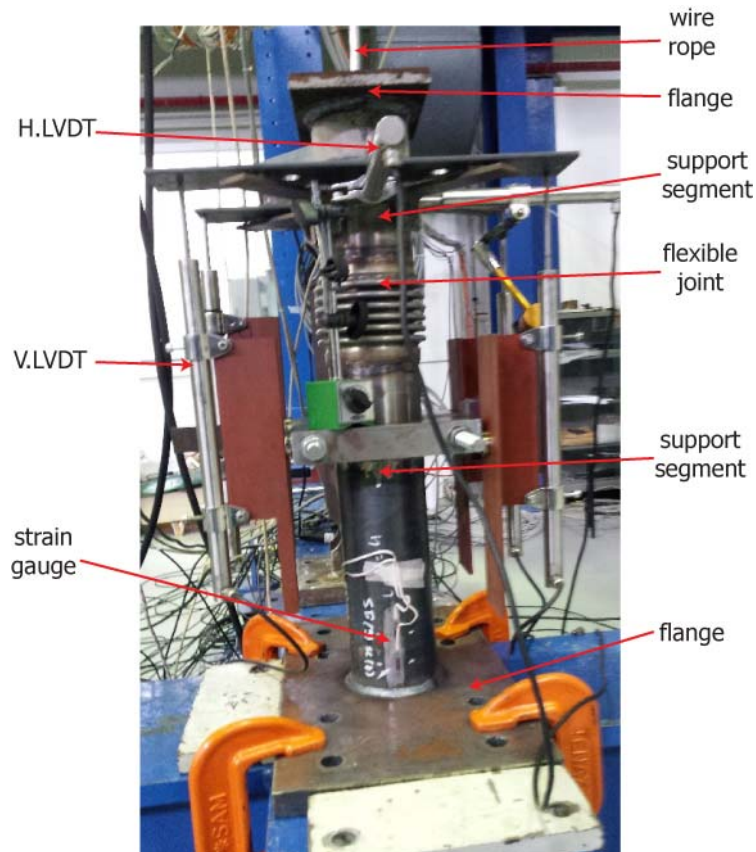


Figure 3-18: Flexible joint tensile test experimental set-up and measuring devices

The experimental results are presented in terms of the equilibrium path in Figure 3-19a, where on the vertical axis the load monitored by the actuator's load-cell is presented and on the horizontal axis the average displacement of the four V.LVDTs. The experimental path includes also the unloading path that was not considered in processing the results. The joint behavior in axial tension was nearly linear until the displacement reached the value of about 72.3mm, where the joint failed through local deformations of the convolutions (Figure 3-19b). It is noted that local deformations were observed to develop in a quite symmetric manner around the circumference of the joint in angles of 120degrees. The joint's convolutions are mechanically created in a joint-forming machine through expansion of a tube. Thus, when the joint was tensioned, the convolutions were subjected to flattening that caused local deformations to form. H.LVDTs provided measurements of maximum displacement equal to 3mm, indicating that the deviation from verticality was insignificant. The maximum tensile strain was equal to $72\mu\text{strain}$, which was adequately low to assume that the applied extension was totally absorbed by the joint.

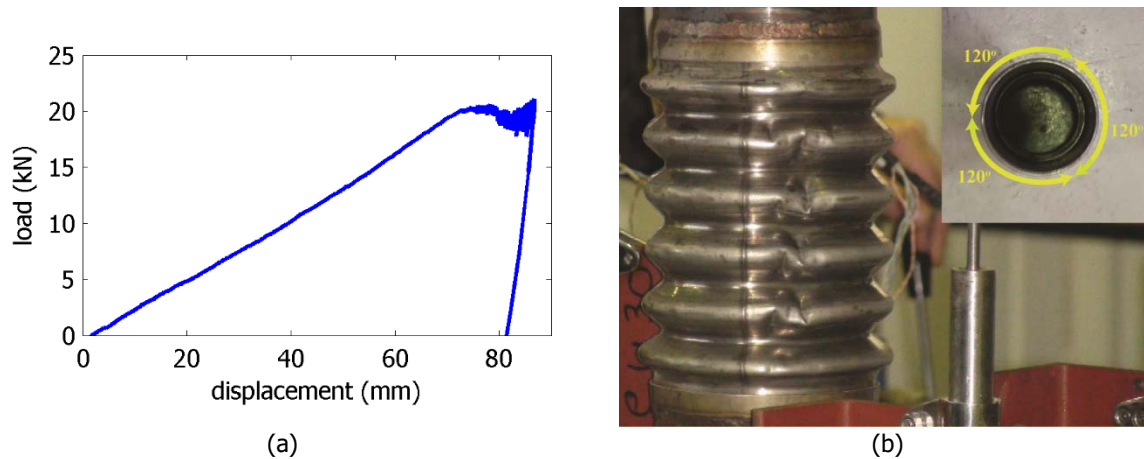


Figure 3-19: (a) Experimental equilibrium path of joint tensile test and (b) joint failure in expansion through local deformation of the convolutions

A second test was performed to measure the joint angular stiffness. The experimental set-up and the measuring devices of the joint bending test are illustrated in Figure 3-20. The joint was welded between two CHS 114.3x3 segments; one edge was free and the other was welded to a thick steel plate, which was properly connected to a rigid base on the testing frame. The displacement-application flange was used for this experiment and was connected to the actuator head via a wire rope. The connection of the wire rope to the actuator was implemented through a hinge formulation, ensuring that no axial force could be applied to the specimen and at the same time the applied load would be always perpendicular to the joint undeformed axis. The test was performed using the laboratory's hydraulic actuator, operating in displacement control with rate equal to 0.032mm/s. Two vertical LVDTs were attached through hinges on the displacement-application flange to measure the vertical displacement. Two strain gauges were mounted at the top and bottom of the segment close to the support flange to monitor any potential bending of the supporting tube, to identify whether the applied angular movement is fully absorbed by the joint.

The experimental results are presented in terms of the equilibrium path in Figure 3-21a (including the unloading path), where the load monitored by the actuator's load-cell is plotted on the vertical axis and the average displacement of the two vertical LVDTs on the horizontal axis. The joint behavior in bending was highly nonlinear, while two turning points were identified, namely for displacement 30mm and 80mm. When the vertical displacement reached the value 118mm, a significant drop in load was detected. It is noted that the unloading path was not considered in the results processing. This point was considered to represent the failure of the joint, as three convolutions got into contact (Figure 3-22).

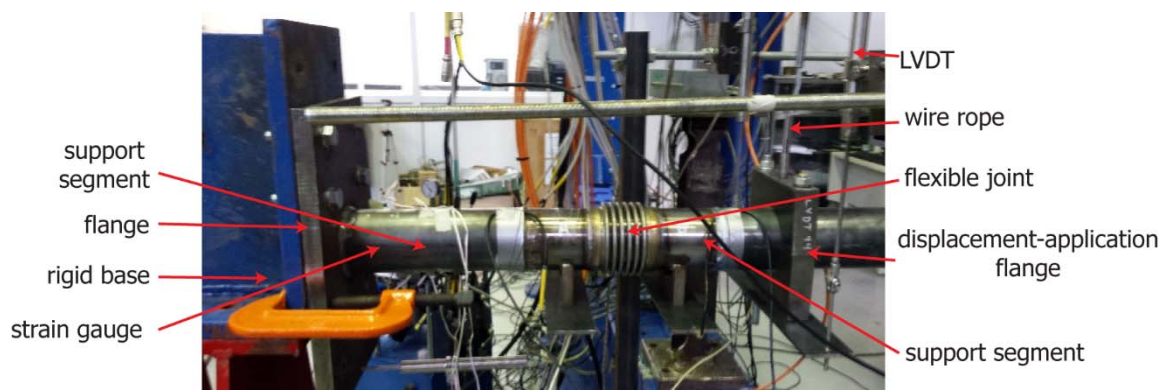


Figure 3-20: Flexible joint bending test experimental set-up and measuring devices

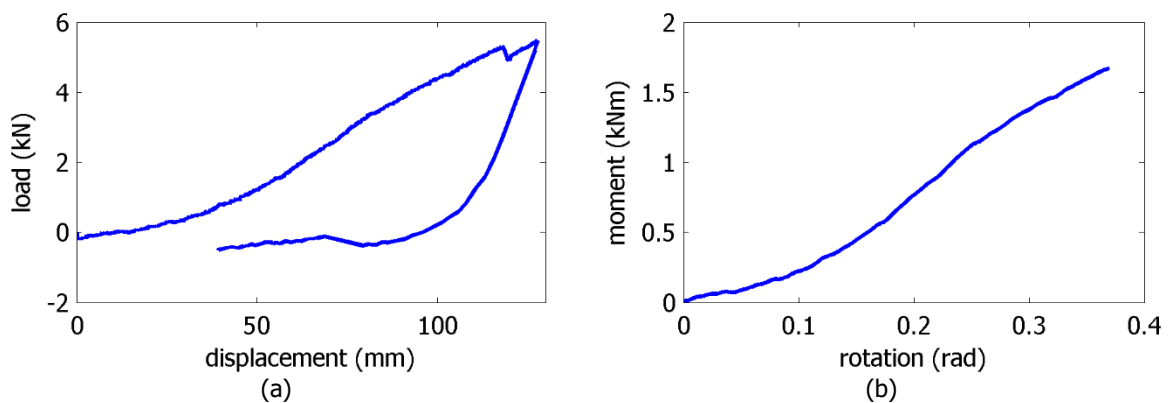


Figure 3-21: Experiment equilibrium path of joint bending test in terms of (a) force – displacement and (b) moment – angle curves

The joint rotation point was found to be in the middle of these three convolutions and the joint rotation angle is depicted in Figure 3-22. Using the geometry of the joint rotation, the force – displacement path was converted to moment – angle terms (Figure 3-21b). Finally, the maximum tensile strain was equal to $425\mu\text{strain}$ and the maximum compressive strain was $457\mu\text{strain}$, indicating on the one hand that no axial force was applied and on the other that strain values were sufficiently low to assume that the angular movement of the specimen was undertaken by the joint. Finally, for the sake of completeness it should be noted that the manufacturers of such flexible joints specify that the maximum joint deformation (axial, lateral and angular) are not concurrent.

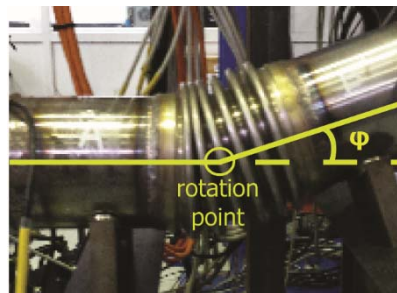


Figure 3-22: Geometry of flexible joint failure in bending through contact of consecutively convolutions

3.5 EXPERIMENTAL RESULTS

In this section the experimental results of continuous specimens and the specimen with flexible joints are presented separately and compared through load – displacement and displacement – strain curves, as well as stress and strain distributions and deformed shapes.

3.5.1 Continuous specimens

The CP specimen deformation took place within the vertical plane defined by the specimen longitudinal axis and the imposed displacement axis. The experimental load – displacement equilibrium paths for the CP specimens are illustrated in Figure 3-23, where the load monitored by the actuator's load-cell is presented on the vertical axis and the average displacement obtained from LVDT-6&7, located on the displacement-application flange (Figure 3-7) is presented on the horizontal axis. The primary observation is that the overall CP specimen behavior is nonlinear. A turning point at displacement equal to about 55mm is detected in the equilibrium path, indicating yielding of the end and middle cross-sections. A good match is observed between the three specimens, indicating good repeatability of the experiment.

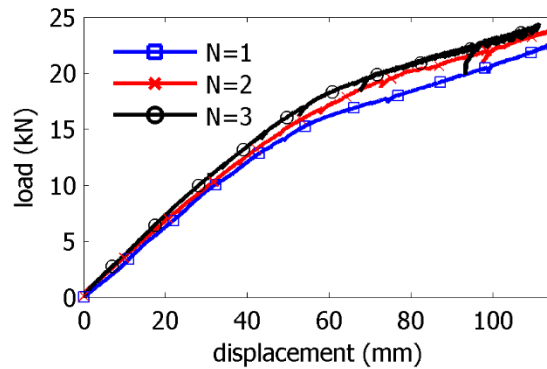


Figure 3-23: Load – displacement experimental equilibrium paths of CP specimens

Further comprehension of the CP specimen’s behavior can be provided by comparing the experimental equilibrium paths to a simplified analytical one, considering concentrated plastic hinge formation. The specimen steel stress – strain relationship is considered as elastic – perfectly plastic without hardening. The equivalent analytical static model in the elastic range is that of a beam with fixed ends with length L and flexural rigidity EI , subjected to concentrating loading P in the middle-span. In such case the maximum moment is developed at the fixed ends and at the middle, where the loading is applied (Figure 3-24). After formation of the plastic hinges, a cable-type behavior is assumed. The analytical load – displacement equilibrium path is compared to the experimental ones in Figure 3-25, where the applied load is presented on the vertical axis and the middle-span deflection on the horizontal axis. A sufficient match is shown regarding the elastic and the post-yielding beam behavior, apart from the transition area, where premature yielding of the specimens is evident.

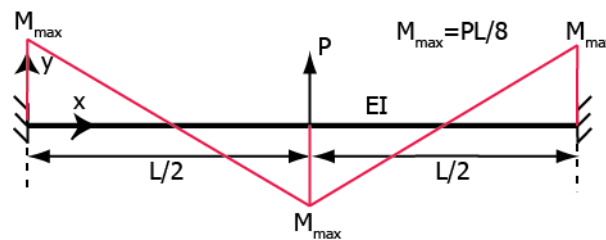


Figure 3-24: Analytical approach of CP specimen’s behavior in the elastic range: static model and bending moment distribution

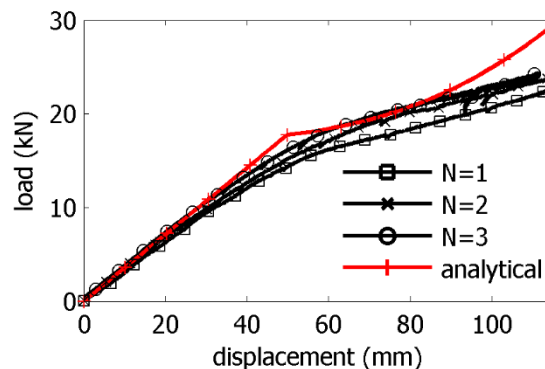


Figure 3-25: Experimental and analytical equilibrium paths of CP specimens

The assumption of plastic hinges’ formation at the ends and the middle is verified via the obtained strain – displacement paths that are presented in Figure 3-26 through Figure 3-28. It is observed that plastification of cross-sections close to end-plates (SG-A1, SG-A2, SG-B1 and SG-B2) and cross-section

at the middle (SG-A3, SG-A4, SG-B3 and SG-B4) occurred roughly for the same level of imposed displacement for all CP specimens for both tensile and compressive strain measurements.

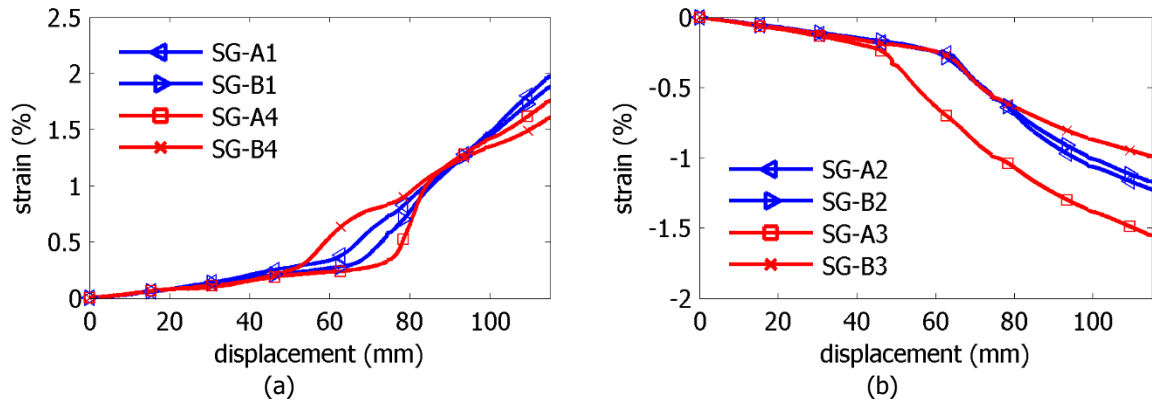


Figure 3-26: (a) Tensile and (b) compressive strain measurements from strain gauges of specimen CP N=1

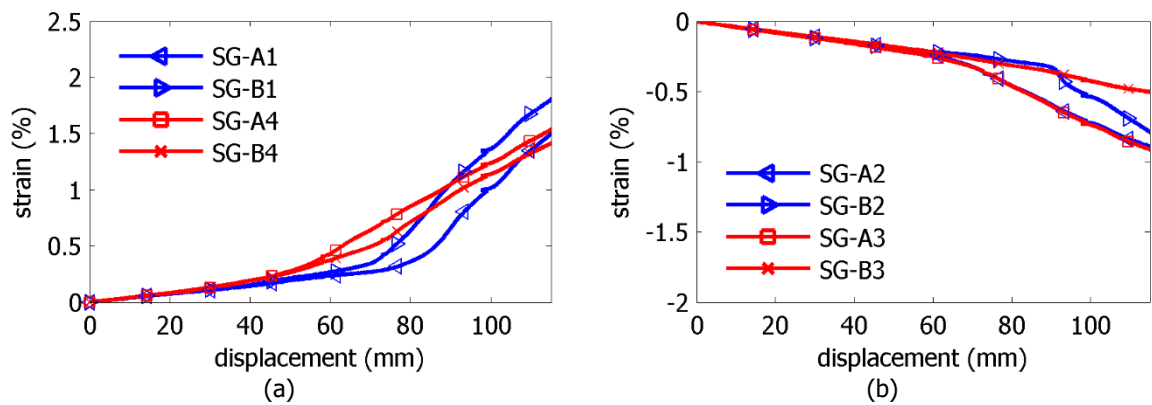


Figure 3-27: (a) Tensile and (b) compressive strain measurements from strain gauges of specimen CP N=2

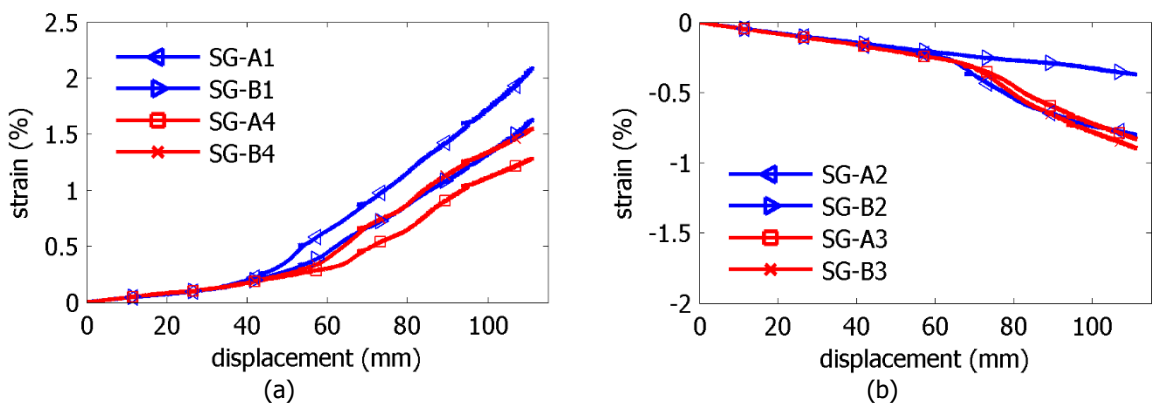


Figure 3-28: (a) Tensile and (b) compressive strain measurements from strain gauges of specimen CP N=3

The deformation of the CP specimen at selected values of the imposed displacement is indicatively presented in Figure 3-29 for specimen N=3, where the progressive formation of the curved s-shape (Figure 3-2) deformation is shown. Additionally, the deformation of the specimen various levels of imposed displacement monitored by the individual LVDTs and the DPs (Figure 3-7) is indicatively displayed in Figure 3-30, indicating very good agreement between the LVDTs and the DPs.

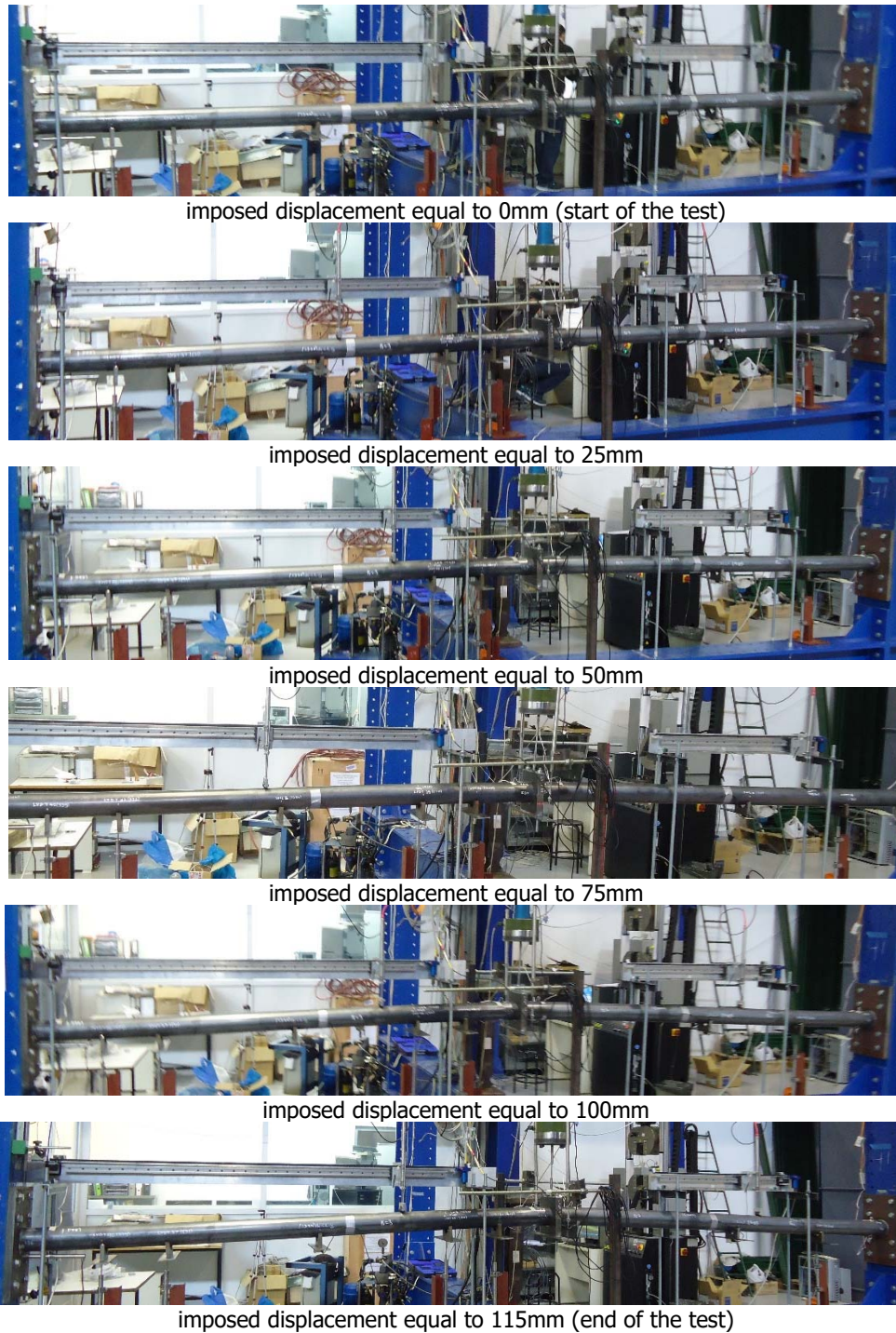


Figure 3-29: N=3 CP specimen experimental deformation for imposed displacement ranging from 0mm to 115mm

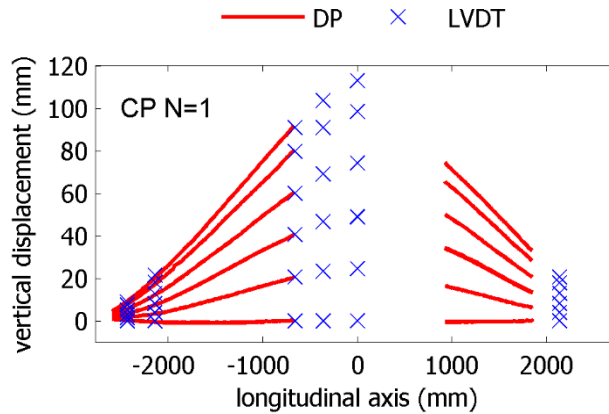


Figure 3-30: Experimental deformation of CP N=1 specimen at various levels of imposed displacement

Furthermore, yielding of the end cross-sections was verified via the strains recorded by the strain gauges. Strains monitored from every strain gauge (Figure 3-7) of the CP specimen are presented in Figure 3-31 and Figure 3-32 for side A and for side B, respectively. It is observed that strain measurements from CP specimens were in practice identical within the elastic range of the tube behavior until yielding took place for displacement equal to around 55 mm. Then, a turning point in the strain – displacement curves was detected and thereafter minor differences were reported on the tensile and the compressive strains. The strain variations after yielding were attributed to the sensitivity of the strain gauges in the post-yielding area in combination with the redistribution of strains within the cross-section due to the gradual formation of the plastic hinge.

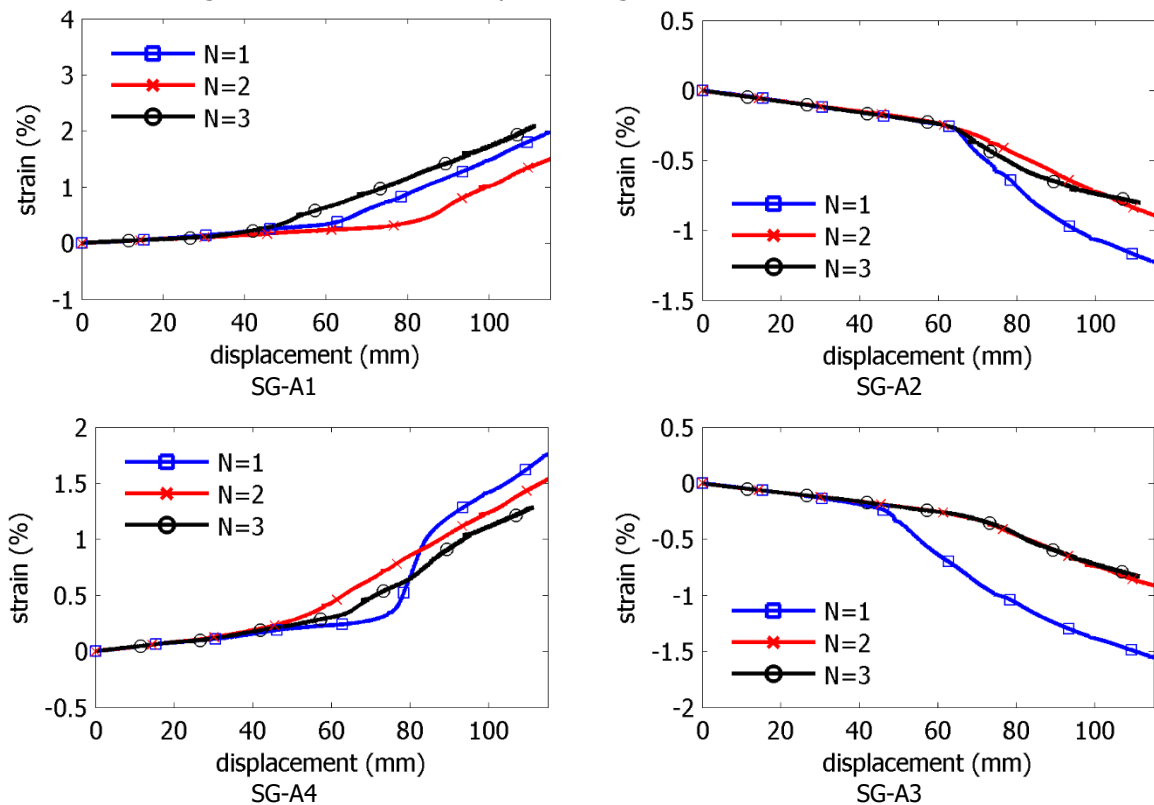


Figure 3-31: Experimentally obtained tensile and compressive strains of CP specimens from side A

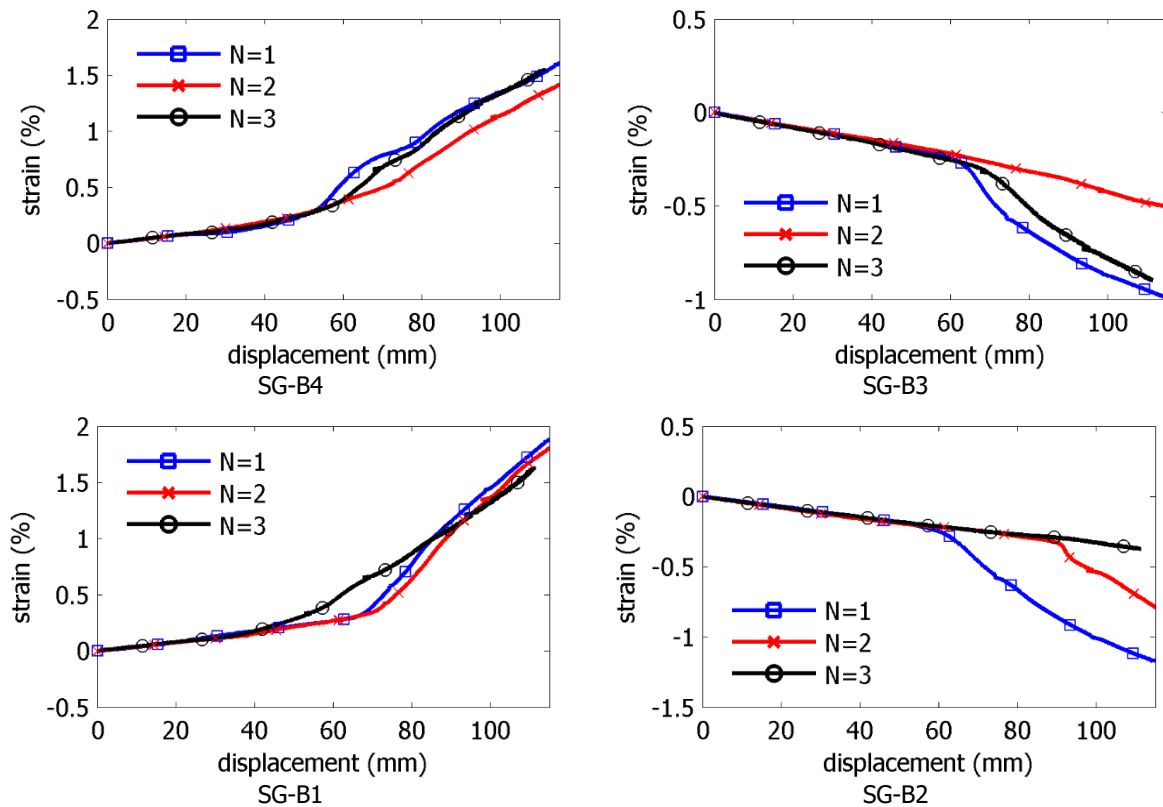


Figure 3-32: Experimentally obtained tensile and compressive strains of CP specimens from side B

3.5.2 Specimen with flexible joints

The experimental load – displacement equilibrium path of PFJ specimen is depicted in Figure 3-33, where the load monitored by the actuator’s load-cell is presented on the vertical axis, while the average displacement obtained from the LVDTs located on the displacement-application flange (Figure 3-7) is presented on the horizontal axis. The major observation is that load values were almost two orders of magnitude smaller than the CP specimens and that there was not a clearly visible equilibrium path, but instead a cloud of measurements was recorded due to the sensitivity of the load-cell that was not fully capable of monitoring such low load values. Additionally, load measurements from the onset of the test were above zero, as the actuator was loaded approximately with half of the specimens’ self-weight, due to the inability of the joints to provide appreciable flexural resistance.

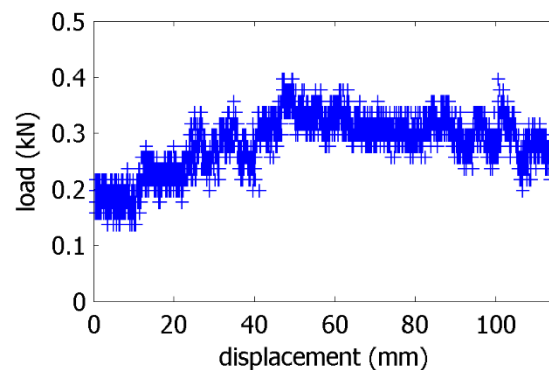
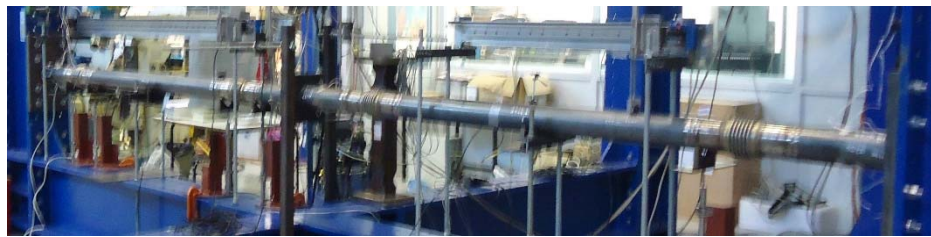


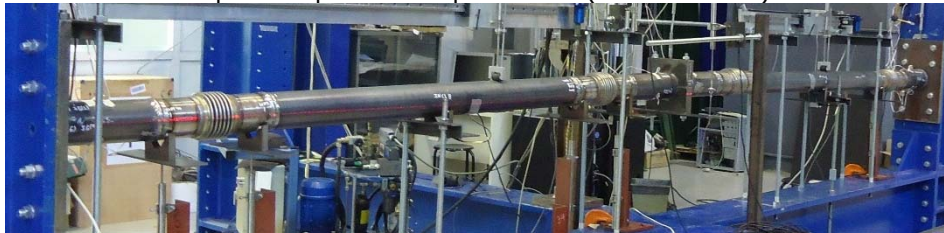
Figure 3-33: Load – displacement experimental equilibrium path of PFJ specimen

The deformation of the PFJ specimen at selected values of the imposed displacement is presented in Figure 3-34, where the expected formation of piece-wise deformation shape is shown. Additionally, the

deformation of the specimen various levels of imposed displacement monitored by the individual LVDTs and the DPs (Figure 3-7) is indicatively displayed in Figure 3-35, indicating very good agreement between the LVDTs and the DPs.



imposed displacement equal to 0mm (start of the test)



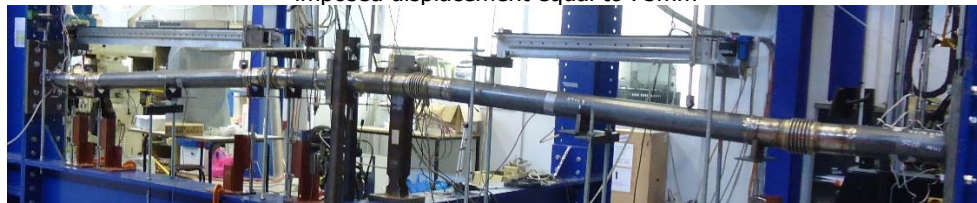
imposed displacement equal to 25mm



imposed displacement equal to 50mm



imposed displacement equal to 75mm



imposed displacement equal to 100mm



imposed displacement equal to 115mm (end of the test)

Figure 3-34: PFJ specimen experimental deformation at level of imposed displacement ranging from 0mm to 115mm (photos from different angles)

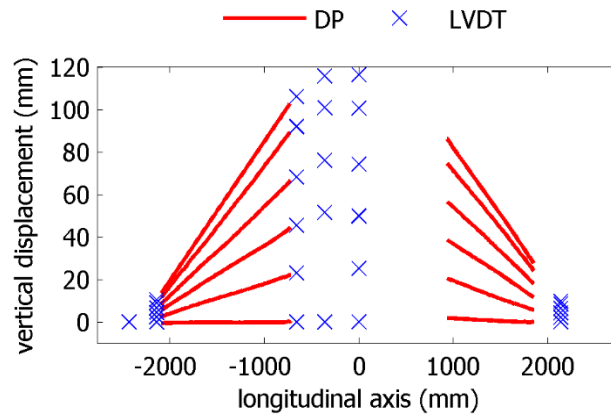


Figure 3-35: Experimental deformation of specimen PFJ at various levels of imposed displacement

Then, similarly to the load – displacement cloud, the recorded strain clouds are shown in Figure 3-36 and Figure 3-37 for side A and side B, respectively. The strain equilibrium paths were ascending in absolute value, indicating the increase of the developing stress-state with reference to the displacement. Most importantly, strains were three orders of magnitude smaller than for the CP specimens, confirming the efficiency of flexible joints in protecting the pipe from strain-related failure modes, such as local buckling and tensile fracture, as outlined in more detail in the following section.

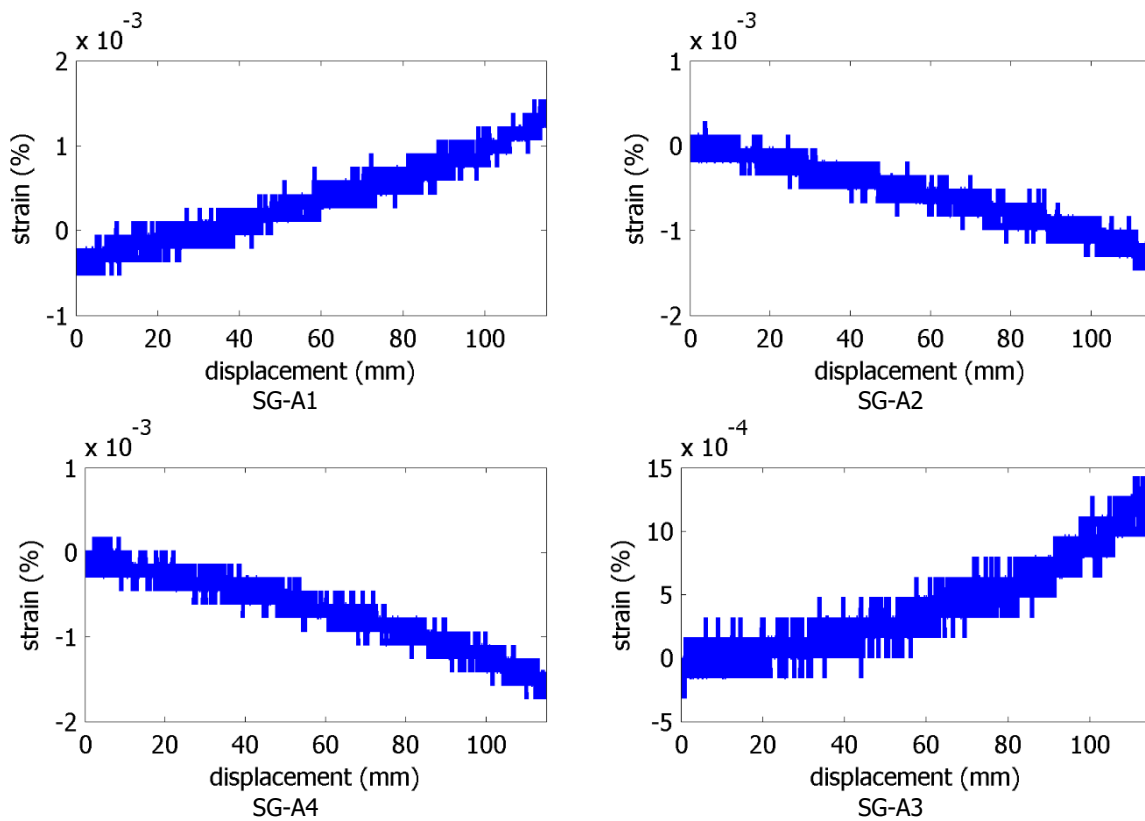


Figure 3-36: Experimentally obtained tensile and compressive strains of PFJ specimen from side A

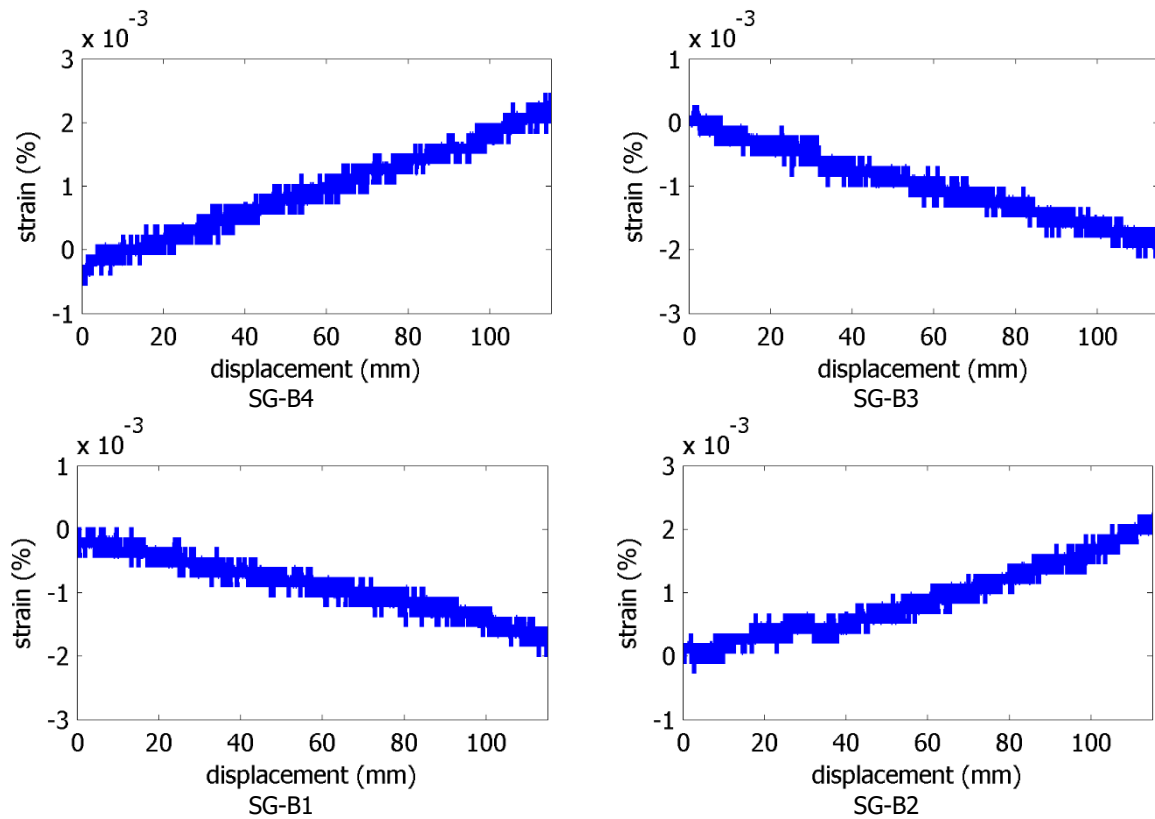


Figure 3-37: Experimentally obtained tensile and compressive strains of PFJ specimen from side B

3.6 COMPARISON OF EXPERIMENTAL RESULTS

The comparison of CP and PFJ specimens' results is crucial to identify and quantify the effect of flexible joints in terms of strain reduction in light that the pipeline design against faulting is strain-based. Results presented in sections 3.5.1 and 3.5.2 for CP and PFJ specimens, respectively, indicate that the introduction of joints has led to a significant decrease of load and developing tensile and compressive strains. Thus, the primary research objective of the present experimental study has been highlighted, namely, the considerable contribution of flexible joints in strain reduction has been confirmed, providing sufficient evidence that flexible joints can be a compelling mitigating measure for the protection of buried pipelines subjected to faulting. It is noted that due to the significant differences regarding strain and force development in CP and PFJ specimens that was reported, the graphical comparison of results through load – displacement and strain – displacement curves could not be viable. Therefore, a tabular comparison is presented by listing the maximum developed load and strains in Table 3-3 for the same level of imposed displacement. It is observed that PFJ load and strains were averagely in the order of two and three times, respectively, lower than those in CP specimens. The significant differences regarding the maximum values of strains obtained from the three CP specimens are due to the local redistribution of strains caused by cross-section yielding, so that maximum strain values do not, in general, occur at the locations of strain gauges.

As a final remark, the transformation of the continuous structural system of the tube to segmented due to the integration of flexible joints can be clearly seen in Figure 3-38, where the CP N=1 and PFJ N=4 specimen's final deformed shapes are presented.

Table 3-3: Comparison of CP and PFJ experimental results

specimen	max load (kN)	max compressive strain at edge (%)	max tensile strain at edge (%)	max tensile strain at middle (%)	max compressive strain at middle (%)
N=1 (CP)	24.61	-1.25	2.24	1.91	-1.08
N=2 (CP)	23.56	-0.79	1.81	1.42	-0.51
N=3 (CP)	23.79	-0.37	1.63	1.55	-0.89
N=4 (PFJ)	0.30	-0.0016	0.0017	0.0015	-0.0017

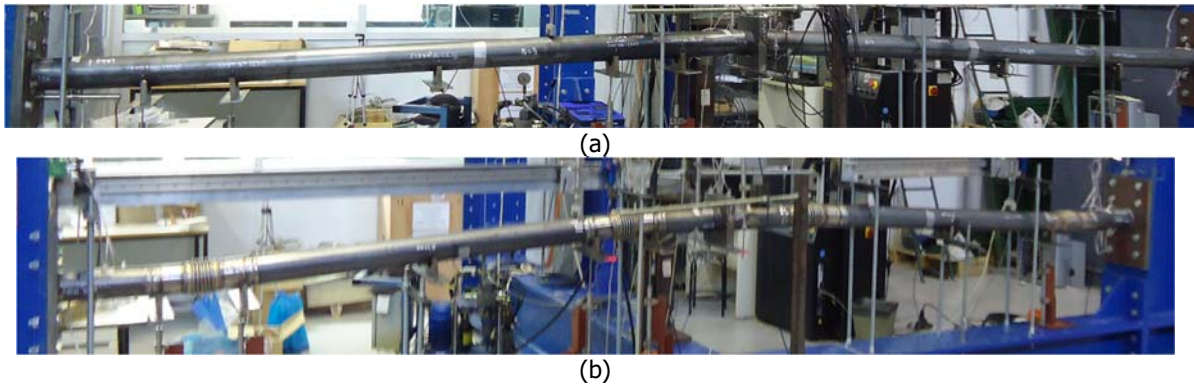


Figure 3-38: Comparison of (a) CP and (b) PFJ specimen's experimental deformations at the end of the tests

3.7 CONCLUSIONS

In the present chapter the execution and results of the experiments carried out in the context of the doctoral thesis were presented. Four specimens of circular hollow section (three continuous and one with internal flexible joints) were tested under concentrated imposed displacement in the middle-span, modeling the deformation of a buried pipe subjected to strike-slip fault rupture. The results associated with global and local response were presented via equilibrium paths (load – displacement curves) and strain – displacement curves, respectively. The main technical conclusions of the experimental study can be summarized in the following:

- The global response of the CP specimens was that of a fixed tube under transverse displacement at the middle-span. Material nonlinearity governed the post-elastic response.
- The integration of internal flexible joints transformed the structural system from continuous to segmented and consequently the developing strains were concentrated at the flexible joints, while the steel parts of the beam remained virtually undeformed and thus unstressed.
- Flexible joints showed to be an effective mitigating measure in terms of protecting the specimen from failure through remarkable strain reduction, compared to the corresponding continuous system.

The obtained experimental results led to qualitative conclusions as presented in this chapter and were encouraging on the use of flexible joints in buried pipelines subjected to seismic fault rupture. Nevertheless, the performance of a very large number of tests using alternative flexible joints is practically impossible due to cost and time constraints. The latter two drawbacks were also the reason for neglecting the effects of the surrounding soil. The experimental results will therefore be reproduced via finite element models in the next Chapter 4 in order to gain confidence in numerical models and subsequently use them for an extended parametric investigation.

4 NUMERICAL MODELING OF EXPERIMENTS

4.1 INTRODUCTION

The numerical modeling of the experimental work presented in Chapter 3 is thoroughly presented in the present chapter taking advantage of the progress that has been made during the last years in the fields of both numerical methods and computer engineering. The finite element method is widely used by the engineering community both in design and research for the analysis of structures. The calibration of numerical models based on experimental results provides researchers the opportunity to perform a large number of numerical analyses by considering alternative configurations and cases and being confident for the reliability of the obtained numerical results.

The corresponding numerical models of the experiments (Chapter 3) are presented in this chapter along with all the pertinent modeling details, regarding the type of finite elements, the boundary conditions, the applied loading, the considered nonlinearities and the methods of analysis. The obtained numerical results are compared to the corresponding experimental ones for both the continuous specimens and the specimen with flexible joints.

4.2 DESCRIPTION OF NUMERICAL MODELS AND ANALYSES

The general purpose finite element software ADINA (ADINA R&D 2006) was employed for the numerical analyses. Different modeling techniques were employed for the CP specimens and the PFJ specimen, based on the experimental results in terms of the developing stress-state.

4.2.1 Continuous specimens

The CP specimen was modeled both with 2-node Hermitian beam elements (FEM-beam) and with 4-node shell elements (FEM-shell), in order to identify the appropriate element type. View of a CP specimen placed in the testing frame and the corresponding numerical models are shown in Figure 4-1. It is noted that the displacement-application flange was not modeled, as preliminary analysis results revealed that modeling the displacement-application through an external node connected to all nodes at the middle section of the specimen via rigid links was sufficient. The connection of the specimen to the column flange of the testing frame was represented either as rigid or through detailed modeling of the bolted connection. The model of the latter approach is presented in Figure 4-2 and the details of the connection modeling are illustrated in Figure 4-3. The column flange of the testing frame was meshed with shell elements and considered to be fixed. The end-plate and the nuts were also meshed with shell elements. The bolts were meshed with bolt elements, which are beam-type finite elements, capable of being subjected to pretension, while they were considered to be fixed on the testing frame.

Appropriate contact elements were introduced to model the contact pairs of nuts – end-plate and end-plate – column flange.

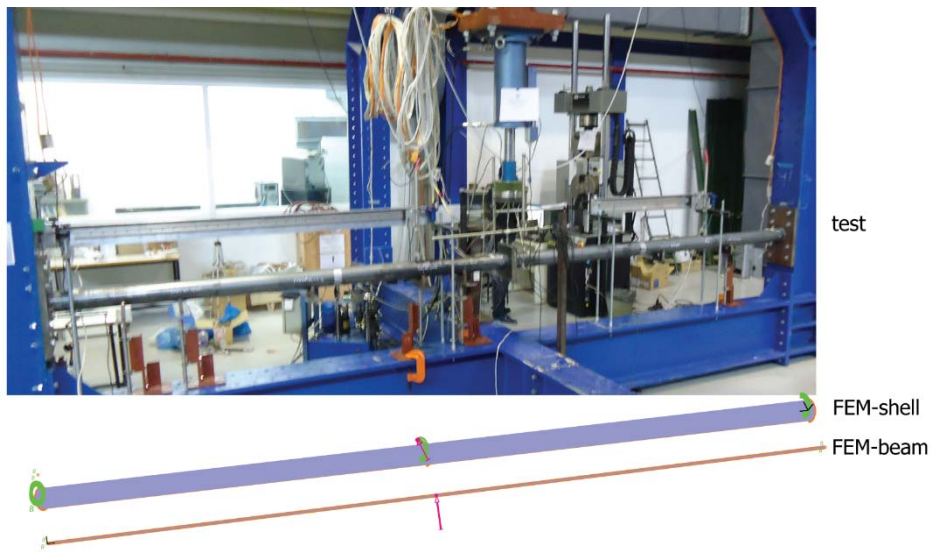


Figure 4-1: CP specimen at the testing frame and corresponding numerical models

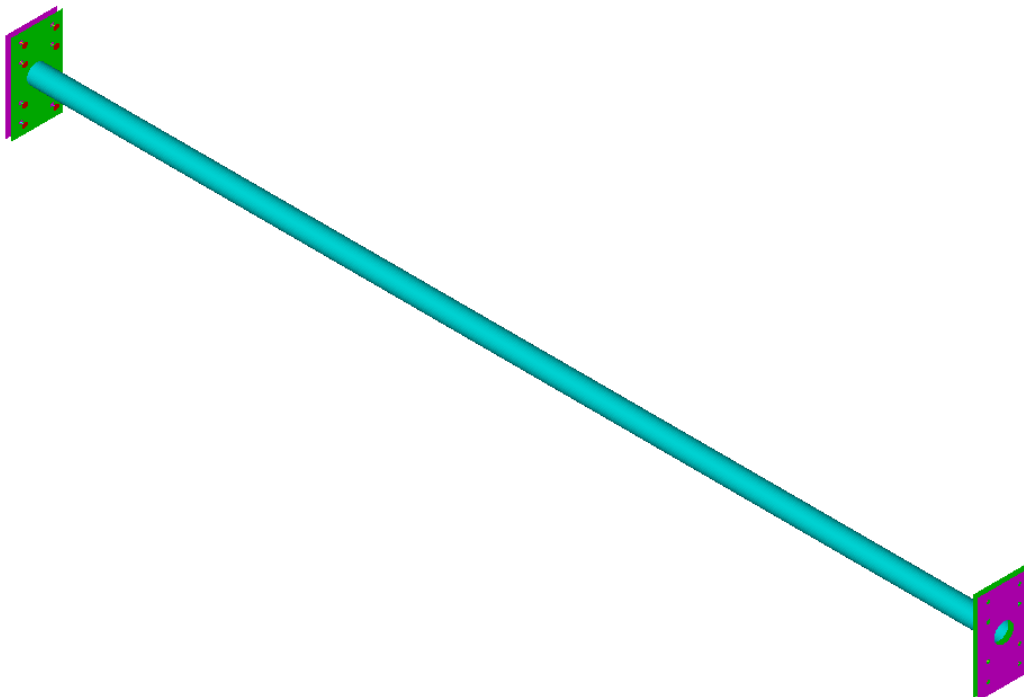


Figure 4-2: Numerical model of CP specimen with detailed modeling specimen – testing frame connection

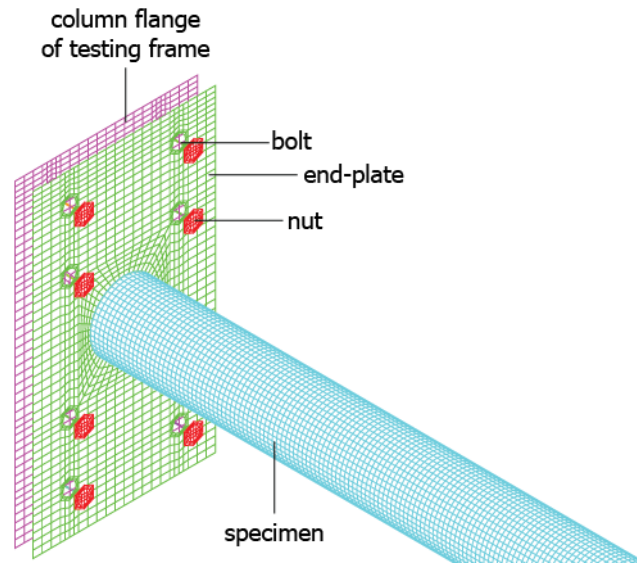


Figure 4-3: Modeling details of the CP specimen – testing frame bolted connection

CHS beams are manufactured through cold-bending of steel sheets and are then seam-welded. Due to this process residual stresses develop over the cross-section and along the steel member. Residual stresses are divided into: (i) circumferential stresses due to cold-bending, having nonlinear distribution through the thickness (Ross and Chen 1976). The thickness of the tube specimens was equal to 3mm and considered to be sufficiently low for the effect of the circumferential residual stresses to be assumed as insignificant. It is noted for the sake of completeness that residual stresses due to the manufacturing process (residual stresses around the perimeter) would be a lot more for a thick pipe. (ii) Longitudinal stresses due to the metallurgical alterations induced within the heat-affected zone during the seam welding procedure. Ross and Chen (1976) carried out experimental tests and measured the longitudinal stresses due to the welding, while Gao et al. (1998) presented a simplified distribution of the residual stresses distribution (Figure 4-4).

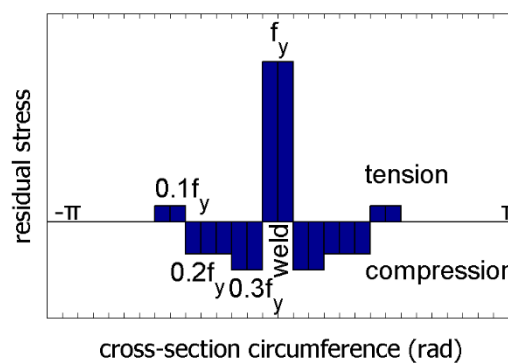


Figure 4-4: Longitudinal residual stresses on circular hollow section due to seam-weld (Gao et al. 1998)

These residual stresses were incorporated in the numerical models through initial strains as proposed in ADINA R&D (2006), taking into account that neither the circumferential, nor the longitudinal residual stresses were measured in the present study. In the FEM-shell numerical approach for the CP specimens, the longitudinal residual stresses were incorporated as initial longitudinal strains, according to the material stress – strain relationship. Their modeling relied on discretizing the specimen shell into zones consisting of different element groups. Then, every element group was assigned appropriate initial strains (Figure 4-5). The location of the seam-weld on the cross-section defines the distribution of the residual stress. As the seam-weld of the CP specimens that were tested within the present study was not at the same circumferential location (Figure 4-6), the effect of residual stresses was different for

every specimen, as will be shown later. The different element groups are illustrated in Figure 4-7 with different color, indicatively for specimen N=3.

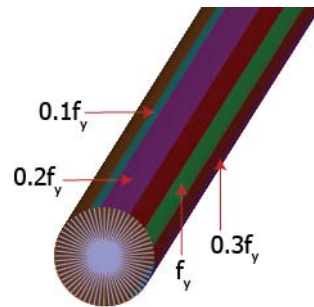


Figure 4-5: Modeling of longitudinal residual stresses through different element groups

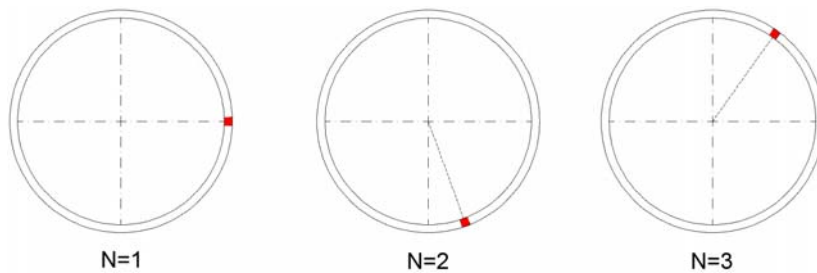


Figure 4-6: Seam-weld location on the cross-sectional circumference of CP specimens

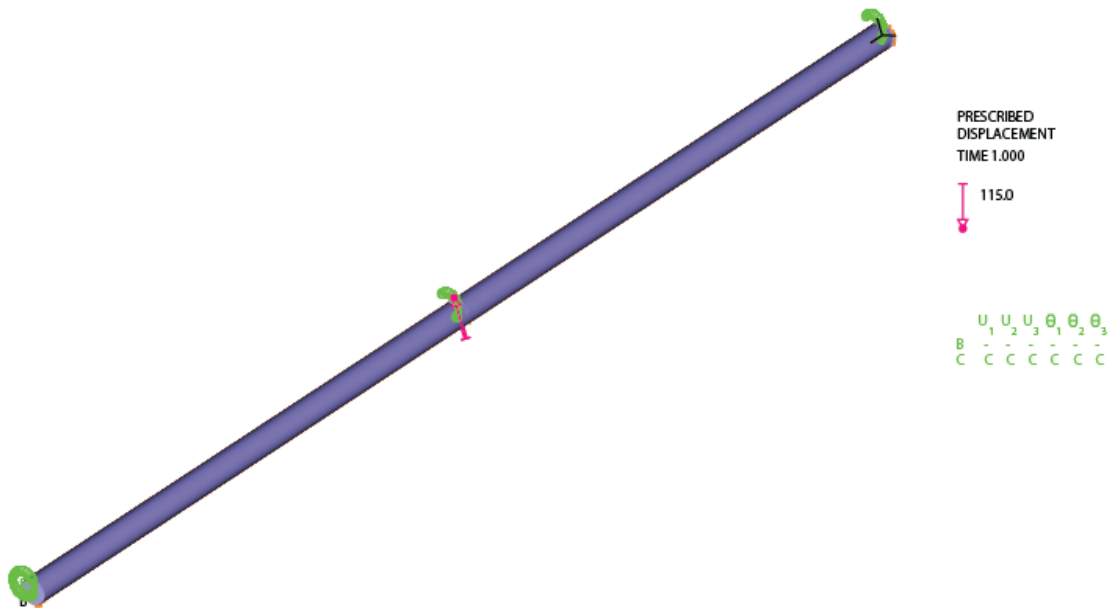


Figure 4-7: Numerical modeling of CP specimen

4.2.2 Specimen with flexible joints

The PFJ specimen was meshed into 2-node Hermitian beam-type finite elements, considering that the experimental results revealed that the specimen’s behavior was entirely elastic. Flexible joints can be modeled either as a general beam finite element with its stiffness matrix being constructed from the spring rates provided by the manufacturer, or as a generic flexible joint, represented by uncoupled springs at the center point, without considering the joint length (Peng and Peng 2009). In the present study, joint modeling as a generic flexible joint was selected and thus joints were represented by three uncoupled nonlinear springs, i.e. a rotational spring to model the angular deformation capability and two translational ones to model the axial and lateral deformations. Axial and angular springs’ properties

were obtained from the tension and bending joint tests (section 3.4), while the lateral spring was estimated through data sheets of joints manufacturers, as stated in section 3.4. The connections of the PFJ specimen to the testing frame were assumed to be rigid. View of the PFJ specimen placed in the testing frame and the corresponding numerical model are shown in Figure 4-8.

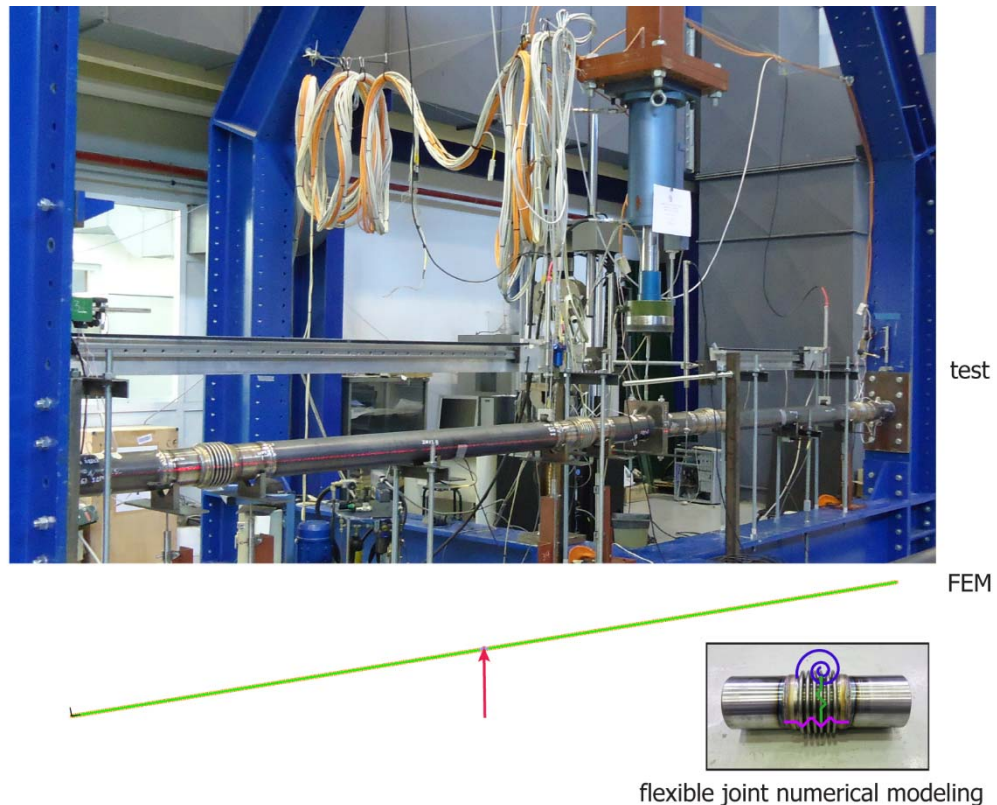


Figure 4-8: PFJ specimen at the testing frame and corresponding numerical model

4.2.3 Analysis method

A uniform and sufficiently dense meshing was used in all numerical models, according to the results of corresponding mesh density sensitivity analyses. The default integration order of finite elements was used, i.e. 2-node beam elements (Gauss integration order is used) and 4-node shell elements (Gauss integration through shell thickness). Additionally, according to previous experience, these elements do not have hourglassing and element locking issues.

The analysis was conducted in all cases in three steps: initial conditions (if applicable) were applied first, then the specimen self-weight was applied and finally, the transverse displacement was imposed. Initial conditions were different in every modeling approach. In case of detailed modeling of the specimen – testing connection, pretension of the bolts was applied in order to close any gaps between nuts – end-plate and end-plate – column flange, while in case residual stresses were considered, analysis was carried out to apply the initial stresses. Finally, the strategy proposed by Gantes and Fragkopoulos (2010) for the numerical verification of steel structures was used in the present study. The numerical results were obtained from Geometrically and Materially Nonlinear Analyses (GMNA), in order to account for both large displacements and material yielding, using the Newton – Raphson solution algorithm and the automatic time-stepping method (ATS). ATS is used to try to obtain a converged solution by using a reduced load step during equilibrium iterations when the predetermined load steps are possibly too large. The implementation of numerical nonlinear analysis considered the practical aspects of FEM presented in Kojic and Bathe (2004). It is also noted that local geometric imperfections were not considered in the analysis, as preliminary results revealed that their effects were practically insignificant.

4.3 EXPERIMENTAL AND NUMERICAL RESULTS

In this section the experimental results are compared with numerical ones separately for CP and PFJ specimens. The experimental results showed that yielding took place at CP specimens at the critical cross-sections, namely the fixed ends and the middle. On the other hand, experimental PFJ results revealed that its behavior was fully elastic.

4.3.1 Continuous specimen

The experimental equilibrium paths are compared to the numerical ones, obtained from GMNA. Two investigations were initially carried out, namely specimen meshing with either beam- or shell-type finite elements and boundary conditions modeling either as rigid or as semi-rigid, by modeling the bolted connection of the end-plate to the testing frame. The comparison of equilibrium paths regarding the type of finite elements by considering rigid boundary conditions is shown in Figure 4-9, where the experimental paths of CP specimens (test) are examined in comparison to the numerical ones (FEM-beam and FEM-shell). The vertical displacement of the displacement-application flange is presented on the horizontal axis and the load on the vertical one. The FEM modeling approach appeared to have a small effect on the post-yielding branch, while the elastic branches practically coincide. Specimen modeling with beam-type elements is shown to be sufficient. However, experimental results showed earlier yielding compared to the FEM model and thus shell-type elements are chosen for the subsequent steps of the investigation in order to model in more detail the specimen – testing frame connection and take into account the residual stresses.

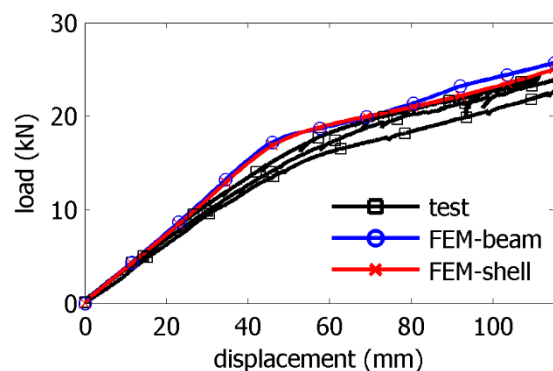


Figure 4-9: Experimental and numerical equilibrium paths of CP specimens considering different finite element type and fixed boundary conditions

Secondly, the effect of boundary conditions was addressed and the corresponding equilibrium paths are illustrated in Figure 4-10, where the CP experimental results (test) are compared to the numerical ones employing shell elements and considering either rigid end conditions (FEM-fixed) or connection modeling (FEM-connection). The major finding was that the boundary conditions did not modify the response of the numerical models, as the corresponding paths practically coincide. Therefore, modeling the boundary conditions as rigid was proven to be sufficient.

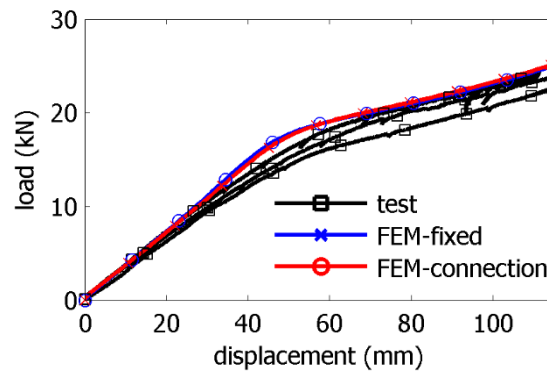


Figure 4-10: Experimental and numerical equilibrium paths of CP specimens (FEM-shell) considering different numerical boundary conditions

Results obtained from the aforementioned investigation indicated that the specimen’s boundary conditions could be handled as fixities and the specimen modeling with shell elements was not necessary. However, numerically obtained equilibrium paths demonstrated that the model was not fully capable of capturing the gradual and premature yielding of the critical cross-sections. This was attributed to longitudinal residual stresses caused by the seam-weld. Therefore, residual stresses were next incorporated in the model, through the process outlined in section 4.2. The location of the seam-weld on the tube circumference was different in every specimen (Figure 4-6). Experimental (test) and numerical equilibrium paths in terms of load – displacement (FEM-residual) are presented in Figure 4-11, while for comparison reasons the numerical equilibrium path without considering residual stresses (FEM-no-residual) is depicted.

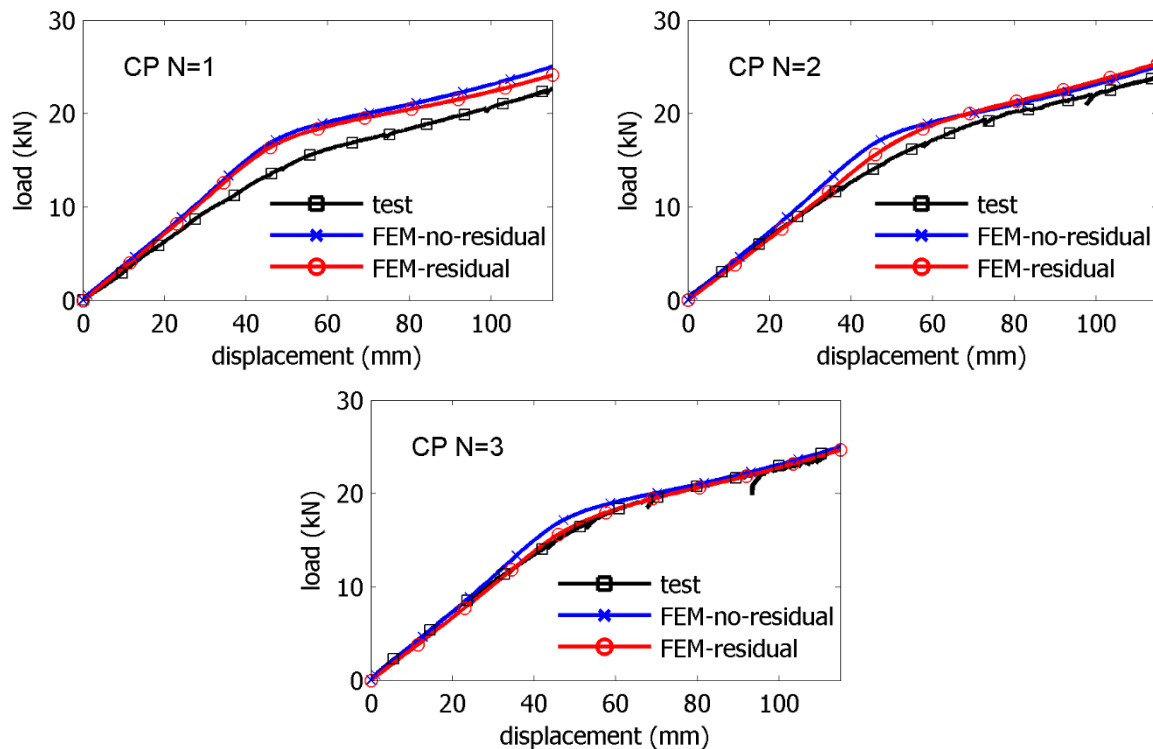


Figure 4-11: Comparison of experimental and numerical load – displacement equilibrium paths of CP specimens by considering or not longitudinal residual stresses

It can be seen in all cases that the incorporation of residual stresses improved the agreement between the numerical and the experimental results. Nevertheless, the seam-weld location played a dominant

role. As shown in Figure 4-4, steel is subjected to tension in the vicinity of the weld due to the heat treatment of the material caused by the welding procedure. Then, along the circumference of the cross-section the subsequent area is compressed to balance the above tension. Similarly, the final narrow affected zones are tensioned. This sequence of residual tension and compression around the seam-weld heavily affects the material behavior, while it expands over half of the cross-section. Based on the aforementioned "analysis", the results of Figure 4-11 can be evaluated. The seam-weld in specimen N=1 was located in the region of the cross-section neutral axis and therefore the weld heat affected zone did not extend over the cross-section areas where maximum tension and compression developed at the critical cross-sections. Hence, considering the longitudinal residual stress did not significantly improve the numerical results. Then, in specimen N=2, the seam-weld was located near the area, where the maximum tension was developed at the critical sections (specimen – end-plate connection). Therefore, the effect of residual tension and compression was more significant than in specimen N=1, which was verified by the fact that the "FEM-residual" model captured the tube yielding more accurately than the "FEM-no-residual" one. Finally, in specimen N=3 the match between the numerical and the experimental results was concluded to be significantly good due to the location of the seam-weld near the maximum developed compression at the critical cross-sections. In practice, the area where compression developed due to external loading was already compressed by the residual stresses and consequently yielding took place for lower displacement level than without accounting for residual stresses.

The numerical predictions of the specimens' deformation at various levels of imposed displacement are presented in Figure 4-12 indicatively for specimen N=1, where the longitudinal specimen axis is presented on the horizontal axis and the specimen vertical displacement on the vertical axis. The numerically obtained specimen's displacements are abbreviated as FEM, the LVDT measurements as test-LVDT and the ones recorded by the deformation plotter as test-DP. Similar results were extracted for specimens N=2 and N=3. Very good agreement is observed.

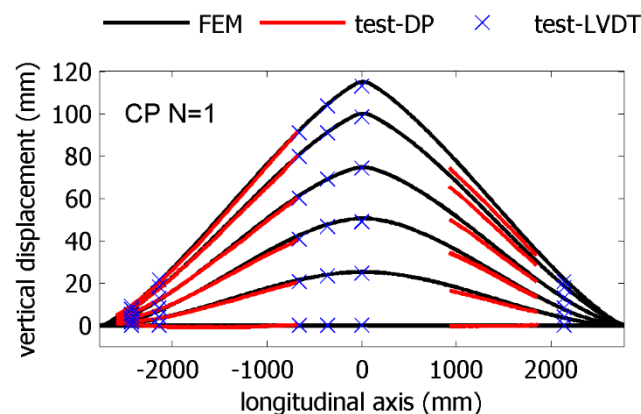


Figure 4-12: Experimental and numerical deformation of CP N=1 specimen at various levels of imposed displacement

Finally, numerical predictions of strains are presented in Figure 4-13 indicatively for specimen N=3 in terms of displacement – strain curves of CP specimens, where the tensile and the compressive strains at all measuring locations according to Figure 3-7 are presented on the vertical axis, while the vertical displacement of the specimen's middle on the horizontal axis (LVDT-6&7). The comparison of numerically and experimentally obtained strains revealed that there was a sufficiently good match in the elastic range. However, numerical models showed steel yielding taking place for higher displacement than experimental results and consequently numerically extracted strains were higher than the experimental ones, which was attributed to the sensitivity of strain measurement in the plastic range. The elastic and plastic regions, as predicted numerically, are shown in Figure 4-14 indicatively for

specimen N=3. The fact that the tensile plastic zones are more extended than the compressive ones indicates that the specimen develops cable-type action after formation of plastic hinges.

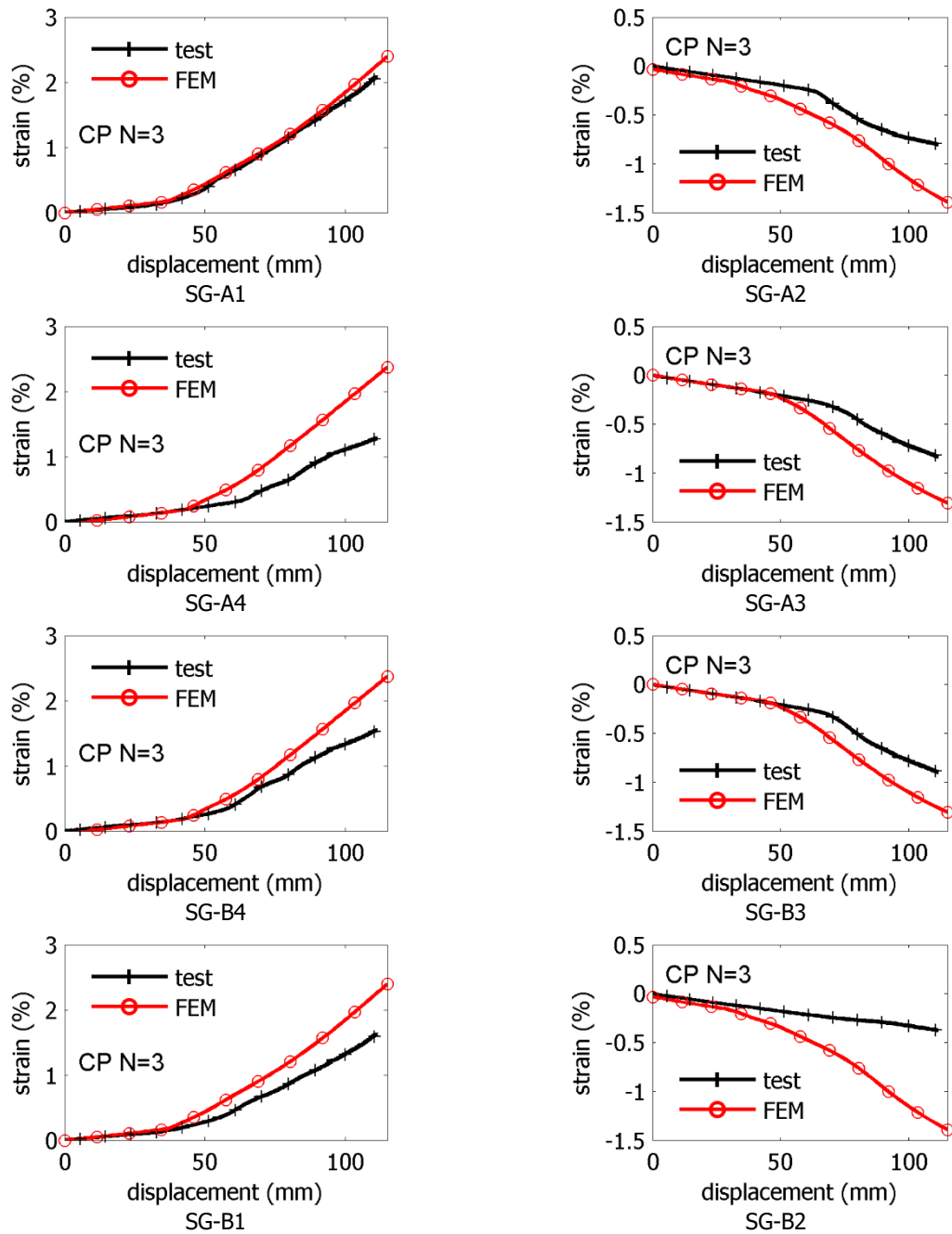


Figure 4-13: Experimental and numerical displacement – strain curves of N=3 CP specimen at measuring locations

The distribution of plasticity on the N=3 CP specimen presented in Figure 4-14 can be explained in more detail by the distribution of von-Mises stresses (Figure 4-15) and longitudinal strains (Figure 4-16), which both demonstrate clearly the critical locations, i.e. the locations where maximum stress-state is developed.

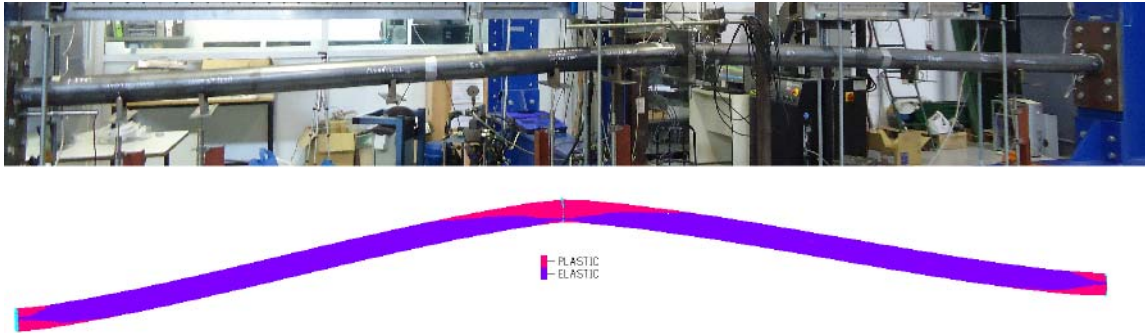


Figure 4-14: Elastic and plastic regions at failure of N=3 CP specimen

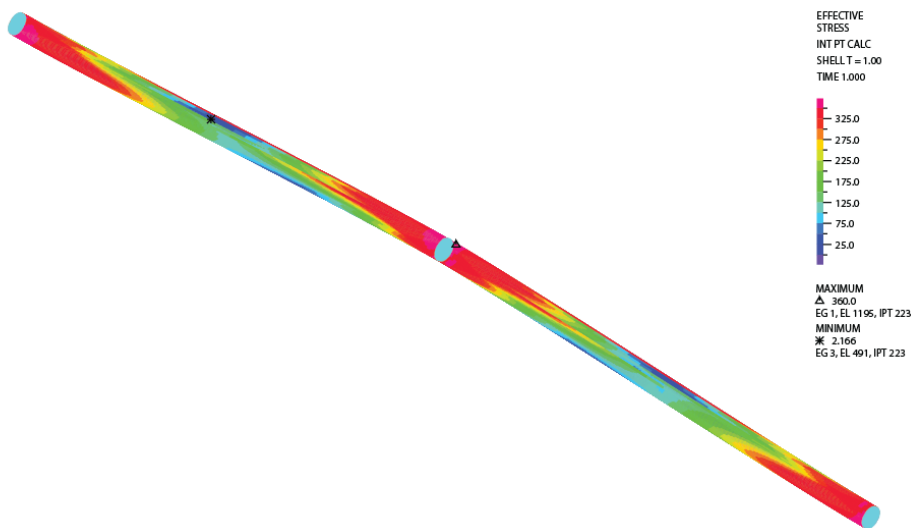


Figure 4-15: Distribution of von-Mises stresses of N=3 CP specimen

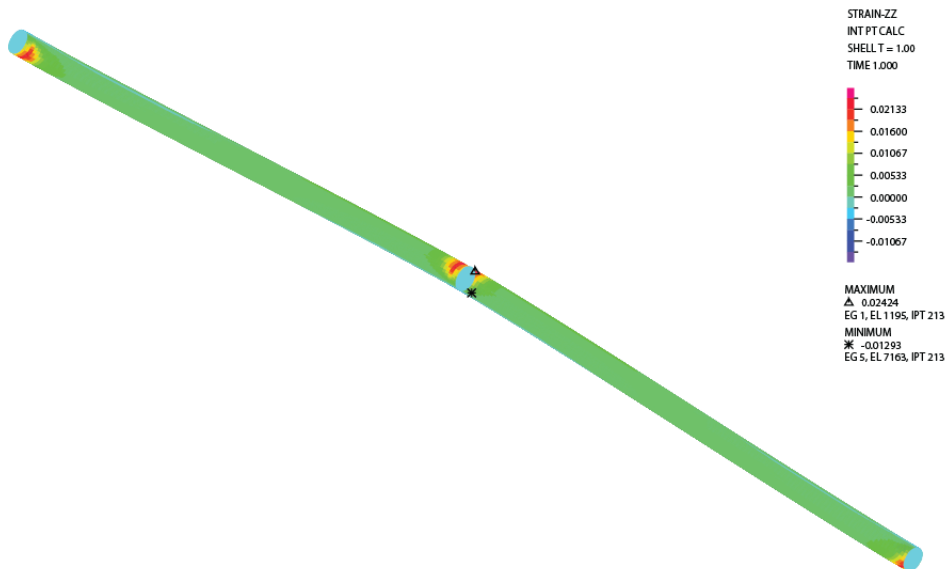


Figure 4-16: Distribution of longitudinal strains of N=3 CP specimen

4.3.2 Specimen with flexible joints

The specimen with flexible joints was modeled with beam-type finite element model, as presented in section 4.2.2, while the boundary conditions were assumed to be rigid. This modeling approach was selected based on the corresponding experimental results, which showed that the developed stress-

state was very low, compared to CP specimens, while experimental recordings were within the range of sensitivity of the measuring devices. The experimental equilibrium path is compared to the numerical one in Figure 4-17a, where the displacement of the displacement-application flange is presented on the horizontal axis and the load on the vertical axis. The numerical path was shown to exhibit different stiffening behavior, indicating cable-type of action, due to the negligible flexural stiffness of the beam with internal flexible joints. The specimen self-weight was considered in the numerical analysis and thus the load – displacement path's onset was equal to about half the self-weight, while due to the limited sensitivity of the load-cell for such low recordings, the onset of the experimental path is quite lower. However, taking the aforementioned limitations of the experimental monitoring process into account, the numerical model prediction of the specimen behavior is considered as satisfactory. It is noted that regarding the joint lateral stiffness, for which no experiment was executed, parametric analyses conducted with reference to the axial stiffness obtained from manufacturers' data revealed that its role to the specimen's behavior was very limited. It was thus decided to adopt an axial over lateral joint stiffness ratio equal to 0.50.

Finally, experimentally and numerically obtained deformed shapes of the specimen at various levels of the imposed displacement are illustrated in Figure 4-17b, where the vertical specimen displacement (in-plane with the imposed displacement) is plotted on the vertical axis, while the specimen's longitudinal axis is plotted on the horizontal axis. The numerically obtained deformed shape is presented as FEM, while the experimental results are represented by the measurements of the individual LVDTs (referred as test-LVDT) and the Deformation Plotters (referred as test-DP). The major finding is that results showed a comprehensive match and the assumed numerical approach is sufficient to model the behavior of the specimen with flexible joints.

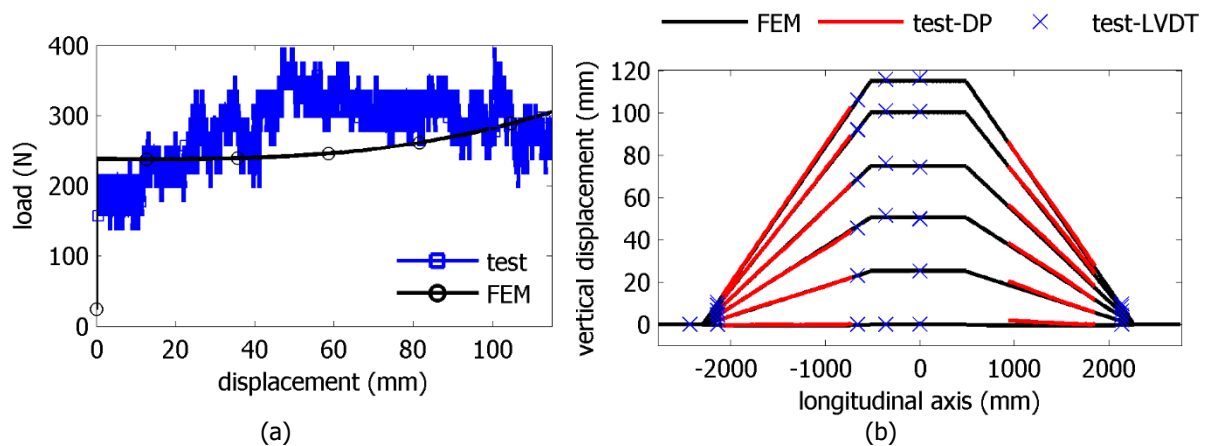


Figure 4-17: Summary of experimental and numerical results of PFJ specimen including: (a) load – displacement equilibrium path and (b) specimen deformation at various imposed displacement levels

4.4 CONCLUSIONS

The calibration of numerical models based on the experimental results (Chapter 3) has been presented. Finite element software ADINA (ADINA R&D 2006) was employed for this purpose and Geometrically and Materially Nonlinear Analysis were performed. The results were presented via equilibrium paths, strain – displacement curves and deformed shapes at various levels of the imposed displacement. The numerical analyses results were presented and compared to the corresponding experimental ones for the continuous specimens and for the specimen with flexible joints.

Initially, the appropriate finite element type and the boundary conditions for the CP specimens were investigated. Then, modeling residual stresses due to the longitudinal seam-weld with a simplified distribution was useful for capturing the gradual degradation of stiffness. Comparison of numerical and

experimental equilibrium paths revealed the effect of the location of the seam-weld on the beam behavior. In general, the numerical analyses' results of the tests were in good agreement with the experimental results, in particular for CP specimens.

The numerical analysis' results of the PFJ test were in moderate agreement with the experimental results, considering that the developing stress-state was very low and marginally within the sensitivity range of the test measuring devices. However, numerical modeling of tubes with internal flexible joints with beam-type finite elements and of flexible joints with rotational and translational springs was found to be sufficient for design purposes.

5 BUCKLING OF BEAMS WITH INTERNAL FLEXIBLE JOINTS RESTING ON FOUNDATION MODELING BURIED PIPELINES

5.1 INTRODUCTION

The introduction of flexible joints in buried steel pipelines subjected to fault rupture is proposed in the present thesis as an innovative approach towards the efficient protection of pipes against the two main consequences of faulting, namely local buckling of pipe wall and tensile fracture of girth welds. However, in case of reverse faulting, high compressive axial forces develop along the pipeline. Taking into account that the integration of joints reduces the pipe global stiffness, flexural buckling, also known as upheaval buckling, may emerge as a third possible failure mode. In such case the pipeline may significantly deform within the trench and even outside of it. A preliminary investigation of the upheaval buckling of continuous buried steel pipelines subjected to reverse faulting in comparison to local buckling and tensile fracture has been presented by Melissianos et al. (2014a).

In the present chapter, a systematic effort is carried out to investigate the effect of internal flexible joints in the buckling and post-buckling response of beams resting on elastic foundation. A Winkler beam with internal flexible joints constitutes an appropriate model to investigate the potential of upheaval buckling when the pipeline is subjected to reverse faulting (Melissianos and Gantes 2014a; b).

5.2 LITERATURE REVIEW AND RESEARCH OBJECTIVES

The so-called Winkler model of a beam resting on elastic foundation is a commonly applied engineering approach in various problems involving interaction between a structural member and the surrounding soil, due to its reliability and computational simplicity and efficiency. Applications of this model can be found in different areas of soil – structure interaction, such as foundation engineering, buried structures and railway tracks. Soil is considered as a single layer that can be represented by a series of closely spaced and mutually independent transverse springs with proportional resistance to deflection. Different aspects regarding the overall buckling behavior of continuous beams resting on elastic foundation can be found in the literature (Amazigo et al. 1970; Hetenyi 1946; Keener 1974; Massalas and Tzivanidis 1979; Massalas et al. 1978). Timoshenko and Gere (1961) showed the impact of soil stiffness on the critical eigenmode shape of axially loaded simply-supported Winkler beams, demonstrating that variation of soil stiffness may lead to eigenmode cross-over. Wu and Zhong (1999) implemented the

energy method to analytically investigate the buckling of elastically supported beams of finite length under compression for different end conditions, identifying eigenmode transition and then carried out post-buckling analysis of perfect beams and used the post-buckling curvature to examine beam stability. Rao and Neetha (2002) developed a detailed analytical methodology to estimate the elastic foundation stiffness that corresponds to the first transition of the critical eigenmode, using free vibrations. Buckling and post-buckling behavior of beams resting on elastic foundation was also investigated by Kounadis et al. (2006), leading to analytical expressions of the post-buckling equilibrium path for a 1-DOF model. Song and Li (2007) focused on thermal buckling and post-buckling of pinned – fixed beams on elastic foundation. The authors introduced a so called “shooting method” to analytically solve the complex boundary condition problem and also adopted the energy method to describe post-buckling behavior considering buckling temperature. Li and Batra (2007) presented equations for buckling and post-buckling behavior of laterally supported simply-supported and clamped beams. The major conclusions of this study included the insignificant impact of the nonlinear foundation parameter on the buckling load temperature and the post-buckling deformation. Aristizabal-Ochoa (2013) introduced a methodology to estimate the critical buckling load of axially loaded columns resting on Winkler foundation with generalized end conditions.

The aforementioned studies deal with beams of finite length. However, elongated structures, such as railway tracks and pipelines, are usually modeled as infinite beams. In such case, buckling localization emerges as an important issue. Localization of the buckling pattern depends among others on the applied axial force and the soil stiffness. Research on this topic is extensive and several researchers have presented rigorous analytical studies, trying to deal with the significant nonlinearity of the problem through advanced mathematical tools, among which prominent is the work by Hunt and Blackmore (1996), Hunt and Wadee (1991), Hunt et al. (1993) and Wadee et al. (1997).

A Winkler beam with internal hinges constitutes an appropriate model to investigate the potential of upheaval buckling when a pipeline with flexible joints is subjected to compression due to reverse faulting. An internal hinge modifies the beam global stiffness and consequently affects the corresponding buckling and post-buckling behavior. The extent of this effect depends on the relative pipeline – joint – soil stiffness and must be taken into account in case such mitigating measures are proposed. The buckling behavior of an axially loaded, clamped beam without lateral support and with two internal hinges was presented by Wang (1992). The author applied an analytical approach to maximize the critical buckling load through the optimization of hinges’ location. Later, Wang (2002) extended the formerly developed model by introducing a single elastic support to strengthen the hinge location. The critical buckling load of an elastic beam with various end conditions was maximized by optimizing the hinge location considering the elastic restraint stiffness. Later, Wang (2008) presented a more detailed model of a beam resting on elastic foundation to address the optimum hinge location for maximizing the critical buckling load and recently the author presented an analytical study on the buckling of an infinite beam resting on elastic foundation with one or more internal hinges subjected to compressive force (Wang 2010).

The topics of buckling behavior and eigenmode cross-over of continuous beams that rest on elastic Winkler foundation have been discussed in depth by previous researchers, as summarized above. However, the pertinent work regarding internally hinged beams is limited. Aiming at addressing this issue, in the present chapter the effect of hinge rotational stiffness on eigenmode cross-over with respect to soil stiffness is first quantified by means of numerical linearized buckling analysis. Furthermore, the beam post-buckling behavior is not adequately addressed in the existing literature. Hence, this study then focuses on the numerical investigation of the beam post-buckling behavior through geometrically nonlinear imperfection analysis. Simply-supported and clamped boundary conditions are considered, with the second being representative of the deformed shape assumed by buried pipelines that are subjected to fault activation. Two cases of internal hinges are analyzed: an

internal hinge located in the beam middle and two internal hinges equally-spaced along the beam. The internal hinges are assumed to be equipped with an elastic rotational spring, while relative translations of the two beam parts at each hinge are restrained, to represent a hinged flexible joint (Figure 2-21c).

The beam buckling behavior is first studied through linearized buckling analysis following the suggestions of Dimopoulos and Gantes (2012). Results are then directly compared to the corresponding ones in cases of continuous beams (Gantes and Melissianos 2014). Parametric studies are conducted to highlight the effect of soil stiffness, hinge rotational stiffness and beam boundary conditions on critical buckling loads and eigenmode shapes. Geometrically nonlinear analyses are then carried out to identify the beam post-buckling behavior, imperfection sensitivity and the effect of soil restraint on ultimate loads. Additionally, the effect of soil nonlinearity on beam response in terms of ultimate loads is examined by considering the soil as tensionless and having different upward and downward compressive stiffness. Concluding, research results are of importance for pipelines with flexible joints, as the design assumptions and safety factors to be considered are highly affected.

5.3 ANALYSIS MODEL

In order to investigate the overall buckling response of an Euler-Bernoulli beam with internal hinges resting on elastic or elastoplastic foundation, an appropriate numerical approach has been selected. This approach is considered as suitable for dealing with this problem from a structural design rather than engineering mechanics point of view, as it can in future be readily extended to issues that are commonly encountered in practice, such as non-straight pipeline route, inhomogeneous soil conditions, varying axial force distribution along the pipeline accompanied by bending moments, etc.

In case of buried pipelines subjected to fault rupture, the source of the applied action on the structure, namely the fault location, is well defined. If the fault is activated, the pipeline is forced to follow the ground motion and to deform on the two sides of the fault in an s-shaped pattern extending to two so-called anchor points, one on each fault side, beyond which the developing stress-state is nearly negligible. If the fault is reverse, significant axial compression develops in the pipeline, with a maximum value at the fault and gradually diminishing towards the anchor points due to soil friction. Aiming at addressing this problem in a simplified, conservative manner, the selected numerical model is that of an elastic Winkler beam of length L , defined by the anchor points, and flexural rigidity EI , subjected to axial compressive force P . It is also noted that the model of a finite beam for the simplified pipeline modeling is sufficient regarding also the issue of buckling localization, taking into account that the location of the source of the applied action is well defined, while the anchor points represent the assumed boundary conditions. To that effect, either hinged or clamped boundary conditions are considered at the two ends, even though for long struts actual boundary conditions are less significant as the deflections and their derivatives all tend to zero near the boundaries. Furthermore, the problem is treated as static, given that the dynamic effects of fault movement are considered by pertinent codes as negligible (American Lifelines Alliance 2005; ASCE 1984; European Committee for Standardization 2006).

The beam longitudinal displacement is denoted by x and the transverse displacement by $y(x)$. Beams rest on Winkler foundation that exhibits stiffness k_s , which is normalized via the expression:

$$K_s = k_s L^4 / EI \quad (5-1)$$

and ranges from a minimum value $K_s=180$ to a maximum value $K_s=20000$. Three characteristic soil stiffness values are selected, namely $K_s=180$, $K_s=10000$ and $K_s=20000$, which correspond to the critical eigenmode shape of the continuous beam being the first symmetric, the first antisymmetric and the second symmetric, respectively. These soil stiffness values are selected based on the fact that soil stiffness increase leads to eigenmode cross-over for the continuous beam among the three above

mentioned types of modes (Gantes and Melissianos 2014). Furthermore, the selected soil stiffness values are reasonable assumptions for the soil stiffness of upward soil springs in buried pipeline analysis. For example, the value $K_s=10000$ corresponds coarsely to a small diameter, shallowly buried pipe in dense backfill sand, while $K_s=180$ stands for a large diameter, deeply buried pipe backfilled with loose sand. Estimation of soil springs' stiffness for buried pipelines is carried out using the suggestions of pertinent codes and provisions (e.g. American Lifelines Alliance 2005; ASCE 1984; European Committee for Standardization 2006) or expressions found in the literature (e.g. O'Rourke and Liu 2012) depending on the backfill material properties. According to these sources, the soil material laws are nonlinear, idealized in practice for the design of buried pipelines against faulting as elastic – perfectly plastic. In the present work, linear soil springs have been assumed, while in section 5.5.9 the effect of soil nonlinearity is investigated, considering different soil stiffness in the upwards and downwards directions. In the numerical model, Winkler soil is modeled with transverse springs that connect beam nodes to fixed "ground" nodes and exhibit stiffness only in the local axial direction corresponding to their undeformed state. It is noted that in the literature nonlinear soil properties with softening effects have also been considered, for example by Yang and Bradford (2015), who showed that the softening soil parameter plays an important role in localization phenomena and the post-buckling response of infinite beams.

The internal hinge of the beam is equipped with an elastic rotational spring of stiffness k_r and practically replaces the beam flexural rigidity. The corresponding rotational stiffness is normalized via the expression:

$$K_r = k_r / (EI / L) \quad (5-2)$$

In the subsequent analyses the internal hinge rotational stiffness is appointed with five characteristic values, i.e. $K_r=0, 2, 5, 10$ and 45 . The value $K_r=0$ represents the case of a "pure" internal hinge without stiffness, while stiffness $K_r=45$ was found to be sufficiently high to almost restore the beam flexural continuity. It is noted that the selected range of rotational stiffness conforms to the corresponding stiffness of commercially available hinged flexible joints. Thus, the rotational stiffness of the internal hinge can be selected by the design engineer in order to monitor the strain reduction of the structure, achieved by the use of the joints. The stiffness of such joints increases as the pipe diameter increases, while the maximum rotational capacity decreases. Thus, the selected range, apart from the maximum value that is related to beam continuity restoration, is realistic for hinged flexible joints in pipeline applications that are expected to undergo large rotations due to faulting.

The beam analysis models are depicted in Figure 5-1 through Figure 5-4 by considering two cases: an internal hinge located at the beam middle or two internal hinges equally-spaced along the beam. In particular, the simply-supported beam with one internal hinge is shown in Figure 5-1, the simply-supported beam with two internal hinges in Figure 5-2, the clamped beam with one internal hinge in Figure 5-3 and the clamped beam with two internal hinges in Figure 5-4.

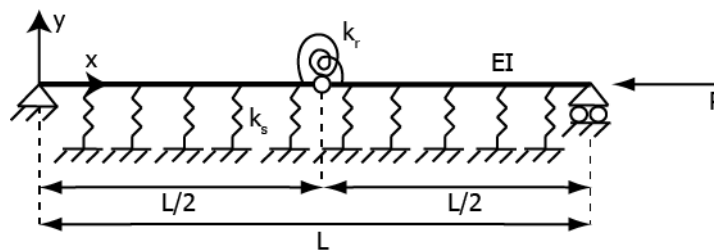


Figure 5-1: Simply-supported beam resting on foundation with one internal hinge

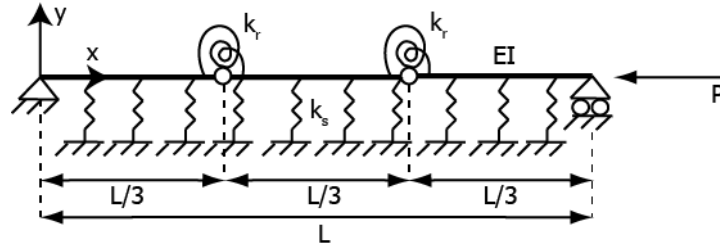


Figure 5-2: Simply-supported beam resting on foundation with two internal hinges

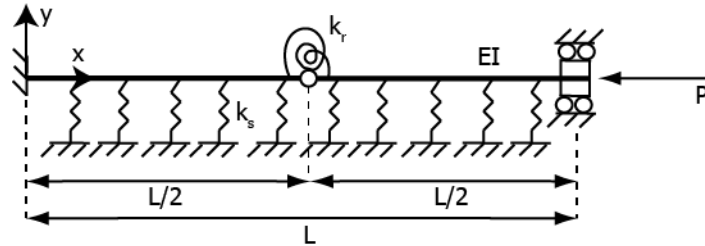


Figure 5-3: Clamped beam resting on foundation with one internal hinge

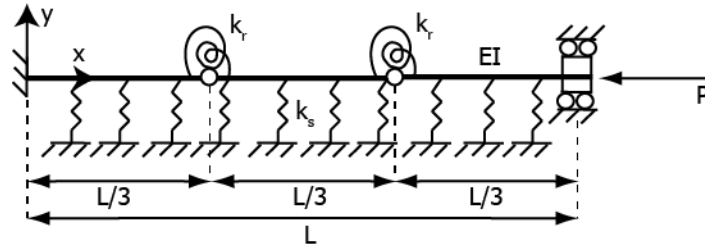


Figure 5-4: Clamped beam resting on foundation with two internal hinges

5.4 LINEARIZED BUCKLING ANALYSIS

5.4.1 General aspects

Linearized Buckling Analysis (LBA) is carried out using the commercial FEM software ADINA (ADINA R&D 2006) according to the so-called "classical" buckling formulation described by Bathe (1995). According to this formulation, eigenmodes and buckling loads are obtained from the equation:

$$\begin{aligned} {}^t_0\mathbf{K}\boldsymbol{\varphi}_i &= \gamma_i ({}^t_0\mathbf{K} - {}^t_0\mathbf{K}_g)\boldsymbol{\varphi}_i \Rightarrow \left(1 - \frac{1}{\lambda_i}\right)({}^t_0\mathbf{K} - {}^t_0\mathbf{K}_g)\boldsymbol{\varphi}_i \Rightarrow {}^t_0\mathbf{K}_g\boldsymbol{\varphi}_i = \frac{1}{\lambda_i}({}^t_0\mathbf{K}_g - {}^t_0\mathbf{K})\boldsymbol{\varphi}_i \Rightarrow \\ &(({}^t_0\mathbf{K} - {}^t_0\mathbf{K}_g) + \lambda_i {}^t_0\mathbf{K}_g)\boldsymbol{\varphi}_i = 0 \Rightarrow ({}^t_0\mathbf{K}_0 + {}^t_0\mathbf{K}_u + \lambda_i {}^t_0\mathbf{K}_g)\boldsymbol{\varphi}_i = 0 \end{aligned} \quad (5-3)$$

where

- ${}^t_0\mathbf{K}$ stiffness matrix of the structures at time t_0
- ${}^t_1\mathbf{K}$ stiffness matrix of the structures at time t_1
- t_0 time at the beginning of the analysis
- $t_1 = t_0 + \Delta t$
- Δt time increment
- $\boldsymbol{\varphi}_i$ i -th eigenmode
- γ_i function of the eigenvalue λ_i with $\gamma_i = 1 - 1/\lambda_i$

The formulation of Eq. (5-3) leads to the evaluation of the classical buckling load when t_0 corresponds to the unloaded situation and t_1 to a loaded structure with sufficiently small applied reference loads ${}^t_1\mathbf{R}$

(Brendel and Ramm 1980). The critical buckling load is determined from the critical load factor λ_1 via the expression:

$$\mathbf{R}_{cr,i} = \lambda_i^{-1} \mathbf{R} \quad (5-4)$$

Verification of the "classical" method of buckling analysis in ADINA has been provided by many researchers, such as Nilsson and Giannakopoulos (1995), Noguchi and Hisada (1993) and Yamashita and Shiro (2001).

5.4.2 Continuous beam

The linearized buckling analysis of an elastic continuous Euler-Bernoulli beam resting on Winkler foundation is presented at first in order to provide the framework of the subsequent analysis of internally hinged beams. The continuous beam under investigation is considered to be either simply-supported or clamped. Initially, the continuous simply-supported beam of Figure 5-5 is examined.

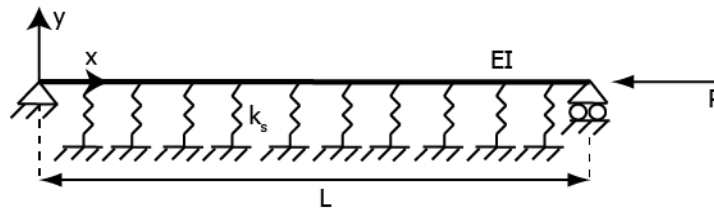


Figure 5-5: Continuous simply-supported beam resting on foundation

The governing fourth order differential equation of equilibrium is given by the expression:

$$EIy''''(x) + Py''(x) + k_s y(x) = 0 \quad (5-5)$$

The general solution of Eq. (5-5) is given by Eq. (5-6), where parameters A and B are defined in Eq.(5-7) with $a^2 = P/EI$ and $b^4 = k_s/(4EI)$.

$$y(x) = C_1 \cos Ax + C_2 \sin Ax + C_3 \cos Bx + C_4 \sin Bx \quad (5-6)$$

$$A = \sqrt{(a^2 - \sqrt{a^4 - 16b^4}) / 2} \quad (5-7)$$

$$B = \sqrt{(a^2 + \sqrt{a^4 - 16b^4}) / 2}$$

The boundary conditions of the simply-supported beam are:

$$y(0) = 0, y(L) = 0, y''(0) = 0, y''(L) = 0 \quad (5-8)$$

The onset of buckling of the beam is determined by the solution of the eigenvalue problem obtained by applying boundary conditions of Eq. (5-8) to Eq. (5-6) that yields the buckling equation:

$$(A^2 - B^2) \sin AL \sin BL = 0 \quad (5-9)$$

The algebraic solution of Eq. (5-9) provides the following cases regarding the calculation of the critical buckling load:

– for $A^2 - B^2 = 0$ the solution is

$$P_{cr} = 2\sqrt{k_s EI} \quad (5-10)$$

– for $\sin AL=0$ or $\sin BL=0$ the solution is:

$$P_{cr,n} = \frac{n^2 \pi^2 EI}{L^2} + \frac{k_s L^2}{n^2 \pi^2} \quad (5-11)$$

where $n=1,2,3,\dots$ is the number of the eigenmode.

It is noted that the buckling load of Eq. (5-10) is independent of beam length L . Substituting Eq. (5-10) into Eq. (5-6), the obtained eigenmode equation equals zero, leading to the conclusion that even though Eq. (5-10) is a mathematical solution of the buckling Eq. (5-9), it has no physical meaning. On the other hand, substituting the buckling loads of Eq. (5-11) into Eq. (5-6) the eigenmode equations of the simply-supported beam on elastic foundation are extracted and presented in Eq. (5-12) and Eq. (5-13):

– for $\sin AL \neq 0$:

$$y(x) = \sin Bx - \frac{\sin BL}{\sin AL} \sin Ax \quad (5-12)$$

– for $\sin BL \neq 0$:

$$y(x) = \sin Ax - \frac{\sin AL}{\sin BL} \sin Bx \quad (5-13)$$

The first four eigenmode shapes are presented in Figure 5-6 and denoted according to symmetry about the center of the beam as [1S] (1st symmetric), [1A] (1st antisymmetric), [2S] (2nd symmetric) and [2A] (2nd antisymmetric).

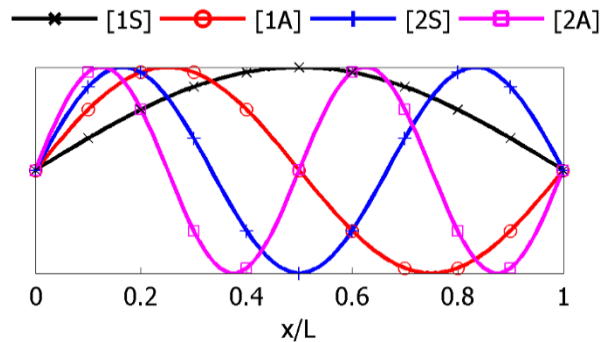


Figure 5-6: First four eigenmode shapes of continuous simply-supported beam resting on foundation

On the basis of the above results, it can be observed that the buckling behavior of such beams is directly dependent on soil stiffness k_s , whose gradual increase leads to eigenmode cross-over. This effect is illustrated in Figure 5-7, where the normalized soil stiffness is plotted on the horizontal axis and the elastic critical buckling load is plotted on the vertical axis, normalized by Euler buckling load of the same beam without elastic support ($P_{cr}/P_{E,ss}$). It is shown that increasing soil stiffness leads to proportional buckling load increase for all eigenmodes but with lower slope for higher modes, so that eigenmode cross-over takes place. In particular, the normalized soil stiffness ranges for critical modes are: for [1S] from 0 to 415, for [1A] from 415 to 3495, for [2S] from 3495 to 14040 and for [2A] larger than 14040.

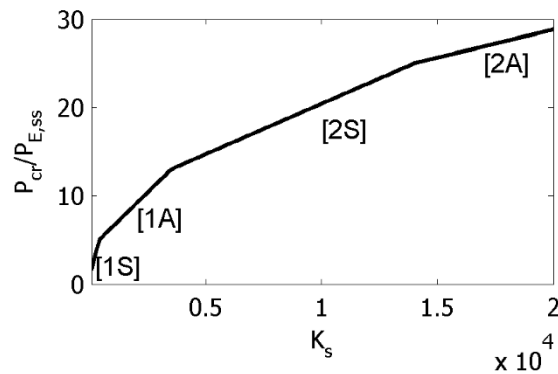


Figure 5-7: Elastic critical buckling load of the lower four eigenmodes of simply-supported continuous beam with respect to normalized soil stiffness

Next, the continuous clamped Euler-Bernoulli beam of Figure 5-8 is examined.

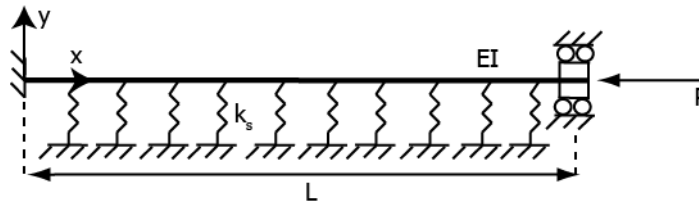


Figure 5-8: Continuous clamped beam resting on foundation

The governing fourth order differential equation of equilibrium is given by Eq. (5-5) and its general solution by Eq. (5-6). The boundary conditions of the clamped beam are:

$$y(0) = 0, y(L) = 0, y'(0) = 0, y'(L) = 0 \quad (5-14)$$

The onset of buckling is determined by the solution of the eigenvalue problem obtained by applying boundary conditions of Eq. (5-14) on Eq. (5-6) that yields the buckling equation:

$$(A^2 - B^2) \sin AL \sin BL + AB (\cos AL \cos BL - 1) = 0 \quad (5-15)$$

However, Eq. (5-15) does not have a closed algebraic form solution due to its high nonlinearity. Therefore, critical buckling loads can be estimated via Eq. (5-15) using a numerical approach.

Then, substituting the critical loads into Eq. (5-6) the eigenmodes of the clamped beam resting on elastic foundation are extracted and presented in Eq. (5-16) and Eq. (5-17).

– for $A \sin AL = B \sin BL$ the solution is:

$$y(x) = \cos Ax - \cos Bx \quad (5-16)$$

– for $A \sin AL \neq B \sin BL$ the solution is:

$$y(x) = W \cos Ax - \frac{B}{A} \sin Ax - W \cos Bx + \sin Bx \quad (5-17)$$

$$\text{with } W = \frac{B \cos BL - B \cos AL}{A \sin AL - B \sin BL}$$

The resulting eigenmode shapes are presented in Figure 5-9, denoted according to symmetry about the center of the beam as [1S], [1A], [2S] and [2A], similarly to the simply-supported beam. It is noted that in this case, increase of soil stiffness does not only lead to eigenmode cross-over but also to the

introduction of internal points of zero value of the eigenvectors (IP), in both symmetric and antisymmetric eigenmodes. Thus, a more detailed description of eigenmode shapes is introduced in Table 5-1 and presented in Figure 5-10.

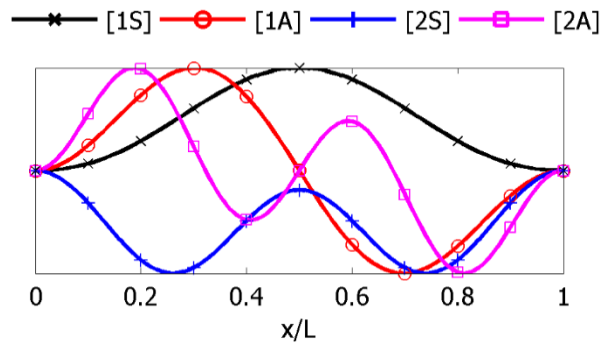


Figure 5-9: First four eigenmode shapes of clamped continuous beam resting on foundation

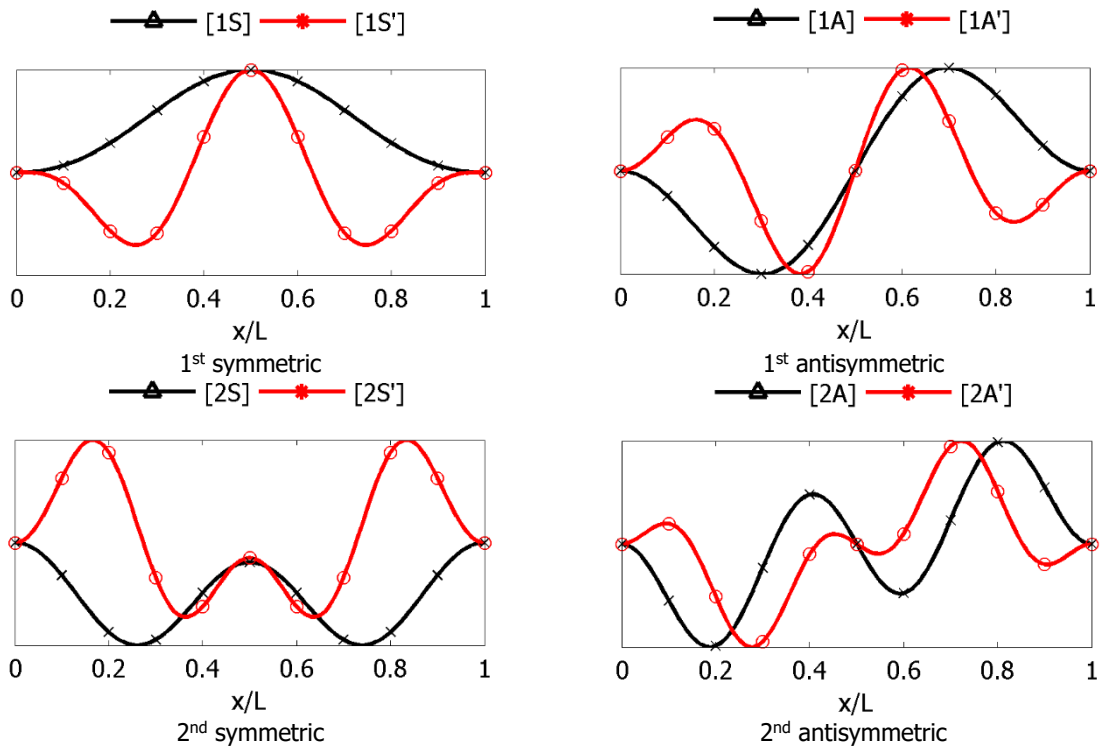


Figure 5-10: Eigenmode shapes of clamped continuous beam resting on foundation

Table 5-1: Clamped beam eigenmodes

mode	IP	mode	IP
[1S]	0	[2S]	0
[1S']	2	[2S']	2
[1A]	1	[2A]	3
[1A']	3	[2A']	5

Buckling behavior of the clamped beam on elastic foundation is also directly dependent on soil stiffness k_s , whose gradual increase leads to eigenmode cross-over. This is illustrated in Figure 5-11, where the normalized soil stiffness is plotted on the horizontal axis and the elastic critical buckling load of the lower four eigenmodes on the vertical axis, normalized by Euler buckling load of a clamped beam without elastic support ($P_{cr}/P_{E,cl}$). As indicated in Figure 5-11, increasing soil stiffness leads to buckling load increase for all eigenmodes, but at a different rate, so that eigenmode cross-over takes place. Thus,

the normalized soil stiffness ranges for critical modes are: for [1S] from 0 to 296, for [1A] from 296 to 889, for [1S'] from 889 to 6221 and for [1A'] larger than 6221.

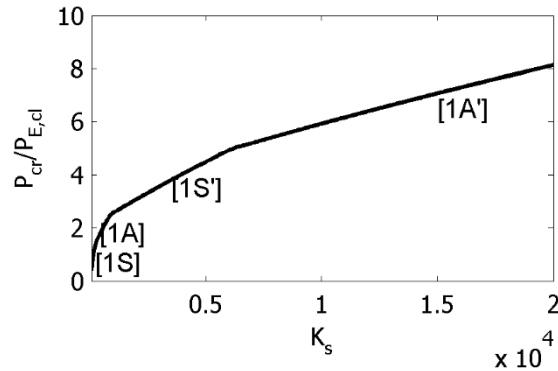


Figure 5-11: Minimum buckling load vs. soil stiffness of clamped continuous beam with respect to normalized soil stiffness

5.4.3 Simply-supported beam with one internal hinge

The critical buckling load of the simply-supported beam with one internal hinge located in the middle (Figure 5-1) with reference to soil stiffness and hinge rotational stiffness is illustrated in Figure 5-12. The critical buckling load (P_{cr}) is plotted on the vertical axis and normalized with respect to the Euler load ($P_{E,ss}$) of the continuous simply-supported beam without elastic support, while the normalized soil stiffness (K_s) is plotted on the horizontal axis. The buckling load of the continuous beam is also presented for comparison reasons. A first observation is that the increase of the rotational stiffness leads to the gradual restoration of the beam continuity. The buckling load curve for small K_r values is a smooth curve without notable turning points, in contrast to the continuous beam, where three evident turning points indicate the eigenmode cross-overs.

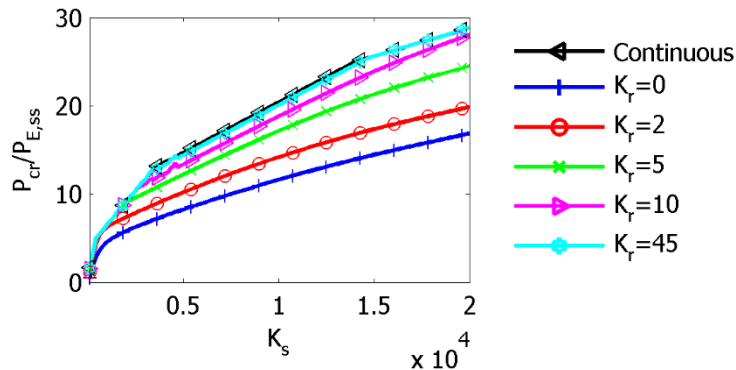


Figure 5-12: Normalized critical buckling load of simply-supported beam with one internal hinge with respect to soil stiffness for varying hinge rotational stiffness

Results extracted from Figure 5-12 regarding the eigenmode cross-over are confirmed by Figure 5-13 that shows the critical eigenmodes. The critical eigenmodes for rotational stiffness ranging from $K_r=0$ to $K_r=10$ are all symmetric and the corresponding shape reveals that eigenmode cross-over is absent as soil stiffness increases. The internal hinge weakens the beam at the middle-span and its location dominates the eigenmode shape. On the other hand, for $K_r=45$, two eigenmode cross-overs take place. The critical eigenmode is symmetric with single curvature for $K_s=180$, becomes symmetric with two intermediate inflection points for $K_s=10000$, and finally it turns into antisymmetric for $K_s=20000$. Eigenmode cross-over is thus encountered, defined as the transition of eigenmode shapes with respect to soil stiffness.

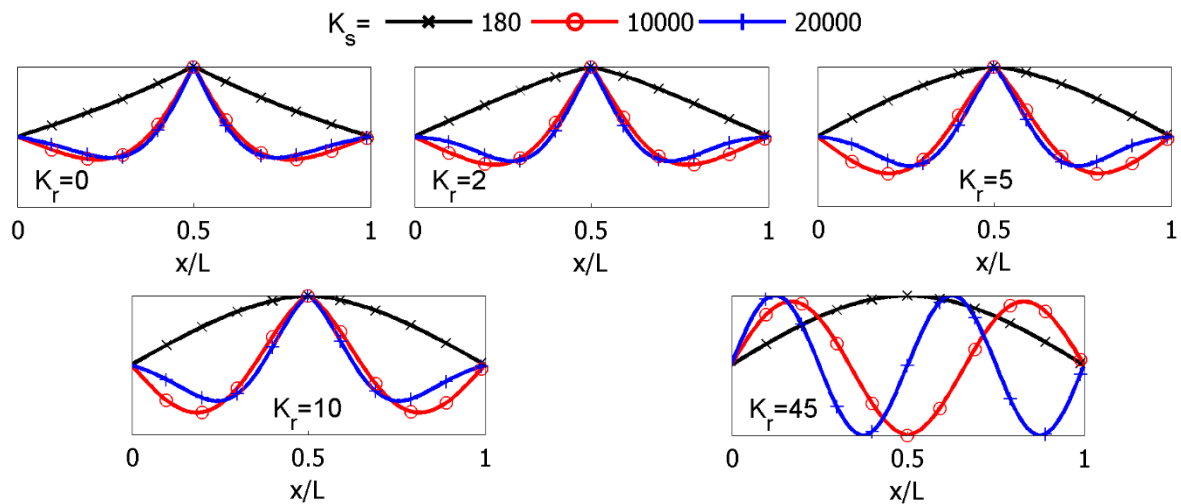


Figure 5-13: Critical eigenmodes of simply-supported beam with one internal hinge with respect to soil stiffness and for varying hinge rotational stiffness

5.4.4 Simply-supported beam with two internal hinges

The critical buckling load of the simply-supported beam with two equally-spaced internal hinges (Figure 5-2) is presented in Figure 5-14, where again the critical buckling load (P_{cr}) is plotted on the vertical axis, normalized with respect to the Euler load of the continuous beam without elastic support ($P_{E,ss}$), and the normalized soil stiffness (K_s) is plotted on the horizontal axis. Similar qualitative conclusions are extracted as in the case of one hinge, with the load P_{cr} increasing with soil stiffness as well as with joint stiffness. For small K_r values the buckling load curve indicates no eigenmode cross-over, and the resulting buckling loads are smaller than the ones of the beam with one hinge. Increasing rotational stiffness reveals the gradual restoration of the beam continuity and consequently the increase of buckling load.

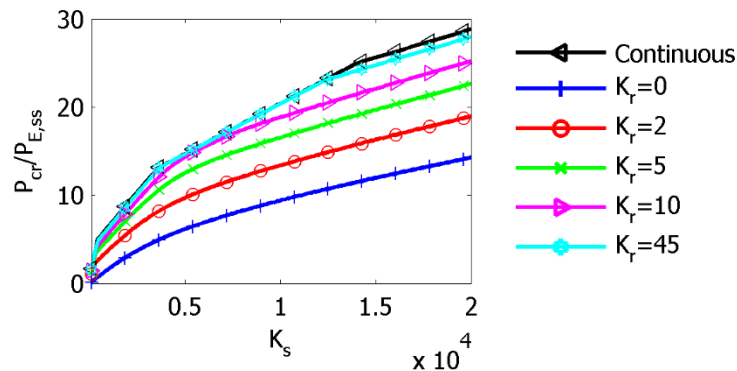


Figure 5-14: Normalized critical buckling load of simply-supported beam with two internal hinges with respect to soil stiffness for varying hinge rotational stiffness

The conclusions derived from Figure 5-14 regarding the eigenmode cross-over are confirmed by Figure 5-15. In case of $K_r=0$ and $K_r=2$ all eigenmodes are antisymmetric. As K_r increases to values of 5 and 10, eigenmode cross-over is detected. The critical eigenmode is symmetric for low soil stiffness and is similar to the first symmetric eigenmode of the continuous beam. Increasing soil stiffness leads to cross-over. Antisymmetric eigenmode shapes are dominated by the location of the hinges. Finally, the maximum rotational stiffness restores the beam continuity and similar results as in the beam with one hinge are observed (see Figure 5-13).

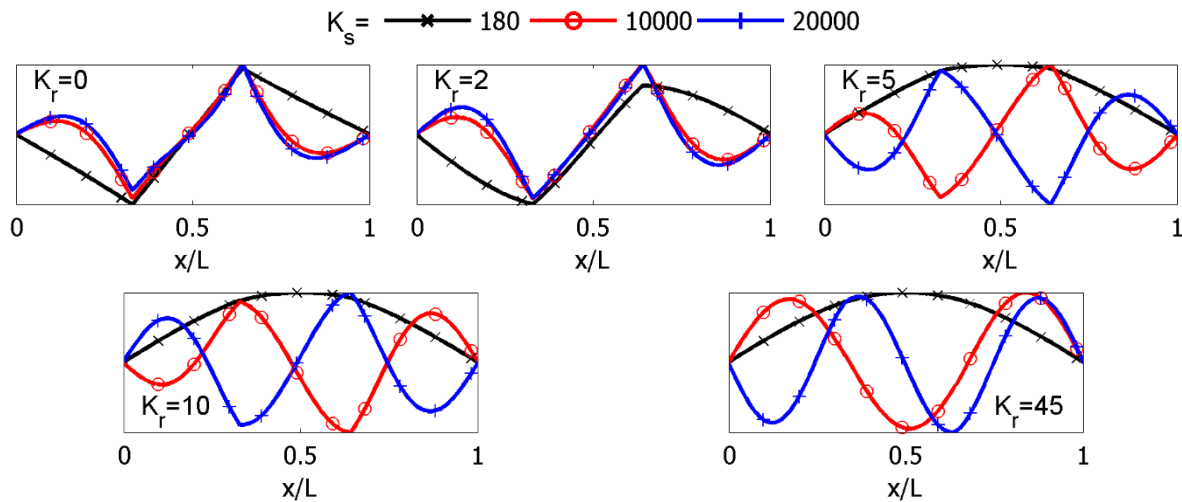


Figure 5-15: Critical eigenmodes of simply-supported beam with two internal hinges with respect to soil stiffness and for varying hinge rotational stiffness

5.4.5 Critical buckling loads of simply-supported beams

The comparison between critical buckling loads of continuous and internally hinged simply-supported beams is necessary to highlight the consequences of internal hinges in terms of reducing beam global stiffness. This direct comparison is illustrated in Figure 5-16 for varying rotational stiffness and soil stiffness, where the continuous beam is denoted by C, the beam with one internal hinge by 1H and the beam with two internal hinges by 2H. The critical buckling loads (P_{cr}) are normalized with respect to the Euler buckling load of the continuous beam without elastic support ($P_{E,ss}$).

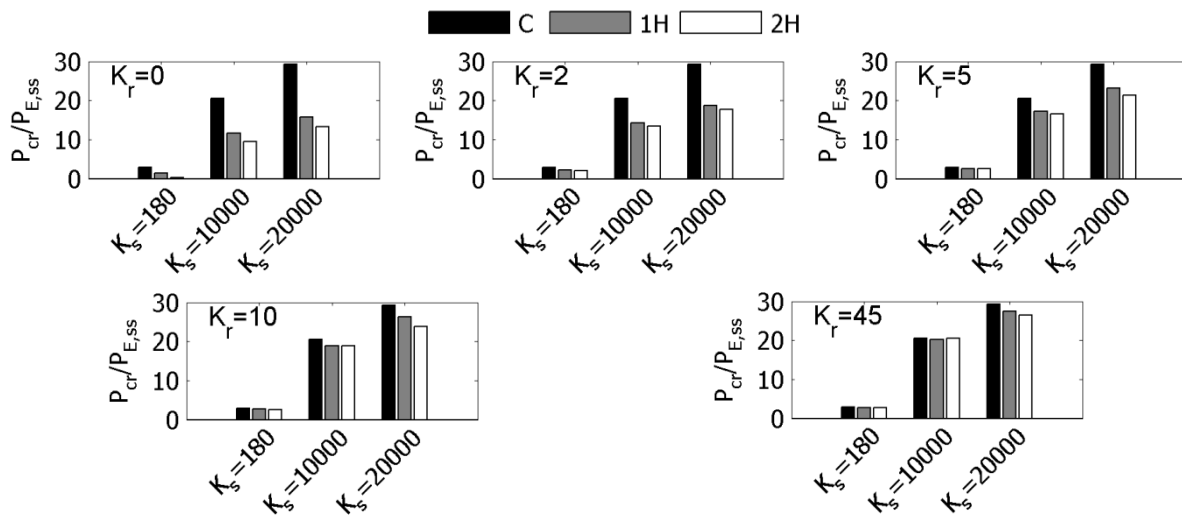


Figure 5-16: Critical buckling loads of simply-supported beams with respect to soil stiffness and for varying rotational stiffness

It is observed that soil stiffness increase leads to buckling load increase for all cases. At the same time, the increase of hinge rotational stiffness leads to the gradual restoration of beam continuity and consequently the difference between buckling loads of C, 1H and 2H beams decreases. Finally, it is noted that the critical buckling load reduction due to the integration of internal hinges in a beam resting on foundation under compressive axial force was also reported for the case of an infinite beam by Wang (2010).

5.4.6 Clamped beam with one internal hinge

The critical buckling load evolution of the clamped beam with one internal hinge (Figure 5-3) with respect to soil stiffness is illustrated in Figure 5-17. The load P_{cr} is presented on the vertical axis and is normalized with respect to the Euler load of the clamped continuous beam without elastic support ($P_{E,cl}$). P_{cr} increases as soil stiffness increases. The increase of rotational stiffness restores the beam continuity and yields to buckling load gradual increase, similarly to previous cases.

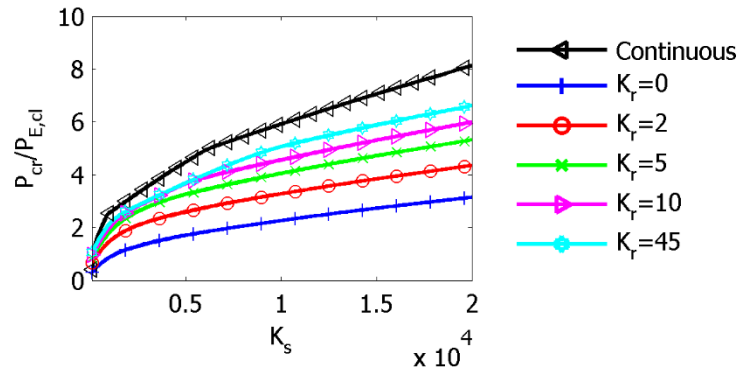


Figure 5-17: Normalized critical buckling load of clamped beam with one internal hinge with respect to soil stiffness for varying hinge rotational stiffness

The eigenmode cross-over is examined in Figure 5-18, where the critical eigenmodes are illustrated. The centrally located internal hinge dominates the symmetric critical eigenmode shapes for K_r values ranging from 0 to 5. As the critical eigenmode shape is transformed consecutively from symmetric to antisymmetric, one eigenmode cross-over for $K_r=10$ and three cross-overs for $K_r=45$ are observed.

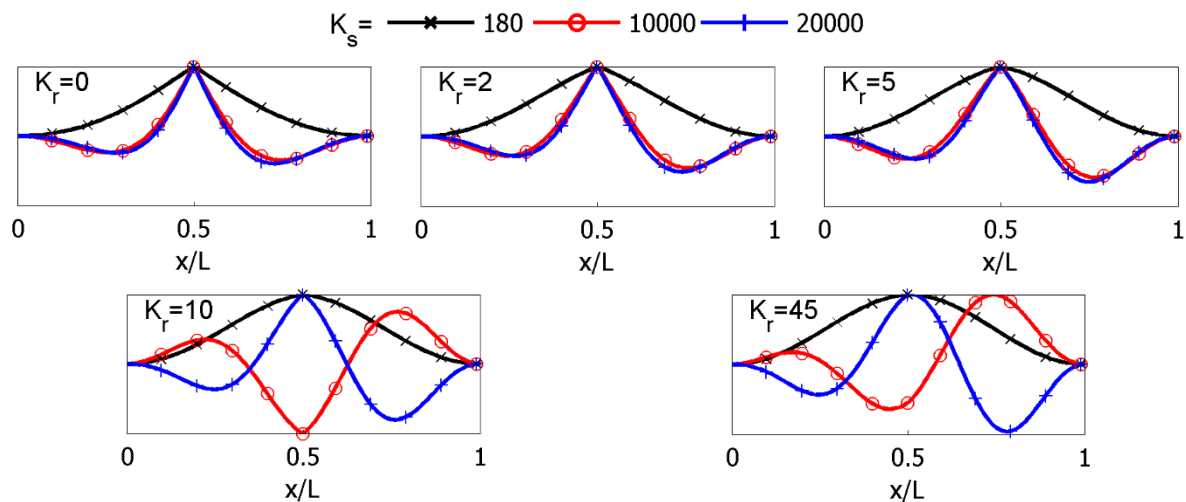


Figure 5-18: Critical eigenmodes of clamped beam with one internal hinge with respect to soil stiffness and for varying hinge rotational stiffness

5.4.7 Clamped beam with two internal hinges

Regarding the clamped beam with two internal hinges (Figure 5-4), the critical buckling load P_{cr} dependence on normalized soil stiffness is shown in Figure 5-19. Buckling load is normalized with respect to the Euler load of the clamped continuous beam without elastic support ($P_{E,cl}$). The load P_{cr} increases as soil stiffness increases, following the same pattern as in all previous cases. The equally-spaced internal hinges alter the beam stiffness depending also on their rotational stiffness. The buckling load curve for small K_r indicates that eigenmode cross-over does not occur. This outcome is confirmed by considering the eigenmode shapes presented in Figure 5-20 for varying rotational stiffness.

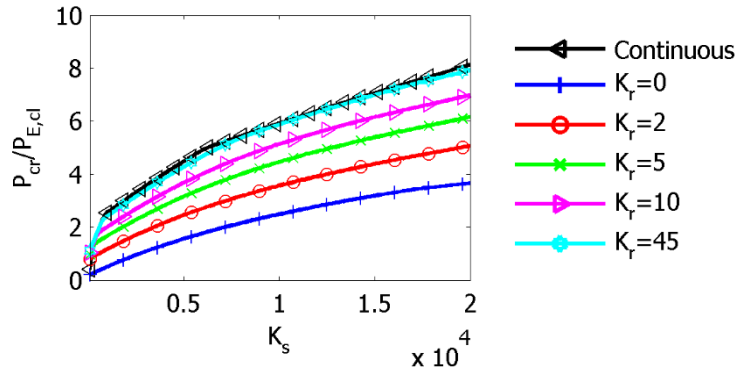


Figure 5-19: Normalized critical buckling load of clamped beam with two internal hinges with respect to soil stiffness for variable hinge rotational stiffness

The symmetrically introduced hinges dominate the critical eigenmode shapes. It becomes clear from Figure 5-20 that for small rotational stiffness all eigenmodes are antisymmetric, even though increasing soil stiffness slightly modifies the shape. As K_r increases to values of 5 and 10, eigenmode cross-over occurs, and the symmetric shape is transformed to antisymmetric for soil stiffness greater than $K_s=10000$. Finally, the maximum rotational stiffness reestablishes beam continuity and similar results to the clamped beam with one internal hinge can be extracted (see Figure 5-18).

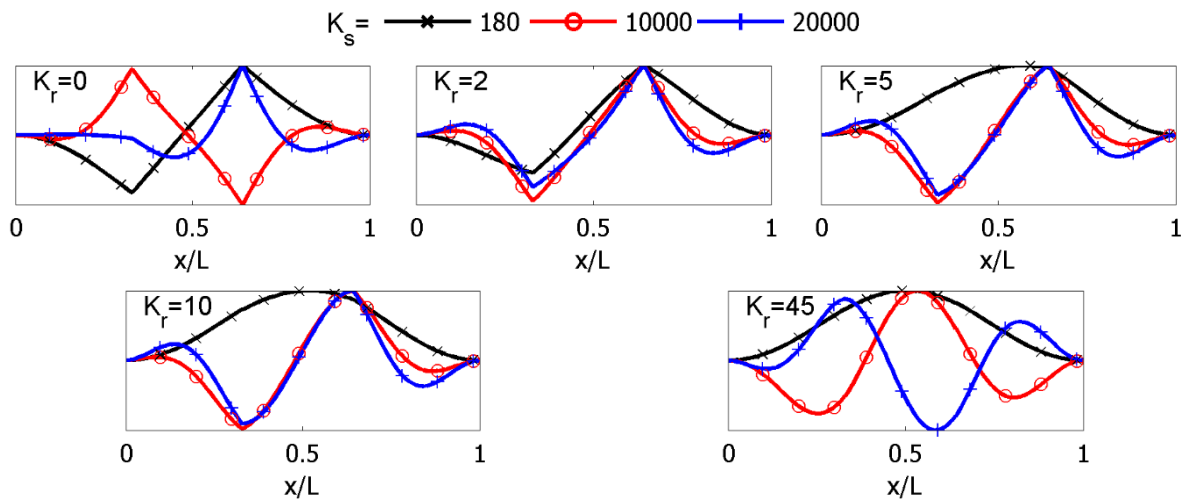


Figure 5-20: Critical eigenmodes of clamped beam with two internal hinges with respect to soil stiffness and for variable hinge rotational stiffness

5.4.8 Critical buckling loads of clamped beams

The introduction of either one or two internal hinges has a direct impact on the clamped beam’s buckling behavior also. The critical buckling loads of the continuous beam (C), the beam with one hinge (1H) and the beam with two hinges (2H) are compared in order to quantify this influence. The normalized buckling loads are presented in Figure 5-21. A pure hinge ($K_r=0$) leads to a decrease of buckling load levels compared to the continuous beam. In this case, the difference in critical buckling loads between the continuous beam, the beam with one internal hinge and the beam with two internal hinges rises as soil stiffness increases. The difference between the buckling loads is reduced as rotational stiffness increases. A significant difference is observed between the simply-supported and the clamped beam. The clamped boundary conditions affect the buckling loads of 1H and 2H beams, as the doubly hinged beam has higher buckling load than the single hinged beam in the majority of the cases presented in Figure 5-21. This is attributed to the fact that the hinges are now closer to the clamped supports, and thus contribute less to beam stiffness reduction.

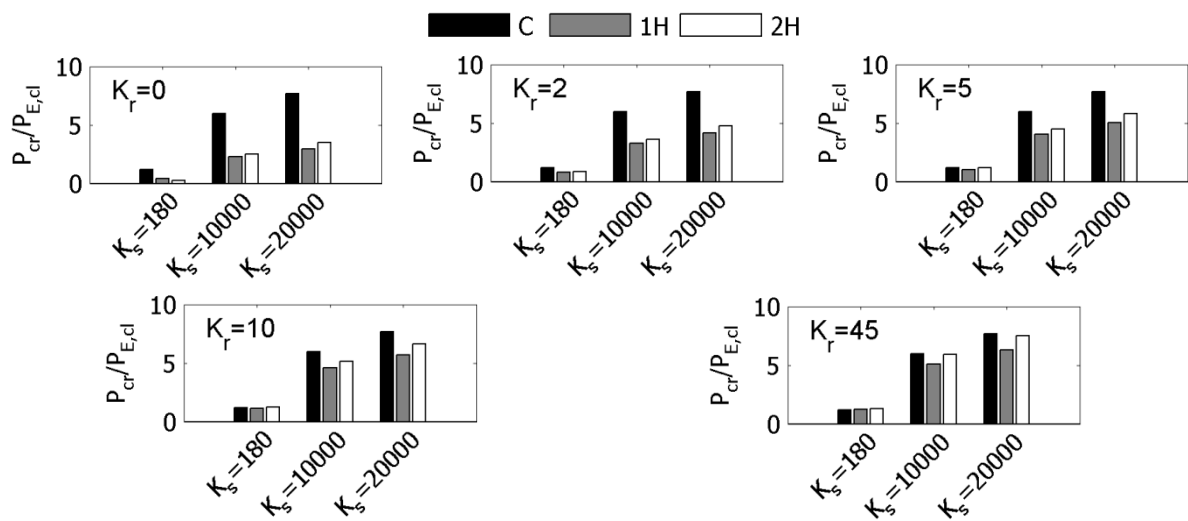


Figure 5-21: Critical buckling loads of clamped beams with respect to soil stiffness and for varying rotational stiffness

5.5 GEOMETRICALLY NONLINEAR ANALYSIS

5.5.1 Analysis methodology and imperfections

The assessment of post-buckling behavior of buckling-sensitive structures necessitates the implementation of advanced numerical techniques (Gantes and Fragkopoulos 2010). In the present study nonlinear numerical analyses are carried out using the commercial FEM software ADINA (ADINA R&D 2006) that incorporates the "Arc-Length" type algorithm for tracing the post-buckling equilibrium path (Bathe and Dvorkin 1983). Results obtained from ADINA using nonlinear solution algorithms have been compared against experimental ones in the literature for a wide range of problems, including among others local and global buckling of steel structures, as indicatively shown by Kalochairetis et al. (2014), Roy et al. (2003), Yaffe and Abramovich (2003) and Zhang et al. (2015a).

The presence of unavoidable initial imperfections may affect significantly the response of buckling-sensitive structures. Considering that actual imperfections are unknown during design, a commonly adopted approach regarding imperfection shape is to use a linear combination of buckling mode shapes (e.g. Agüero et al. 2015; Gantes and Fragkopoulos 2010; Yoo and Choi 2008). According to this approach, linear combinations of the first four global eigenmodes are adopted as initial imperfections and incorporated in the geometrically nonlinear analysis. Every eigenmode is weighted with 25%, i.e. the first four eigenmodes are equally considered in the linear combinations. The shape of eigenmodes is extracted from Linearized Buckling Analysis (section 5.4). Linear combinations of eigenmode shapes that are used as initial imperfections in the subsequent nonlinear analysis are listed in Table 5-2, aiming at quantifying the effects of imperfections in the structural response and detecting all possible imperfection sensitivities. Buckling and hence post-buckling behavior of beams resting on elastic foundation is dominated by soil stiffness, as a potential increase may lead to eigenmode cross-over. Consequently, various initial imperfection shapes are considered, given that the shape of the first symmetric eigenmode may not be adequate to identify any potential imperfection sensitivity. The imperfections under consideration are normalized so that their amplitude equals $L/500$, as a typical, rather small value employed in practice for steel members according to code provisions, e.g. Eurocode 3 – Part 1 (European Committee for Standardization 2007).

Table 5-2: Imperfection combinations of global eigenmode shapes for geometrically nonlinear analysis

Imperfection	Linear combination
I	mode 1 + mode 2 + mode 3 + mode 4
II	mode 1 + mode 2 - mode 3 + mode 4
III	mode 1 + mode 2 + mode 3 - mode 4
IV	mode 1 + mode 2 - mode 3 - mode 4

It is important to point out that the choice of buckling modes as imperfection patterns is not unique and may not cover all eventualities, as in many cases it has been found to lead to lower compliance to experimental results than other shapes of initial imperfections (e.g. Gantes and Fragkopoulos 2010). Additionally, Schneider and Brede (2005) and Schneider et al. (2005) have shown that considering different imperfection patterns may be important, depending also on the imperfection magnitude, while amplitude-dependent imperfection patterns cannot be determined with confidence. Hence, GNIA results should be interpreted accordingly and imperfection size must also be investigated, as will be shown in the following.

In Geometrically Nonlinear Imperfection Analysis, equilibrium equations are formulated in the deformed configuration of the structure that is allowed to differ significantly from the undeformed one. This type of analysis is necessary for investigating buckling and, mainly, post-buckling structural behavior, through the equilibrium path relating the applied action with the deformation corresponding to a characteristic degree of freedom of the structure. In the present investigation the position along the beam with maximum transverse displacement (y_{\max}) at the analysis end is selected for all equilibrium paths. Hence, the transverse displacement normalized with respect to the beam length (y_{\max}/L) is plotted on the horizontal axis, while the applied axial load normalized with respect to the critical buckling load of the continuous beam resting on soil ($P/P_{cr,cs}$), either simply-supported (Hetenyi 1946) denoted as $P_{cr,cs,ss}$ or clamped (Melissianos and Gantes 2014b) denoted as $P_{cr,cs,cl}$, is plotted on the vertical axis, while the dashed line represents the critical buckling load obtained from LBA. The beam deformed shape at the analysis end is displayed and compared to the shapes of initial imperfections and eigenmodes, leading to interesting conclusions.

A double-parameter problem with soil stiffness and hinge rotational stiffness acting as the two dominant parameters is formulated. For the sake of brevity, indicative values of the parameters are selected and the associated numerical results are presented. The linearized buckling analysis results (section 5.4) and the relationships between soil stiffness and critical buckling loads with reference to hinge rotational stiffness (Figure 5-12, Figure 5-14, Figure 5-17, Figure 5-19) indicate that the rotational stiffness value $K_r=5$ leads to beam continuity restoration by almost 50%, thus nonlinear analysis results are presented for this case.

5.5.2 Simply-supported beam with one hinge

The simply-supported beam with one internal hinge resting on elastic foundation (Figure 5-1) is at first numerically investigated and results for soil stiffness $K_s=180$, $K_s=10000$ and $K_s=20000$ are outlined in the following sections.

5.5.2.1 Low soil stiffness $K_s=180$

The first four eigenmodes are presented in Figure 5-22a and the initial imperfection shapes according to Table 5-2 are illustrated in Figure 5-22b. The nonlinear analysis results are presented in terms of equilibrium paths in Figure 5-23a and beam deformed shapes at the end of the analysis in Figure 5-23b, for all different cases of initial imperfections.

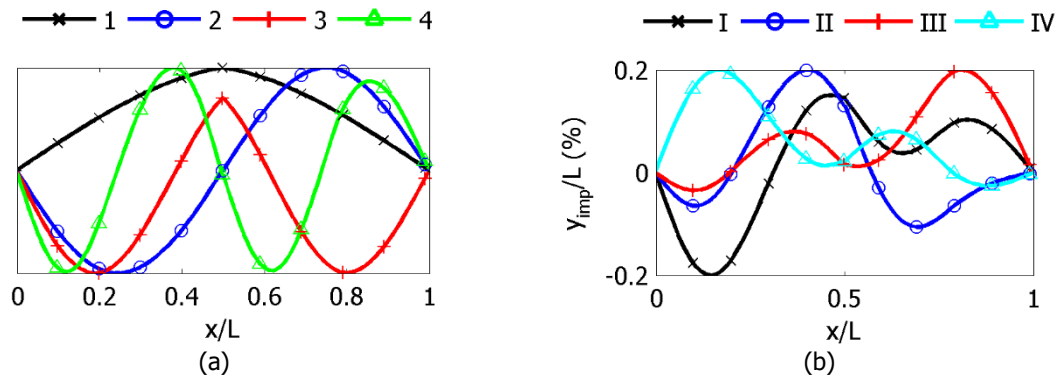


Figure 5-22: (a) Eigenmode shapes and (b) imperfection shapes considered in GNIA for simply-supported beam with one internal hinge for $K_s=180$ and rotational stiffness $K_r=5$

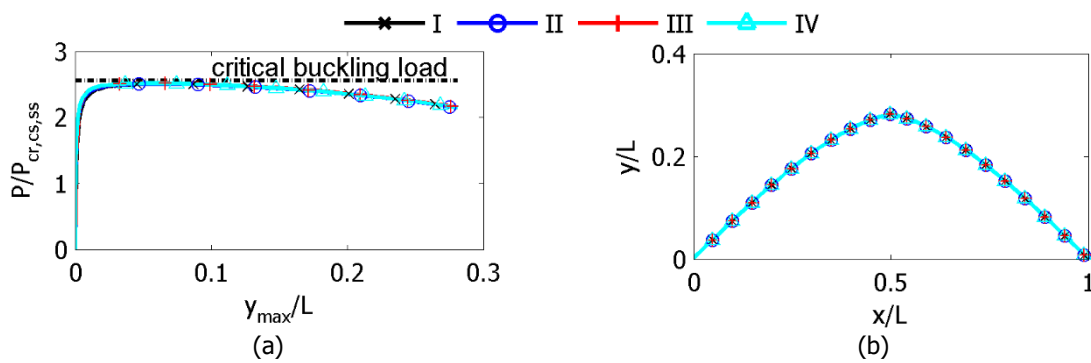


Figure 5-23: (a) Equilibrium paths and (b) beam deformed shapes obtained from GNIA of simply-supported beam with one internal hinge for $K_s=180$ and rotational stiffness $K_r=5$

5.5.2.2 Medium soil stiffness $K_s=10000$

The first four eigenmodes are presented in Figure 5-24a and the initial imperfection shapes according to Table 5-2 are illustrated in Figure 5-24b. The nonlinear analysis results are presented in terms of equilibrium paths in Figure 5-25a and beam deformed shape at the end of the analysis in Figure 5-25a, for all different cases of initial imperfections.

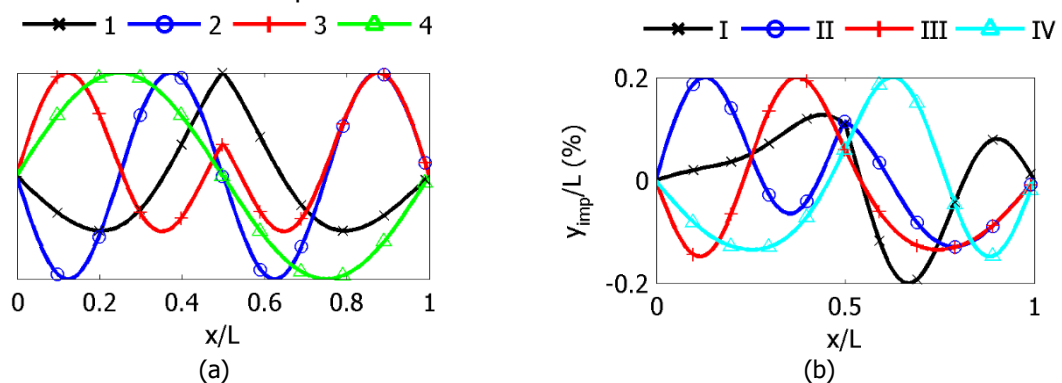


Figure 5-24: (a) Eigenmode shapes and (b) imperfection shapes considered in GNIA for simply-supported beam with one internal hinge for $K_s=10000$ and rotational stiffness $K_r=5$

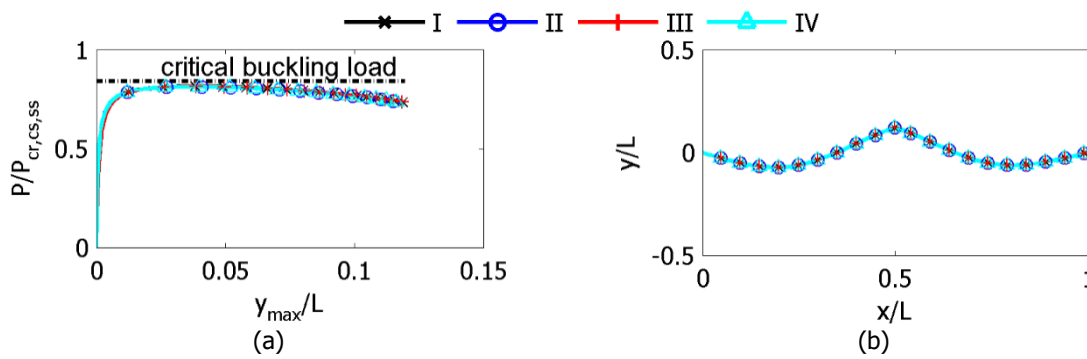


Figure 5-25: (a) Equilibrium paths and (b) beam deformed shapes obtained from GNIA of simply-supported beam with one internal hinge for $K_s=10000$ and rotational stiffness $K_r=5$

5.5.2.3 High soil stiffness $K_s=20000$

The considered initial imperfections (Figure 5-26b) are derived from the first four eigenmodes (Figure 5-26a) after Table 5-2. Equilibrium paths and beam deformed shapes at the end of the analysis obtained from GNIA are shown in Figure 5-27a and Figure 5-27a, respectively.

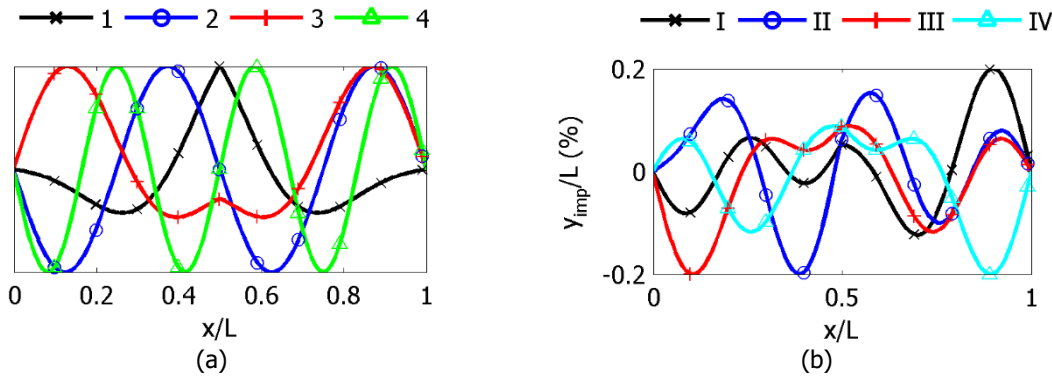


Figure 5-26: (a) Eigenmode shapes and (b) imperfection shapes considered in GNIA for simply-supported beam with one internal hinge for $K_s=20000$ and rotational stiffness $K_r=5$

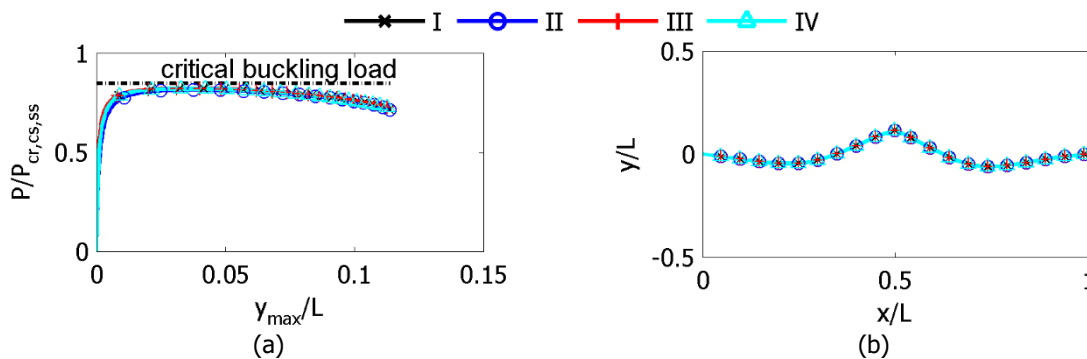


Figure 5-27: (a) Equilibrium paths and (b) beam deformed shapes obtained from GNIA of simply-supported beam with one internal hinge for $K_s=20000$ and rotational stiffness $K_r=5$

5.5.2.4 Discussion of results

For all cases of soil stiffness, it is observed that all equilibrium paths practically coincide regardless of shape of initial imperfection and have descending post-buckling behavior, as shown in Figure 5-23a, Figure 5-25a and Figure 5-27a. Such unstable post-buckling behavior is crucial from design point of view and should be addressed accordingly through appropriate safety factors, as structural safety cannot rely on post-buckling strength. It is also noted that the ultimate loads are close to the critical buckling load that is displayed with the dashed line. The beam deformed shape is also not affected by

imperfection shapes, but is dominated by the critical eigenmode shape (see Figure 5-13), as illustrated in Figure 5-23b, Figure 5-25b and Figure 5-27b.

Finally, it should be noted that nonlinear analyses carried out for soil stiffness much lower than the minimum value considered here, i.e. $K_s=180$, showed that the overall buckling response is stable indicating that in such case the response is similar to the simply-supported beam without lateral support. Indicatively, the equilibrium path for $K_s=2$, considering only the first combination of eigenmodes as imperfection shape, is presented in Figure 5-28a. The range of soil stiffness that affects the post-buckling behavior is illustrated in Figure 5-28b, where for stiffness lower than approximately $K_s=30$ the post-buckling behavior is stable and for higher stiffness value the behavior is unstable.

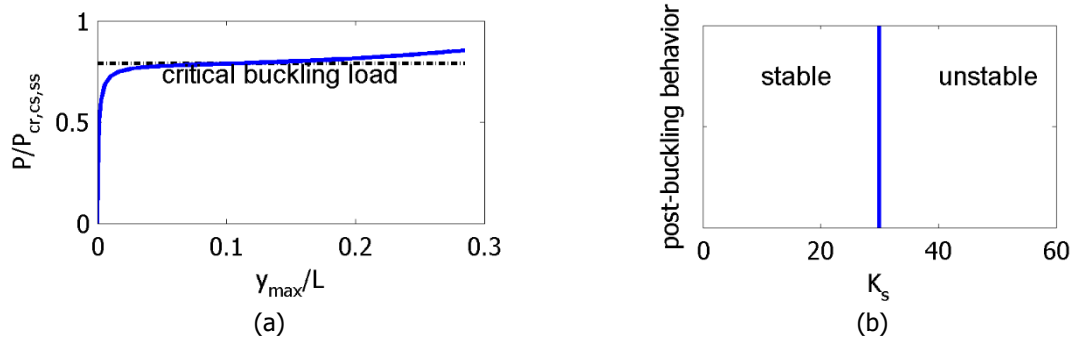


Figure 5-28: (a) Equilibrium paths from GNIA of simply-supported beam with one internal hinge for $K_s=2$ and rotational stiffness $K_r=5$ and (b) soil range regarding the post-buckling behavior of simply-supported beam with one internal hinge with respect to soil stiffness and rotational stiffness $K_r=5$

5.5.2.5 Considerations on eigenmode cross-over

The increase of soil stiffness leads to eigenmode cross-over with reference to the hinge rotational stiffness. It is therefore essential to examine the beam behavior and especially the beam deformed shape at the end of nonlinear analysis by considering soil stiffness values being close enough to the value that corresponds to the cross-over point $K_s \approx 533$, characterized by the critical eigenmode being symmetric before and antisymmetric after this point. Thus, the simply-supported beam is considered to rest on soil with $K_s=526$ (before the cross-over) or $K_s=540$ (after the cross-over), with the critical buckling load ratio of the two cases being equal to 0.99. The first four eigenmodes obtained from LBA for both cases of soil stiffness are presented in Figure 5-29, where it is shown that before the cross-over point the first eigenmode is symmetric, while after the cross-over point the first eigenmode is antisymmetric. Additionally, the normalized buckling loads for both soil stiffness cases and for all eigenmodes are listed in Table 5-3. The numerical results (considering the first linear combination of the eigenmodes for the imperfection shape after Table 5-2) are presented in terms of the equilibrium paths and the beam deformed shapes at the end of the analysis in Figure 5-30a and Figure 5-30b, respectively. It is observed that the equilibrium paths coincide as the soil stiffness values considered are very close, while the beam deformed shapes are affected by both critical eigenmode shapes, but not to the same extent. Thus, the deformed shape for $K_s=526$ (before the cross-over) is closer to symmetric, having no intersection points with the horizontal axis, while the deformed shape for $K_s=540$ (after the cross-over) has an intersection with the horizontal axis, and it is closer to antisymmetric.

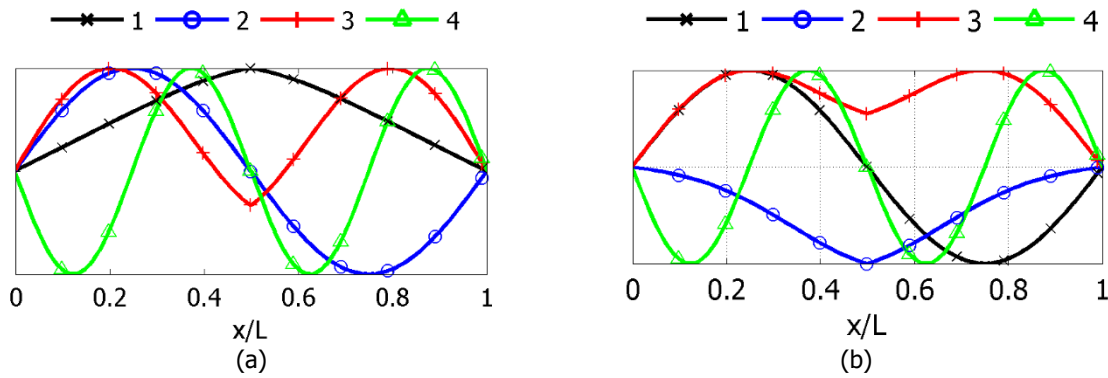


Figure 5-29: Eigenmode shapes obtained from LBA for simply-supported beam with one internal hinge for (a) $K_s=426$ (before cross-over) and (b) $K_s=540$ (after cross-over) and rotational stiffness $K_r=5$

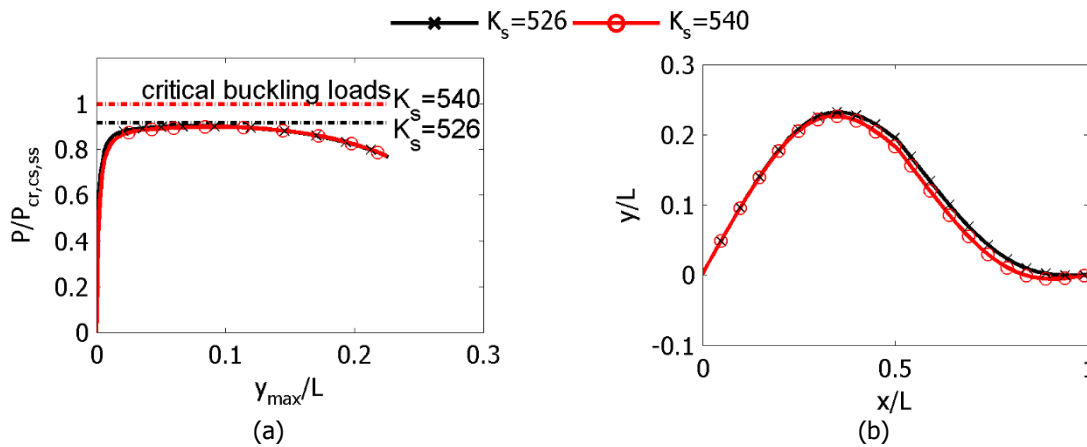


Figure 5-30: (a) Equilibrium paths and (b) beam deformed shapes obtained from GNIA of simply-supported beam with one internal hinge for $K_r=5$ before ($K_s=526$) and after ($K_s=540$) the cross-over point

Table 5-3: Buckling loads of eigenmodes for soil stiffness $K_s=526$ and $K_s=540$

soil stiffness	eigenmode			
	1	2	3	4
$K_s=526$	0.91	0.95	1.41	3.04
$K_s=540$	1.05	1.28	1.53	3.05

5.5.3 Simply-supported beam with two hinges

Next, the simply-supported beam with two internal hinges resting on elastic foundation (Figure 5-2) is investigated through nonlinear analysis and results for soil stiffness $K_s=180$, $K_s=10000$ and $K_s=20000$ are shown in the subsequent sections.

5.5.3.1 Low soil stiffness $K_s=180$

The first four eigenmodes exported from LBA are illustrated in Figure 5-31a and are combined according to Table 5-2 to create the imperfection shapes of Figure 5-31b. The beam overall buckling behavior in terms of the equilibrium paths and the beam deformed shapes at the end of the analysis, obtained from GNIA, are presented in Figure 5-32a and Figure 5-32b, respectively, for all different cases of initial imperfections.

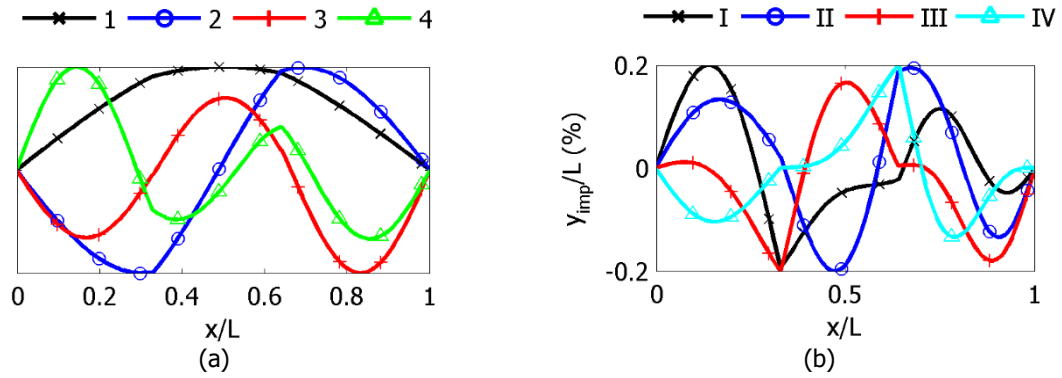


Figure 5-31: (a) Eigenmode shapes and (b) imperfection shapes considered in GNIA for simply-supported beam with two internal hinges for $K_s=180$ and rotational stiffness $K_r=5$

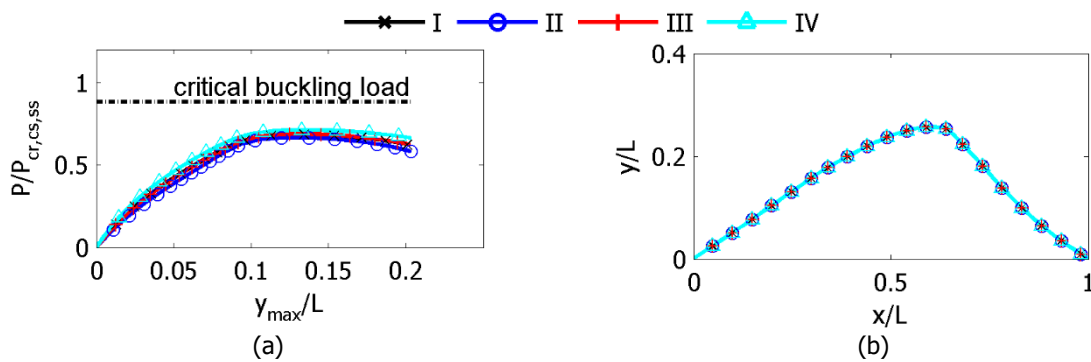


Figure 5-32: (a) Equilibrium paths and (b) beam deformed shapes obtained from GNIA of simply-supported beam with two internal hinges for $K_s=180$ and rotational stiffness $K_r=5$

5.5.3.2 Medium soil stiffness $K_s=10000$

LBA is carried at first and the obtained eigenmodes are presented in Figure 5-33a. Then, eigenmodes are combined linearly according to Table 5-2 in order to create the shape of the initial imperfections (Figure 5-33b) that are considered in the GNIA.

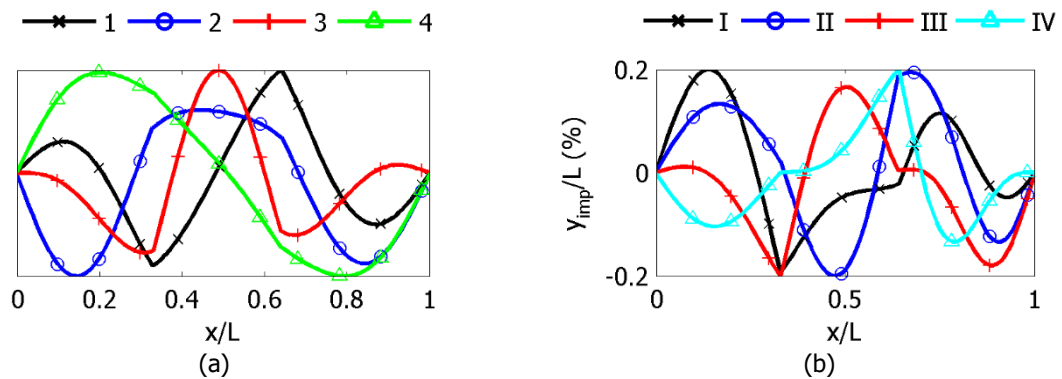


Figure 5-33: (a) Eigenmode shapes and (b) imperfection shapes considered in GNIA for simply-supported beam with two internal hinges for $K_s=10000$ and rotational stiffness $K_r=5$

Nonlinear analysis results are presented in terms of equilibrium paths and the beam deformed shapes. In particular, the equilibrium paths and the beam deformed shapes at the end of the analysis are presented in Figure 5-34a and Figure 5-34b, respectively, for all different cases of initial imperfections.

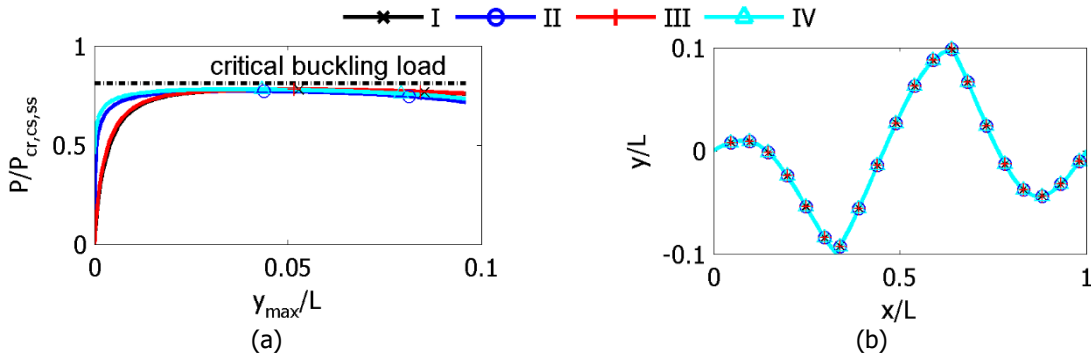


Figure 5-34: (a) Equilibrium paths and (b) beam deformed shapes obtained from GNIA of simply-supported beam with two internal hinges for $K_s=10000$ and rotational stiffness $K_r=5$

5.5.3.3 High soil stiffness $K_s=20000$

The first four eigenmodes are depicted in Figure 5-35a following LBA and consequently are used to create the imperfection shapes through linear combinations (Table 5-2) that are shown in Figure 5-35b. The beam overall buckling behavior in terms of equilibrium path and the beam deformed shapes at the end of the analysis, obtained from GNIA, are presented in Figure 5-36a and Figure 5-36b, respectively, for all different cases of initial imperfections.

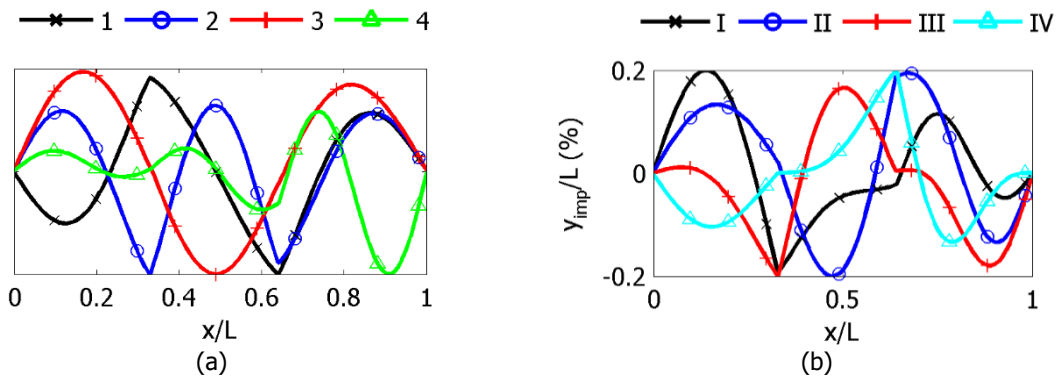


Figure 5-35: (a) Eigenmode shapes and (b) imperfection shapes considered in GNIA for simply-supported beam with two internal hinges for $K_s=20000$ and rotational stiffness $K_r=5$

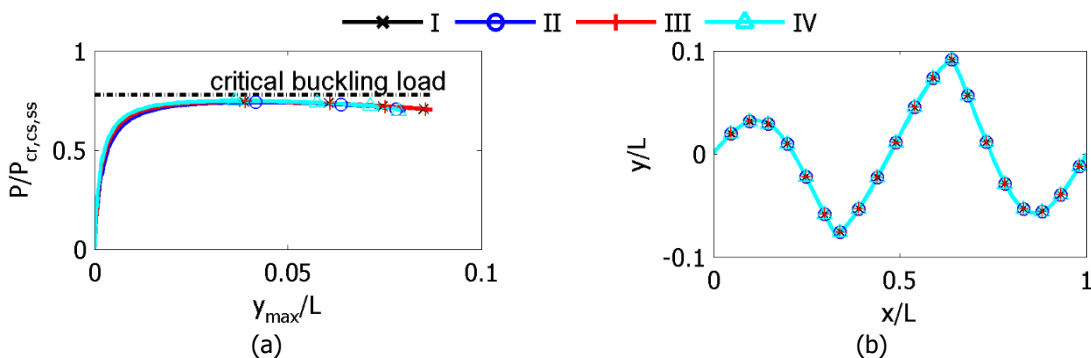


Figure 5-36: (a) Equilibrium paths and (b) beam deformed shapes obtained from GNIA of simply-supported beam with two internal hinges for $K_s=20000$ and rotational stiffness $K_r=5$

5.5.3.4 Discussion of results

The equilibrium paths are highly nonlinear and the beam post-buckling behavior is unstable, as clearly indicated by the ultimate load and the subsequent descending equilibrium path (Figure 5-32a, Figure 5-34a and Figure 5-36a). It is noted that in case of soil stiffness $K_s=10000$ and $K_s=20000$ the difference between the ultimate load and the critical buckling load is very small. On the contrary, for $K_s=180$ the

difference between the ultimate load and the buckling load is about 24%, which is attributed to the fact that the equally-spaced internal hinges are located close to the hinged supports of the beam and at the same time the soil stiffness is low enough, compared to the other examined cases, to provide sufficient support to the beam in order for the ultimate load to reach the critical buckling load. Moreover, compared to the beam with one internal hinge, in case of the beam with two internal hinges, the difference of the ultimate load from the critical buckling load obtained from LBA is higher. The beam deformed shape is highly affected by the antisymmetric critical eigenmode, due to the presence of two equally-spaced internal hinges, as presented in Figure 5-32b, Figure 5-34b and Figure 5-36b, but is not affected by the shape of the initial imperfections.

Finally, GNIA was carried out to investigate whether the post-buckling behavior of the simply-supported beam with two internal hinges is unstable for lower soil stiffness than the one considered, i.e. $K_s=180$. Results showed that for soil stiffness lower than approximately $K_s=30$ (Figure 5-37) the behavior of the beam is stable. Similar results were obtained for the simply-supported beam with one internal hinge (section 5.5.2.4).

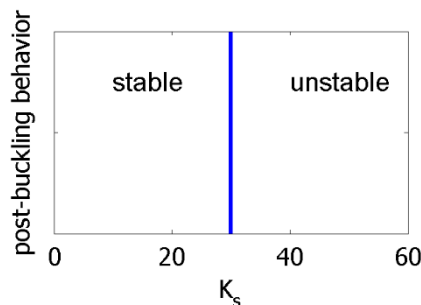


Figure 5-37: Soil range regarding the post-buckling behavior of simply-supported beam with two internal hinges with respect to soil stiffness and rotational stiffness $K_r=5$

5.5.4 Comparison of simply-supported beam ultimate loads

The comparison of normalized ultimate loads of a simply-supported continuous beam (C), a beam with an internal hinge (1H) and a beam with two internal hinges (2H) is illustrated in Figure 5-38 for varying soil stiffness and rotational stiffness $K_r=5$. A crucial conclusion is that increasing soil stiffness leads to ultimate load increase in correspondence to critical buckling loads. The internal hinges reduce the ultimate loads with reference to the continuous beam, even though the load levels do not vary significantly among the 1H and the 2H cases, except for case $K_s=180$ that is attributed to low lateral support provided by the soil. Additionally, it is observed that the differences between the ultimate loads in cases $K_s=10000$ and $K_s=20000$ are quite the same, as soil provides lateral support to the beam.

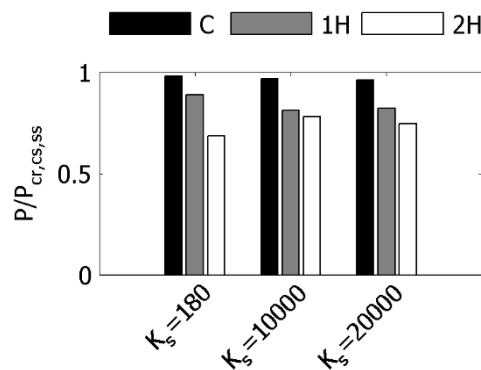


Figure 5-38: Ultimate loads comparison of simply-supported beams (continuous (C), with one internal hinge (1H) and with two internal hinges (2H)) with respect to soil stiffness and for hinge rotational stiffness $K_r=5$

5.5.5 Clamped beam with one hinge

The overall buckling response of the clamped beam with an internal hinge resting on elastic foundation (Figure 5-17) is numerically investigated through GNIA by considering soil stiffness $K_s=180$, $K_s=10000$ and $K_s=20000$.

5.5.5.1 Low soil stiffness $K_s=180$

Initially, the results obtained from LBA and specifically the first four eigenmodes are shown in Figure 5-39a. The imperfections shapes considered in GNIA are illustrated in Figure 5-39b. The numerical results from GNIA are shown in terms of the equilibrium path in Figure 5-40a and the beam deformed shapes at the end of the analysis in Figure 5-40b.

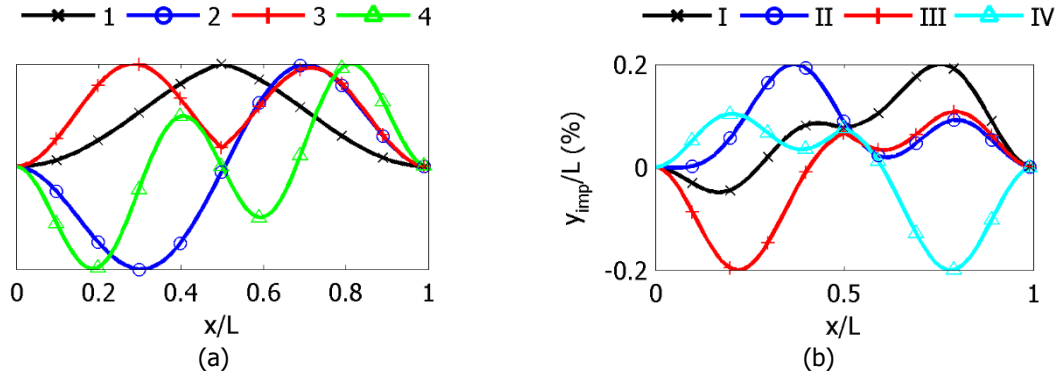


Figure 5-39: (a) Eigenmode shapes and (b) imperfection shapes considered in GNIA of clamped beam with one internal hinge for $K_s=180$ and rotational stiffness $K_r=5$

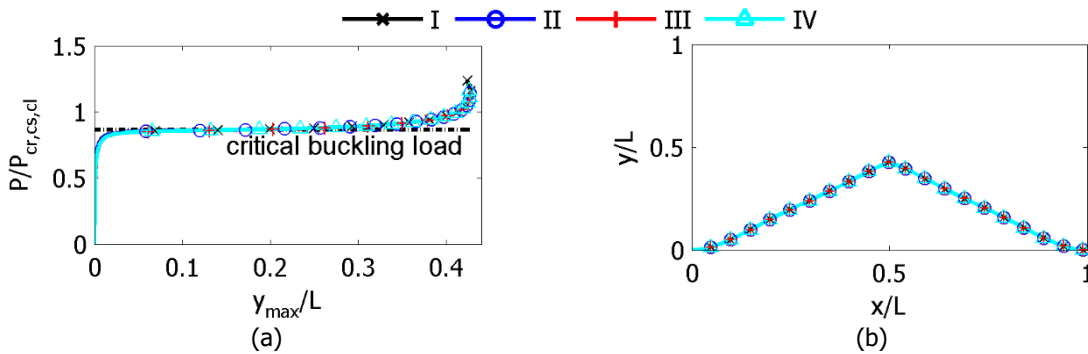


Figure 5-40: (a) Equilibrium paths and (b) beam deformed shapes obtained from GNIA of clamped beam with one internal hinge for $K_s=180$ and rotational stiffness $K_r=5$

5.5.5.2 Medium soil stiffness $K_s=10000$

The initial geometric imperfections (Figure 5-41b) considered in GNIA are derived from the eigenmode shapes (Figure 5-41a). The GNIA results are shown in Figure 5-42 in terms of the equilibrium paths and the beam deformed shapes at the end of the analysis, taking into account all imperfection shapes (Table 5-2).

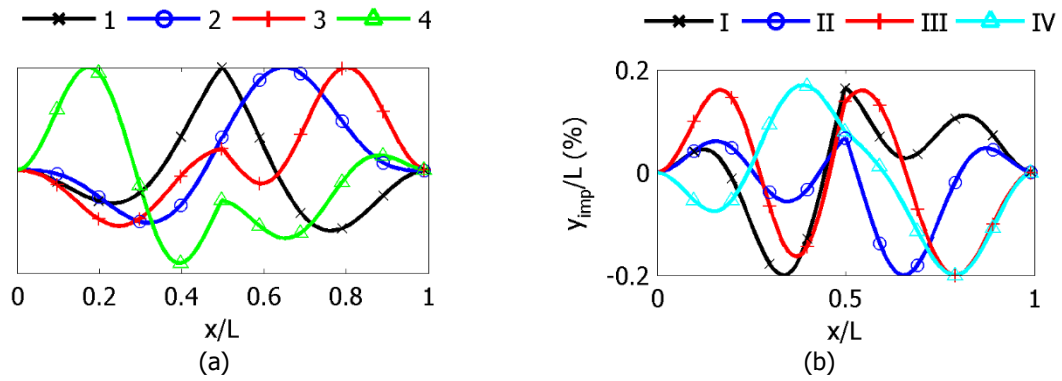


Figure 5-41: (a) Eigenmode shapes and (b) imperfection shapes considered in GNIA of clamped beam with one internal hinge for $K_s=10000$ and rotational stiffness $K_r=5$

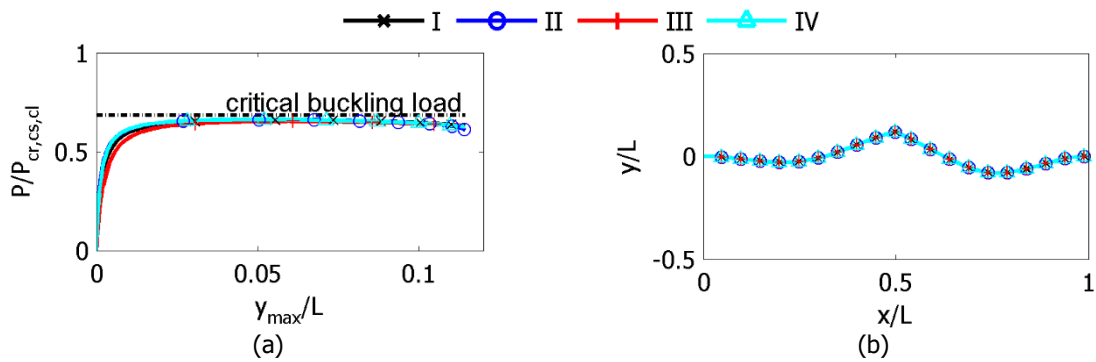


Figure 5-42: (a) Equilibrium paths and (b) beam deformed shapes obtained from GNIA of clamped beam with one internal hinge for $K_s=10000$ and rotational stiffness $K_r=5$

5.5.5.3 High soil stiffness $K_s=20000$

The eigenmode shapes obtained from LBA (section 5.4.6) and the imperfection shapes considered in GNIA are illustrated in Figure 5-43a and Figure 5-43b, respectively. GNIA results are presented in terms of the equilibrium path in Figure 5-44a and the beam deformed shape at the end of the analysis in Figure 5-44b.

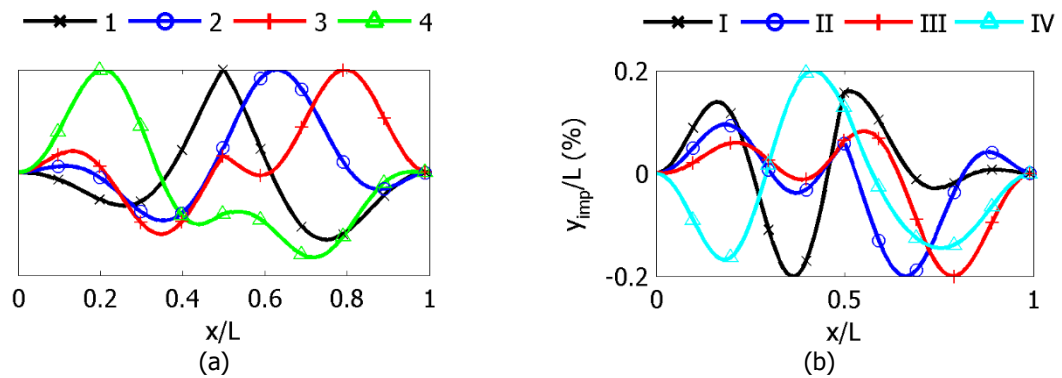


Figure 5-43: (a) Eigenmode shapes and (b) imperfection shapes considered in GNIA of clamped beam with one internal hinge for $K_s=20000$ and rotational stiffness $K_r=5$

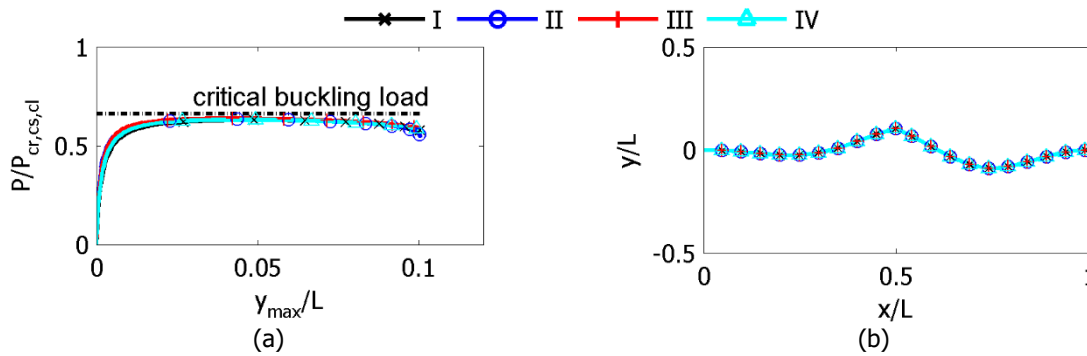


Figure 5-44: (a) Equilibrium paths and (b) beam deformed shapes obtained from GNIA of clamped beam with one internal hinge for $K_s=20000$ and rotational stiffness $K_r=5$

5.5.5.4 Discussion of results

The primary observation regarding the clamped beam overall buckling behavior is that soil conditions influence the nature of post-buckling response. It is thus observed for $K_s=180$ (Figure 5-40a) the post-buckling behavior is stable and is similar to that of a clamped beam without elastic support, i.e. the elastic beam has post-buckling strength. On the contrary, numerical results for soil stiffness $K_s=10000$ and $K_s=20000$ in terms of the equilibrium paths are presented in Figure 5-42a and Figure 5-44a, respectively, indicating unstable post-buckling behavior. Analyses carried out within the range of soil stiffness from $K_s=180$ up to $K_s=10000$ revealed that corresponding threshold regarding the soil stiffness is about $K_s=300$, i.e. for lower soil stiffness the beam post-buckling behavior is stable and for higher the behavior is unstable (Figure 5-45).

The beam deformed shape at the end of the analysis is independent of the imperfections shape and mainly affected by the critical eigenmode shape for any soil stiffness, as presented in Figure 5-40b, Figure 5-42b and Figure 5-44b.

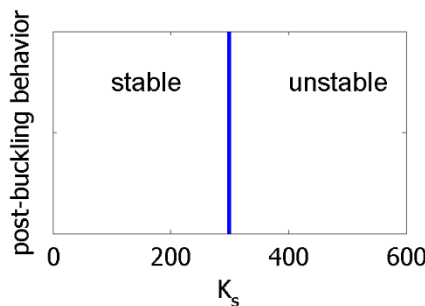


Figure 5-45: Soil range regarding the post-buckling behavior of clamped beam with one internal hinge with respect to soil stiffness and rotational stiffness $K_r=5$

5.5.6 Clamped beam with two hinges

The clamped beam with two equally-spaced internal hinges resting on elastic foundation (Figure 5-4) is numerically examined through GNIA and the corresponding results for varying soil stiffness are presented in the subsequent sections.

5.5.6.1 Low soil stiffness $K_s=180$

GNIA are carried out by considering the initial geometric imperfections shown in Figure 5-46b, which are created through linear combinations (Table 5-2) of the eigenmode shapes (Figure 5-46a) obtained from LBA. GNIA results in terms of the equilibrium paths and the beam deformed shapes obtained from GNIA are depicted in Figure 5-47a and Figure 5-47b, respectively.

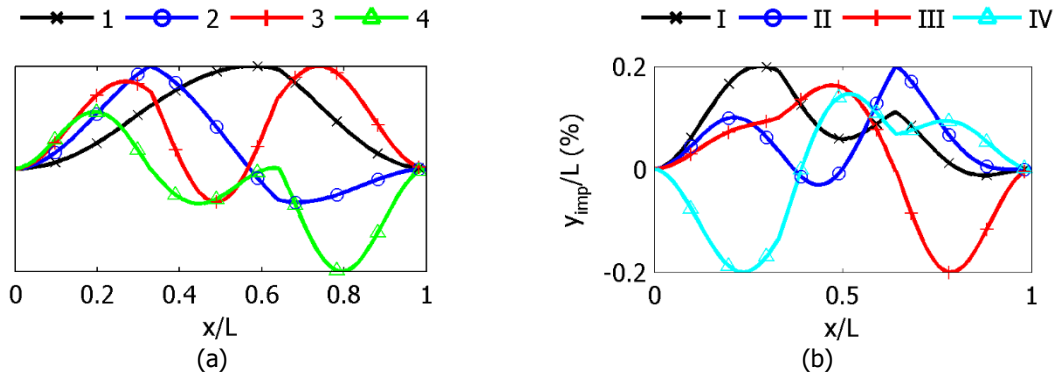


Figure 5-46: (a) Eigenmode shapes and (b) imperfection shapes considered in GNIA of clamped beam with two internal hinges for $K_s=180$ and rotational stiffness $K_r=5$

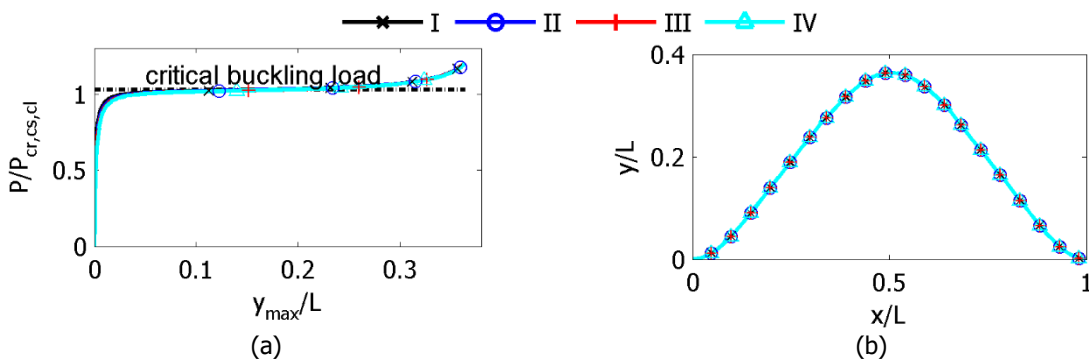


Figure 5-47: (a) Equilibrium paths and (b) beam deformed shapes obtained from GNIA of clamped beam with two internal hinges for $K_s=180$ and rotational stiffness $K_r=5$

5.5.6.2 Medium soil stiffness $K_s=10000$

The eigenmode shapes of the beam are presented in Figure 5-48a and the imperfections shapes (Figure 5-48b) are created through linear combinations. The equilibrium paths and the beam deformed shapes obtained from GNIA are presented in Figure 5-49a and Figure 5-49b, respectively.

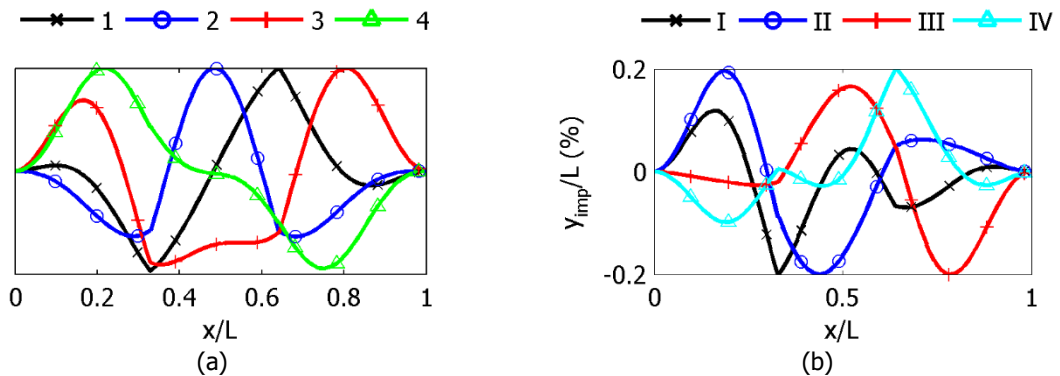


Figure 5-48: (a) Eigenmode shapes and (b) imperfection shapes considered in GNIA of clamped beam with two internal hinges for $K_s=10000$ and rotational stiffness $K_r=5$

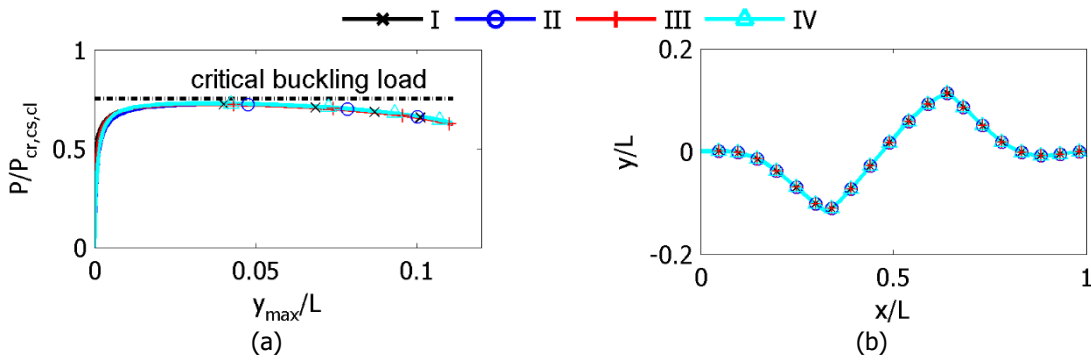


Figure 5-49: (a) Equilibrium paths and (b) beam deformed shapes obtained from GNIA of clamped beam with two internal hinges for $K_s=10000$ and rotational stiffness $K_r=5$

5.5.6.3 High soil stiffness $K_s=20000$

The imperfection shapes (Figure 5-50b) considered in GNIA are created through linear combinations (Table 5-2) of the eigenmode shapes (Figure 5-50a) obtained from LBA. The overall buckling response is examined through the equilibrium paths (Figure 5-51a) and the beam deformed shapes obtained from GNIA (Figure 5-51b).

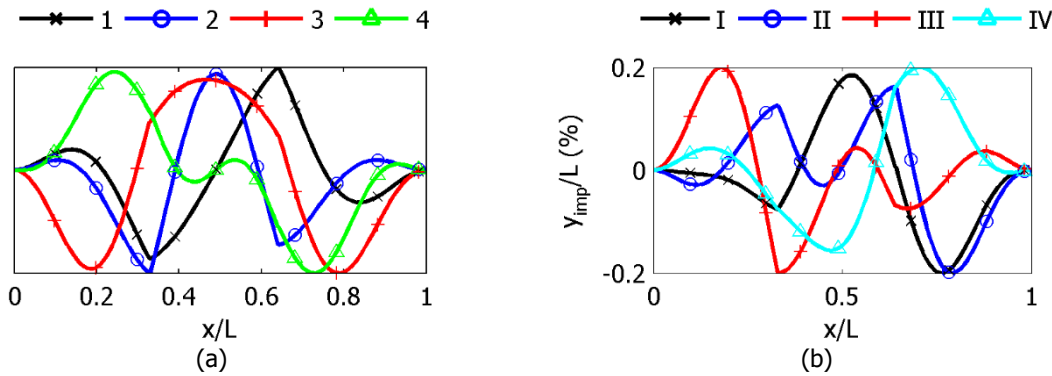


Figure 5-50: (a) Eigenmode shapes and (b) imperfection shapes considered in GNIA of clamped beam with two internal hinges for $K_s=20000$ and rotational stiffness $K_r=5$

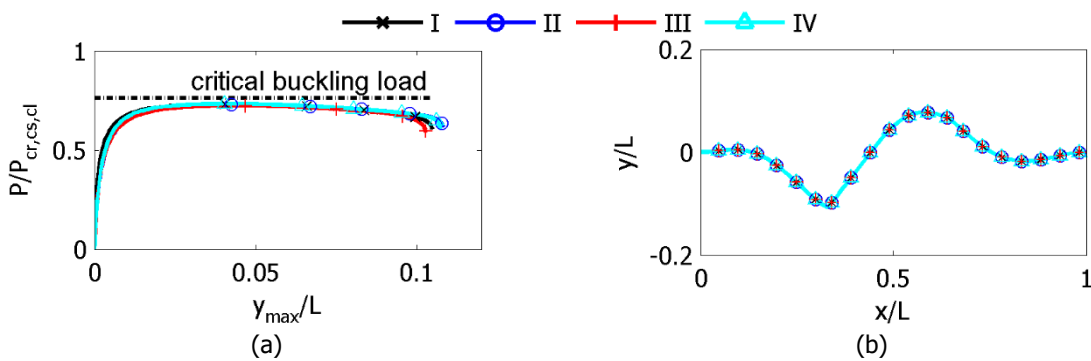


Figure 5-51: (a) Equilibrium paths and (b) beam deformed shapes obtained from GNIA of clamped beam with two internal hinges for $K_s=20000$ and rotational stiffness $K_r=5$

5.5.6.4 Discussion of results

The beam equilibrium path for low soil stiffness $K_s=180$ (Figure 5-47a) is ascending and exceeds the critical buckling load. This stable post-buckling behavior is attributed to the very low soil stiffness that does not laterally restrain the beam sufficiently for altering the nature of its behavior with respect to a beam without lateral support. Additionally, the comparison of the buckling behavior of the simply-supported and the clamped beam for the same low soil stiffness ($K_s=180$) reveals that in case of fixed

end conditions the boundaries contribute to the stability of the beam. Thus, the beam response is similar to that of a continuous clamped beam without elastic support and of a clamped beam with one internal hinge resting on foundation (Figure 5-40a). On the other hand, the beam post-buckling behavior for $K_s=10000$ (Figure 5-49a) and $K_s=20000$ (Figure 5-51a) is reported to be unstable. Initial imperfections do not affect the buckling behavior in all previous cases. GNIA results for soil stiffness between $K_s=180$ and $K_s=10000$ showed that the beam post-buckling behavior is stable for soil stiffness roughly lower than $K_s=325$, while the behavior is unstable for higher soil stiffness (Figure 5-52). Note that the corresponding soil stiffness threshold of the clamped beam with one internal hinge was marginally lower (section 5.5.5.4). The beam deformed shapes are depicted in Figure 5-47b, Figure 5-49b and Figure 5-51b for soil stiffness $K_s=180$, $K_s=10000$ and $K_s=20000$, respectively, and are dominated by the critical eigenmode shape, while geometrical imperfections do not alter the deformed shapes.

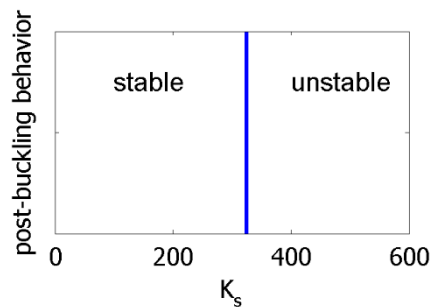


Figure 5-52: Soil range regarding the post-buckling behavior of clamped beam with two internal hinges with respect to soil stiffness and rotational stiffness $K_r=5$

5.5.7 Comparison of clamped beam ultimate loads

The integration of internal hinges in a clamped beam resting on elastic foundation affects the overall buckling and post-buckling response. The ultimate loads obtained from GNIA are evaluated to quantify the effects of hinges with reference to the continuous beam. The normalized ultimate loads are compared in Figure 5-53, where the ultimate loads of a continuous beam (C), a beam with an internal hinge (1H) and a beam with two internal hinges (2H) are presented with respect to soil stiffness $K_s=10000$ and $K_s=20000$. The rotational stiffness of the internal hinges is $K_r=5$. As already noted, the post-buckling behavior of a clamped beam with one or two internal hinges for $K_s=180$ is stable, thus there is no ultimate load and consequently this soil stiffness is excluded from the comparison. A first observation is that the presence of hinges reduces the ultimate loads, while the difference between C and 1H/2H cases increases in terms of loads, as soil stiffness increases. However, the 2H case ultimate load is higher or marginally equal to the 1H for all cases of soil stiffness under investigation. This conclusion is related to the location of the two hinges that are far from the beam center and thus their impact on global stiffness is reduced in contrast with the case of a simply-supported beam (Figure 5-38).

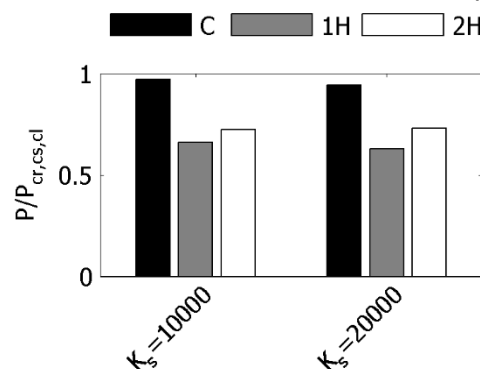


Figure 5-53: Ultimate loads comparison of clamped beams (continuous (C), with one internal hinge (1H) and with two internal hinges (2H)) with respect to soil stiffness and for hinge rotational stiffness $K_r=5$

5.5.8 Imperfection magnitude sensitivity

The ultimate load of a structure with unstable post-buckling behavior is usually sensitive to the size of initial geometric imperfections that are considered in the nonlinear analysis. Regarding the beam resting on elastic foundation, either simply-supported or clamped with one or two internal hinges, it has been shown in sections 5.5.2 through 5.5.7 that the shape of the initial imperfection for the considered very low magnitude of the imperfection has very low effect on the post-buckling behavior and the ultimate load. It is then of considerable practical significance to investigate the effect of the imperfection magnitude. In sections 5.5.2 through 5.5.7 the imperfection magnitude was considered equal to $L/500$, which is a relatively low value. Purpose of that choice was to establish the stable or unstable nature of the post-buckling behavior and to confirm that, in such case, the ultimate load is practically coincident with the linear buckling load.

However, regarding buried pipelines, due to constructional reasons and the inherent non-flatness of the trench bottom, the expected initial geometrical imperfections are expected to be much higher than $L/500$. In order to quantify these considerations, the effect of the initial imperfections magnitude is investigated by considering the clamped beam with two internal hinges (Figure 5-4), considering this simplified structural model being a reasonable assumption for buried pipelines crossing a fault. Nonlinear numerical analyses are carried out taking into account all linear combinations of eigenmodes listed in Table 5-2 as imperfection shapes. Four values of imperfection magnitudes are considered, namely $L/500$, $L/100$, $L/50$ and $L/10$.

At first, to identify the effect of imperfection magnitude, only the first linear combination of eigenmodes is chosen as imperfection shape and the corresponding analysis results are presented in terms of equilibrium paths in Figure 5-54a for soil stiffness $K_s=180$, where it is shown that the size of initial imperfections modifies the equilibrium path, but the overall buckling response remains stable, even though the linear part of the response is minimized. Next, the equilibrium paths for $K_s=20000$ are illustrated in Figure 5-54b, where the primary important observation is that the increase of initial imperfection size leads to a significant decrease of the ultimate load.

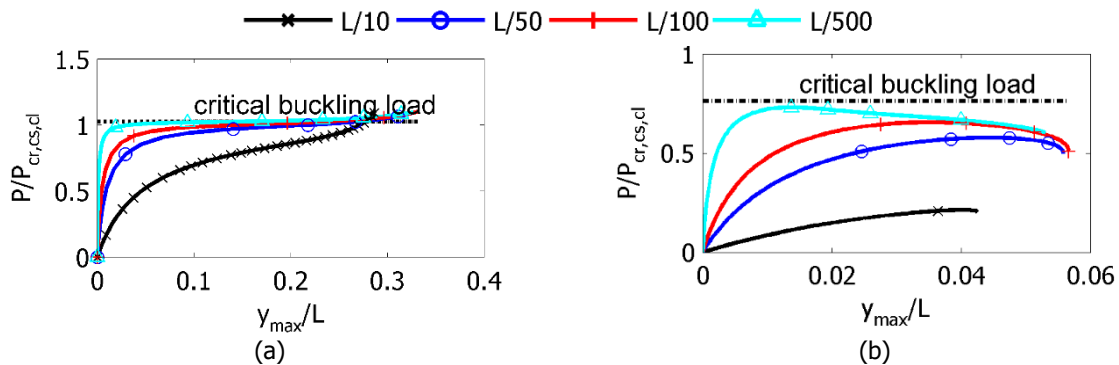


Figure 5-54: Equilibrium paths for varying imperfection magnitude of clamped beam with two internal hinges for (a) $K_s=180$ and (b) $K_s=20000$ and rotational stiffness $K_r=5$, considering the first linear combination of eigenmodes as the imperfection shape

Then, in order to investigate the interaction between the imperfection shape and magnitude in terms of affecting the ultimate load and the post-buckling behavior of the beam, all imperfection shapes after Table 5-2 are considered and the equilibrium paths for $K_s=20000$ are shown in Figure 5-55 for imperfection magnitudes $L/50$ and $L/100$. It is observed that the increase of imperfection magnitude increases the effect of imperfection shape in terms of altering the ultimate load. Moreover, it has been shown in Figure 5-51a that the buckling and post-buckling response of the clamped beam with two internal hinges is not affected when relatively low imperfection magnitude is considered, namely $L/500$. Then, the beam deformed shapes at the ultimate load are presented in Figure 5-56 for varying imperfection magnitude and all considered imperfection shapes (Table 5-2). It is observed that for

increased imperfection magnitude the different shapes of initial imperfection lead to modified beam deformed shapes at the ultimate load level in terms of magnitude, while the deformation pattern is not affected and is dominated by the critical eigenmode shape (see Figure 5-20 for $K_s=20000$ and $K_r=5$).

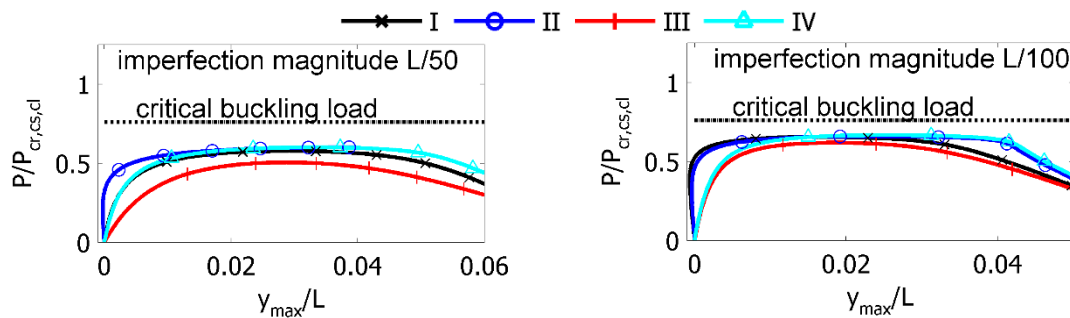


Figure 5-55: Equilibrium paths for varying imperfection magnitude and shape of clamped beam with two internal hinges for $K_s=20000$ and rotational stiffness $K_r=5$

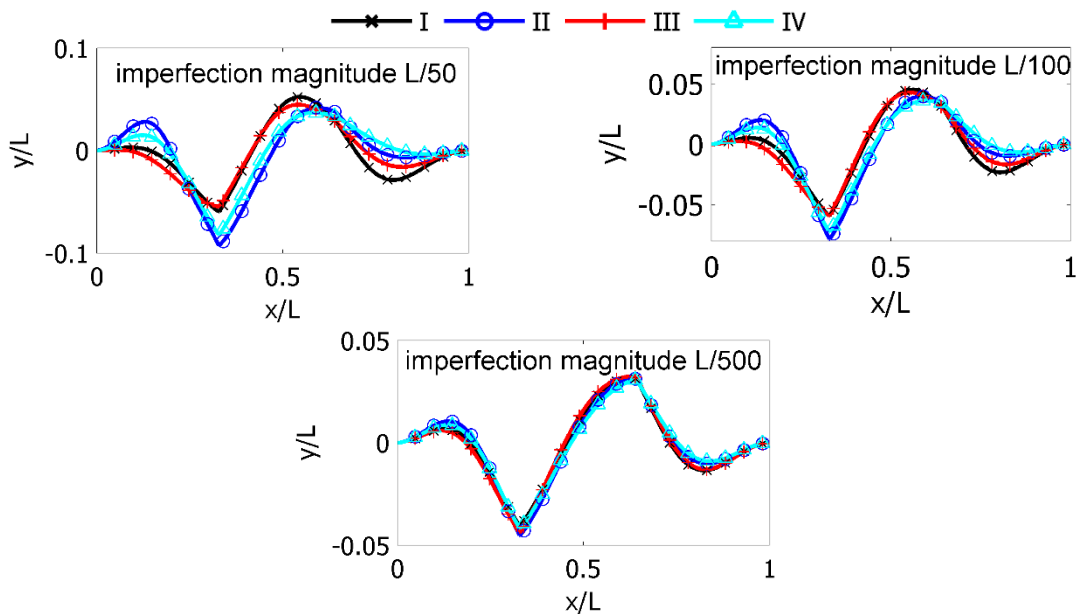


Figure 5-56: Beam deformed shapes for varying imperfection magnitude and shape of clamped beam with two internal hinges for $K_s=20000$ and hinge rotational stiffness $K_r=5$

The above results are considered as alarming for design engineers of critical structures of this type (e.g. pipelines, railway tracks) with respect to the crucial impact of the imperfection size on the structure's ultimate load, which has to be consequently taken into account in the design through proper safety factors.

5.5.9 Effect of soil nonlinearity

Modeling soil as an elastic medium is a common and, in most cases, sufficiently reliable engineering approach to overcome the introduction of complex soil properties in numerical modeling. This approach is viable for elongated structures resting on the ground, such as railway tracks, spread footings, above ground pipelines, etc. However, buried pipelines, which are also critical elongated structures, are embedded below the ground surface, within a trench, which is then backfilled with loose granular soil. In such case the assumption of linear soil (exhibiting same stiffness in tension and compression) is actually far from accurate, as the overburden backfill soil has much lower stiffness than the native underlying soil. In order to investigate this effect, two cases are addressed by considering soil as tensionless or exhibiting different stiffness for upward and downward movement.

Firstly, the soil is considered to be tensionless as soil natural properties are related to significantly low tensile strength. The effects of tensionless soil on the ultimate loads of continuous and internally hinged beams ultimate loads are investigated. The obtained ultimate loads from GNIA are compared in Figure 5-57 for simply-supported beams. The lack of soil tensional resistance leads to a significant decrease of the ultimate loads for all cases, given that the buckled beams are practically detached from soil over a significant length, as presented in Figure 5-58. These results are representative of structures resting on the ground, such as railway tracks.

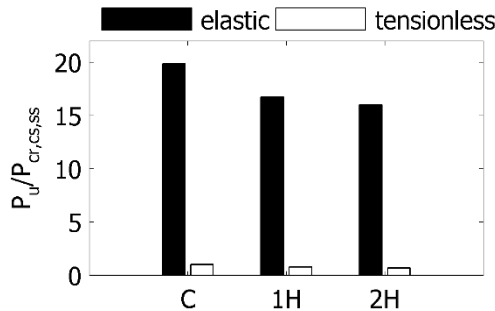


Figure 5-57: Ultimate loads comparison of simply-supported beams resting on elastic vs. tensionless soil for hinge rotational stiffness $K_r=5$

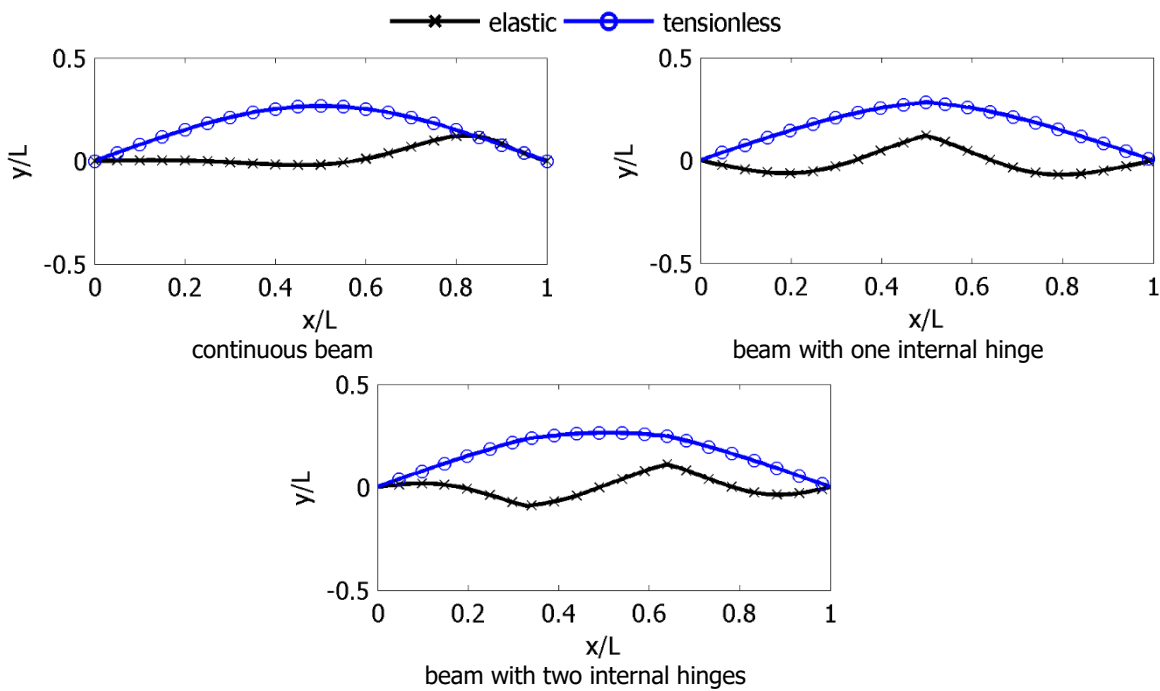


Figure 5-58: Deformation shapes obtained from GNIA of continuous beam and beam with one or two internal hinges resting on elastic and tensionless soil for hinge rotational stiffness $K_r=5$

Secondly, the effect of soil nonlinearity is investigated by considering different upward and downward soil stiffness, which is a more appropriate model for buried pipelines (Figure 5-57). Values of upward and downward soil stiffness can be extracted from the American Lifelines Alliance (2005) provisions, or other pertinent structural codes for the design of buried pipelines against permanent ground displacements (e.g. EC8 – Part 4 (European Committee for Standardization 2006), ASCE (1984)). Thus, a reasonable estimate of the ratio of the upward soil stiffness (K_{su}) to the corresponding downward stiffness (K_{sd}) is $K_{su}/K_{sd} \approx 0.05$. The effect of the different upward and downward soil stiffness is evaluated by considering the clamped beam with two internal hinges of Figure 5-4 as an appropriate structural model for buried pipelines crossing a fault. Nonlinear numerical analyses are performed by taking into

account, for the sake of simplicity, only the first linear combination of eigenmodes (Table 5-2) as the initial geometrical imperfection shape, with magnitude $L/100$, based on the results of section 5.5.8 and the eigenmode shapes of the clamped beam with two internal hinges, resting on elastic soil with stiffness $K_s=10000$, in order to carry out the comparison. The assumed hinge rotational stiffness is $K_r=5$.

The considered soil stiffness cases are listed in Table 5-4 and presented in Figure 5-59, where elastic loose and elastic stiff soil are considered to exhibit $K_s=500$ and $K_s=10000$, respectively, while nonlinear soil exhibits different upward and downward stiffness.

Table 5-4: Soil stiffness for elastic and nonlinear soil properties

Soil case	K_{su}	K_{sd}
elastic loose	500	500
elastic stiff	10000	10000
nonlinear	500	10000

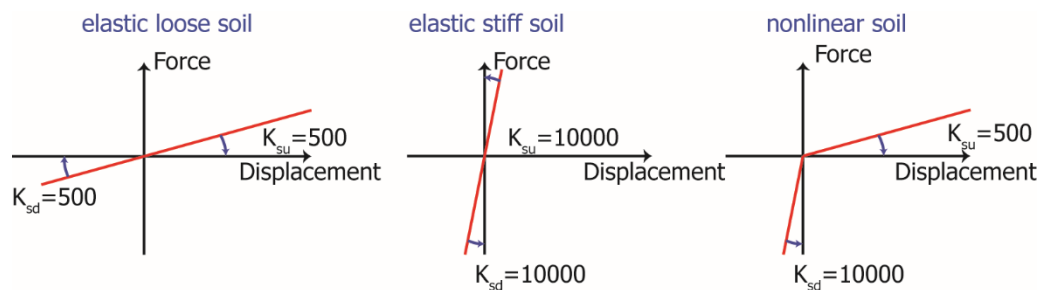


Figure 5-59: Elastic loose and stiff and nonlinear soil considered for the investigation of the effect of soil nonlinearity

Numerical results in terms of the equilibrium paths are presented in Figure 5-60a indicating unstable post-buckling behavior in all cases. However, soil stiffness and soil nonlinearity highly affect the beam response. The beam’s ultimate load in case of elastic loose and of nonlinear soil is quite similar, unlike the elastic stiff case, where the beam reaches an ultimate load that is about 130% higher than the other two cases. Then, the beam deformed shapes are shown in Figure 5-60b, where the beam deformation in cases of elastic soil is similar to the critical eigenmode for $K_s=10000$ (see Figure 5-20 for $K_s=10000$ and $K_r=5$). On the other hand, the soil nonlinearity and specifically the stiffer downward soil restricts the beam to deform downwards and consequently most of the deformation takes place upwards.

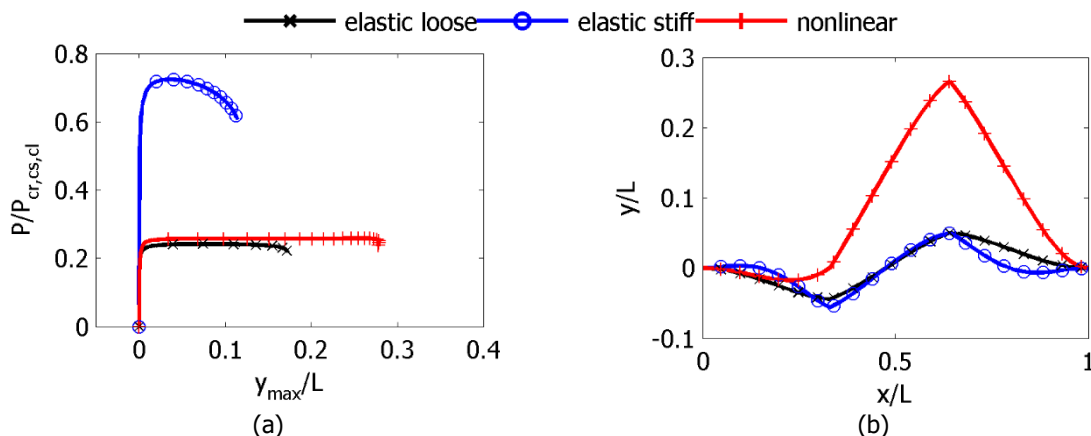


Figure 5-60: (a) Equilibrium paths and (b) deformed shapes of clamped beam with two internal hinges for $K_s=10000$ and considering either uniform or nonlinear soil with rotational stiffness $K_r=5$

The investigation’s outcomes regarding the soil nonlinearity effects highlight the necessity of considering thus nonlinearity in the analysis and design of buried structures (e.g. pipelines), as different upward

and downward soil properties reduce the ultimate load and affect the structure's deformation. It is important to point out that the downward movement of a buried structure is usually highly restricted by the native soil properties. In light of this, modeling soil as an elastic medium for such structures is not on the safe side.

5.6 SUMMARY AND CONCLUSIONS

The buckling and post-buckling behavior of axially loaded Winkler beams with internal hinges representing flexible joints has been investigated, aiming at providing a qualitative evaluation for the potential danger of upheaval buckling caused by reverse fault rupture of buried pipelines with flexible joints. For that purpose, a numerical approach has been selected, using the well-known and sufficiently verified commercial FEM software ADINA. This approach is considered as appropriate for dealing with the problem from a structural design rather than engineering mechanics point of view. Even though in the present investigation a straight beam model has been analyzed, supported laterally by elastic Winkler-type springs and subjected to constant axial force, the employed modeling and analysis methodology can be readily extended to issues that are commonly encountered in practice, such as non-straight pipeline route, inhomogeneous soil conditions, varying axial force distribution along the pipeline accompanied by bending moments, etc.

The beams have been analyzed as either simply-supported or clamped, having one or two internal hinges that are equipped with an elastic rotational spring, while axial and transverse displacement continuity has been assumed, modeling commercial hinged flexible joints of bellow-type. Numerical linearized buckling analysis and geometrically nonlinear analysis with initial imperfections are employed to cover eigenmode cross-over and beam post-buckling behavior, particularly imperfection sensitivity, as influenced by the relation between soil stiffness and hinge rotational stiffness.

As expected, the numerical results indicate that the internal hinges reduce the beam global stiffness and thus hinged beams have lower linear and nonlinear buckling loads than continuous ones, even though this influence is substantially smaller for elastically supported beams than for laterally free ones. Increasing rotational stiffness progressively restores beam continuity. Increasing soil stiffness leads to eigenmode cross-over, provided that hinge rotational stiffness is sufficiently high. Furthermore, antisymmetric eigenmode shapes are dominated by the hinges' locations on the beam, while symmetric shapes are not affected.

In nonlinear analyses, emphasis is placed on imperfection sensitivity, due to its potential significance for the ultimate buckling response. Imperfection shapes are derived from linear combinations of the first four eigenmode shapes, following common analysis practice when geometrical imperfection shapes are unknown a priori. The descending post-buckling equilibrium paths in the majority of the cases under investigation indicates that the post-buckling behavior of such internally hinged beams on Winkler foundation is unstable, with the exception of very low soil stiffness, which leads to stable post-buckling response, same as in laterally free beams. The imperfection magnitude has been found to highly influence the beam ultimate load, highlighting the need of conservative design assumptions and adoption of appropriately high safety factors. On the contrary, the imperfection shape was shown to play a relatively small role compared to imperfection magnitude for the overall buckling behavior, at least among considered imperfection shapes. Finally, considering soil to exhibit different stiffness for the upward and the downward movement, with the latter being stiffer, was found to have significant effect on the beam overall buckling response in terms of deformation shape as well as ultimate load.

The above conclusions can be useful for reevaluating the safety standards in the design against buckling of internally hinged buried pipelines subjected to reverse seismic faults. The strong dependence of the response on the relation of soil stiffness to hinge rotational stiffness, and on the size of initial imperfections, combined with the inherent uncertainties in soil properties and in excavation trench

geometry, highlight the need for appropriately large safety factors. Finally, the simplified model has been used to investigate the potential of upheaval buckling, emerging as a potential failure mode for pipes with flexible joints subjected to reverse faulting. Numerical analysis results revealed that this potential depends on the relative pipe – joint – soil stiffness and for stiffness values encountered in practical application, the potential of global buckling is limited due to the restraints provided by the surrounding soil, contrary to the case of a laterally free pipe. In conclusion, for realistic soil stiffness regarding the upward movement, upheaval buckling will not emerge as a critical failure mode.

Part of the work presented in this chapter has been published in Melissianos and Gantes (2016).

6 NUMERICAL INVESTIGATION OF PIPELINES WITH FLEXIBLE JOINTS

6.1 INTRODUCTION

In this chapter a thorough numerical study is presented on the numerical evaluation of buried steel pipelines subjected to strike-slip faulting (Figure 6-1) featuring a preliminary feasibility study on the effectiveness of joints in terms of drastically reducing the developing longitudinal tensile and compressive strains and consequently reducing the risk of pipe failure. Taking into account that hinged bellow-type flexible joints have not been used before as seismic countermeasures in buried pipes under faulting, the investigation aims at demonstrating the structural advantage of the proposed solution, provided that the technological and practical aspects of such joints are solve.

The appropriate numerical model will at first be established and the procedure for the selection of the optimum number and location of flexible joints will be outlined. Then, considering that pipelines with flexible joints behave as segmented pipes under fault rupture and the response is characterized by rotation at the joints and small deformation of the parts between the pipes, it is necessary to investigate the effect of various parameters affecting the behavior, provided that the relative pipe – joint – soil stiffness render the actual response unknown. Thus, the main parameters affecting the performance of pipes with flexible joints will be investigated and results for practical applications will be extracted. Preliminary results on the numerical evaluation of buried pipes with flexible joints have been published by Gantes et al. (2015) and Melissianos and Gantes (2014c, 2015a).

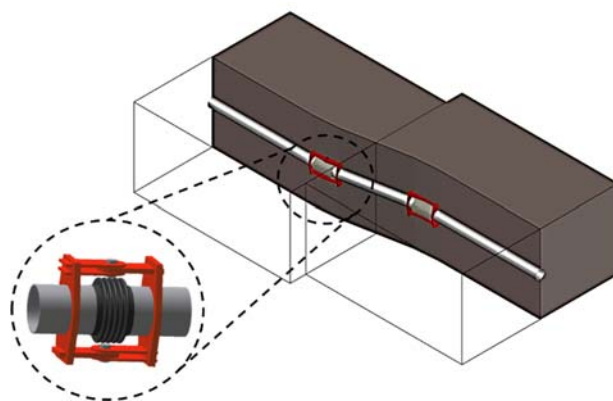


Figure 6-1: Schematic illustration of a pipeline with hinged bellow-type flexible joints subjected to strike-slip fault rupture

6.2 PIPELINE – FAULT CROSSING NUMERICAL MODELING

The behavior of pipelines subjected to strike-slip fault movement is addressed, hence the pipeline deformation is assumed to take place within a horizontal plane (Figure 1-8a). A planar fault with zero thickness is considered in the analysis, intercepting a straight pipeline segment at the middle of its modeled length. The pipeline stress-state is directly related to the pipe – fault crossing angle β whose selection depends among others on the route selection procedure, seismological and geotechnical aspects of the seismic fault and the expected fault offset. Crossing angles $\beta \leq 90^\circ$ lead to pipeline bending and tension, while angles $\beta > 90^\circ$ lead to bending and compression (Abdoun et al. 2009) and their effect will be discussed in more detail later.

Pipeline numerical modeling is carried out using the general purpose finite element software ADINA (ADINA R&D 2006). The pipe is discretized into PIPE elements that are Hermitian 2-node beam-type finite elements with extra degrees of freedom to account for the stresses caused by cross-section ovalization. A longitudinal mesh density equal to 0.25m is selected, after a mesh density sensitivity analysis has been performed to define the optimum length of pipe elements with respect to accuracy and computational cost efficiency. Geometrical nonlinearity is considered in the analysis to account for the second order effects resulting from potential fault activation in the order of meters. Soil modeling is carried out using discrete springs after American Lifelines Alliance (2005) provisions (Figure 6-2). Elastic – perfectly plastic soil springs are modeled in ADINA using nonlinear SPRING elements that exhibit stiffness only in the local axial direction and connect pipe nodes to “ground” nodes. Soil “ground” nodes on the fault footwall are considered fixed, while the corresponding ones on the fault hanging wall are subjected to the imposed displacement caused by the fault movement. Non-seismic and in service actions (e.g. internal pressure, corrosion, overburden soil weight, hydraulic transient actions, etc.) are not considered thereafter.

Flexible joints can be modeled either as a general beam-type finite element with its stiffness matrix being constructed from the spring rates provided by the manufacturer, or as a generic flexible joint, represented by a rotational spring at the center point, without considering the joint length (Peng and Peng 2009). The second modeling approach for the joint has been selected in the present study. The joint lateral and axial relative movements at the two ends are restrained. The joint torsional movement is generally prohibited by the manufacturers (EJMA 2008) and thus rotation about the longitudinal axis is restricted through appropriate constraints.

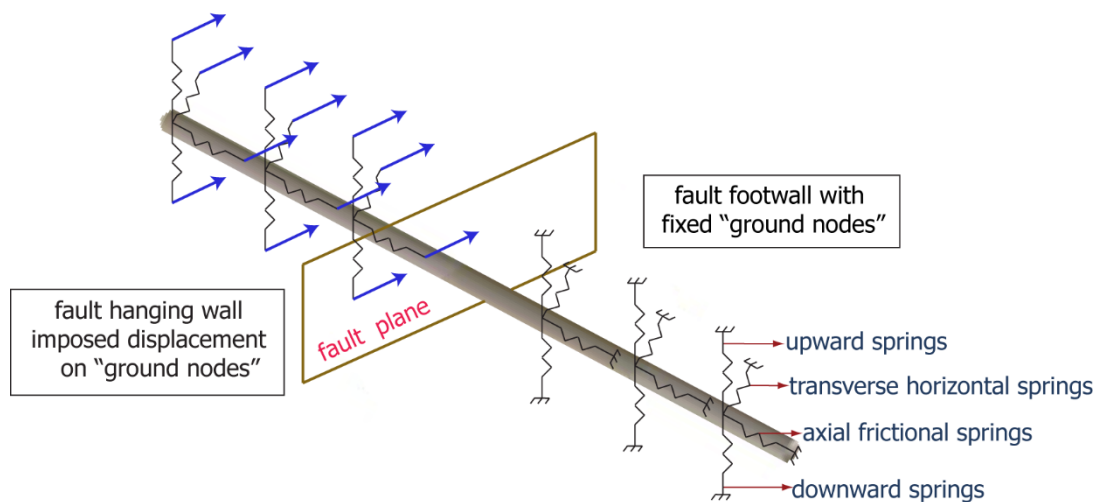


Figure 6-2: Beam-type finite element model for pipeline – fault crossing numerical modeling

The imposed displacements caused by fault movement evolve at an adequately slow rate that allows the engineer to neglect any dynamic phenomena, considering the fault offset as a quasi-static process

(American Lifelines Alliance 2005; European Committee for Standardization 2006; Ha et al. 2010). Accordingly, fault rupture is treated herein as a static phenomenon. The problem's inherent nonlinearity is handled through the implementation of the Newton-Raphson or the Arc-Length solution algorithms (Bathe and Dvorkin 1983). Numerical convergence and smooth displacement application are achieved by selecting a proper number of analysis steps so that the external loading application follows closely the response evolution.

A typical high-pressure, large diameter natural gas pipeline is considered as a case study. The pipe's modeled length is 1000m, following a sensitivity analysis to define a sufficient length within which the soil reactions have vanished. The cross-section is of diameter $D=914\text{mm}$ (36in) and thickness $t=12.7\text{mm}$ (0.5in). Material nonlinearity is considered through an elastic – plastic bilinear law with isotropic hardening. While pipeline steel is commonly modeled via the Ramberg-Osgood formula, in the present study nonlinear material modeling is actually of very minor importance, taking into account that the response of buried pipelines with flexible joints is well into the elastic range (section 6.4). Steel is of type API5L-X65 with the properties being listed in Table 6-1 and the corresponding stress – strain relation illustrated in Figure 6-3.

Table 6-1: API5L-X65 steel properties

Property	Value
Elastic Young's modulus (GPa)	210
Plastic modulus (GPa)	0.464
Yield stress (MPa)	448.5
Yield strain (%)	0.214
Failure stress (MPa)	510
Failure strain (%)	18

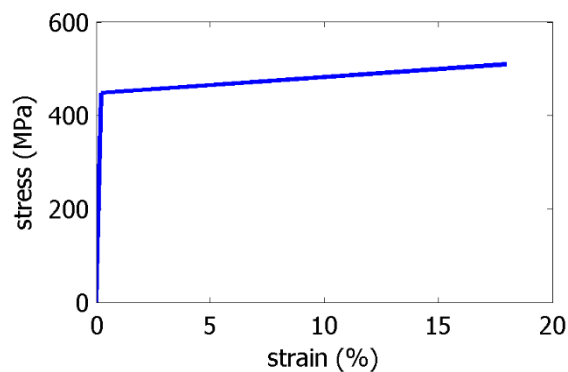


Figure 6-3: API5L-X65 pipeline steel bilinear stress – strain relationship

The pipeline is assumed to be coal-tar coated and embedded under 1.30m of granular loose sand with unit weight $\gamma=18\text{kN/m}^3$, cohesion $c=0\text{kPa}$ and internal friction angle $\phi=36^\circ$.

Axial soil springs model the pipeline – soil friction and their properties are related to backfill soil properties and pipeline coating material. Friction forces are estimated using geotechnical approaches that are used to simulate force transfer on axially loaded interfaces of piles. For sand and cohesionless soil types, friction forces are calculated through integration of shear stresses along the pipeline – soil interface. Given the roughness of the pipe surface, friction angle δ equals 50% to 100% of soil friction angle ϕ . Maximum soil resistance is achieved for relatively small displacement within 2.5mm to 5.0mm for dense to loose sand (Sanghal 1980). In the present study it is assumed that soil resistance is achieved at 3.0mm.

Transverse horizontal (lateral) springs model the soil resistance to any horizontal transverse movement of the pipeline in the trench. Thus, pipeline – soil interaction mechanisms are similar to those of vertical

anchor plates or horizontal moving foundations by activating passive earth pressure. For cohesionless soil, the transverse force is expressed through a hyperbolic equation proposed by Trautmann and O'Rourke (1983). Given that the force – deformation relationship is assumed elastic – perfectly plastic, the nonlinear equation is bilinearized by multiplying the relative soil displacement with a factor of 0.26. Vertical upward and downward springs model the vertical movement of the pipeline in the trench, but their properties differ significantly, as backfill soil above the pipeline has very low stiffness in order to reduce friction, while native soil below the pipeline has much higher stiffness. Upward movement perpendicular to the pipeline axis results to vertical forces at the pipe – soil interface, whose maximum corresponds to the weight of an inverted triangle prism of soil above the pipeline top. Downward movement perpendicular to the pipeline axis results to vertical forces at the pipe – soil interface, which correspond to the vertical bearing capacity of a footing (O'Rourke and Liu 2012). Both for upward and downward springs the nonlinear equation is bilinearized and the soil yield displacement is estimated in the analysis as 13% of the maximum provided by American Lifelines Alliance (2005). The soil spring properties are listed in Table 6-2 and the corresponding force – displacement relationships of soil springs are presented in Figure 6-4.

Table 6-2: Soil spring properties

Spring type	Yield force (kN/m)	Yield displacement (mm)
Axial (friction)	40.69	3
Transverse horizontal	320.07	23
Vertical (downward displacement)	1493.65	114
Vertical (upward displacement)	45.46	4.6

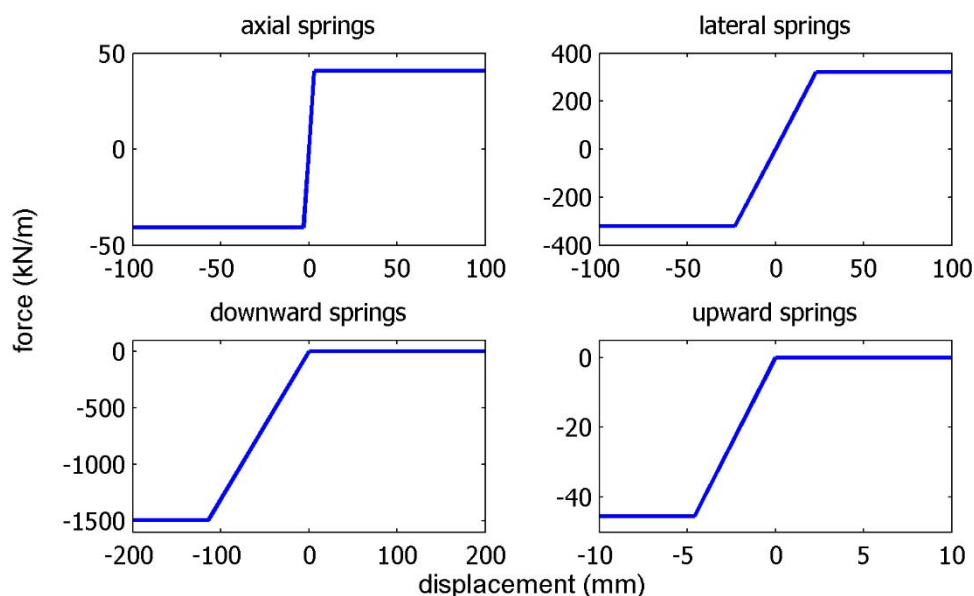


Figure 6-4: Soil springs' force – displacement relations

Finally, the flexible joints introduced in the pipeline exhibit rotational stiffness equal to 100kNm/rad and angular capacity equal to 40° (e.g. BOA Group 2016, Witzenmann GmbH 2016). Note that in case of large diameter and high pressure pipelines, the potential of flow disruption due to excessive flexible joint rotation should be checked.

6.3 INTRODUCTION OF FLEXIBLE JOINTS

6.3.1 Investigation of optimum number and locations of flexible joints

The primary consideration in adopting flexible joints as mitigating measures is the determination of their optimum number and locations in order to minimize the cost and maximize the efficiency in terms of preventing failure through strain reduction. The joint locations are initially selected based on the bending moment distribution of the continuous pipeline caused by faulting, given that joints act as internal hinges in the structural system. Specifically, primary candidate locations for joints are the sections of maximum bending moment of the continuous pipeline on either sides of the fault trace. The distance between the maximum bending moment location and the fault trace is defined as L_j (Figure 6-5). At this stage the uncertainty regarding the fault trace is disregarded.

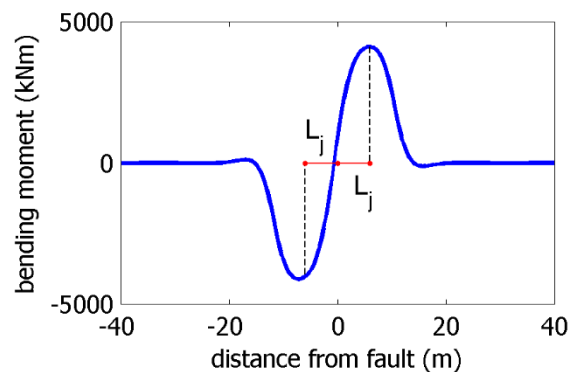


Figure 6-5: Definition of length L_j in bending moment distribution of a continuous pipeline

To investigate the best combination of joints, six different cases of pipes with joints are investigated with respect to length L_j (Table 6-3). Throughout this study, the continuous pipeline is abbreviated as CP and the pipeline with flexible joints as PFJ. The pipelines are assumed to intercept a strike-slip fault with crossing angle $\beta=90^\circ$ and subjected to normalized fault offset magnitude of $\Delta/D=2$. In the case under investigation the distance L_j equals 6.5m.

Table 6-3: Cases of pipelines with flexible joints under investigation

Case	Number of joints	Joints location
2PFJ	2	$-L_j, +L_j$
3PFJ	3	$-L_j, 0, +L_j$
4PFJ(1)	4	$-L_j, -L_j/2, +L_j/2, +L_j$
4PFJ(2)	4	$-2L_j, -L_j, +L_j, +2L_j$
6PFJ(1)	6	$-3L_j/2, -L_j/2, -L_j, +L_j/2, +L_j, +3L_j/2$
6PFJ(2)	6	$-2L_j, -L_j, -L_j/2, +L_j/2, +L_j, +2L_j$

The effectiveness of flexible joints for significantly decreasing the bending moment in all PFJ cases is demonstrated in Figure 6-6. It is noted that, for this crossing angle $\beta=90^\circ$, the pipeline behavior is predominantly flexural, corresponding to optimum conditions for hinge-type flexible joints, as pipe axial strains are very small. The bending moment reduction with respect to the continuous pipeline is also quantified in Table 6-4, accompanied also by the maximum rotations of all joints for all PFJ cases. The maximum moment reduction is reported in 4PFJ(1), 6PFJ(1) and 6PFJ(2) cases, while cases 2PFJ, 3PFJ and 4PFJ(2) exhibit smaller reduction. In cases 4PFJ(2), 6PFJ(1) and 6PFJ(2) the joints that are located beyond distance L_j ($\pm 2L_j$ and $\pm 3L_j/2$) exhibit almost zero rotation, while joints located at $L_j/2$ in 4PFJ(1), 6PFJ(1) and 6PFJ(2) cases exhibit the same rotation, as well as joints at L_j in 2PFJ and 4PFJ(2) cases. Hence, the optimum case is 4PFJ(1), as joints located beyond L_j distance nearly do not rotate (shown also in Figure 6-6) and consequently they are inactive. The case 4PFJ(1) of the pipeline with four joints

located at distances L_j and $L_j/2$ on each side of the fault trace (abbreviated in the following for simplicity as PFJ) is hence selected hereinafter to further investigate the parameters affecting the joint's efficiency. The configuration of the flexible joints is schematically shown in Figure 6-7.

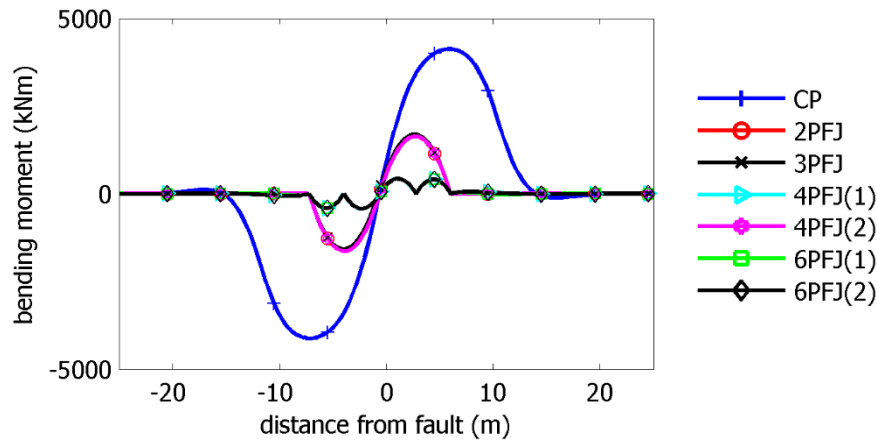


Figure 6-6: Bending moment distributions of continuous pipeline and pipelines with flexible joints subjected to strike-slip faulting

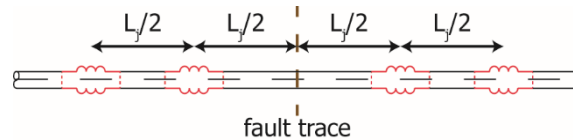


Figure 6-7: Optimum configuration of flexible joints for a pipe subjected to strike-slip fault rupture, without considering fault trace uncertainty

Table 6-4: Maximum bending moment reduction and joint rotation in all cases of pipelines with flexible joints

Case	Number of joints	Bending moment reduction (%)	Maximum joint rotation (°)
2PFJ	2	60.29	8.39
3PFJ	3	59.86	8.24
4PFJ(1)	4	89.64	8.10
4PFJ(2)	4	60.29	8.39
6PFJ(1)	6	89.64	8.10
6PFJ(2)	6	89.64	8.10

6.3.2 Response features of pipeline with flexible joints

The introduction of flexible joints in a buried steel pipeline modifies the structural system from continuous to segmented. In order to evaluate and quantify this effect, the continuous pipeline (CP) and the pipeline with four flexible joints (PFJ), as obtained from section 6.3.1, are examined in more detail. The pipeline displacements are plotted in Figure 6-8 with respect to the distance from the fault, indicating a smooth curved shape for CP, while PFJ follows a piece-wise linear shape.

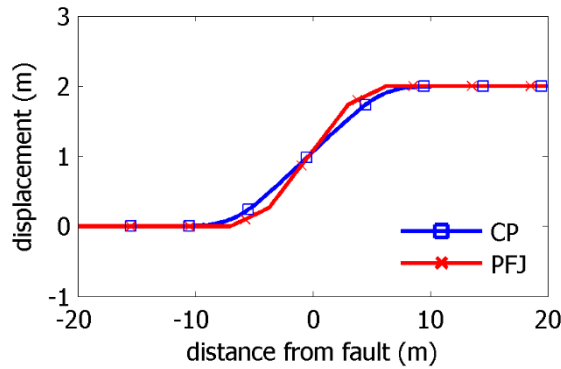


Figure 6-8: CP and PFJ displacements

Furthermore, axial forces and bending moments are compared in Figure 6-9. It is observed that the introduction of flexible joints leads to a very significant decrease of bending moment (Figure 6-9b), while a minor increase in axial force is observed (Figure 6-9a). The continuous pipeline response is dominated by bending as can be deduced from the fact that stresses due to axial force are roughly of the order $N/A=600\text{kN}/0.034\text{m}^2\approx 176\text{MPa}$, while maximum stresses due to bending are approximately equal to $M/W=4122\text{kNm}/0.008\text{m}^3\approx 515\text{MPa}$. Thus, the introduction of flexible joints leads to an important reduction of longitudinal maximum effective stresses, as shown in Figure 6-10. The stress distribution along the pipeline is symmetric around the fault trace, given the strike-slip faulting and the symmetric soil response to any lateral pipeline movement in the trench.

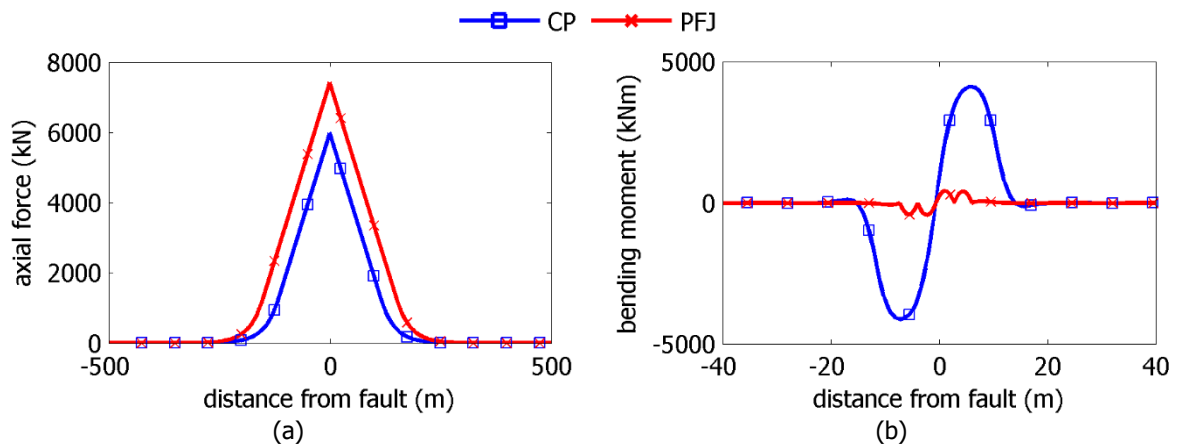


Figure 6-9: (a) Axial force and (b) bending moment distributions of CP and PFJ

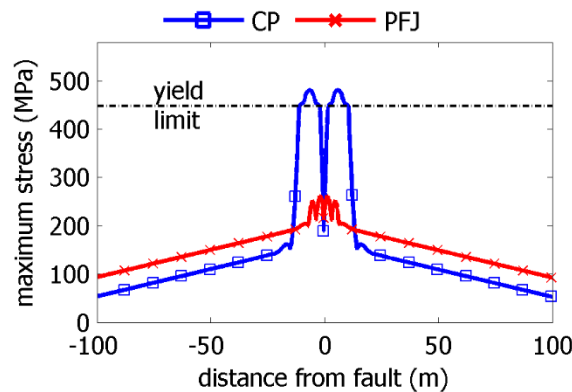


Figure 6-10: Maximum effective stress distributions along CP and PFJ

As the pipeline design against permanent ground displacements is carried out in strain terms (section 2.2), it is crucial to identify the PFJ response in terms of developing longitudinal strains, which are the

summation of axial and bending strains. The longitudinal tensile strains are illustrated in Figure 6-11a and the compressive strains in Figure 6-11b, respectively, both indicating that the flexible joints contribute decisively to a sharp decrease of strains, thus minimizing the potential of pipeline failure due to either tensile fracture or local buckling. The compressive strains are reduced, particularly vanishing. The strain reduction is explained by the structural system's modification from continuous to segmented, as strains are concentrated at the joints, retaining the steel pipe parts nearly undeformed. The longitudinal strain distributions (Figure 6-11) in combination with axial force (Figure 6-9a) and bending moment (Figure 6-9b) distributions confirm that bending strains are much higher than axial strains and thereby hinged joints are the appropriate joint type for strike-slip faults.

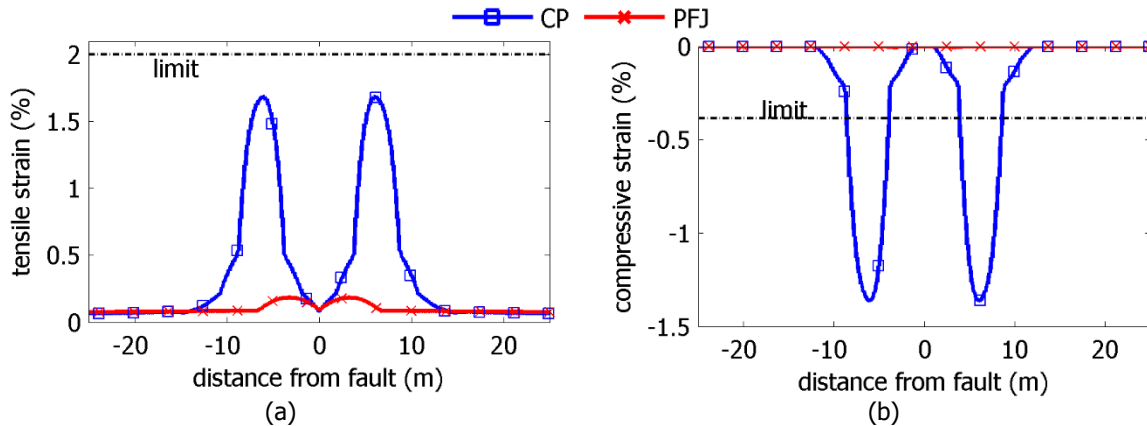


Figure 6-11: Longitudinal (a) tensile and (b) compressive strain distributions along CP and PFJ

The modification of the pipeline deformed shape due to faulting achieved by the integration of flexible joints (Figure 6-8) has also some effect on the soil response due to pipeline movement in the trench. This is depicted by the frictional soil force distribution along CP and PFJ (Figure 6-12a), showing a minor increase in the soil plastification length around the fault vicinity, while decrease of the soil plastification length regarding the lateral soil response is observed for PFJ in Figure 6-12b.

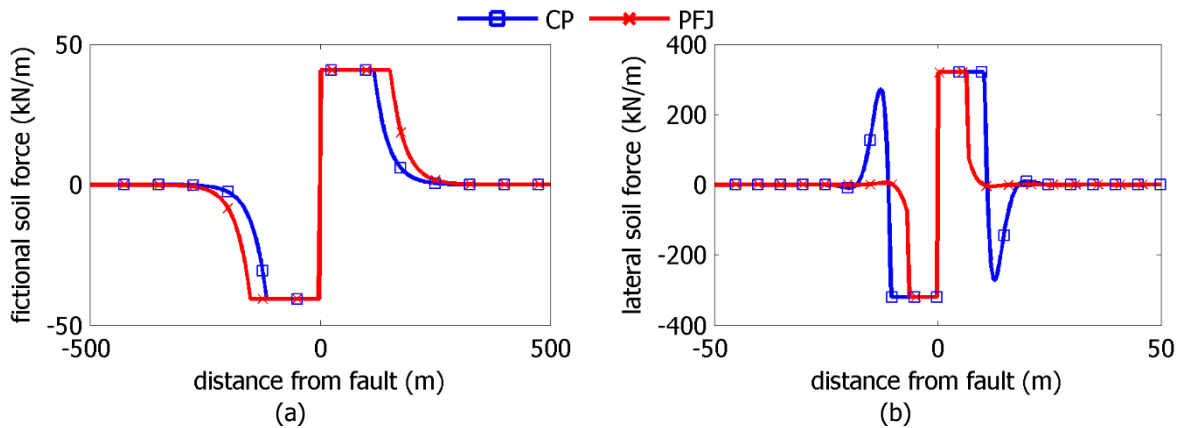


Figure 6-12: (a) Frictional soil force and (b) lateral soil force distributions along CP and PFJ

6.4 EFFECT OF PIPELINE – FAULT CROSSING ANGLE

6.4.1 Pipeline under bending and tension

The pipeline – fault crossing angle β is a dominant parameter of the pipeline mechanical behavior when subjected to strike-slip faulting. The major effect of angle β is its influence on the relationship of developing pipe tension and bending moment with respect to the fault movement magnitude. When angle β tends to 90° , the pipeline intercepts the fault plane nearly perpendicularly and bending

dominates the response. Tension is the primary stress-state when angle β is lower, as the pipeline tends to become parallel to the fault trace. The relation between the developing tension and bending with reference to the crossing angle β depends in practice on the pipe elongation, which is schematically illustrated in Figure 6-13. The anchor points beyond which the pipe is assumed to be unstressed are denoted by A and D, while (BC) is the curved segment of the pipe due to fault offset. In case of angle $\beta=90^\circ$, the pipe elongation equals $(BC')-(BC)$ as the fault offset is equal to the transverse displacement (δ_y) of reference point C. Then, in case of angle $\beta<90^\circ$ there is displacement of point C along the longitudinal axis x of the pipe and consequently the pipe elongation equals $(BC'')-(BC)=(BC')-(BC)+\delta_x > (BC')-(BC)$ ($\beta=90^\circ$ case).

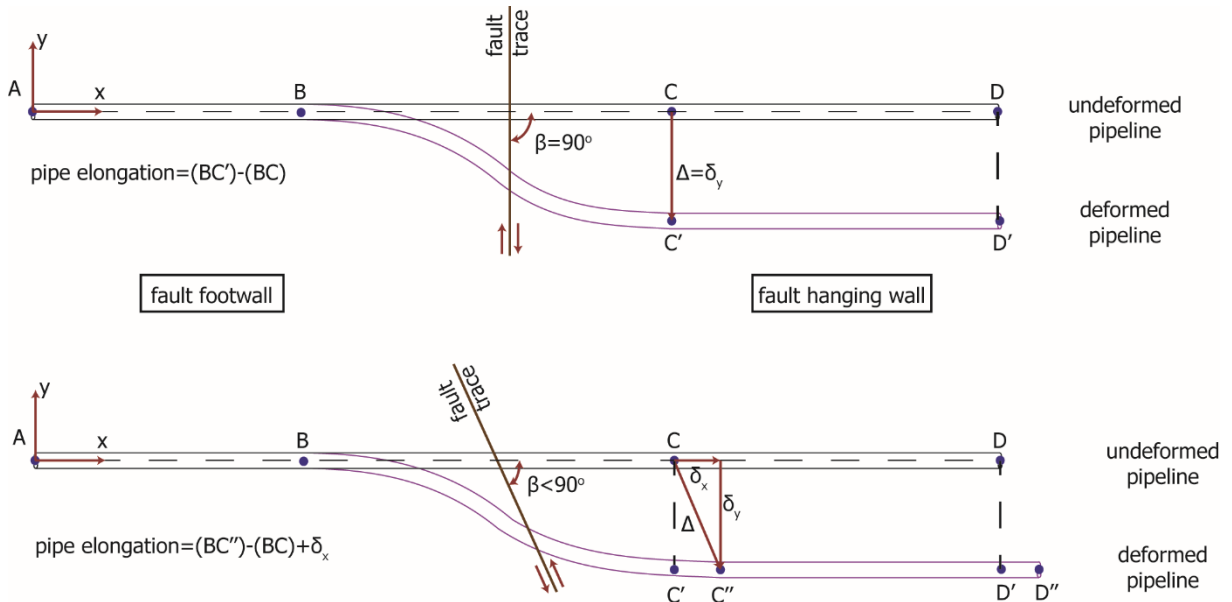


Figure 6-13: Effect of pipe –fault crossing angle β in pipe elongation

It is thus essential to investigate the impact of the crossing angle β on the response of pipelines with flexible joints. The integrated joints act as internal hinges in the structural system and consequently their efficiency depends on the degree of flexural versus axial response. Within this framework, a continuous pipeline and the corresponding pipeline with four flexible joints are investigated. The joints are located in each case according to the procedure described in section 6.3.1. Three characteristic crossing angles are considered, namely $\beta=50^\circ$, $\beta=70^\circ$ and $\beta=90^\circ$. The maximum normalized fault movement is assumed equal to $\Delta/D=4$.

The displacements of the continuous pipeline (CP) and the pipeline with four flexible joints (PFJ) are illustrated in Figure 6-14, where on the horizontal axis the distance from the fault trace is presented and on the vertical axis the normalized pipeline transverse displacement with respect to pipe diameter D is shown, at levels of fault offset magnitude equal to $\Delta/D=0.5$, $\Delta/D=2$ and $\Delta/D=4$, in order to demonstrate the effect of the fault offset magnitude. It is noted that in cases of crossing angles $\beta=50^\circ$ and $\beta=70^\circ$, according to Figure 2-1, thus the pipeline is subjected to longitudinal and transverse imposed displacement with respect to its axis. In all cases the joint angular demand is well below the 40° capacity, as the highest joint rotation reported equals 8.10° for the $\beta=90^\circ$ case. Increasing fault offset and decreasing angle β lead to more intense pipe tension than bending and consequently the differences between the CP and the PFJ deformations tend to be negligible.

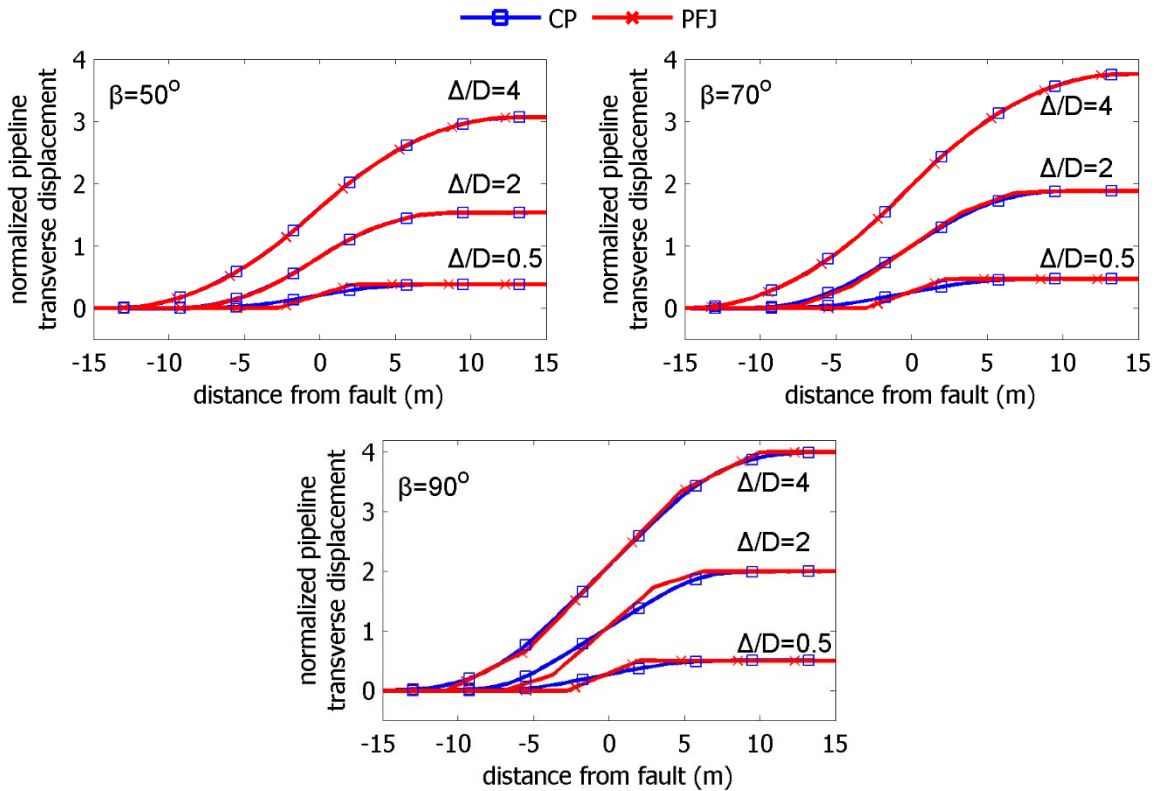


Figure 6-14: CP and PFJ displacements for $\beta=50^\circ$, $\beta=70^\circ$ and $\beta=90^\circ$ at various levels of fault offset magnitude

The effect of angle β on the pipe response is clearly demonstrated through the comparison of developing axial forces and bending moments of CP and PFJ. The distributions of axial force of CP and PFJ for various crossing angles β and levels of fault offset Δ/D are presented in Figure 6-15 and Figure 6-16 with respect to the distance from fault. Summarizing the results, the maximum developing axial force (N_{max}) with respect to the normalized fault offset (Δ/D) is depicted in Figure 6-17 for the considered crossing angles β . The major outcome is that axial force and consequently N_{max} is analogous to fault offset. Additionally, as angle β increases to $\beta=90^\circ$, more tension is developed in PFJ than in CP.

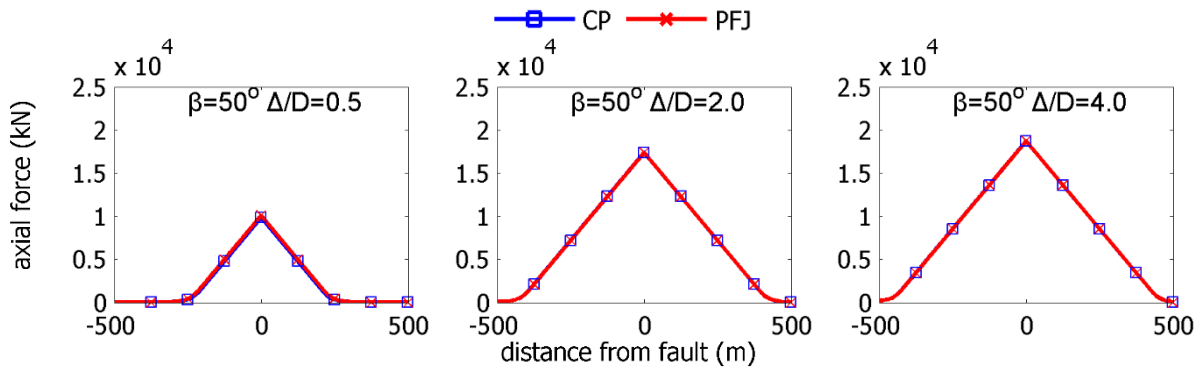


Figure 6-15: Distributions of axial force on CP and PFJ pipelines with respect to fault offset (Δ/D) for $\beta=50^\circ$

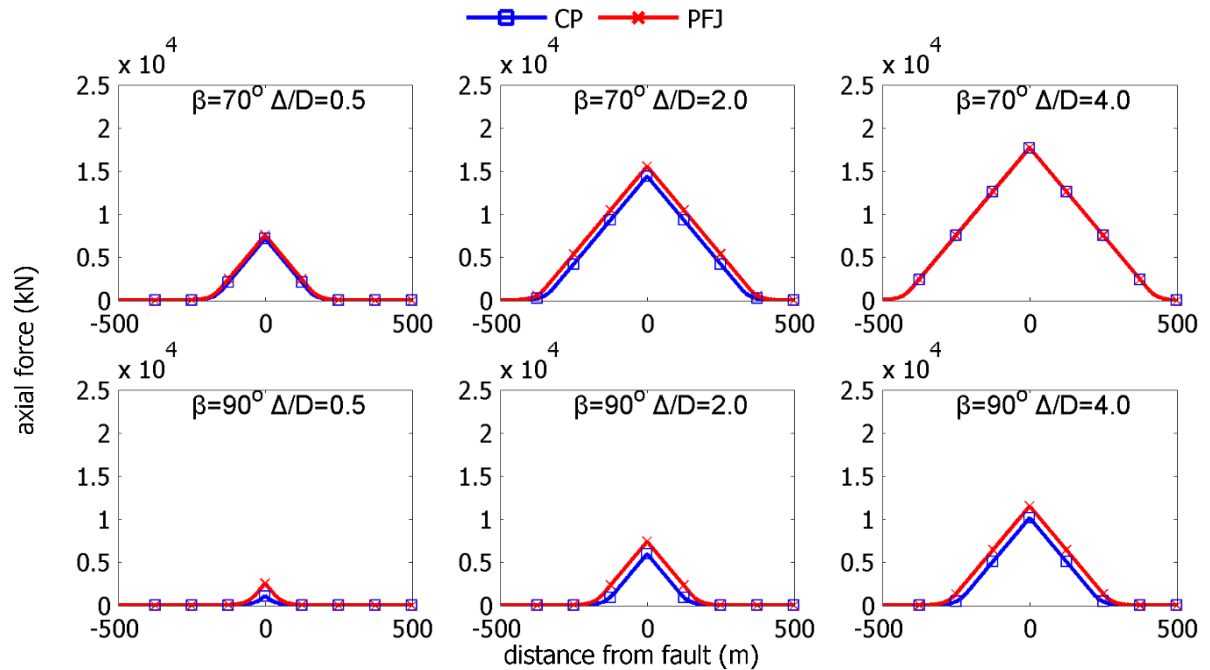


Figure 6-16: Distributions of axial force on CP and PFJ pipelines with respect to fault offset (Δ/D) for $\beta=70^\circ$ and $\beta=90^\circ$

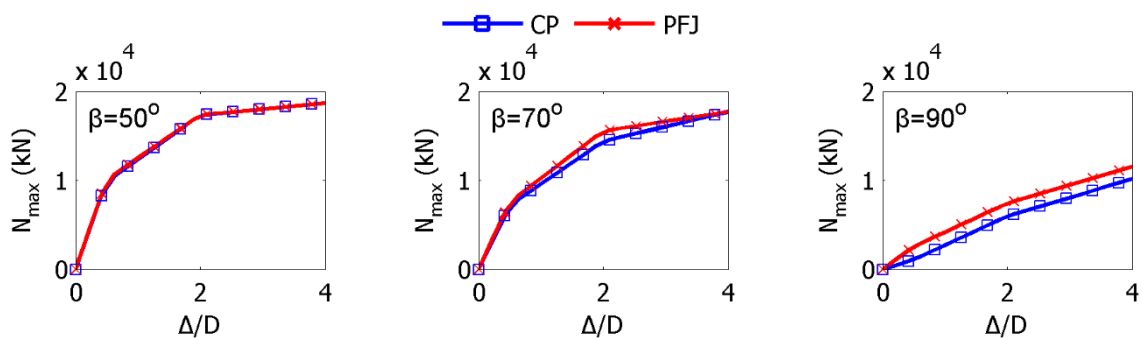


Figure 6-17: Maximum axial force (N_{max}) of CP and PFJ with respect to fault offset (Δ/D) for $\beta=50^\circ$, $\beta=70^\circ$ and $\beta=90^\circ$

The integrated flexible joints act in practice as internal hinges and therefore it is of importance to identify the development of bending moment with respect to varying crossing angle β and different levels of fault offset. For that purpose, the bending moment evolution is presented in Figure 6-18 and then the maximum developing bending moment (M_{max}) with respect to the fault offset (Δ/D) is extracted and illustrated in Figure 6-19. It is noted for comparison reasons to the developing bending moment that the plastic moment of the pipe cross-section is 4620kNm.

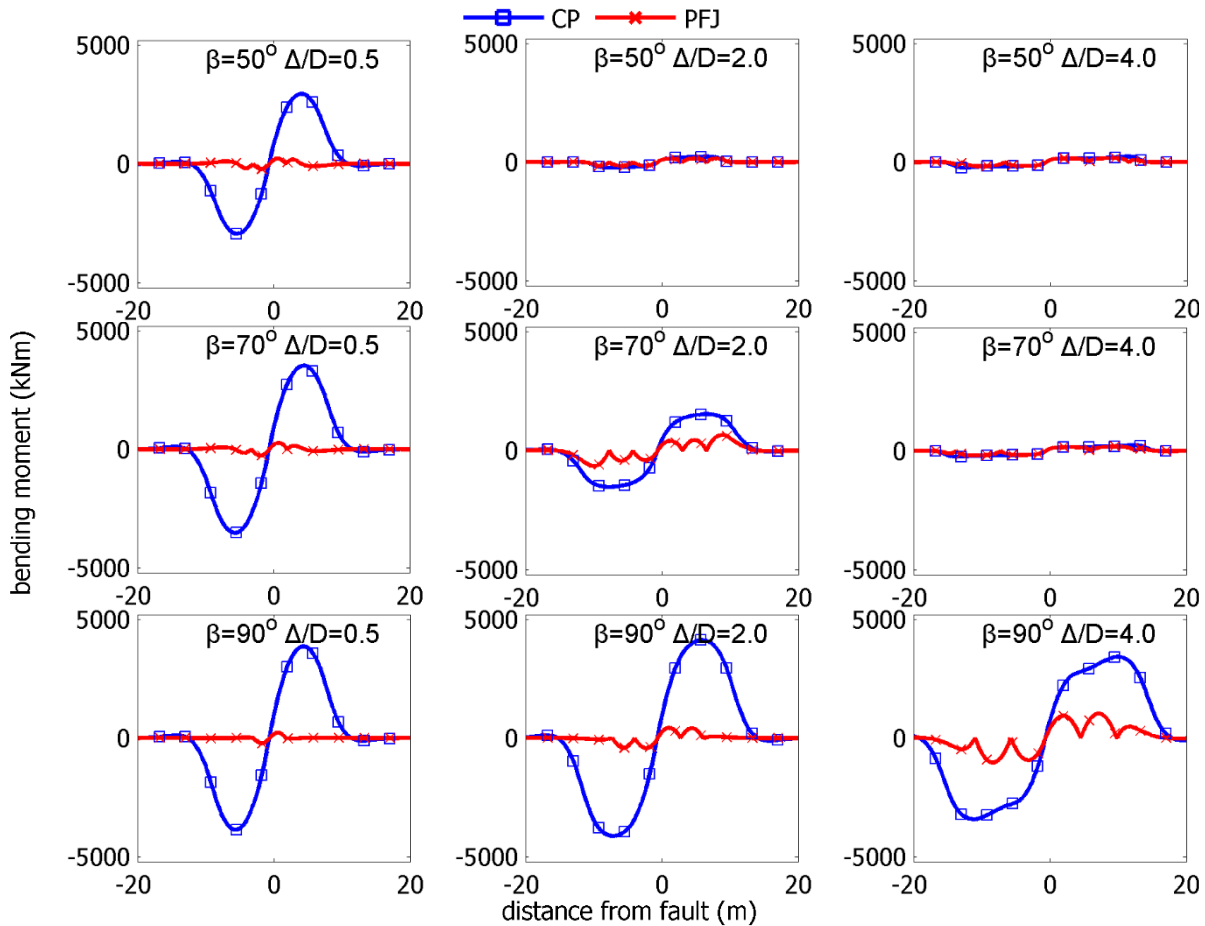


Figure 6-18: Distributions of bending moment on CP and PFJ pipelines with respect to fault offset (Δ/D) for $\beta=50^\circ$, $\beta=70^\circ$ and $\beta=90^\circ$

The efficiency of the integrated hinged joints increases as angle β increases and the pipeline crosses the fault trace close to perpendicularly. Another aspect is that the increasing fault offset and the decreasing angle β lead to the decrease of the difference between the M_{max} of the CP and the PFJ. In general, increasing of fault offset leads to decreasing bending moment, especially for $\beta < 90^\circ$, due to the increasing axial force. The latter is verified through the comparison of maximum axial force (Figure 6-17) and maximum bending moment (Figure 6-19) for increasing fault offset.

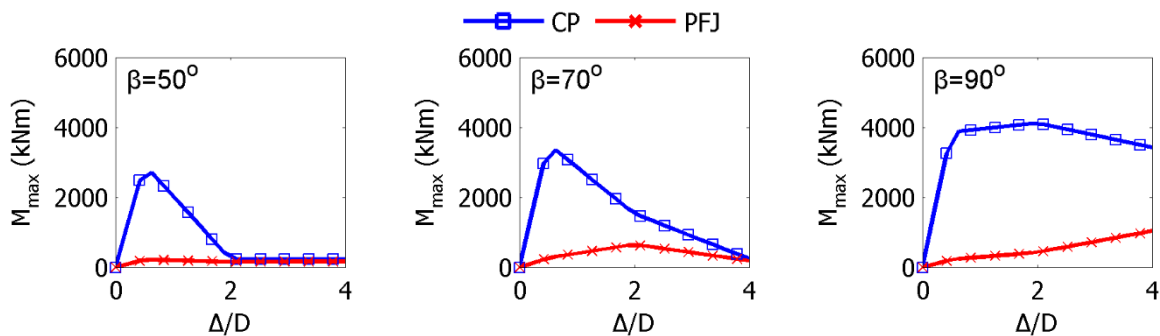


Figure 6-19: Maximum bending moment (M_{max}) of CP and PFJ with respect to fault offset (Δ/D) for $\beta=50^\circ$, $\beta=70^\circ$ and $\beta=90^\circ$

To identify the effects of flexible joints in developing strains, the corresponding distributions along the pipeline are presented in Figure 6-20 for tensile strains, considering various fault offset levels and crossing angles $\beta=50^\circ$, $\beta=70^\circ$ and $\beta=90^\circ$. The tensile strain limit of 2% is also presented with a dashed

line. Then, results are summarized in Figure 6-21, where the maximum developing longitudinal tensile strain ($\epsilon_{t,max}$) of CP and PFJ with respect to the fault offset (Δ/D) is shown.

The major finding is that the development of tensile strains is directly dependent on the crossing angle β . Thus, the decrease of β increases the importance of tension and thereby in case of $\beta=50^\circ$, joints do not provide strain reduction. It is noted that for $\beta=50^\circ$ within a range of fault displacement ($0.5 \leq \Delta/D \leq 2$), the rate of strain increase (for both CP and PFJ) is very low due to the transition from dominant flexural to axial pipe behavior, i.e. the bending strains decrease and the axial strains increase with their summation being more or less constant. In the intermediate case of $\beta=70^\circ$, joints sufficiently prevent tensile fracture by “keeping” strains below the code-based limit, up to $\Delta/D \approx 3$. For larger imposed displacements the pipe stretching dominates and the entailing tension cancels the joint’s efficiency in strain reduction. The maximum tensile strain decrease is achieved for $\beta=90^\circ$, which is in general the most desirable case for a safe and economically efficient design of a pipeline – fault crossing.

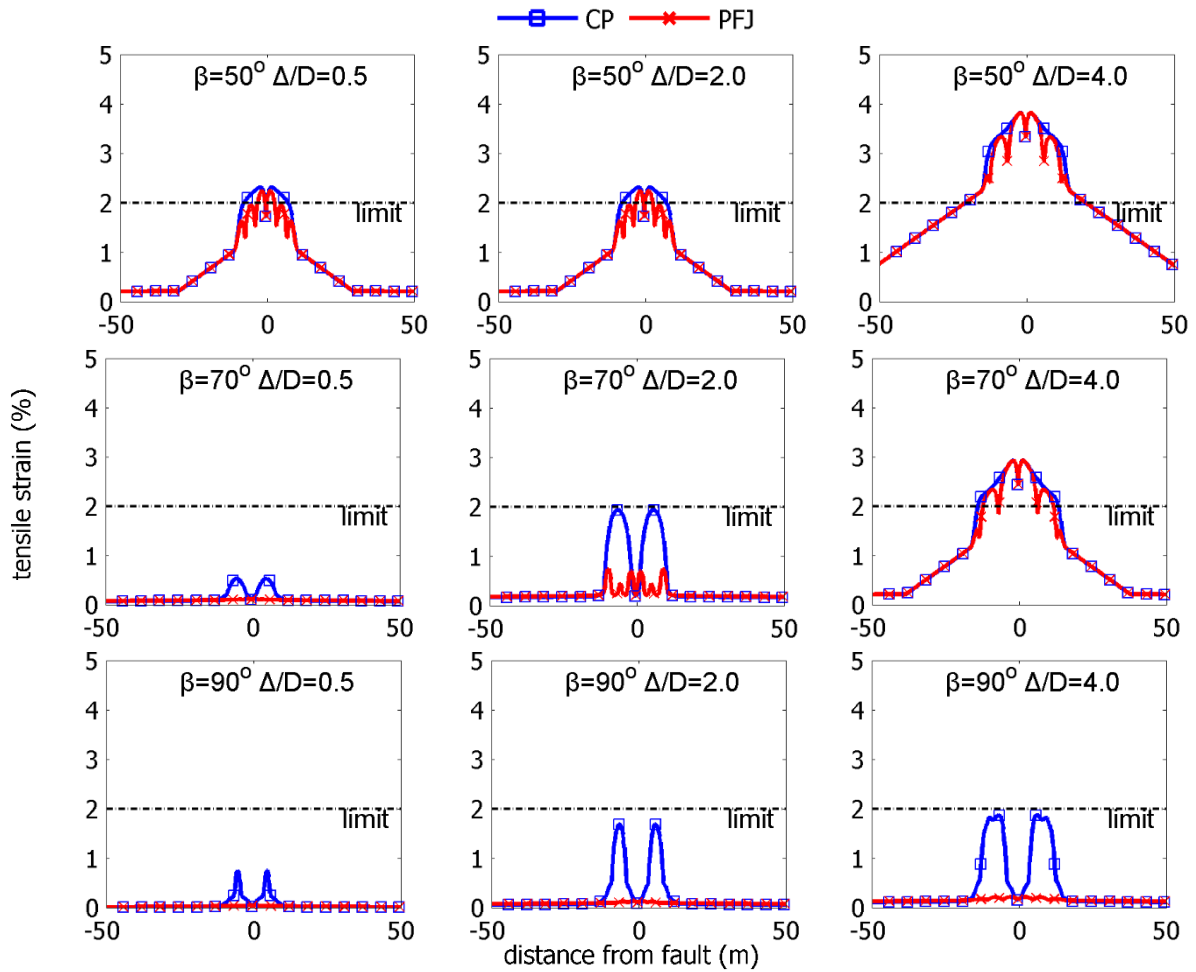


Figure 6-20: Distributions of longitudinal tensile strains on CP and PFJ pipelines with respect to fault offset (Δ/D) for $\beta=50^\circ$, $\beta=70^\circ$ and $\beta=90^\circ$

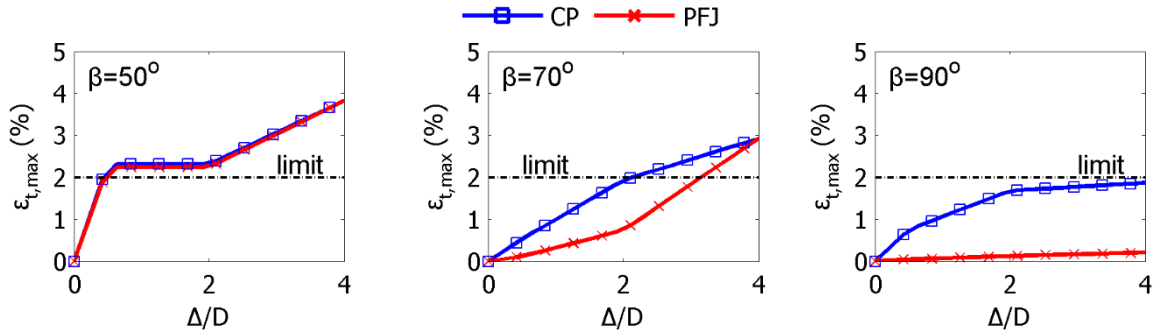


Figure 6-21: Maximum longitudinal tensile strain ($\epsilon_{t,max}$) of CP and PFJ with respect to fault offset (Δ/D) for $\beta=50^\circ$, $\beta=70^\circ$ and $\beta=90^\circ$

The procedure carried out previously to investigate the effect of flexible joints in tensile strains, is presented subsequently for the compressive strains. The distributions of compressive strains along the pipeline are presented in Figure 6-22, considering various fault offset levels and crossing angles. A major finding is that the compressive strains obtained from the integration points of the beam finite elements are very low for small crossing angles β and high fault offset. This is attributed to the fact that tension dominates the pipe behavior and consequently compression due to bending is drastically decreased.

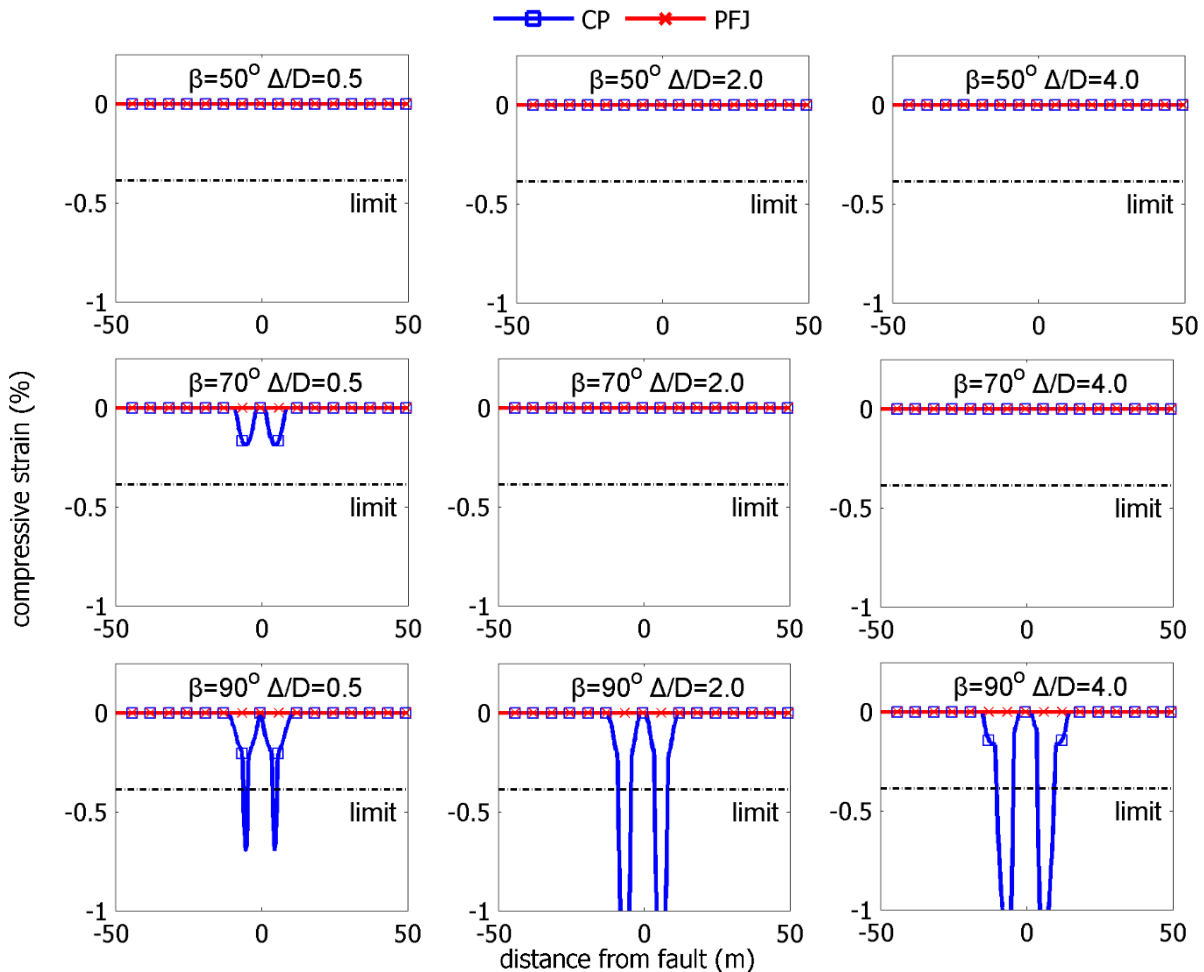


Figure 6-22: Distributions of longitudinal compressive strains on CP and PFJ pipelines with respect to fault offset (Δ/D) for $\beta=50^\circ$, $\beta=70^\circ$ and $\beta=90^\circ$

Summarizing the results in terms of the maximum developing compressive strain ($\epsilon_{c,max}$) from each case, the corresponding curves with reference to the fault offset and the crossing angle are presented in

Figure 6-23 for CP and PFJ. Results reveal that pipelines with flexible joints develop very low, almost negligible, compressive strains, hence the potential of local buckling is avoided in all cases. It has to be pointed out, though, that for low crossing angles β there is no risk of local buckling for the continuous pipeline due to the prevailing tensile behavior.

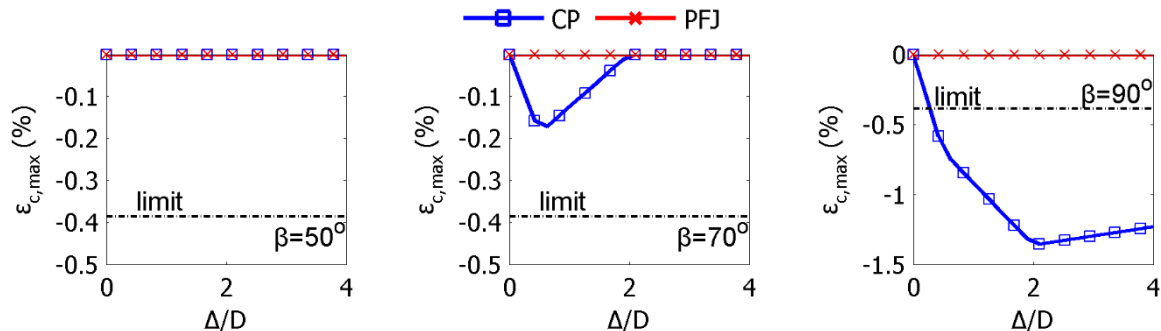


Figure 6-23: Maximum longitudinal compressive strain ($\epsilon_{c,max}$) of CP and PFJ with respect to fault offset (Δ/D) for $\beta=50^\circ$, $\beta=70^\circ$ and $\beta=90^\circ$

The numerical evaluation of pipelines with flexible joints crossing a strike-slip fault with angle β equal or lower to 90° indicates that the introduction of joints is in most cases a very effective countermeasure that can notably protect a buried steel pipeline against the consequences of faulting. The joints performance is directly related to the pipe – fault crossing angle. The strain reduction is maximized when the pipeline crosses the fault plane close to $\beta=90^\circ$. For $\beta<70^\circ$ in combination with higher fault displacements, joints' contribution to pipe protection through strain reduction is limited. In such cases, the use of joints that are capable of undergoing some axial displacement, in addition to rotation, would be more beneficial.

6.4.2 Pipeline under bending and compression

While in case of tension pipe integrity can rely on the steel's post-yielding strength, in case of compression local buckling can lead to pipe failure at much lower absolute strain levels. Pertinent standards and provisions (e.g. Eurocode 8 – Part 4 (European Committee for Standardization 2006)), as well as engineering practice, suggest to avoid crossing angle $\beta>90^\circ$, which would result in the development of bending and compression along the pipe. Crossing angles $\beta>90^\circ$ might, however, be unavoidable due to limitations encountered in the route selection procedure, or it might occur unintentionally, due to insufficient data regarding the fault behavior. The repercussions of such values of angle β on the pipeline response are again investigated through the numerical evaluation of a continuous pipeline (CP) and a pipeline with four flexible joints (PFJ). The pipes are assumed to intercept the fault plane with angles $\beta=100^\circ$, $\beta=110^\circ$ and $\beta=120^\circ$, selected in light that $\beta>90^\circ$ is an undesirable design approach and thus higher values would be unrealistic in common design practice. The maximum normalized fault offset is assumed equal to $\Delta/D=2$.

Indicative results regarding the CP and PFJ displacements for all crossing angles are illustrated in Figure 6-24, where the distance from the fault trace is presented on the horizontal axis and the normalized pipe transverse displacement with respect to pipe diameter D on the vertical axis. The comparison of pipe displacements between cases of $\beta<90^\circ$ and $\beta>90^\circ$ reveals that compression magnifies the difference between CP and PFJ displacements due to pipe shortening and intense joint rotation. The larger PFJ displacements compared to CP are the cause of the effectiveness of joints in all cases of $\beta>90^\circ$, as will be shown later. The maximum joint rotation reported in the results equals 39.9° . It is therefore necessary to pay special attention to the angular capacity of the joint in terms of providing sufficient rotational capacity. It is also important to point out that even though the integration of flexible joints leads to pipe protection, the PFJ is severely deformed in terms that the pipe has suffered global

instability. In such case, also, special design considerations are necessary regarding the trench dimensions.

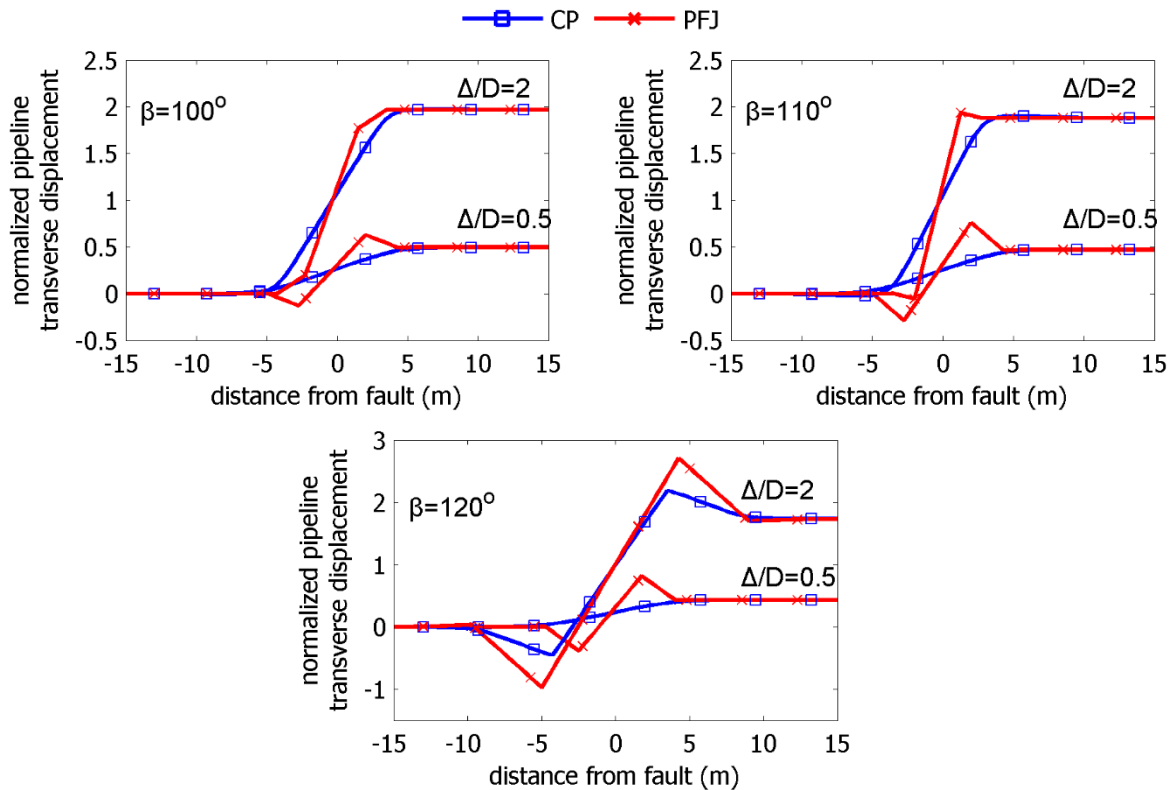


Figure 6-24: CP and PFJ displacements for crossing angles $\beta=100^\circ$, $\beta=110^\circ$, $\beta=120^\circ$ and at various levels of fault offset magnitude

The introduction of flexible joints leads in general to a significant decrease of the pipe stress-state in terms of developing axial forces, bending moments and longitudinal strains for the crossing angles $\beta=100^\circ$, $\beta=110^\circ$ and $\beta=120^\circ$ under consideration. Specifically, the distributions of axial force are presented in Figure 6-25. In case of $\beta=100^\circ$ and $\Delta/D=2$, tension is reported for PFJ due to the evolution of the pipe deformation, while for $\beta=110^\circ$ and $\beta=120^\circ$ the PFJ is subjected to compression. To identify this outcome, the maximum axial force developed on PFJ with respect to fault offset is presented in Figure 6-26 for various crossing angles β . It is observed that for low crossing angles the pipe exhibits compression for low fault offset and then, as fault offset increases the pipe exhibits tension. This statement can be verified by the evolution of pipe deformation with respect to fault offset. To that effect, PFJ displacements for crossing angle $\beta=100^\circ$ at various levels of fault offset are illustrated in Figure 6-27a. It is observed that for low fault offset, flexible joints exhibit significant rotation, leading to compression of the pipeline segment between the joints close to the fault trace. Consequently, the increase of fault offset leads to decrease of joints' rotation and particularly joints at distance L_j rotate in the opposite direction. Thus, the pipe segment that is intercepted by the fault is subjected to tension, rather than compression. This deformation pattern is attributed to the crossing angle, namely for angles lower than 110° the compression imposed by the fault movement is smaller than for larger angles. For comparison, PFJ displacements for crossing angle $\beta=110^\circ$ at various levels of fault offset are illustrated in Figure 6-27b.

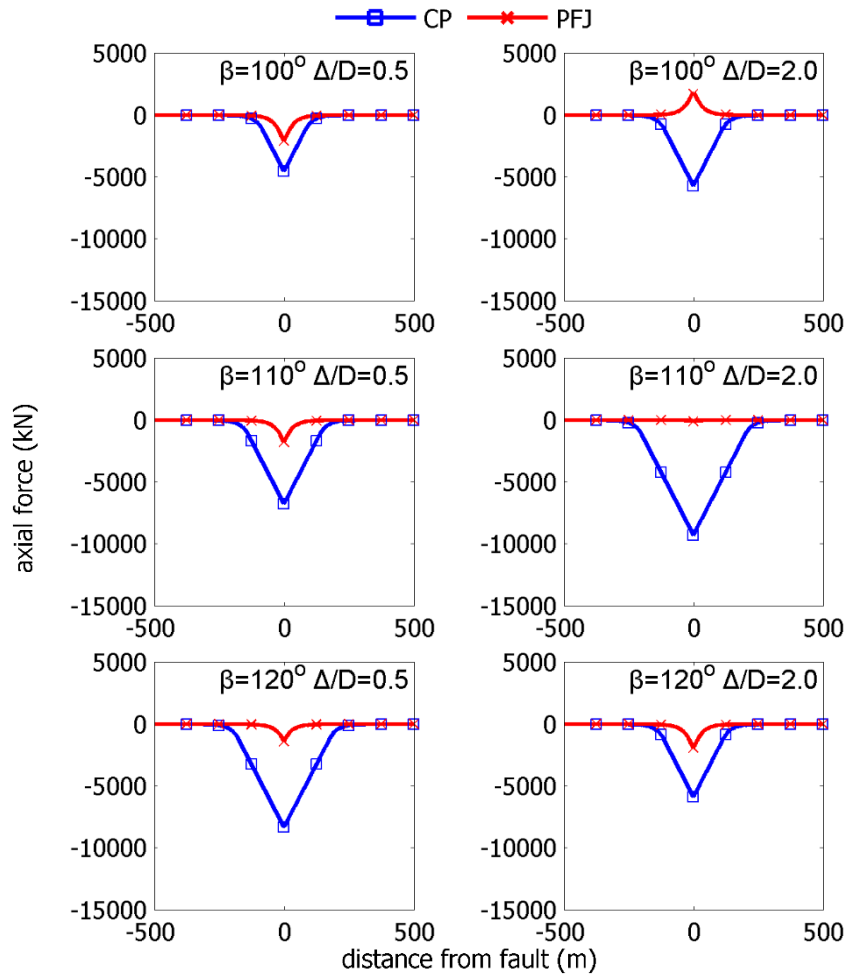


Figure 6-25: Distributions of axial force on CP and PFJ pipelines with respect to fault offset (Δ/D) for $\beta=100^\circ$, $\beta=110^\circ$ and $\beta=120^\circ$

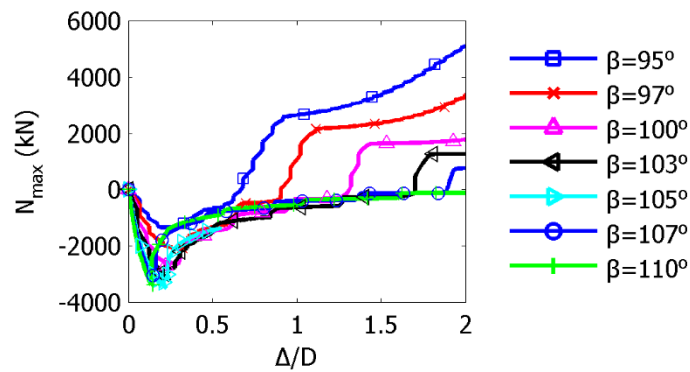


Figure 6-26: Maximum axial force (N_{max}) of PFJ with respect to fault offset (Δ/D) for various crossing angles

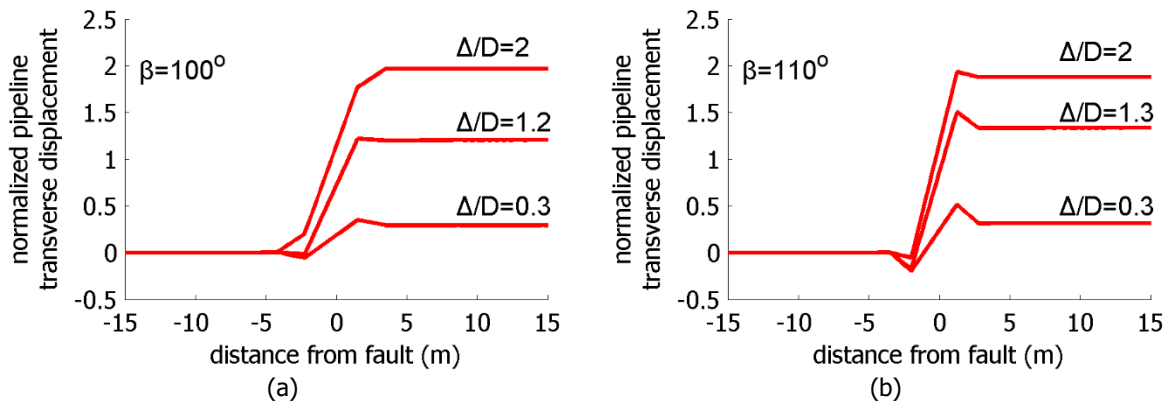


Figure 6-27: PFJ displacements for $\beta=100^\circ$ and $\beta=110^\circ$ at various levels of fault offset magnitude

The obtained maximum developing compressive force (N_{max}) is depicted in Figure 6-28 with respect to angle β and fault offset magnitude. Axial compressive forces of PFJ are much lower than CP due to the pipe deformation. The increase of fault offset magnitude leads to axial force increase up to approximately $\Delta/D=0.5$ and then axial force gradually decreases. This is attributed to the fact that for small fault offset, PFJ behavior is predominantly axial due to the imposed compression, but for larger fault offset there is significant deformation of the pipeline due to high rotation of the joints and consequently axial force decreases.

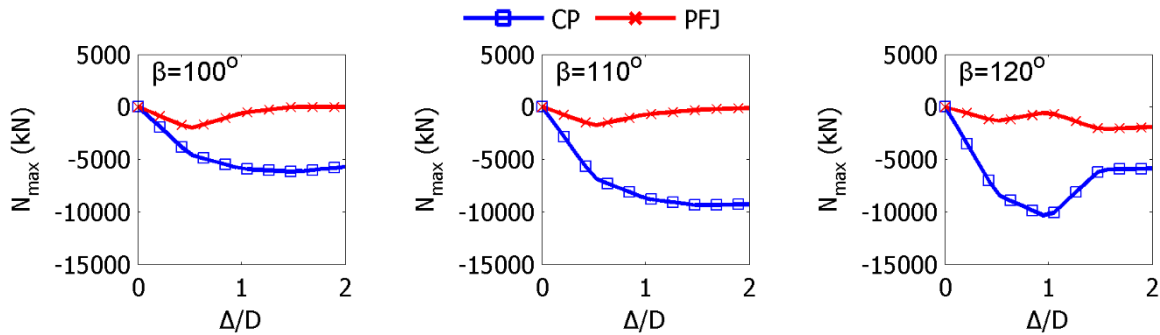


Figure 6-28: Maximum axial force (N_{max}) of CP and PFJ with respect to fault offset (Δ/D) for $\beta=100^\circ$, $\beta=110^\circ$ and $\beta=120^\circ$

The distributions of bending moment on CP and PFJ are presented in Figure 6-29 with respect to crossing angle and fault offset (Δ/D). The obtained maximum developing bending moments (M_{max}) are shown in Figure 6-30, illustrating that bending moments of PFJ are several times lower than those of CP. Regarding the case of $\beta=120^\circ$ and $\Delta/D=2$ the bending moment distribution for CP indicates several locations of steel yielding that act as plastic hinges, thus as virtual “flexible joints”.

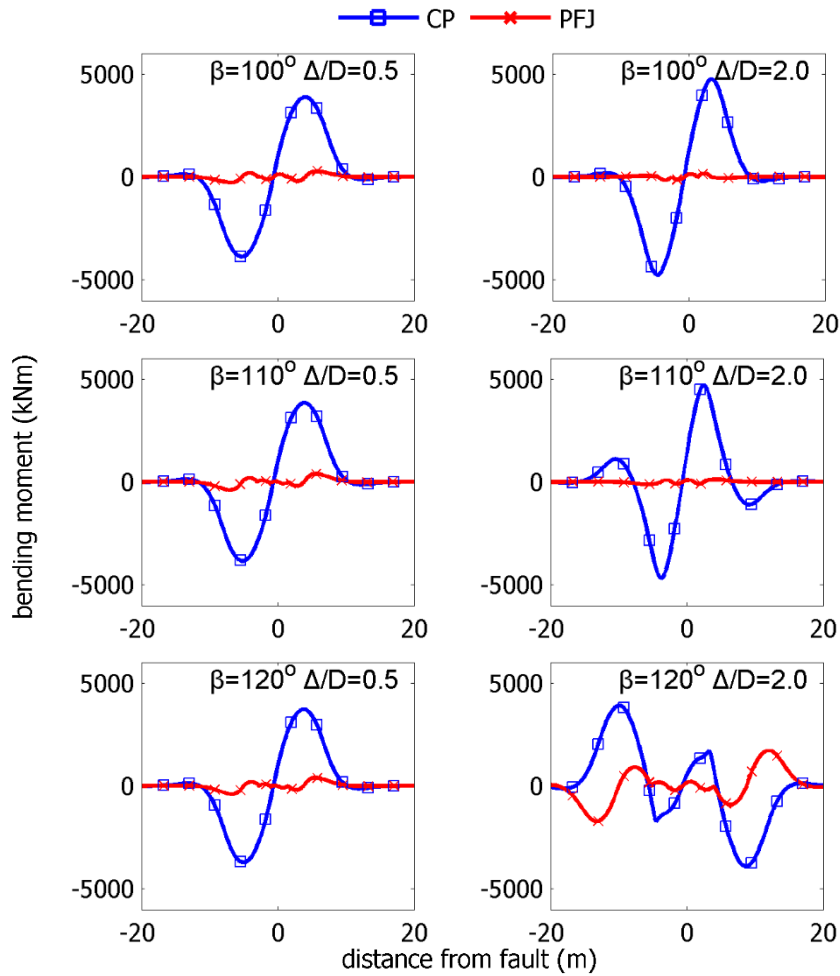


Figure 6-29: Distributions of bending moment on CP and PFJ pipelines with respect to fault offset (Δ/D) for $\beta=100^\circ$, $\beta=110^\circ$ and $\beta=120^\circ$

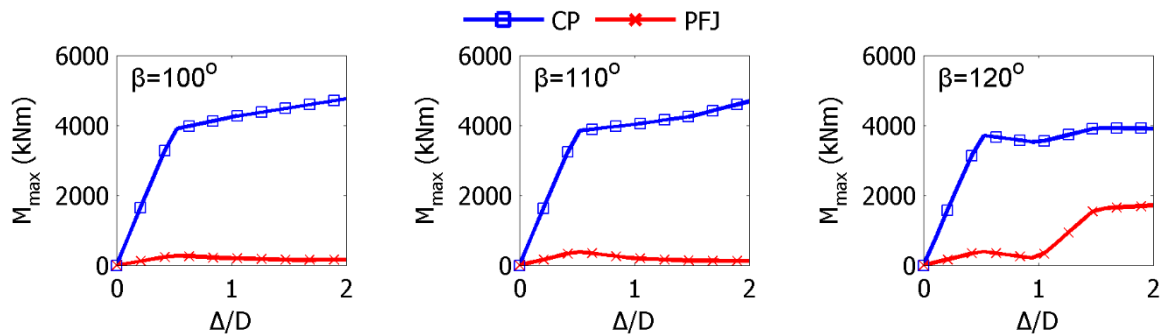


Figure 6-30: Maximum bending moment (M_{max}) of CP and PFJ with respect to fault offset (Δ/D) for $\beta=100^\circ$, $\beta=110^\circ$ and $\beta=120^\circ$

In order to evaluate pipeline safety, the distributions of tensile and compressive longitudinal strains along CP and PFJ pipes are presented in Figure 6-31 and Figure 6-33, respectively, considering various levels of fault offset and different crossing angles. The summary of these results in terms of the maximum tensile strains ($\epsilon_{t,max}$) and compressive strains ($\epsilon_{c,max}$) of CP and PFJ with respect to fault offset (Δ/D) are shown in Figure 6-32 and Figure 6-34, respectively, along with code-based strain limits. The evaluation of results reveals that tensile strains increase as the fault offset increases, but in general they decrease as the crossing angle increases due to the higher compression. In either case, tensile strains of PFJ are almost negligible, thus ensuring the integrity of girth welds. Regarding, then, the

compressive strains, one can notice (Figure 6-33) that the CP is going to suffer severe damage, mainly due to local buckling, even for relatively small fault offset ($\Delta/D < 0.5$).

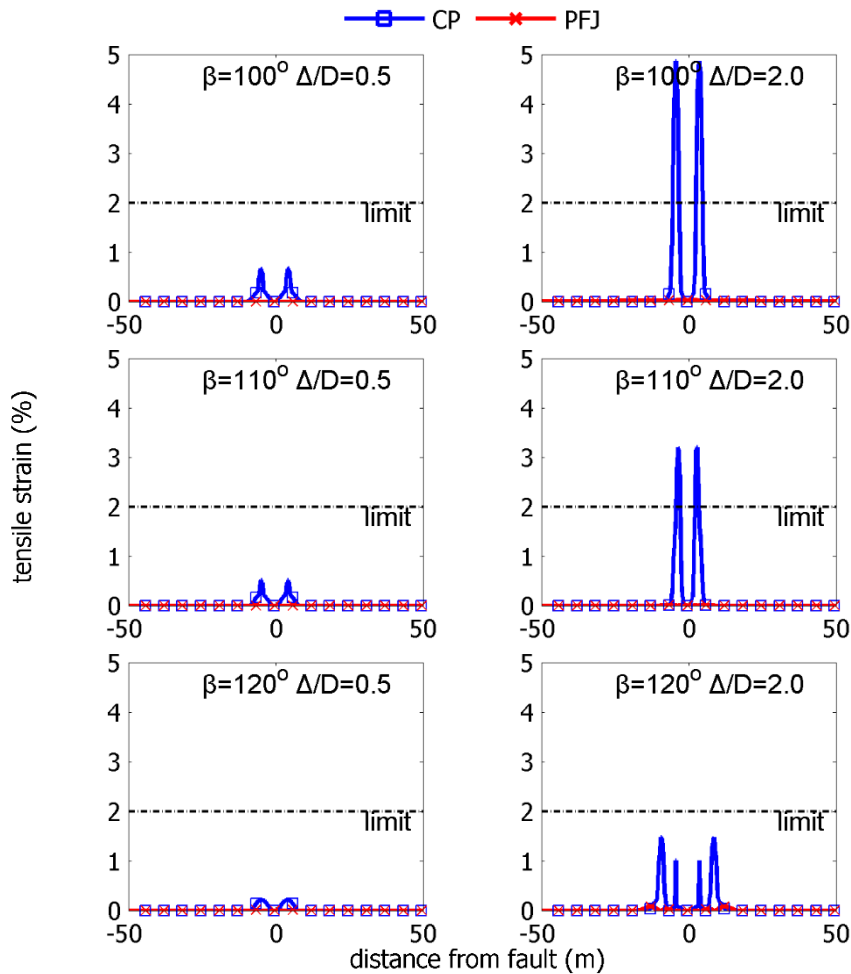


Figure 6-31: Distributions of longitudinal tensile strains on CP and PFJ pipelines with respect to fault offset (Δ/D) for $\beta = 100^\circ, \beta = 110^\circ$ and $\beta = 120^\circ$

Summarizing the results regarding compressive strains in Figure 6-34 through curves of the maximum developing compressive strains with respect to the fault offset magnitude for various crossing angles β , it follows that compressive strains of CP for $\Delta/D > 0.5$ are too high in practice to be fairly compared with the corresponding ones of PFJ in the same chart for $0 \leq \Delta/D \leq 2$. It then follows that flexible joints in buried pipelines with $\beta > 90^\circ$ can very efficiently protect the pipe against local buckling in all cases under consideration.

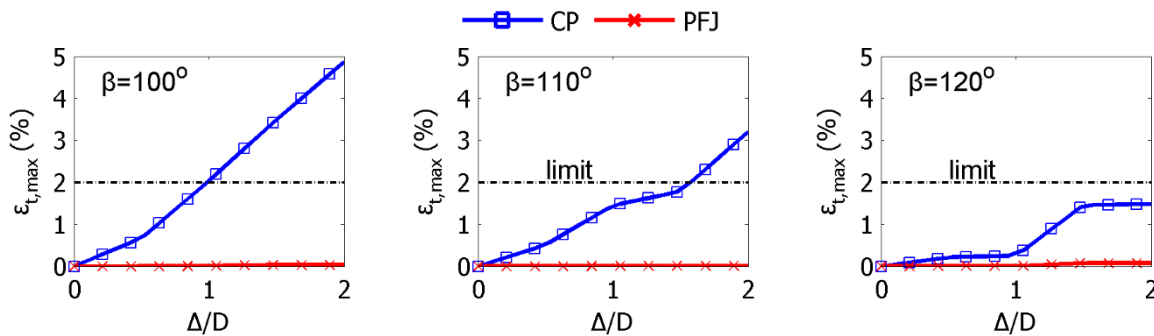


Figure 6-32: Maximum longitudinal tensile strain ($\epsilon_{t,max}$) of CP and PFJ with respect to fault offset (Δ/D) for $\beta = 100^\circ, \beta = 110^\circ$ and $\beta = 120^\circ$

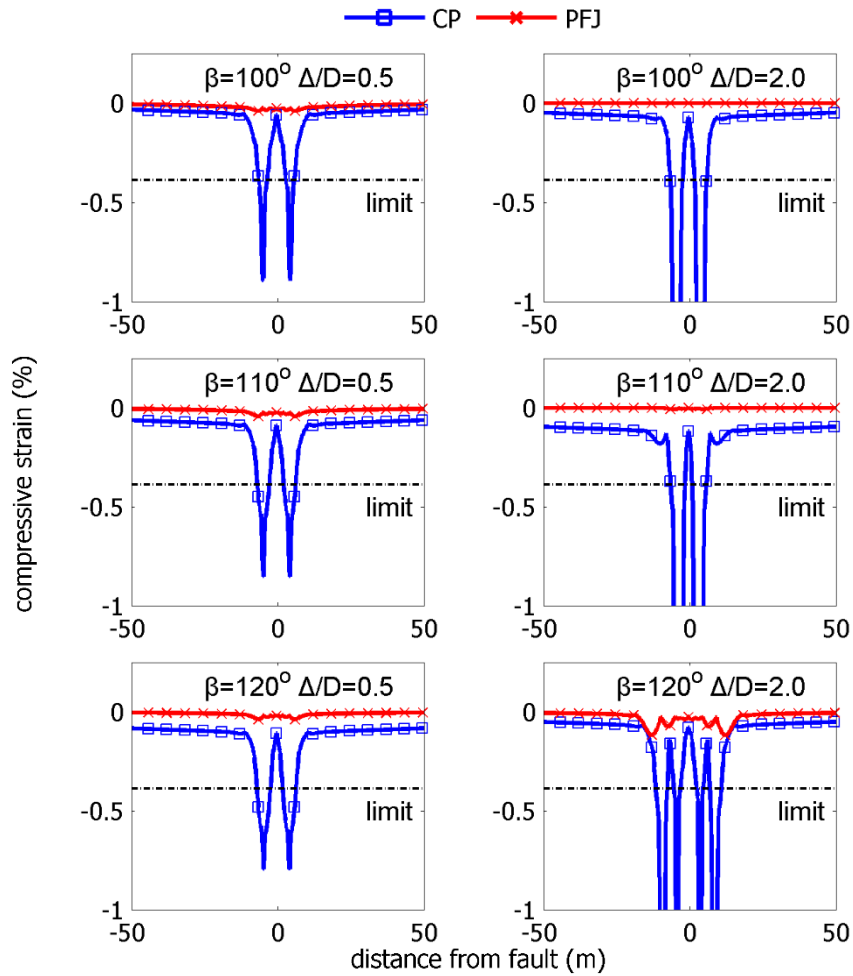


Figure 6-33: Distributions of longitudinal compressive strains on CP and PFJ pipelines with respect to fault offset (Δ/D) for $\beta=100^\circ$, $\beta=110^\circ$ and $\beta=120^\circ$

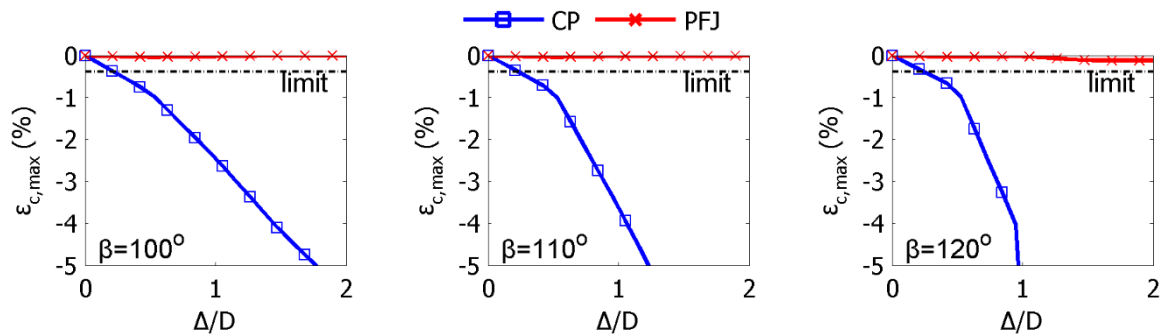


Figure 6-34: Maximum longitudinal compressive strain ($\epsilon_{c,max}$) of CP and PFJ with respect to fault offset (Δ/D) for $\beta=100^\circ$, $\beta=110^\circ$ and $\beta=120^\circ$

6.5 EFFECT OF D/t RATIO

The geometry of the pipeline cross-section is defined through the process analysis of the pipeline system and in particular pipe diameter (D) and wall thickness (t) are related to operating flow capacity, temperature, pressure, etc. The diameter over thickness ratio (D/t) plays a dominant role in the pipeline response and especially on the buckling behavior, as it defines the local pipe slenderness. Shallowly buried pipelines with low D/t under compression may buckle upwards as a beam, while deeper buried pipes with higher D/t tend to buckle locally (Yun and Kyriakides 1990). The D/t ratio is therefore a

significant parameter, whose effect on pipelines with flexible joints is hereafter examined by considering CP and PFJ crossing a strike-slip fault with angle $\beta=70^\circ$ and subjected to $\Delta/D=1$ of fault movement. Pipe diameter is considered to be constant $D=914\text{mm}$, while three cases of commercial thickness values are considered, namely $t=7.92\text{mm}$, $t=12.70\text{mm}$ and $t=19.05\text{mm}$. The corresponding ratios are then $D/t=115.40$, $D/t=71.97$ and $D/t=47.98$.

The tensile and compressive strain distributions for all cases are illustrated in Figure 6-35. The first important observation for CP is that higher D/t ratios increase the structure's slenderness and consequently higher strains are developed due to reduced stiffness. The integration of flexible joints between the adjacent pipe parts transforms the structural system from continuous to segmented and the effect of ratio D/t is almost eliminated. The latter is verified by the strain distributions of PFJs that indicate almost no interaction between the ratio D/t and flexible joints effectiveness in terms of reducing strains.

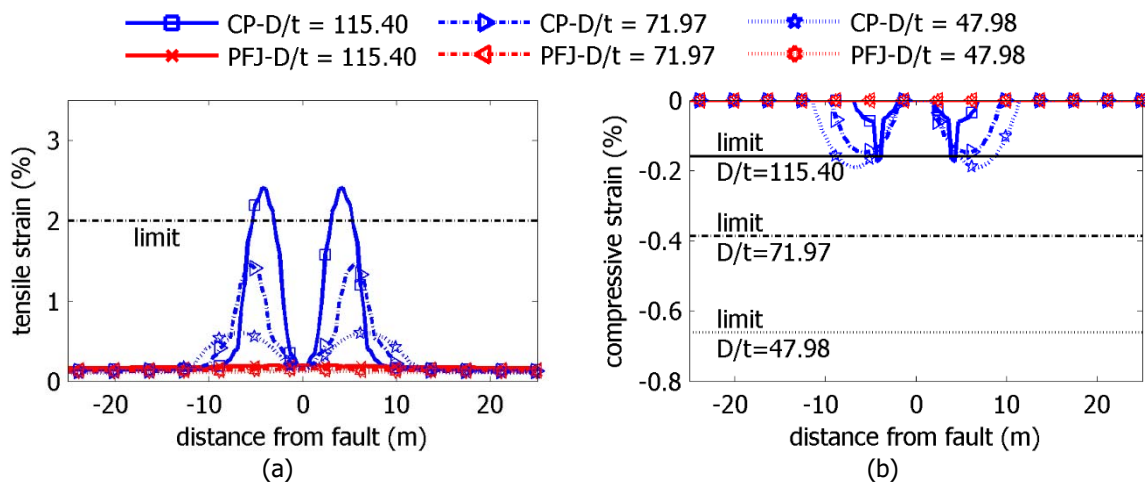


Figure 6-35: (a) Tensile and (b) compressive strains distributions of CP and PFJ for various D/t ratios

6.6 EFFECT OF BURIAL DEPTH

Oil and gas pipelines are usually embedded in a trench for protection against corrosion and third party damage. Soil response to any pipe movement in the trench is related to the pipe burial depth that defines the level of soil pressure acting on the pipe. In numerical modeling, increase of burial depth leads to stiffer soil springs and consequently pipeline movement in the trench becomes more difficult, thus the developing pipe stress-state is higher. It is therefore meaningful to investigate the effect of burial depth on the strain reduction efficiency of flexible joints. Engineering and constructional practice suggest that the burial depth equals about one to two times the pipe diameter in fault crossings. The pipeline under investigation is considered to intercept a strike-slip fault with crossing angle $\beta=70^\circ$ and subjected to $\Delta/D=1$ of fault offset, representing a typical case. Three cases of burial depths for the continuous pipeline (CP) and the corresponding pipeline with flexible joints (PFJ) are considered, namely $H/D=1$, $H/D=1.5$ and $H/D=2$, where H is the soil height above the top of the pipe.

Pipeline response is examined through the longitudinal tensile and compressive strain distributions (Figure 6-36). The increase of burial depth leads to strain increase for the continuous pipeline, as expected due to stiffer soil springs, and threatens its integrity in terms of exceeding code-based tensile strain limit. On the contrary, nearly negligible differences are reported for PFJ cases regarding the strain reduction on the steel pipe parts due to the integration of flexible joints. The effect of burial depth on joints efficiency can be thus described as negligible.

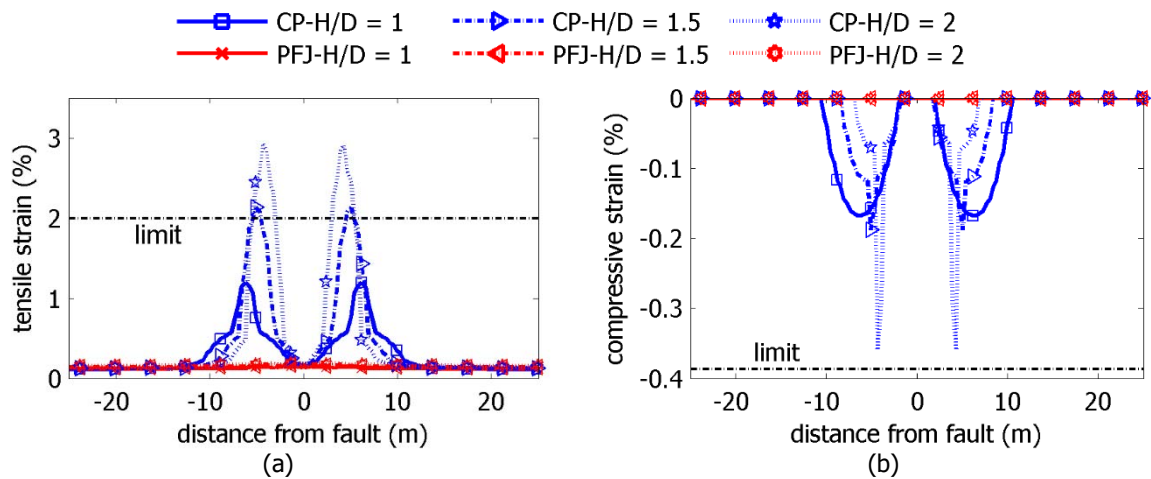


Figure 6-36: (a) Tensile and (b) compressive strain distributions of CP and PFJ for various burial depths (H/D)

6.7 UNCERTAINTY REGARDING FAULT TRACE

6.7.1 Origins of fault trace uncertainty

The analysis of buried pipeline – fault crossing is usually based on the assumption of a planar fault, intercepting the pipeline at a specific location. The optimum configuration of flexible joints has been defined in section 6.3.1 and implemented in the parametric studies of sections 6.4 through 6.6 based on the assumption that the fault trace location is known a priori, i.e. the fault will appear on the ground where it is expected. This assumption, however, may be violated in nature by the native soil conditions. Soil stratigraphy may affect the direction of rupture propagation to the surface. In case the native soil conditions are rocky, the rupture propagation from the underlying bedrock to the ground surface may not be disturbed and thus the planar fault assumption is sufficiently accurate. Nevertheless, the upper soil layers are usually earth fill with inhomogeneous properties (e.g. alluvial deposits) that can alter the rupture propagation to the surface. This can result to a shift of the fault trace from where it is expected to appear on the ground surface. An example of this effect is presented in Figure 6-37 from the Gulf of Mexico, where the geometry of the fault planes indicates a change in facies (sand/shales) of the stratigraphic intervals.

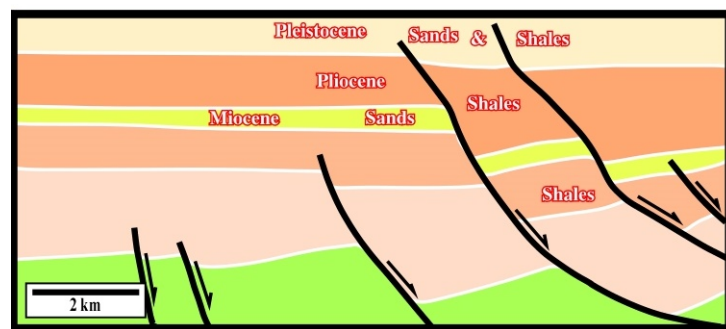


Figure 6-37: Schematic illustration of fault rupture propagation being affected by the soil stratigraphy (Plate tectonic & northern Pacific 2016)

The fault trace uncertainty is usually not considered in the analysis of a pipeline subjected to fault rupture, especially within research studies. In practice, design engineers deal with the fault trace uncertainty by applying seismic countermeasures to protect the pipeline (section 2.5) along the length of fault trace uncertainty. It has to be noted that the latter is estimated by seismological, geological and geotechnical surveys of the fault crossing area and in practice can range from a few meters to a few hundred meters. Regarding, then, the application of flexible joints as mitigating measures accounting

for the potential fault trace uncertainty, two questions arise: (i) in case the fault trace “appears” on the ground surface at a different location from the expected one, what is the effect of a particular configuration of flexible joints on the pipeline behavior and (ii) considering a given pipeline length along which the fault trace may be encountered, accounting for uncertainty, what is the optimum configuration of flexible joints, assuming that joints shall be integrated in the pipeline at equal distances for practical and constructional reasons.

Therefore, the following section 6.7.2 aims at answering the first question considering that the fault trace will be encountered at a different location from the theoretical one, while section 6.7.3 aims at providing to design engineers practical guidelines regarding the optimum distance between flexible joints along the entire pipeline length over which the trace may appear. For that purpose, a pipeline with flexible joints (PFJ) is subjected to normalized strike-slip fault offset of magnitude $\Delta/D=2$ and the pipeline – fault crossing angle is assumed to be $\beta=70^\circ$. The continuous pipeline (CP) is also considered for reference.

6.7.2 Effects of different fault location

The pipeline with four flexible joints (PFJ) is considered. The joints are located at distances L_j and $L_j/2$ on each side of the assumed fault trace, following the procedure described in section 6.3.1. In order to quantify the effect on the behavior of PFJ of fault occurrence at a different location from the expected one, the fault trace is assumed at four different locations, apart from the assumed theoretical one that is located at $x=0$ (Figure 6-38). The potential trace locations are selected for simplicity at distances from $x=0$ that are related to distance L_j , as shown in Figure 6-38.

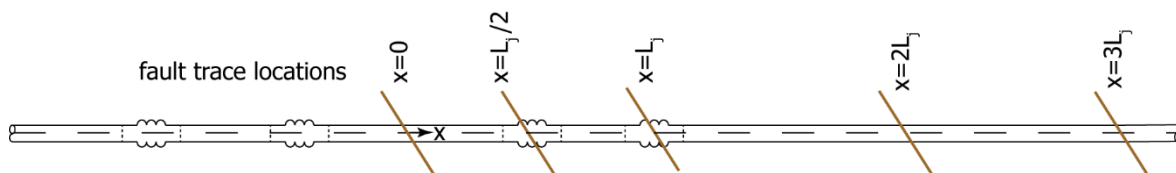


Figure 6-38: Assumed alternative fault trace locations along the pipeline

The resulting distributions of tensile strains along the pipeline are depicted in Figure 6-39, indicating that in case the fault trace is located at larger distance than L_j from its theoretical location, flexible joints neither provide strain reduction, nor cause any unexpected damage to the pipeline in terms of strains. The latter is of importance for design engineers, as the metallic hinged bellows, integrated in buried pipelines subjected to PGDs, do not have harmful effect on the pipe, in contrast to Dresser type expansion joints, as outlined in section 2.7.1. The main outcome from Figure 6-39 is that when alternative fault trace locations are considered, the pipeline mechanical behavior is similar to that of a continuous pipe, as the strain distributions are shifted along the pipeline. A minor exception is in case the fault is located at distance $L_j/2$ from its theoretical location, where only a minor strain reduction is observed.

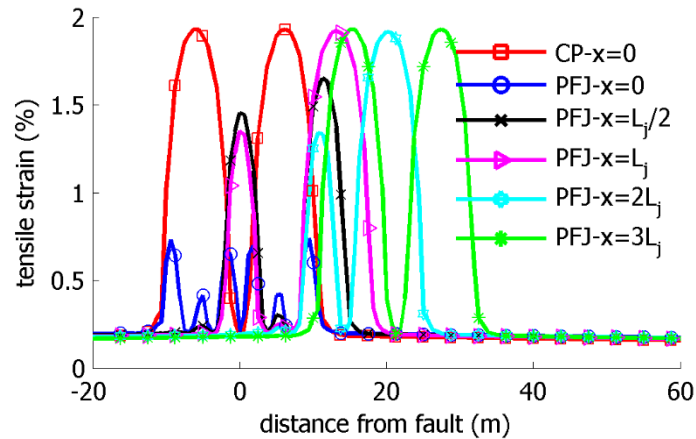


Figure 6-39: Tensile strain distributions for varying fault trace location and crossing angle $\beta=70^\circ$

6.7.3 Optimum distance between flexible joints

The uncertainty regarding the exact location of the fault trace is a common problem that engineers have to deal with during the design of a pipeline – fault crossing, due to reasons outlined in section 6.7.1. Thus, the primary consideration regarding the use of flexible joints as mitigating measures is the estimation of the optimum configuration with respect to efficiency and cost. In order to address this task, the following procedure is proposed:

- Estimation of the length over which the fault may “appear” on the ground surface.
- Analysis of a continuous pipeline subjected to the maximum fault offset, as defined by relevant geological and seismological studies of the area, by assuming the theoretical fault trace being located at the middle of the length of uncertainty.
- Plot of the bending moment distribution of the continuous pipeline and estimation of distance L_j (Figure 6-5), which is the distance between the assumed fault trace location and the maximum bending moment location.
- Integration of a flexible joint at the theoretical fault trace location and consequently at distances equal to L_f on each side of the fault trace, as schematically illustrated in Figure 6-40. Additionally, two joints are introduced outside the “borders” of uncertainty area, in order to address the worst case scenario of the fault being activated at the margins of the uncertainty area.
- Estimation of distance L_f , by considering alternative fault trace locations.

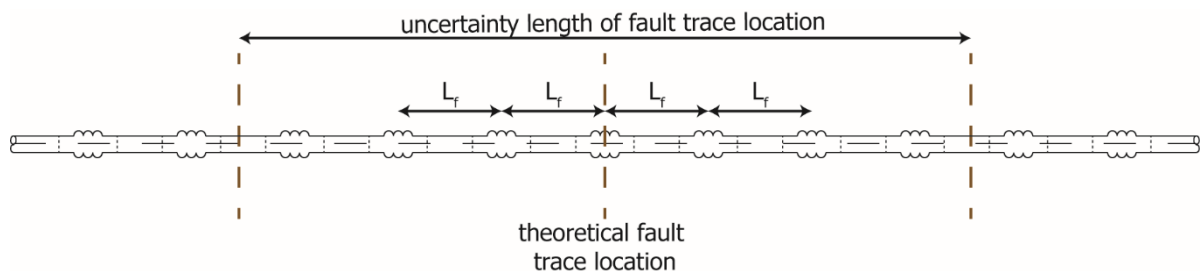


Figure 6-40: Configuration of equally-spaced flexible joints over the length of fault trace uncertainty

The primary consideration regarding the integration of flexible joints along the uncertainty length is the estimation of distance L_f . To that effect an illustrative example is presented and the corresponding indicative results are shown hereinafter. Initially, taking into account that the optimum configuration of joints for a given fault trace location is at distance $L_j/2$ between two joints and the fault trace (section 6.3.1), analyses are carried out consequently, assuming indicatively that $L_f=L_j/2$ or $L_f=L_j$. Alternative fault trace locations are examined, while two cases are considered being the worst-case scenario,

namely the fault trace being located between two subsequent joints or on a joint. The pipeline with flexible joints (PFJ) is subjected to strike-slip fault offset of magnitude $\Delta/D=2$ and the pipeline – fault crossing angle is assumed to be either $\beta=70^\circ$ and $\beta=90^\circ$. The continuous pipeline (CP) is also considered for reference.

The distributions of tensile strains along the pipeline are depicted in Figure 6-41 for both crossing angles considered. It is observed that regardless the fault trace location, the optimum configuration of flexible joints in terms of reducing the developing tensile strains is at distance $L_f=L_j/2$ for crossing angle $\beta=70^\circ$. On the contrary, for $\beta=90^\circ$ it is observed that both configurations, namely $L_f=L_j$ and $L_f=L_j/2$, are roughly equally efficient and thus for pipeline – fault crossing close or equal to perpendicularity it is suggested that joints are integrated at distance $L_f=L_j$ in order to minimize the cost. It is noted that if there is uncertainty regarding the pipe – fault crossing angle β , then joints should be integrated at distance $L_f=L_j/2$ in order to address the worst case scenario.

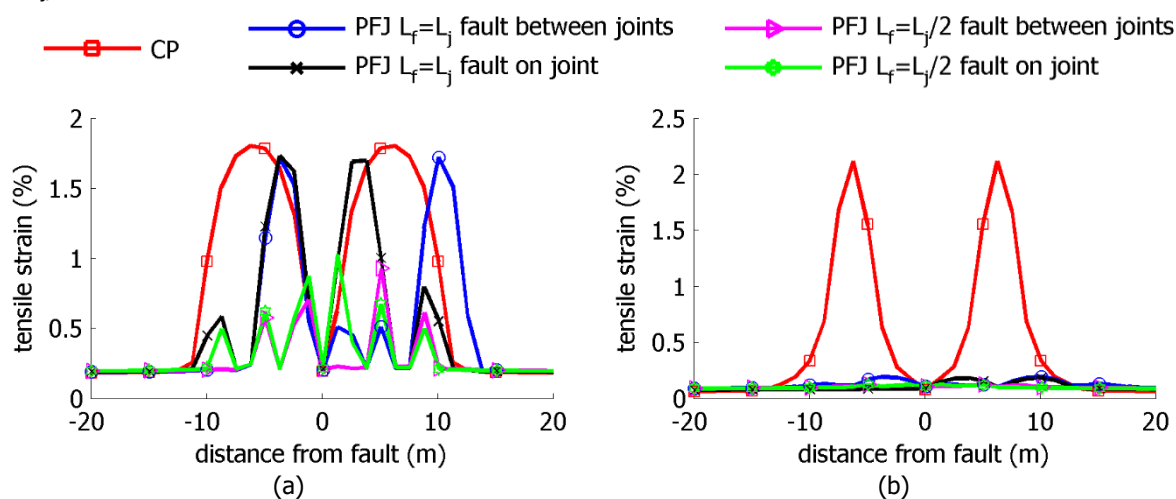


Figure 6-41: Tensile strain distributions for crossing angle (a) $\beta=70^\circ$ and (b) $\beta=90^\circ$ considering different configuration of flexible joints and fault trace being located either between two adjacent joints or on a joint

6.8 COMPARISON AMONG MITIGATING MEASURES

Several measures are adopted in practice to mitigate the consequences of faulting on buried pipes (section 2.5). The use of flexible joints has been numerically evaluated in the present chapter as a reliable and efficient measure, succeeding in concentrating strains and retaining steel parts virtually unstressed. The advantageous performance of joints is hereinafter compared to other mitigating measures in terms of pipe developing strains. The reference model is an API5L-X65 pipeline with four flexible joints (PFJ) according to section 6.3.1, featuring diameter $D=914\text{mm}$ and pipe wall thickness $t=12.70\text{mm}$. The reference PFJ is compared to continuous pipelines where commonly adopted mitigating measures are applied:

- Steel grade upgrade to API5L-X80 with elastic Young's modulus 210GPa , plastic modulus 0.513GPa , yield stress 530MPa , yield strain 0.252% , failure stress 621MPa and failure strain 18% .
- Increase of pipe wall thickness from 12.70mm to 15.88mm and 19.05mm .
- Trench backfilling with pumice having unit weight $\gamma=8\text{kN/m}^3$, cohesion $c=0$ and internal friction angle $\phi=33^\circ$.
- Pipe placement within culverts over the pipeline length that bending moment is developed. When culverts are used for pipe protection, the pipe is not backfilled. Thus, numerical modeling of this case is carried out by ignoring soil springs over the length along which the pipe is placed within culverts.

Pipelines under investigation are subjected to strike-slip faulting of magnitude $\Delta/D=2$. Three characteristic cases of crossing angles are addressed: (i) $\beta=70^\circ$ that leads to pipe bending and tension, (ii) $\beta=90^\circ$ that is the optimum case regarding the efficiency of joints and the one recommended by rules of good practice and (iii) $\beta=110^\circ$ as a less favorable situation that leads to pipe bending and compression and consequently maximizes the potential of local buckling failure. The cases under investigation are summarized in Table 6-5.

Table 6-5: Cases under investigation to compare mitigating measures

Pipeline	Steel grade	Thickness (mm)	Backfill soil
CP	X65	12.70	sand
CP	X65	15.88	sand
CP	X65	19.05	sand
CP	X80	12.70	sand
CP	X80	15.88	sand
CP	X80	19.05	sand
CP	X65	12.70	pumice
CP	X65	12.70	(culverts)
PFJ	X65	12.70	sand

The maximum tensile and compressive strain with respect to fault offset (Δ/D) for angle $\beta=70^\circ$ are shown in Figure 6-42. The primary observation is that steel grade upgrade and thickness increase provide a minor tensile strain decrease (Figure 6-42a), while tensile strains are almost halved when pumice is used for trench backfilling or pipe is placed within culverts. Flexible joints are then the most efficient among the compared measures. However, as fault offset increases, tension dominates over bending and thus the strain reduction in PFJ declines compared to the pumice backfilling case, while tensile strains in case of culverts are gradually increasing. The relationship between tension and bending, as offset evolves, directly impacts the development of compressive strains (Figure 6-42b), which are nearly eliminated by the introduction of joints. Pumice backfilling does not help as compressive strains increase proportionally to fault offset. Nonetheless, steel grade upgrade and thickness increase result in pipe stiffness increase. Thus, as fault offset increases, strains increase too until a certain value, but then strains decrease as tension dominates the pipe response. Regarding the compressive strains, flexible joints are as efficient as culverts.

Pipeline response in terms of maximum developing strains with respect to fault offset (Δ/D) for $\beta=90^\circ$ is depicted in Figure 6-42c. Crossing angle $\beta=90^\circ$ is a highly desirable case that might be difficult to achieve in practice due to the various limitations encountered during the route selection procedure of a pipeline. It is however useful to assess the impact of alternative mitigating measures as bending dominates the pipe behavior and consequently high curvature develops and local buckling emerges as the dominant failure mode. The tensile strain distributions, indicate the dramatic decrease of tensile strains due to the integration of joints or the use of culverts, while pumice backfill is clearly beneficial compared to the steel grade upgrade and the thickness increase. Then, regarding the compressive strain distribution (Figure 6-42d), flexible joints prevail universally over the other choices, as they almost eliminate strains. The other measures cannot protect the pipeline against compressive strain concentration that causes local buckling.

Pipeline – fault crossing angle $\beta>90^\circ$ leads to pipe bending and compression. This situation is in general undesirable but sometimes unavoidable due to restrictions in the route selection procedure. The pipeline response in terms of maximum developing tensile and compressive strains is shown in Figure 6-42e and Figure 6-42f, respectively, by adopting flexible joints, pumice backfilling, steel grade upgrade, thickness increase and the use of culverts as mitigating measures to protect pipeline against failure. Fault offset leads to excessive pipe compression and bending, with the latter being related to very high curvature.

So, the development of significantly high strains is expected, which exceed the corresponding code-based strain limits, even for small fault rupture magnitude. The comparison of the considered alternative mitigating measures reveals that flexible joints is the only choice to provide a significant decrease of the developing strains. However, it is crucial for design engineers to bear in mind that strain reduction caused by joints is due to the significant rotation of the joints and consequently excessive deformation of the pipe in the trench, which leads to constructional considerations regarding the trench proper width. It is thus crucial to consider on the one hand that the excessive joint rotation might violate its capacity and on the other hand pipe operability issues related to the pipe significant deformation (e.g. flow interruption, difficulties in in-line inspection, etc.).

- CP-X65-t=12.70mm-sand
 ▲ CP-X80-t=12.70mm-sand
 ◆ CP-X65-t=12.70mm-pumice
- CP-X65-t=15.88mm-sand
 ● CP-X80-t=15.88mm-sand
 ▼ CP-X80-t=12.70mm-culverts
- ✱ CP-X65-t=19.05mm-sand
 ✱ CP-X80-t=19.05mm-sand
 ▲ PFJ-X65-t=12.70mm-sand

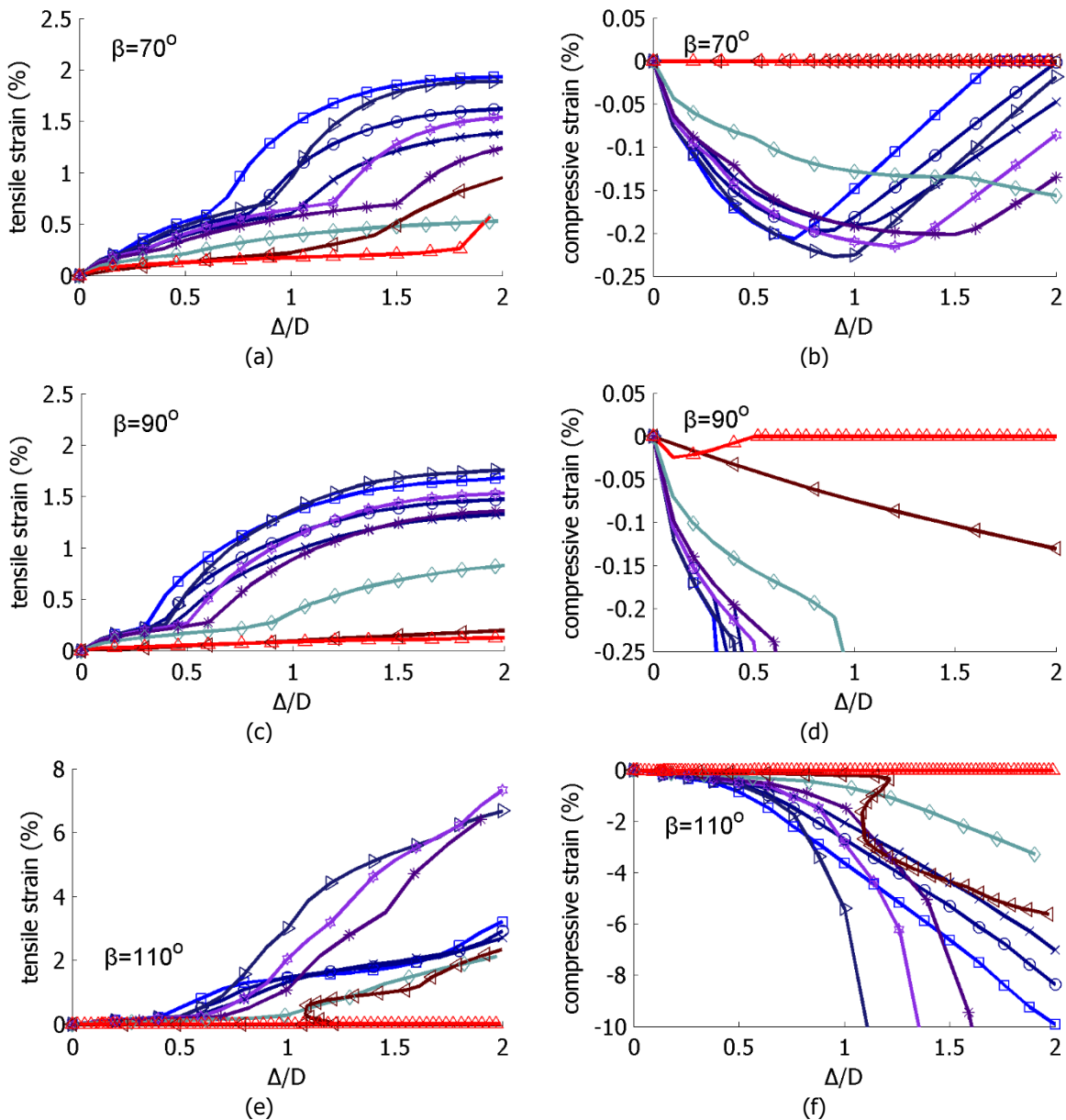


Figure 6-42: Maximum tensile and compressive strains with respect to fault offset for crossing angles $\beta=70^\circ$, $\beta=90^\circ$ and $\beta=100^\circ$ considering alternative mitigating measures

The general outcome derived from the comparison of commonly used mitigating measures and flexible joints is that the joints are the most efficient measure, while pumice backfilling has important advantages versus the steel grade upgrade and the thickness increase. In some cases, pumice backfilling efficiency can be considered competitive to flexible joints with reference to the expected level of developing strains that the pipeline operator can accept after a seismic fault activation. However, within a techno-economic framework, design and constructional engineers have to consider: (i) the cost of well graded pumice, the availability to remote construction sites and the requirement for special backfilling process and (ii) the cost of construction and transportation of culverts at the construction site. Hence, it follows that the introduction of flexible joints contributes significantly to the risk reduction of tensile rupture or local buckling. Additionally, preliminary analysis carried out by Bouckovalas et al. (2015) regarding the cost of using joints instead of the other seismic countermeasures revealed that the introduction of joints is also an economically competitive choice.

Finally, it is noted that the presented comparison on the efficiency of alternative mitigating measures, included the introduction of flexible joints, has been conducted without considering the uncertainty regarding the exact location of the trace. However, according to the current engineering practice, all seismic countermeasures are applied along the pipeline length where the fault trace may be encountered.

6.9 CONCLUSIONS

The numerical evaluation of buried steel pipelines with flexible joints subjected to strike-slip fault offset has been investigated using advanced numerical modeling and nonlinear analysis, employing the beam-type model. The presented investigation stands as a preliminary feasibility study on the effectiveness of flexible joints as innovative mitigating measures against the consequences of faulting on pipeline. Joints are introduced in continuous pipes to concentrate strains at the joints and retain the steel pipe parts virtually unstressed. The study highlights the effectiveness of joints in terms of drastically reducing the developing longitudinal tensile and compressive strains and consequently reducing the risk of pipe failure, provided that the technological and practical aspects of such joints are solved. The optimum configuration of flexible joints on the pipeline were examined in case of strike-slip faulting, while the main parameters affecting their efficiency were investigated, namely pipeline – fault crossing angle, fault offset magnitude, burial depth and ratio D/t . Additionally, the uncertainty on fault trace was addressed and suggestions were formulated for practical applications. The main conclusions of the present study can be summarized as follows:

- Metallic hinged bellow-type joints are the appropriate type of commercial flexible joints for buried pipeline – fault crossing applications. Such joints exhibit low rotational stiffness, while the axial and lateral relative movements are constrained, to withstand large internal pressure and pipe movements due to faulting.
- The joints location is selected based on the bending moment distribution of the continuous pipeline. The length L_j is the distance between the location of the maximum developing bending moment of the continuous pipeline from the fault trace and is the parameter of joints location selection. The corresponding parametric study revealed that the optimum joints' layout is the introduction of two joints on each side of the fault trace at distances L_j and $L_j/2$, in case there is no uncertainty on the exact fault trace location.
- The introduction of flexible joints transforms the pipeline structural system from continuous to segmented. The continuous pipe deformation is a smooth curve, while the pipeline with flexible joints deformation is a linear piece-wise curve. Numerical results indicated significant strain reduction due to the integration of joints. The efficiency of hinged flexible joints depends on the relation between

the pipe developing axial force and bending moment. The effectiveness of joints is increased if the pipe behavior is predominantly flexural.

- Crossing angle β lower or equal than 90° leads to pipe tension and bending. Parametric studies carried out showed that the joints efficiency is maximized for angles closer to 90° , where bending moment dominates the pipeline behavior. As angle β decreases and fault offset increases, tension dominates the pipe behavior and joints contribution to strain reduction deteriorates. Thus, commercial hinged flexible joints should be used until $\beta=70^\circ$.
- Crossing angle $\beta>90^\circ$ leads to pipe bending and compression. Parametric studies conducted revealed that the introduction of joints can ensure the pipe integrity. The response of pipelines with flexible joints under compression differs from the corresponding response under tension. In case $\beta>90^\circ$ the excessive deformation relieves the pipe from axial force. However, special attention has to be paid on the joint's angular capacity and the pipe capability to deform significantly within the trench.
- Results of the parametric study on the effect of crossing angle β revealed that hinged flexible joints are very effective in the reduction of pipe developing strains for crossing angles β close to 90° . For lower crossing angles and especially lower than 70° , joints that can accommodate some axial deformation are desirable.
- The performance of flexible joints in reducing longitudinal tensile and compressive strains has been shown to be independent of D/t ratio and burial depth.
- Integration of joints is necessary along the entire pipe length where the appearance of fault trace on the ground surface is likely, considering the inherent uncertainty in the exact location, akin to engineering practice for the usual mitigation approaches. Indicative results showed that joints should be integrated in the pipeline at constant distances L_j when pipe – fault crossing angle is close to 90° , while for lower angles the optimum distance is $L_j/2$. If there is uncertainty regarding the angle β , then distance $L_j/2$ should be selected. Length L_j is defined as the distance between the location of the maximum moment and the fault trace of the corresponding continuous pipe.
- The effectiveness of flexible joints has been compared to other commonly used mitigating measures, namely steel grade upgrade, increase of pipe wall thickness, backfilling with pumice and use of culverts. The integration of joints can, in general, provide higher strain reduction, thus efficiently protecting the pipeline, better than the other measures considered in the study.

The introduction of commercial hinged bellow-type flexible joints in continuous buried steel pipes has thus been shown leading to significant strain reduction and consequently protecting the pipeline against fault activation. Analysis results suggest also the need for commercial production of flexible joints with adequate axial stiffness that can accommodate large PGD due to faulting without decreasing their capacity to withstand high internal pressure. Hinged joints were examined in case of strike-slip faulting but the encouraging results indicate their potential applicability in cases of normal or reverse faulting. It is finally noted that fault offset is three-dimensional in nature, therefore hinged joints with biaxial angular capability (Figure 2-22a) should be implemented.

Part of this work has been submitted for publication (Melissianos et al. 2016a).

7 PERFORMANCE ASSESSMENT OF BURIED PIPELINES AT FAULT CROSSINGS

7.1 INTRODUCTION

Pipelines are hazardous structures and thus the necessity to perform a comprehensive seismic performance assessment of buried pipeline – fault crossing becomes crucial. Earthquakes and the associated fault displacements are naturally random events and thus the question arises as to what is the appropriate distribution of fault displacement that has to be taken into account during the design of the pipeline. Moreover, the seismic risk may be calculated in order to design or evaluate financial (insurance) or physical (retrofitting or upgrading) mitigating measures against the consequences of faulting on pipeline. Additionally, regarding the construction of a new pipeline project, hazard estimation is necessary so that the appropriate measures are taken to control the subsequent levels of risk through redirecting the design procedure. Regarding the financial loss estimation for insurance purposes, the failure hazard quantification is mandatory as vital information required to fix premiums (Bommer 2002; Cornell 1968). Then, with reference to seismic hazard assessment, there are two approaches: the first one is the deterministic that is implemented through the Deterministic Seismic Hazard Analysis (DSHA) and the second one is the probabilistic, implemented through the Probabilistic Seismic Hazard Analysis. The differences among the approaches are:

- The aim of DSHA is the development of earthquake scenarios, which consist of a postulated occurrence of an earthquake of a specified magnitude, i.e. characteristic earthquake, at a specific location that could affect the structure under consideration. However, the implementation of DSHA does not yield further information regarding the expected level of shaking, or the fault activation during a finite time period and the effects of uncertainties in the various methodology steps.
- The PSHA aims at quantifying the probabilistic nature of earthquake effects. The hazard from different sources is treated in a whole different way than DSHA as each seismogenic source is separately considered and its influence on the final outcome is transparent (Bommer 2002). Moreover, the contribution of all sources under consideration is combined through PSHA into a single exceedance rate for each level of a specified ground-motion parameter.

Acknowledging the financial, social and environmental consequences of a potential pipeline failure, the probabilistic approach is selected. The probabilistic approach is also necessary to account for the variable nature of earthquake loading and the commonly accepted incomplete knowledge about the complex properties of the pipeline – soil interacting system.

The performance assessment is based on the probabilistic framework for seismic performance of Cornell and Krawinkler (2000) and consists of: (i) seismic hazard analysis for the quantification of the probabilistic nature of fault displacement, (ii) pipeline structural analysis for the assessment of pipe mechanical behavior and (iii) combination of the results to estimate the potential of failure. In more detail, the Probabilistic Fault Displacement Hazard Analysis is performed to quantify the probabilistic nature of the fault offset, while the magnitude of the three fault displacement components in space is determined. Then, the pipe three-dimensional structural analysis is performed, using the nonlinear beam-type finite element model. Finally, the convolution of seismic hazard and structural response results in joint hazard surfaces of compressive and tensile strains leading to the estimation of the mean annual rate of exceeding any limit-state of interest. The performance assessment is moreover suggested as a tool: (i) to design or evaluate financial (insurance) and physical (retrofitting or upgrading) mitigating measures against the consequences of faulting on pipeline, (ii) during the route selection procedure and (iii) for developing measures to control the subsequent levels of risk through redirecting the design procedure of the earthquake-resistant design (vulnerability assessment).

In the present chapter a methodology for the performance assessment of buried pipelines at fault crossings is presented, whose preliminary versions has been published by Melissianos et al. (2014b, 2015).

7.2 SEISMIC HAZARD ANALYSIS

7.2.1 Probabilistic fault displacement hazard analysis framework

The most suitable tool to quantify the probabilistic nature of fault movement is the Probabilistic Fault Displacement Hazard Analysis (PFDHA). The necessary data to perform PFDHA were firstly provided by Coppersmith and Youngs (2000) and the basis of PFDHA has been established by Youngs et al. (2003). Angell et al. (2003) employed PFDHA as part of site investigations for BP America's Mad Dog and Atlantis Fields based on extended geophysical, geological and geotechnical analysis of the site under investigation. Focus was on the effects of soil properties and seabed stratigraphy on the style and origin of faulting that could affect offshore pipelines. Liu et al. (2013) applied PFDHA for a pipeline – fault crossing in China in order to investigate the differences resulting by considering the maximum and the permanent fault displacement.

PFDHA aims at quantifying the mean annual rate of exceeding arbitrary fault displacement levels at a site by considering the fault location, the fault slip rate, the distribution of earthquakes as well as the corresponding epistemic uncertainties. The PFDHA methodology includes two discrete approaches within it, the "earthquake approach" and the "displacement approach". The "earthquake approach" is derived from the Probabilistic Seismic Hazard Analysis (PSHA), which was introduced by Cornell in his pioneering work (Cornell 1968), and explicitly relates the occurrence of fault displacement on a fault at a site near or at the ground surface to the occurrence of earthquakes in the site region. To directly relate the "earthquake approach" of PFDHA to PSHA, the mean annual rate (MAR) of exceeding $\lambda_k(z)$ a ground motion parameter z at site k , taken into account n seismic sources, is evaluated as:

$$\lambda_k(z) = \sum_n v_n \int_{M_{\min,n}}^{M_{\max,n}} f_{M,n}(m) \left[\int_0^{\infty} f_{kn}(r|m) P(Z > z | m, r) dr \right] dm \quad (7-1)$$

where v_n is the rate of all earthquakes on source n above a minimum magnitude of engineering significance M_{\min} , $f_n(m)$ is the probability density of earthquake size that seismic source n can produce between values M_{\min} and M_{\max} , $f_{kn}(r|m)$ is the conditional probability density function for distance from site k to an earthquake of magnitude m occurring at source n and finally $P(Z > z | m, r)$ is the conditional probability that, given an earthquake of magnitude m at distance r from site k , the ground motion

parameter will exceed level z . It is noted that the random variables are denoted by uppercase letters (e.g. Δ), while their discrete values by lowercase letters (e.g. δ).

Contrary, the "displacement approach" needs extensive recorded and/or paleoseismic data, which are not always available. In practice, a transmission pipeline crossing a seismic area will be intercepted by numerous major and minor tectonic faults and thus no data for every fault will be available. So, the application of the "displacement approach" is not viable and consequently the "earthquake approach" is adopted for the performance assessment of buried pipelines at fault crossings. Furthermore, in the "earthquake approach" of PFDHA the distinction between two types of fault displacement is introduced, i.e. "principal faulting" and "distributed faulting". In more detail:

- "Principal faulting" is defined as slip along the main plane or planes of crustal weakness responsible for the release of seismic energy during the earthquake. Where the principal fault rupture extends to the surface, it may be represented by displacement along a single narrow trace or over a zone that may range from a few to many meters wide. The faults of concern are those that may produce earthquakes and thus are directly related to the primary source of energy release.
- "Distributed faulting" is defined as displacement that occurs on other faults, shears, or fractures in the vicinity of the principal rupture in response to the principal faulting. It is expected that distributed faulting will be discontinuous in nature and occurs over a zone that may extend outward several tens of meters to many kilometers from the principal rupture. A fault that can produce principal rupture may also undergo "distributed faulting" in response to principal rupture on other faults.

For the purposes of the proposed methodology, the "principal faulting" is adopted within PFDHA assuming that the pipeline intercepts a main fault, without considering distributed faulting issues. Additionally, the "principal faulting" concept is compatible with displacement along a single narrow trace, i.e. planar fault without thickness. The principal faulting approach is schematically illustrated in Figure 2-1, where the pipeline – fault crossing is represented by a point on the ground surface.

PFDHA provides the necessary information to assess any potential effects on the integrity of a buried pipeline and to make a risk-informed decision regarding the crossing site suitability. The product of PFDHA is a hazard curve, where the fault displacement is plotted versus the mean annual rate of exceeding every fault displacement value. The MAR of exceeding fault displacement δ is estimated as (Youngs et al. 2003):

$$\lambda_{\Delta,k}(\delta) = \sum_n v_n \int_{M_{\min,n}}^{M_{\max,n}} f_{M,n}(m) \left[\int_0^{\infty} f_{kn}(r|m) P_{kn}(\Delta > \delta | m, r) dr \right] dm \quad (7-2)$$

where $P(\Delta > \delta | m, r)$ is the conditional probability that, given an earthquake of magnitude m at a distance r from crossing site, the fault displacement will exceed displacement δ . However, for pipeline – fault crossing only one source zone is considered, namely the fault and consequently Eq. (7-2) for $n=1$ is simplified to:

$$\lambda_{\Delta}(\delta) = v \sum_{i=1}^{N_M} \sum_{j=1}^{N_R} f_M(m_i) P(\Delta > \delta | m_i, r_j) P(M = m_i) P(R = r_j | m_i) \quad (7-3)$$

where the density functions $f_n(m)$ and $f_{kn}(r|m)$ of Eq. (7-2) are replaced by the discrete mass functions $P(M=m_i)$ and $P(R=r_j|m_i)$ and the integrals of Eq. (7-2) are replaced by summations assuming a sufficient discretization of values, while v is the rate of all earthquakes above a minimum magnitude of engineering significance and is calculated based on the equation describing the seismicity of the investigated seismic source zone, $f_M(m_i)$ is the probability of earthquake magnitude between a minimum magnitude value under consideration and the maximum value that the fault can produce using for example the Bounded Gutenberg-Richter Recurrence Law (Gutenberg and Richter 1944), as presented in section 7.2.2.4,

$P(r_j|m_i)$ is the conditional probability mass function (PMF) of the crossing site distance to an earthquake of magnitude m . The term $P(\Delta > \delta | m_i, r_j)$ relates the occurrence of fault displacement at the crossing site to the occurrence of an earthquake through an attenuation model and thus it is referred as the Displacement Attenuation Function, which differs from the usual ground motion attenuation function. Source identification and characterization of the rate and size distribution of earthquakes are identical to those steps in PSHA, as well as the distance distribution. However, supplementary information regarding the geometry of the ruptures may be reserved to define fault displacement. The conditional probability of exceeding displacement δ is computed using a displacement attenuation relationship that differs from that for ground motion in that there is a finite probability that no slip will occur. It consists of two terms and is evaluated as:

$$P(\Delta > \delta | m_i, r_j) = P(\text{Slip} | m_i) P(\Delta > \delta | m_i, r_j, \text{Slip}) \quad (7-4)$$

where the first term $P(\text{Slip} | m_i)$ is the "Conditional Probability of Slip" and expresses the probability that the rupture on the fault reaches the surface or an adequate distance under the surface that affects underground lifelines, such as buried pipelines. The rupture is randomly placed on the fault plane, according to the specified location. Then, the distance to site is computed to estimate the probability $P(R=r_j|m_i)$ for the pipeline crossing site under investigation. It is assumed, typically, that the rupture location is uniformly distributed along the length of the fault trace. The "Conditional Probability of Slip" can be estimated using either simulation or empirical models. Coppersmith and Youngs (1993) suggest an empirical expression for the occurrence of principal surface rupture given an earthquake has occurred. They have analyzed worldwide data from 276 earthquakes and came up with the following "logistic regression model":

$$P(\text{Slip} | m_i) = \frac{e^{a+bm_i}}{1 + e^{a+bm_i}} \text{ with } a = -12.15, b = 2.053 \quad (7-5)$$

Other researchers like DePolo (1994) and Pezzopane and Dawson (1996) have also presented data sets that define the rate at which earthquakes of various magnitudes rupture the surface. However, Coppersmith and Youngs (1993) have incorporated such a large amount of recorded data from worldwide earthquakes in their regression model by considering also all types of faults. Furthermore, Moss and Ross (2011) especially for reverse fault type presented a logistic regression model to obtain the conditional probability of surface rupture occurrence:

$$P(\text{Slip} | m_i) = \frac{1}{1 + e^{a+bm_i}} \text{ with } a = 7.30, b = -1.03 \quad (7-6)$$

The second term $P(\Delta > \delta | m_i, r_j, \text{Slip})$ of Eq. (7-4) stands for the "Conditional Probability of Exceedance", which represents the probability that given rupture has occurred on the crossing site, fault displacement will exceed a specified fault displacement value δ for an earthquake of magnitude m . This probability is an inverse CDF that is based on empirical data models, such as ground motion attenuation relationships are constructed. Using data sets from past earthquakes, fault displacement can be normalized either by the maximum displacement (Δ/MD), or the average displacement (Δ/AD) measured for each rupture. Historical data are used to define a distribution for these ratios. The distribution is expressed as a function of the pipeline crossing distance from the fault closest edge (L_p) and is normalized by rupture length L_F , providing ratio L_p/L_F . It is noted that analysis carried out for patterns of fault displacement along surface rupture have shown roughly that displacements are larger in the middle of the rupture and consequently smaller near the fault ends (Petersen et al. 2011; Youngs et al. 2003). Therefore, the displacement along the length of the rupture can be normalized by the AD or MD and the distribution for ratios Δ/AD or Δ/MD fit with an appropriate probability model. So, the probability $P(\Delta > \delta | m_i, r_j, \text{Slip})$

is computed by convolving the distribution for Δ/AD or Δ/MD with an empirical lognormal distribution for AD or MD as a function of earthquake magnitude. Youngs et al. (2003) provide data fit distributions for normal faulting and Moss and Ross (2011) for reverse faulting.

– Normal faulting:

Data sets for Δ/AD ratio are fitted with a gamma distribution (section 10.6), which contrary to MD , has no need for upper bound limit to its range:

$$f(y) = \frac{1}{\Gamma(a)} \int_0^{y/b} e^{-t} t^{a-1} dt, \quad y = \Delta / AD$$

$$\text{with } a = \exp(-0.193 + 1.628x / LF) \quad (7-7)$$

$$b = \exp(0.009 - 0.476x / LF)$$

$$0 \leq x / LF \leq 0.5$$

Data sets for ratios Δ/MD are fitted with a beta distribution (section 10.8) that has an upper bound limit in its range:

$$f(y) = \frac{\Gamma(a+b)}{\Gamma(a)\Gamma(b)} \int_0^y z^{a-1} (1-z)^{b-1} dz, \quad 0 \leq y = \Delta / MD \leq 1$$

$$\text{with } a = \exp(-0.705 + 1.138x / LF) \quad (7-8)$$

$$b = \exp(0.421 - 0.257x / LF)$$

$$0 \leq x / LF \leq 0.5$$

– Reverse faulting:

Data sets for ratios $z=\Delta/AD$ are fitted with a Weibull distribution (section 10.7) according to:

$$f(y) = \frac{k}{\lambda} \left(\frac{z}{\lambda}\right)^{k-1} e^{-\left(\frac{z}{\lambda}\right)^k}$$

$$\text{with } k = \exp\left(-31.8(L_p / LF)^3 + 21.5(x / LF)^2 - 3.32x / LF + 0.431\right) \quad (7-9)$$

$$q = \exp\left(17.2(L_p / LF)^3 - 12.8(x / LF)^2 + 3.39x / LF - 0.38\right)$$

$$0 \leq x / LF \leq 0.5$$

Also, they can be fitted with a Gamma distribution (section 10.6) according to:

$$f(y) = z^{k-1} \times \frac{e^{-z/\theta}}{\theta^k \Gamma(k)}$$

$$\text{with } k = \exp\left(-30.4(x / LF)^3 + 19.9(x / LF)^2 - 2.29x / LF + 0.574\right) \quad (7-10)$$

$$\theta = \exp\left(50.3(x / LF)^3 - 34.6(x / LF)^2 + 6.60x / LF - 1.05\right)$$

$$0 \leq x / LF \leq 0.5$$

Data sets for Δ/MD ratio are fitted with a beta distribution (section 10.8) that has an upper bound limit in its range, according to:

$$f(z) = \frac{\Gamma(\alpha + \beta)}{\Gamma(\alpha)\Gamma(\beta)} z^{\alpha-1}(1-z)^{\beta-1}, 0 \leq z = \Delta / MD \leq 1$$

(7-11)

with $\alpha = 0.901x + 0.713$
 $\beta = -1.86x + 1.74$
 $x \leq x / LF \leq 0.5$

The choice of either the maximum displacement (MD) or the average displacement (AD) for a deterministic assessment remains a major consideration. According to Wells and Kulkarni (2014) MD is expected to occur over a limited reach of the fault. On the other hand, AD is more representative of the expected displacement along a bigger part of the fault. In practice, MD can be encountered as conservative, while AD is more representative of the likely displacement. In PFDHA, though, the effect of changing one over the other is not obvious.

7.2.2 PFDHA aspects

7.2.2.1 PFDHA application concerns and advances

The Probabilistic Fault Displacement Hazard Analysis has two major advantages: (i) it is based on the well-known and established PSHA and (ii) a wide range of fault displacement probabilities can be estimated. However, there are some disadvantages that have to be considered regarding the implementation of PFDHA in practice. The main issue under question refers to the estimation of earthquake magnitude, as magnitude estimations rely on offsets from past earthquake events. Additionally, there is uncertainty about the fault displacement data from paleoseismic events; either they are maximum, average or other (Strom et al. 2011). Similarly, there is vagueness about the relationship between fault displacement and rupture length, even though methodologies have been proposed by some authors to improve paleoseismic data estimation. However, still the most complete data set evaluation among earthquake characteristics remains the one of Wells and Coppersmith (1994). During the past years some improvements of PFDHA have been published by several authors. Petersen et al. (2011) extended the earthquake approach of Youngs et al. (2003) to strike-slip faulting by including options in their formulation for advanced accuracy concerning fault mapping and fault complexity. Strom et al. (2011) present a combination of PFDHA and Deterministic Fault Displacement Hazard Analysis (DFDHA) for the Sakhalin-II project. After performing a thorough geological investigation of the fault under consideration they estimated the deterministic fault displacement design value. Then, the probability of fault rupture was calculated as a product of probabilities of exceeding the maximum deterministic value, the probability that pipeline will suffer maximum displacement and probability of surface rupture. Shantz (2013) computed the rate of fault offset exceeding a specific value as the product of the inverse of return period for the characteristic earthquake and the probability of fault offset exceeding a specific value given the occurrence of characteristic earthquake.

Nevertheless, as the proposed methodology aims to create a reliable tool for the performance assessment of pipelines at fault crossings, where data regarding the fault behavior are inadequate, the Youngs et al. (2003) approach is the appropriate. In the final design of pipeline – fault crossing project, where sufficient and detailed data might be available regarding fault geometry as well as paleoseismic data, advances of PFDHA shall be adopted and minimize the potential disadvantages.

7.2.2.2 Earthquake magnitude

Earthquake magnitude in seismic hazard analysis stands for the moment magnitude (Hanks and Kanamori 1979), which is a quantity used by earthquake seismologists to measure the "size" of an earthquake. The moment magnitude M is given by the expression:

$$M = \frac{\log_{10} M_0}{1.5} - 10.7 \quad (7-12)$$

where $M_0 = \mu A_r \Delta_{\text{average}}$

where M_0 is the seismic moment, μ (dyn/cm²) is the rupture strength of the materials along the fault, A_r (cm²) is the area of rupture and Δ_{average} (cm) is the average displacement on A_r . Seismic moment stands for a measure of the work done by the earthquake. The seismic moment of an earthquake is typically estimated using whatever information is available to constrain its factors. For modern earthquakes, moment is usually estimated from ground motion recordings of earthquakes, while for earthquakes that occurred in the past before modern instruments were available, moment may be estimated from geologic estimates of the size of the fault rupture and the displacement.

Moment Magnitude Scale (MMS) is used by seismologists to measure the size of earthquakes in terms of the released energy. The moment magnitude (M) is based on the seismic moment of the earthquake, which is equal to the rigidity of the earth multiplied by the average amount of slip on the fault and the size of the area that slipped. The MMS was developed in the 1970s to succeed the 1930s-era Richter magnitude scale. Even though the formulae are different, the new scale retains the familiar continuum of magnitude values defined by the older one. Nowadays MMS is used to estimate magnitudes for all modern large earthquakes by the United States Geological Survey. Moment magnitude is the most accurate quantitative measurement of earthquake size based on instrumental measurement, as the main difference to other empirical magnitude scales, such as the body wave and Richter local magnitudes, is that it does not saturate. Saturation refers to the phenomenon where for strong earthquakes the measured ground-shaking characteristics become less sensitive to the size of the earthquake, than for smaller earthquakes (Kramer 1996).

7.2.2.3 Poisson model

The Poisson model provides a simple framework to evaluate the probabilities of events that follow a Poisson process. This process yields values of a random variable describing the number of occurrences of a particular event during a given time interval or in a specified spatial region. Poisson model possess three main properties:

- the number of occurrences in a time interval are independent of the number that occur in any other non-overlapping time interval;
- the probability of occurrence during a very short time is proportional to the length of time interval;
- the probability of more than one occurrence during a very short time interval is negligible.

These properties lead to the conclusion that events following Poisson model occur randomly with “no memory” of the time, size or location of the event (Kramer 1996). The Poisson Model can be better understood through a characteristic example. Assuming that during 20 earthquake events that have occurred in a sampling period of 100 years, slip has occurred along a fault, recorded fault offset showed that only two slip measurements exceeded $\delta=1\text{m}$, which is the fault offset magnitude of interest, while the rest 18 slips were $\delta < 1\text{m}$. In such case the rate of earthquake events is estimated as:

$$v = 20 / 100 = 20 \text{ events per year} \quad (7-13)$$

The probability of fault displacement exceeding the value $\delta=1\text{m}$ given an event happened is:

$$P(\delta > 1\text{m} | \text{event happend}) = 2 / 20 = 10\% \quad (7-14)$$

Then, the requested mean annual rate of exceeding the fault displacement $\delta=1\text{m}$ is evaluated through what is known as Poisson Filtering:

$$\lambda_{\Delta}(\Delta > 1m) = \nu P(\Delta > 1m | \text{event happend}) = 0.2 \times 0.1 = 0.02 \quad (7-15)$$

It is noted that the rate of events calculated in Eq. (7-13) would be more accurate if the sampling period was 1000 years or even 10000 years for example.

Another characteristic example is that if the mean annual rate of exceeding fault displacement $\delta=1m$ is $\lambda_{\Delta}=0.00211$, then fault displacement will exceed 1m averagely once in 475 years or with 10% probability in 50 years.

7.2.2.4 Gutenberg – Richter Bounded Recurrence Law

Gutenberg and Richter (1944) used data from California earthquakes and divided the number of exceedances of each magnitude by the length of the time period to define the mean annual rate of exceedance λ_M , of an earthquake of magnitude m . The resulting law for earthquake recurrence is expressed as:

$$\lambda_M(m) = a - bm \quad (7-16)$$

However, because the expression of Eq. (7-16) expands to an infinite range of magnitudes, an upper (m_u) and a lower (m_o) bound are introduced in the Gutenberg – Richter Bounded Recurrence Law:

$$F_M(m) = P(M < m | M_{\max} \leq m \leq M_{\min}) = \frac{1 - \exp[-\beta(m - M_{\min})]}{1 - \exp[-\beta(M_{\max} - M_{\min})]} \quad (7-17)$$

Even though the Gutenberg – Richter recurrence relationship is significantly important for the seismic hazard analysis, it has been questioned by several researchers. However, Bommer (2002) states that the real variation of ground-motion parameters can be plotted after records from accelerograph stations are collected, following their operation for thousands of years. Then, the seismologists will be capable to evaluate the hazard curves and decide whether they correctly predict the forthcoming earthquakes. Therefore, the Gutenberg – Richter Law is the best available relationship to “predict” future earthquake magnitudes.

7.2.3 PFDHA implementation for pipeline – fault crossing

The implementation of PFDHA for pipeline – fault crossings consists of four elements: (i) earthquake magnitude, (ii) surface rupture length, (iii) position of surface rupture length along the fault trace and (iv) position of the crossing site. The earthquake magnitude stands as the key factor for describing a seismic source. It ranges from a minimum value of engineering significance M_{\min} , assuming an insignificant impact of lower values on hazard levels, to a maximum value M_{\max} as constrained by the finite fault size. Acknowledging that different earthquakes may rupture fault lengths of different size, the surface rupture length (SRL) along the fault trace is introduced as the second element. The third element under consideration is the SRL position along the fault trace to determine whether the rupture will intercept the pipeline (fourth element).

PFDHA is implemented using the total probability theorem, an example of which is Eq. (7-2), and given the aforementioned considerations, Eq. (7-3) can be re-written to explicitly account for them:

$$\lambda_{\Delta}(\delta) = \nu \sum_i P(\Delta > \delta | m_i) P_M(m_i) \quad (7-18)$$

where $P_M(m_i)$ is the probability of magnitude M falling within the i -th bin characterized by m_i at its center. $P(\Delta > \delta | m_i)$ is the probability that the fault displacement Δ exceeds a defined value δ at the crossing site, given an earthquake of magnitude m_i has occurred. Further discretization is needed for estimation of this term. Discrete values of SRLs are simply defined as integer multiples of a minimum length that is of engineering significance by relating SRL and M_{\min} via the expressions of Wells and Coppersmith

(1994), while Wells and Kulkarni (2014) suggest to step the rupture length along the fault with a uniform interval of 1km. Lacking better information, SRLs of the same size are considered to have equal probability of rupturing. Therefore, every SRL size is accounted for at all possible locations $Pos_{k,j}$, keeping track of the cases where the rupture crosses the pipeline and thus contributing to the fault displacement hazard. Finally, we also discretize the average or the maximum displacement of the entire fault rupture are, FD. Further breakdown of probability $P(\Delta > \delta | m_i)$ yields:

$$P(\Delta > \delta | m_i) = \sum_j \sum_t \sum_k P(\Delta > \delta | SRL_j, FD_t, Pos_{k,j}) P(SRL_j, FD_t | m_i) P(Pos_{k,j}) \quad (7-19)$$

The first term is the conditional probability of exceedance, where detailed calculations are carried out over each combination, SRL, position of SRL relative to the crossing site and value FD. Given these parameters, this term becomes magnitude-independent. The second term is the conditional joint probability of the SRL and FD, given the magnitude. The third term, $P(Pos_{k,j})$, estimates the probability of SRL_j position along the fault. Equal-length SRL_j positions are assumed to be equiprobable and independent of the magnitude and thus the probability function is substituted by $1/N_k$, where N_k is the number of potential SRL_j positions considered. This conceptual algorithm applies for both the two alternative approaches of PFDHA for estimating FD, namely the average displacement (AD) and the maximum displacement (MD) approach that are used to normalize fault displacement data via empirical expressions.

Regarding the correlation of SRL and FD in the second term of Eq. (7-19), the best known distribution of SRL and FD comes from Wells and Coppersmith (1994) and allows the calculation of the probability by correlating SRL and the estimate of maximum or average displacement (AD/MD) along its length. This probability can be expressed as a joint lognormal function with positive correlation $f(SRL, FD | m_i)$. Assuming that the discretization is sufficiently fine, the probability of SRL_j and FD_t falling in a bin given the magnitude m_i can be approximated via a single PDF value at its center through the expression:

$$P_{i,j,t} = \int_{FD_t - \frac{FD_{step}}{2}}^{FD_t + \frac{FD_{step}}{2}} \int_{SRL_j - \frac{SRL_{step}}{2}}^{SRL_j + \frac{SRL_{step}}{2}} f(SRL_j, FD_t | m_i) dFD dSRL \cong f(SRL_j, FD_t | m_i) \Delta FD \Delta SRL \quad (7-20)$$

The sum of $P_{i,j,t}$ over j and k for all SRL_j and FD_t should equal one. Thus, to account for minor numerical issues, the derived probability mass function approximation is appropriately renormalized as:

$$P(SRL_j, FD_t | m_i) = \frac{P_{i,j,t}}{\sum_j \sum_t P_{i,j,t}} \quad (7-21)$$

Estimating the distribution of SRL_j and FD_t given an earthquake magnitude m_i is based on the empirical equations among fault characteristics proposed by Wells and Coppersmith (1994):

$$\log \hat{SRL} = a + bM \quad \text{see Table 7-1} \quad (7-22)$$

$$\log \hat{FD} = a + bM \quad \text{see Table 7-2 and Table 7-3} \quad (7-23)$$

where M is the earthquake magnitude, \hat{SRL} (km) is the median estimate of surface rupture length, \hat{FD} is the median estimate of FD, while parameters a and b are listed in Table 7-1 and Table 7-2 for SRL and FD, respectively.

However, Wells and Coppersmith (1994) state that regressions for reverse faults are not significant at a 95% probability. Thus, Moss and Ross (2011) suggested the parameters listed in Table 7-3 for Eq.

(7-23). Yet, fault displacement, either average, or maximum, is correlated according to the expression after Wells and Coppersmith (1994):

$$\ln \log \hat{SRL} = a + b \log FD \quad \text{see Table 7-4} \quad (7-24)$$

Thus, by combining such information, function $f(SRL_j, FD_i | m_i)$ is estimated as a multivariate joint lognormal PDF using the mean values matrix and the covariance matrix:

$$[\mu] = \begin{bmatrix} \mu_{\log SRL} \\ \mu_{\log FD} \end{bmatrix} \quad (7-25)$$

$$[\rho] = \begin{bmatrix} \sigma_{\log SRL}^2 & \rho_{\log SRL, \log FD} \sigma_{\log SRL} \sigma_{\log FD} \\ \rho_{\log SRL, \log FD} \sigma_{\log SRL} \sigma_{\log FD} & \sigma_{\log FD}^2 \end{bmatrix} \quad (7-26)$$

where the $\mu_{\log SRL}$ is the log-mean value of SRL from Eq. (7-22), $\mu_{\log FD}$ is the log-mean value of FD from Eq. (7-23), $\sigma_{\log SRL}$ is the log-standard deviation from Table 7-1, $\sigma_{\log FD}$ is the log-standard deviation from Table 7-2 or Table 7-3 and $\rho_{\log SRL, \log FD}$ is the correlation coefficient from Table 7-4.

Table 7-1: Empirical equation coefficients for $\log SRL = a + bM$ (Wells and Coppersmith 1994)

slip type	N events	a	b	σ	ρ
strike-slip	43	-3.55	0.74	0.23	0.91
reverse	19	-2.86	0.63	0.20	0.88
normal	15	-2.01	0.50	0.21	0.81

Table 7-2: Empirical equation coefficients for $\log FD = a + bM$ (Wells and Coppersmith 1994)

FD	slip type	N events	a	b	σ	ρ
AD	strike-slip	29	-6.32	0.90	0.28	0.89
AD	reverse	15	-0.74	0.08	0.38	0.10
AD	normal	12	-4.45	0.63	0.33	0.64
MD	strike-slip	43	-7.03	1.03	0.34	0.90
MD	reverse	21	-1.84	0.29	0.42	0.36
MD	normal	16	-5.90	0.89	0.38	0.80

Table 7-3: Empirical equation coefficients for $\log FD = a + bM$ (Moss and Ross 2011)

FD	slip type	a	b	σ	ρ
AD	reverse	-2.2192	0.3244	0.17	0.62
MD	reverse	-3.1971	0.5102	0.31	0.52

Table 7-4: Empirical Equation coefficients for $\log SRL = a + b \log FD$ (Wells and Coppersmith 1994)

FD	slip type	N events	a	b	σ	ρ
AD	strike-slip	35	1.68	0.65	0.26	0.82
AD	reverse	17	1.45	0.26	0.36	0.28
AD	normal	14	1.52	0.28	0.17	0.59
MD	strike-slip	55	1.49	0.64	0.27	0.86
MD	reverse	21	1.36	0.35	0.39	0.38
MD	normal	19	1.36	0.35	0.20	0.73

7.2.4 Fault displacement components

The classic PFDHA deals with the fault displacement magnitude and therefore neglects its distribution into x/y/z spatial components. The fault offset in nature is three-dimensional, regardless the fault type. However, usually one fault displacement component is sufficiently larger than the other two and practically defines the fault type as normal, strike-slip or reverse. This fault displacement component is the principal one. In case it is the vertical Δ_3 , then the fault is normal or reverse and if it is the horizontal

Δ_1 , the fault then is strike-slip (Figure 2-1 and Figure 7-1). Thereby, the distribution of fault displacement components in 3D space is necessary to identify the fault type. Also, the pipeline structural response due to faulting is directly related to the fault type; in addition to ubiquitous pipe bending, normal faulting induces tension, reverse faulting introduces compression, while strike-slip faults can cause either of the two depending on the geometry. Thus, the necessity emerges to incorporate the individual fault components magnitude in the seismic hazard analysis. As there is not always sufficient data regarding the fault components distribution a simple and approximate procedure is chosen, where the principal component is uncertain, assuming a uniform (section 10.3) or normal distribution (section 10.4) within 75 to 90% of Δ (Table 7-5). Such distributions are reasonable assumptions to be re-evaluated if adequate data become available in the future. The lower bound of 0.75Δ stands for a rational assumption to ensure that the magnitude of the principal component is compatible with the fault type and no other component will exceed the principal one. The upper bound of 0.90Δ is based on the assumption that while a fault is characterized by the principal component, this in nature does not exclude movement in the other two directions.

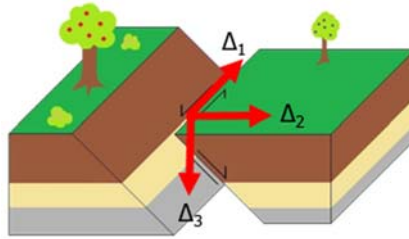


Figure 7-1: Schematic illustration of fault displacement components

Table 7-5: Uniform and normal distribution parameters of the principal fault displacement component

Distribution	Parameters			
	Mean	C.O.V.	Lower bound	Upper bound
Truncated normal	0.80Δ	0.20	0.75Δ	0.90Δ
Uniform	-	-	0.75Δ	0.90Δ

Thus, of the two independent components, Δ_1 and Δ_3 , the principal one for the given faulting type is sampled according to Table 7-5. The other component is determined according to Eqs (2-1) and (2-2) given the fault displacement magnitude Δ . Then, a certain bookkeeping exercise is needed of discretizing $\lambda_{\Delta}(\delta)$ and distributing its constituents to bins of Δ_1 and Δ_3 . This is facilitated by changing from the bins of MAR of exceedance λ_{Δ} to the bins of MAR of equaling, $\Delta\lambda_{\Delta}(\delta)$:

$$\Delta\lambda_{\Delta}(\delta) = \left| \lambda_{\Delta}(\delta + w) - \lambda_{\Delta}(\delta - w) \right| = \lambda_{\Delta}(\delta - w) - \lambda_{\Delta}(\delta + w) \quad (7-27)$$

where $2w$ is the displacement bin width. It is noted that whereas the mean annual rate differential $d\lambda_{\Delta}(\delta)$ is negative due to decreasing hazard with δ , $\Delta\lambda_{\Delta}(\delta)$ is defined to be always positive. The method becomes clearer if for example an oblique strike-slip fault ($\psi \neq 0$) is considered, where the principal component is Δ_1 . The MAR of equaling is then evaluated as:

$$\Delta\lambda_{\Delta_1, \Delta_3}(\delta_1, \delta_3) = \Delta\lambda_{\Delta}(\delta) P(\Delta_1(\delta) \in [\delta_{1,t}, \delta_{1,t+1}] | \delta) \quad (7-28)$$

where $\delta = \sqrt{\delta_1^2 + \delta_3^2 \left(1 + \frac{1}{\tan^2 \psi} \right)}$

where the range of the fault displacement Δ has already been discretized into a sufficiently large user-specified number of bins $[\delta_{1,t}, \delta_{1,t+1}]$, $t=1,2,3,..N_{bin}$ in the fault displacement hazard calculation. The first

term, $\Delta\lambda_{\Delta}$, is here estimated as the difference of the λ_{Δ} at the bin edges. The second term is the probability of Δ_1 falling in the t-bin for given fault displacement δ , evaluated according to the distribution of Table 7-5. For a given fault displacement δ the probability of Δ_1 falling in the t-bin is evaluated from the assumed uniform or normal CDF.

7.2.5 Seismic hazard uncertainty

Identification and quantification of uncertainties is integral to seismic hazard analysis, as a hazard curve without considering the pertinent uncertainties is highly sensitive to the most severe of the alternative models. It is thus necessary to incorporate in PFDHA all the pertinent quantifiable uncertainties. Uncertainties are mainly divided into two categories that demand a distinct treatment and it is still a good practice to keep them separate in order to allow the identification of key uncertainties, even though this is not always easy:

- Aleatory uncertainty results from the inherent variability of the nature over time, e.g. randomness in earthquake magnitude, fault location, ground motion, fault displacement, etc. Aleatory uncertainty can difficultly be reduced due to its origin and in practice shapes the hazard curve. It is, also, directly incorporated in hazard calculation and can be refined as the scientific knowledge improves.
- Epistemic uncertainty results from the inadequate understanding of nature and can in time be reduced with better observations. Epistemic uncertainty is related to the earthquake, ground motion models etc. that are adopted. In practical terms, epistemic uncertainty leads to alternative hazard curves (Bommer and Scherbaum 2008).

Epistemic uncertainty is handled in seismic hazard analysis through logic trees, which are considered to be the state-of-the-art tool to quantify and incorporate epistemic uncertainty (Bommer and Scherbaum 2008). The set-up of a logic tree includes the production of alternative models for various input variables and then the assignment of weight factors to the different tree branches. After setting up a logic tree, the hazard calculations are performed following each possible branch of the tree. Every branch leads to the estimation of a hazard curve with the total weight factor of the branch being adopted as the product of the weights of considered weights for the particular calculation. However, weight factors must be chosen in such way that according to Abrahamson and Bommer (2005) are not frequently-based probabilities and possess the following main four characteristics:

- their summation is one;
- all possibilities are included in the corresponding events;
- they are defined for mutually exclusive events;
- they represent the relative rate at which alternative events occur.

Epistemic uncertainties are handled within the seismic hazard analysis of the proposed methodology through the formulation of a logic tree. An example of a potential three-level logic tree is illustrated in Figure 7-2, where the seismic rate ν , the maximum earthquake magnitude M_{\max} and the fault displacement approach of PFDHA are considered to be uncertain. The seismic rate ν (weights $w_{\nu i}$) is the determining feature of a seismic source, where a mean value is usually provided. Unlike the minimum magnitude M_{\min} that is chosen by decision, the maximum magnitude M_{\max} is usually under question as provided by seismologists for the source under investigation. The PFDHA displacement option (AD/MD) is also incorporated in the uncertainty analysis with weights w_D .

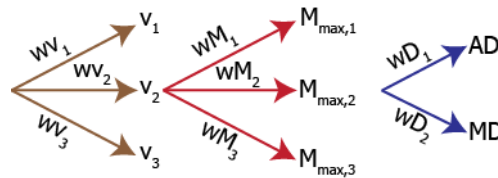


Figure 7-2: Hazard uncertainty logic tree for determining the fault displacement Δ hazard by considering seismic rate v , maximum earthquake magnitude M_{max} and the AD or MD referring to the two different approaches of PFDHA

7.3 PIPELINE STRUCTURAL ANALYSIS

The performance assessment of pipes at fault crossings is based on the convolution of seismic hazard results with pipe structural analysis results. The link that acts as an interface variable between the seismologists and the structural engineers is the intensity measure (IM), which is an indicative quantity of the magnitude of fault rupture. Typically, IM is a scalar variable, for example in building assessment it could be $S_a(T_1)$. The structural engineer needs to estimate the structural response to given IM values in pipeline – fault crossing assessment. An appropriate scalar IM could be the fault displacement Δ . However, the distribution of fault displacement components in the three-dimensional space determines the pipeline mechanical behavior. Therefore, the independent fault displacement components (Δ_1, Δ_3) are selected as the vector IM (Bazzurro and Cornell 2002). Based on the assumption that the fault is planar, components Δ_1 and Δ_3 are fault displacement components that can fully describe the structural model loading conditions. It should be noted that if the proposed methodology is to be extended to encompass duration-dependent failure, such as low cycle fatigue, this IM will probably become insufficient and require improvement.

Buried pipeline design against faulting is carried out in strain terms (section 2.2) and thus strains obtained from pipe structural analysis are the appropriate Engineering Demand Parameters (EDP). Strain demand (ϵ_{dem}) in terms of the maximum developing tensile and compressive strain can be estimated using any available structural analysis procedure (section 2.3). Then, strain demand is compared against strain capacity (ϵ_{cap}) through the strain hazard analysis to assess the potential of failure, or in other words to perform the check for capacity exceedance:

$$\epsilon_{dem} \leq \epsilon_{cap} \quad (7-29)$$

7.4 PIPELINE STRAIN HAZARD ANALYSIS

7.4.1 Framework of failure limit states

Performance assessment is carried out in order to quantify the potential of failure of a structure. Engineers aim at characterizing a structure as completely as possible and thus define limit states (LS) that have an actual meaning for the behavior of the structure. This procedure stands in practice as a translation of the engineering aspects of EDPs to physical consequences. The violation of a limit state is then triggered by the exceedance of capacity. For buried pipe – fault crossing two potential states are defined within the ultimate limit state: (i) local buckling due to compressive strains and (ii) tensile rupture due to tensile strains.

The pipeline strain hazard analysis proposed within the present study lies under the Performance-Based Earthquake Engineering (PBEE) framework. PBEE was originally developed by the Pacific Earthquake Engineering Research (PEER) Center and stands as an alternative to the well-established Load and Resistance Factor Design (LRFD). The PBEE methodology is summarized into the Cornell – Krawinkler

framing equation adopted by the Pacific Earthquake Engineering Research (PEER) Center (Cornell and Krawinkler 2000) that can be written symbolically as:

$$\lambda(DV) = \int \int \int G(DV | DM) | dG(DM | EDP) | | dG(EDP | IM) | | d\lambda(IM) \quad (7-30)$$

where $G(x|y)=P(X>x|Y=y)$ is the conditional complementary cumulative distribution function (CCDF) of a random variable X given the value y of another random variable Y . In more detail, $\lambda(DV)$ is the MAR of exceeding of the Decision Variable (DV), $G(DV|DM)$ is the probability of the decision variable exceeding specific values, given the state of damage measured by a Damage Measure (DM). Moreover, $G(EDP|IM)$ is the probability that the EDP exceeds these values given that the IMs equal particular values. Changing the order of integrations on Eq. (7-30) can provide intermediate results (e.g. Miranda and Aslani 2003). In particular, the integration of IM, as adopted hereinafter, provides the MAR of exceeding the remaining variables, i.e. hazard curves. Furthermore, conditioning on IM leads to the estimation of the fragility curve $G(DM|IM)$ and $G(DV|IM)$ is the corresponding vulnerability function. In general, "vulnerability" refers to the loss measurements (e.g. casualties, monetary loss, downtime) and should by no means be considered interchangeable to "fragility", as the latter refers to a damage state only.

Performance assessment of pipelines at fault crossings does not include loss assessment (DV is not considered) and therefore, the generic Eq. (7-30) can be simplified to:

$$\lambda_{LS} = \int G(EDP | IM) | d\lambda(IM) \quad (7-31)$$

where LS is the event $EDP > EDP_{cap}$ and EDPs are the tensile and compressive strains, the intensity measure (IM) is the vector of the fault components Δ_1 and Δ_3 and $G(EDP|IM)$ represents the probability of exceeding values of the EDP given the vector IM, defining a fragility surface. Thus, the conceptual Eq. (7-31) becomes a double integral over the two IM components for a pipeline – fault crossing:

$$\lambda_{LS} = \lambda_{\epsilon_{dem} > \epsilon_{cap}} = \int_0^{+\infty} \int_0^{+\infty} P(\epsilon_{dem} > \epsilon_{cap} | \delta_1, \delta_3) d\lambda_{\Delta_1, \Delta_3}(\delta_1, \delta_3) \quad (7-32)$$

where $d\lambda_{\Delta_1, \Delta_3}(\delta_1, \delta_3)$ is the mean annual rate differential of fault displacement components obtained from Eq. (7-28) and $P(\epsilon_{dem} > \epsilon_{cap} | \delta_1, \delta_3)$ is the probability of strain demand exceeding strain capacity estimated for given/specified values δ_1, δ_3 of the fault components, i.e. the fragility function. The fragility function describes the vulnerability of the pipeline to experience seismic damage and here in particular, fault rupture. It is noted that in the present work, the fragility is estimated on the basis of numerical data, as Meslem et al. (2015) suggest for buildings, and refers to the entire pipeline structure, while individual pipe components' failure is not addressed. For the sake of completeness, the symbolic definition of the fragility function $F_{LS}(IM)$ is:

$$F_{LS}(IM) = P[LS \text{ is violated} | IM] \text{ or } F_{LS}(IM) = P[\text{Demand} > \text{Capacity} | IM] \quad (7-33)$$

provided that the LS violation is defined through the event [Demand>Capacity].

Then, the integrals of Eq. (7-32) through appropriate discretization are substituted by easier-to-compute summations:

$$\lambda_{LS} = \sum_i \sum_j P(\epsilon_{dem} > \epsilon_{cap} | \delta_{1,i}, \delta_{3,j}) \Delta\lambda_{\Delta_1, \Delta_3}(\delta_{1,i}, \delta_{3,j}) \quad (7-34)$$

Limit state assessment can incorporate the uncertainty of both strain demand and strain capacity. The simpler case of course is to treat both as non-random variables by neglecting the uncertainty, regarding

the structural model parameters (demand) and the code-based limits (capacity). It is noteworthy that for buried pipelines at fault crossing there is no appreciable "record-to-record" variability in practice (i.e. dispersion of EDP given IM), compared to the usual procedure in building assessment (e.g. Vamvatsikos and Cornell 2002). In other words, given the intensity measure values Δ_1 and Δ_3 , there is little uncertainty in the level of pipeline demand that is not model-related in contrast to building assessment studies. The reason is that a pipeline subjected to a given level of imposed ground displacement at a well defined crossing position as assumed herein, represents a much more certain loading condition compared to a building subjected to an accelerogram of which only the spectral acceleration is known. Thus, variability in demand given the fault displacement components is derived mainly from the model uncertainty (e.g. soil properties) that is not easy to quantify and thus it may not be unusual to assume that strain demand is practically deterministic given fault displacement components Δ_1 and Δ_3 . Finally, code-based strain limits (section 2.2.2) are adopted for defining the strain capacity.

The strain hazard curves can also be constructed using the general Eq. (7-34). Strain hazard curves are a useful visual tool for understanding the pipeline performance and the probabilistic estimation of a potential pipeline failure by comparing strain demand and strain capacity. The first step is to estimate strain demand for every combination of fault displacement components. A useful strategy for computational efficiency is to perform pipeline structural analysis that convey the entire range of pipeline response, from no damage to leakage or rupture, akin to an Incremental Dynamic Analysis (Vamvatsikos and Cornell 2002). Secondly, the strain hazard curves are constructed by considering the results through the IM. A range of tensile (ϵ_t) and compressive strains (ϵ_c) is thus selected by the engineer to cover the anticipated range of the demand values. Strain values are then sufficiently discretized into a number of bins and the strain hazard surface is calculated by summing the MAR of equaling values corresponding to tensile and compressive strains that cause exceedance (failure).

7.4.2 Estimation of limit states

7.4.2.1 Limit states with deterministic demand and capacity

Considering the special case for strain demand and capacity being non-random variables, the fragility function of Eq. (7-34) becomes a step function:

$$P(\epsilon_{\text{dem}} > \epsilon_{\text{cap}} | \delta_{1,i}, \delta_{3,j}) = \begin{cases} 0, & \epsilon_{\text{dem}} < \epsilon_{\text{cap}} \\ 1, & \epsilon_{\text{dem}} > \epsilon_{\text{cap}} \end{cases} \quad (7-35)$$

The mean annual rate of equaling $\Delta\lambda_{\epsilon}(\epsilon_c, \epsilon_t)$ for strains that fall within each bin is then estimated via the expression:

$$\Delta\lambda_{\epsilon}(\epsilon_c, \epsilon_t) = \sum_i \sum_j P(\epsilon_{c,ij} \in I[\epsilon_c] \text{ and } \epsilon_{t,ij} \in I[\epsilon_t]) \Delta\lambda_{\Delta_1, \Delta_3}(\delta_{1,i}, \delta_{3,j}) \quad (7-36)$$

where $\epsilon_{c,ij}$ and $\epsilon_{t,ij}$ are the strain estimates for concurrent displacement components $\delta_{1,i}$ and $\delta_{3,j}$, while $I[\epsilon_c]$ denotes the interval $[\epsilon_c - c_w, \epsilon_c + c_w]$, where c_w is the bin width for discretizing compressive strains and $I[\epsilon_t] \equiv [\epsilon_t - t_w, \epsilon_t + t_w]$, where t_w is the bin width for discretizing tensile strains. For non-random demand and capacity, the MAR of equaling $\Delta\lambda_{\epsilon}(\epsilon_c, \epsilon_t)$ given ϵ_c and ϵ_t is practically estimated by summing the MAR of equaling values for strains that fell within the failure region.

7.4.2.2 Limit states with deterministic demand and uncertain capacity

Considering the demand as deterministic and the capacity as uncertain, the fragility function of Eq. (7-34) yields:

$$P(\varepsilon_{\text{dem}} > \varepsilon_{\text{cap}} \mid \delta_{1,i}, \delta_{3,j}) = \sum_{n=1}^N \left(\begin{cases} 0, & \varepsilon_{\text{dem}} < \varepsilon_{\text{cap},n} \\ 1, & \varepsilon_{\text{dem}} > \varepsilon_{\text{cap},n} \end{cases} \right) \frac{1}{N} \quad (7-37)$$

where the capacity distribution is discretized into N equiprobable points $\varepsilon_{\text{cap},n}$ using, for example, stratified or random sampling.

7.4.2.3 Limit states with uncertain demand and capacity

Finally, considering the general case for both demand and capacity being uncertain parameters, the fragility function of Eq. (7-34) becomes:

$$P(\varepsilon_{\text{dem}} > \varepsilon_{\text{cap}} \mid \delta_{1,i}, \delta_{3,j}) = \int_0^{+\infty} P(\varepsilon_{\text{dem}}(\delta_{1,i}, \delta_{3,j}) > \varepsilon_{\text{cap}} \mid \delta_{1,i}, \delta_{3,j}, \varepsilon_{\text{cap}}) P(\varepsilon_{\text{cap}}) d\varepsilon_{\text{cap}} \quad (7-38)$$

Using then a sufficiently fine discretization, the integral of Eq. (7-38) can be replaced by summations over N equiprobable $\varepsilon_{\text{cap},n}$ values:

$$P(\varepsilon_{\text{dem}} > \varepsilon_{\text{cap}} \mid \delta_{1,i}, \delta_{3,j}) = \sum_{n=1}^N P(\varepsilon_{\text{dem}}(\delta_{1,i}, \delta_{3,j}) > \varepsilon_{\text{cap},n} \mid \delta_{1,i}, \delta_{3,j}, \varepsilon_{\text{cap},n}) / N \quad (7-39)$$

The first term of Eq. (7-39) is essentially the cumulative distribution function of ε_{dem} evaluated at given values of sampled capacity $\varepsilon_{\text{cap},n}$. For example, assuming that demand follows a lognormal distribution, the probability can be expressed as:

$$P(\varepsilon_{\text{dem}}(\delta_{1,i}, \delta_{3,j}) > \varepsilon_{\text{cap},n} \mid \delta_{1,i}, \delta_{3,j}, \varepsilon_{\text{cap},n}) = \Phi \left(\frac{\ln \varepsilon_{\text{dem}}(\delta_{1,i}, \delta_{3,j}) - \ln \varepsilon_{\text{cap},n}}{\sigma_{\ln \varepsilon_{\text{dem}}}} \right) \quad (7-40)$$

7.5 CASE STUDY 1

As a case study to demonstrate the performance assessment methodology a typical API5L-X65 high-pressure natural gas transmission pipe is investigated, featuring an external diameter of $D=914\text{mm}$ and a wall thickness of $t=12.7\text{mm}$. The pipe steel is assumed to follow a bilinear stress-strain material law and the properties are presented in Table 6-1. Moreover, the pipe is coated with coal-tar and buried under 1.30m of medium-density cohesionless ($c=0\text{kPa}$) sand with internal friction angle $\varphi=36^\circ$ and unit weight $\gamma=18\text{kN/m}^3$.

The pipeline is considered to be intercepted by a normal fault with fault trace length $LF=40\text{km}$, pipe crossing site at distance $L_p=10\text{km}$ from the fault closest edge, fault dip angle $\psi=70^\circ$ and pipe – fault crossing angle $\beta=80^\circ$. The assumed seismological parameters of the fault and the corresponding uncertainty weight factors are listed in Table 7-6 and the minimum earthquake magnitude under consideration is $M_{\text{min}}=4.50$.

Table 7-6: Seismological parameters and uncertainty weight factors considered in case study 1

Parameter	Weight factor	Parameter	Weight factor	Parameter	Weight factor
$v_1=1.60$	$wv_1=0.30$	$M_{\text{max},1}=7.00$	$wM_1=0.25$	AD approach	$wD_1=0.50$
$v_2=2.00$	$wv_2=0.40$	$M_{\text{max},2}=7.20$	$wM_2=0.25$	MD approach	$wD_2=0.50$
$v_3=2.40$	$wv_3=0.30$	$M_{\text{max},3}=7.40$	$wM_3=0.25$		

7.5.1 Seismic hazard analysis

The mean fault displacement hazard curve at the pipeline crossing site is illustrated in Figure 7-3a. The descending curve shape is predictable, as the lower the fault displacement is, the higher is the mean annual rate of exceeding. The dispersion around the mean hazard curve is shown in Figure 7-3b together

with the plus/minus one standard deviation curves. The significant dispersion that is identified in Figure 7-3b depends on the selected seismological parameters and mainly the seismic rate v considered in this case study.

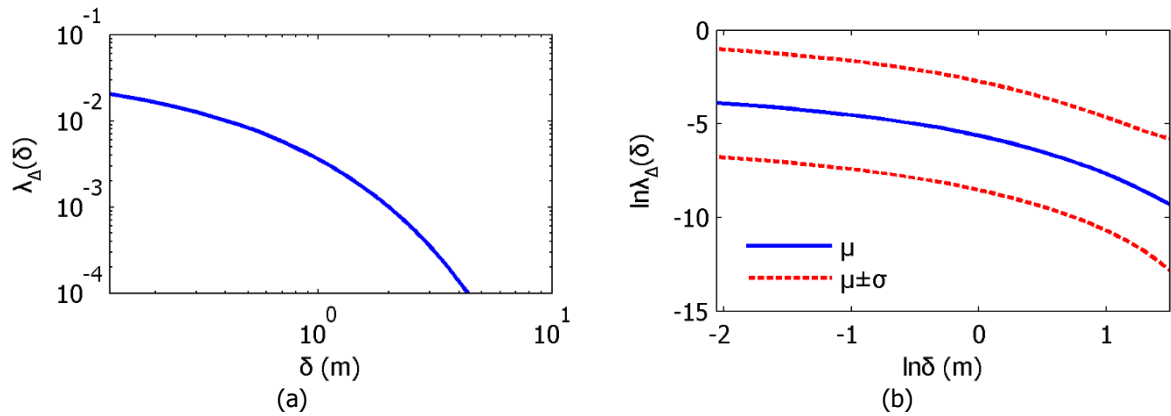


Figure 7-3: (a) Mean fault displacement hazard curve on pipeline crossing site, (b) mean fault displacement hazard curve and its dispersion

The MAR of equaling surface of the independent fault displacement components Δ_1 and Δ_3 is presented in Figure 7-4. This surface can be used by engineers to evaluate the rate of components reaching a specific value with reference to the fault type and the fault displacement magnitude. Additionally, the MAR of equaling surfaces for displacement components Δ_1 - Δ_2 and Δ_2 - Δ_3 are presented in Figure 7-5.

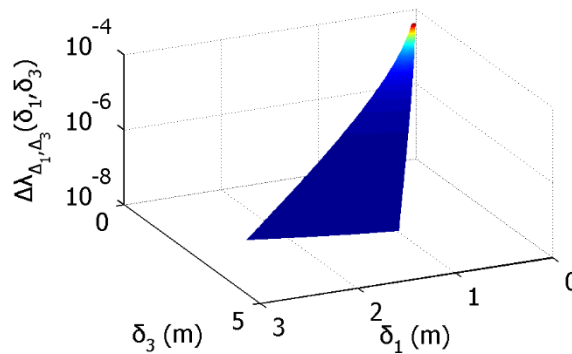


Figure 7-4: Mean annual rate of equaling surface for the independent fault displacement components Δ_1 - Δ_3

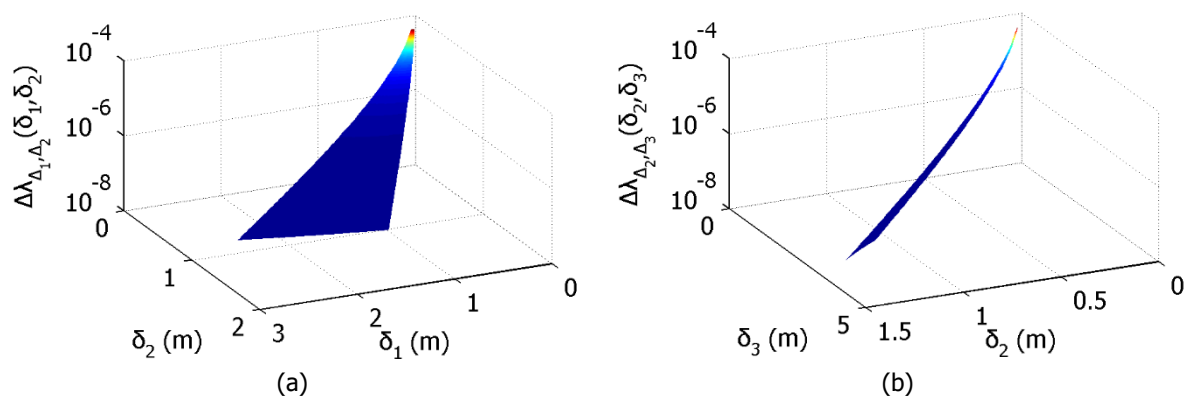


Figure 7-5: Mean annual rate of equaling surface for the dependent fault displacement components (a) Δ_1 - Δ_2 and (b) Δ_2 - Δ_3

The conditional probability of exceeding fault displacement is the spine of PFDHA and within it the normalization of fault displacement values can be carried out using either the average displacement

(AD) or the maximum fault displacement (MD). The identification of the AD versus MD approach impact on λ_{Δ} calculation is crucial. Thus, it is illustrated in Figure 7-6 that in this case the AD approach generally leads to higher rates than MD, while the AD approach curve has lower slope for the case study area.

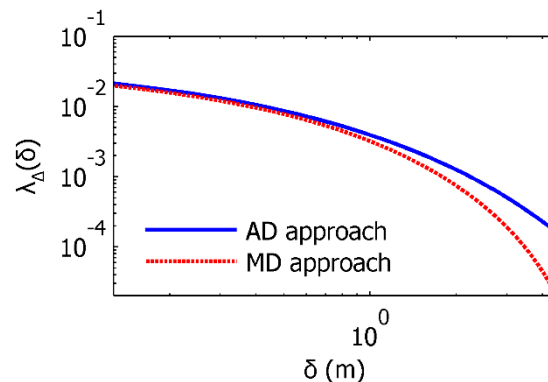


Figure 7-6: Mean fault displacement hazard curve adopting the AD versus the MD approach

Furthermore, in Eurocode 8 – Part 4 (European Committee for Standardization 2006) two limit states are introduced for buried pipelines: the Ultimate Limit State (ULS) related to 10% probability of exceedance in 50 years and the Damage Limit State (DLS) with 10% probability of failure in 10 years. The corresponding maximum allowable limit state rates are $\lambda_{ULS}=0.0021$ and $\lambda_{DLS}=0.0105$, respectively. For the example under investigation, the rates of limit states correspond to fault displacement $\delta_{ULS}=1.39\text{m}$ and $\delta_{DLS}=0.38\text{m}$, respectively. Disaggregation on earthquake magnitude is then performed to identify the contribution of earthquake magnitude to each limit state, assuming a maximum earthquake magnitude $M_{max}=7.20$. The earthquake magnitude contribution to seismic hazard is evaluated through the simplified form:

$$P(m_i | \delta) = \lambda_{\Delta}(\delta | m_i) / \lambda_{\Delta}(\delta) \quad (7-41)$$

where $P(m_i | \delta)$ is the probability of earthquake magnitude m_i given displacement δ , $\lambda_{\Delta}(\delta | m_i)$ is the MAR of exceeding fault displacement δ given magnitude m_i and $\lambda_{\Delta}(\delta)$ is the MAR of exceeding fault displacement considering all earthquake magnitudes. The disaggregation results on earthquake magnitude are presented in Figure 7-7 where the magnitude values are plotted on the horizontal axis and the magnitude probability on the vertical axis. It is highlighted in Figure 7-7 that earthquake magnitude 6.88 contributes more to ULS, while magnitude 6.54 contributes more to DLS.

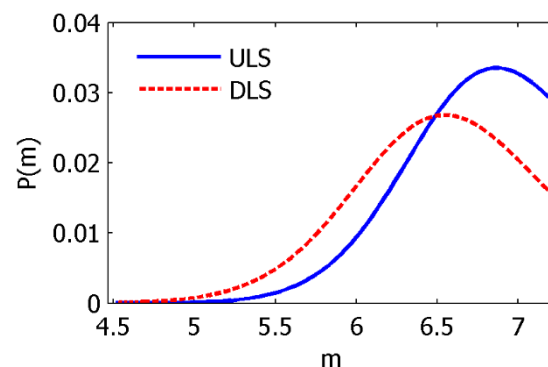


Figure 7-7: Disaggregation results on earthquake magnitude regarding the Eurocode 8 limit states

7.5.2 Pipeline structural analysis

Pipeline structural analysis provides the maximum developing tensile and compressive strain demand anywhere along the modeled length, without attention to its location. The numerical analysis of the

pipeline is carried out according to section 6.2. The pipeline response is shown in Figure 7-8 in terms of tensile and compressive strain demands. Failure modes such as local buckling and tensile rupture, are generally not correlated, as soil resistance, pipe – fault crossing angle, fault type and fault offset magnitude heavily affect pipeline structural response and the case of maximum tensile and compressive strain coexistence at the same location along the pipeline is rather rare. The pipeline response in terms of tensile and compressive strains is provided in Figure 7-8 within a wide range of the independent fault displacement components Δ_1 and Δ_3 . It is, however, more efficient to perform a set of structural analyses for the combination of fault displacement components that are consistent with the geometry of the pipeline – fault system for the fault crossing under investigation. Thus, the structural response of interest is enclosed by the marked sector in Figure 7-8, given that other combinations of fault displacement components are physically impossible for this case study. As the pipeline is subjected to large offsets of normal faulting, tension dominates the pipe response and consequently compression is limited.

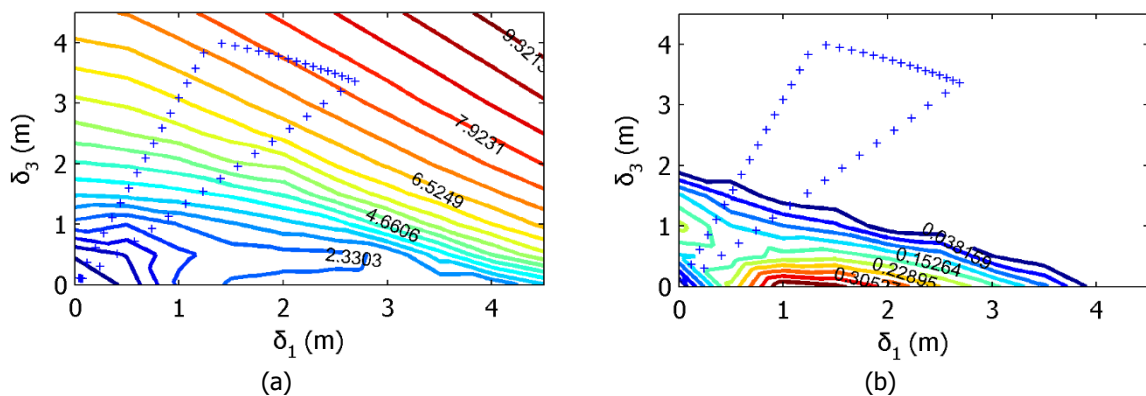


Figure 7-8: Pipeline structural response – (a) tensile strain demand and (b) compressive strain demand

7.5.3 Pipeline strain hazard analysis

Strain hazard is the combination product of seismic hazard and structural analysis results. Seismic hazard results, within the scope of case study 1, are represented by their mean values, accounting also for all pertinent uncertainties. The rates of failure mode limit states can be estimated by considering strain demand and/or capacity being either deterministic or probabilistic. In case of uncertain strain capacity, within the proposed methodology the capacity is assumed to be normally distributed with the corresponding parameters being listed in Table 7-7. The compressive strain limits, especially, have been extracted from experimental results of pipes subjected to bending without considering the effects of surrounding soil, which neglect its beneficial effect. The compressive limit equations are in practice enveloping curves and are extracted from data regression on the side of safety. Thus, compressive strain limits might be quite conservative and therefore the existence of 20% bias is assumed between the real mean value of the experimental results and the code expression. The assumed bias is based on judgement on results from Gresnigt and Karamanos (2009). The probabilistic demand is then assumed to follow a lognormal distribution with 30% dispersion, mainly due to soil randomness. The obtained limit states rates are finally listed in Table 7-8 considering both the operable limits and the pressure integrity limits after American Lifelines Alliance (2005).

Table 7-7: Probabilistic strain capacity uncertainty parameters

Parameter	Operable limits		Pressure integrity limits	
	Tensile	Compressive	Tensile	Compressive
Mean value	Eq. (2-8)	Eq. (2-4)	Eq. (2-9)	Eq. (2-5)
C.O.V.	20%	20%	20%	20%
Assumed bias	-	20%	-	20%

Table 7-8: Mean annual rate of exceeding tensile fracture and local buckling limit states by considering demand and capacity being either non-random or random

Demand	Capacity	Equation	Operable condition		Pressure integrity	
			$\lambda_{LS,t}$	$\lambda_{LS,c}$	$\lambda_{LS,t}$	$\lambda_{LS,c}$
non-random	non-random	(7-34) – (7-36)	0.0025	0	0.00076	0
non-random	random	(7-34), (7-36) – (7-37)	0.0026	0	0.00084	0
random	random	(7-34), (7-36), (7-39) – (7-40)	0.0027	2.83×10^{-7}	0.0093	1.69×10^{-18}

Assuming firstly that strain demand and capacity are deterministic and equal to the mean values of Table 7-7, the MAR of equaling strains after Eq. (7-35) is plotted in Figure 7-9, which shows that compressive strain demand remains sufficiently below the code-based limit, while tensile strain demand may exceed the corresponding limit for this tension-dominated setting.

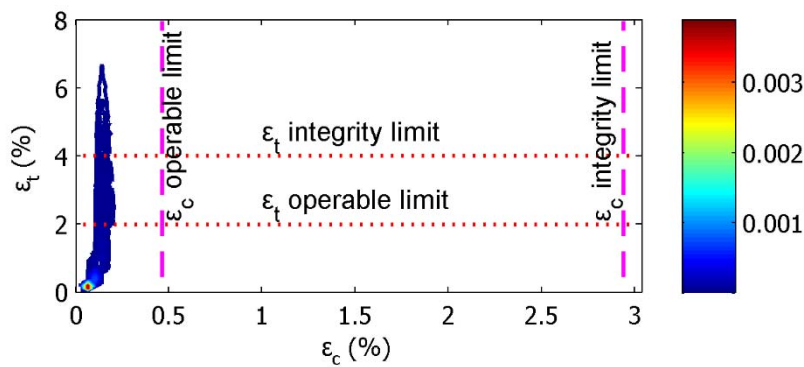


Figure 7-9: Contours of tensile and compressive strain mean annual rate of equaling (deterministic demand and capacity)

The decomposition of Figure 7-9 for tensile and compressive strains mean annual rates of equaling yields Figure 7-10. The MAR of equaling strain curves are similar to marginal probability mass functions and provide the mean annual rate of strain reaching a defined value. The corresponding hazard curves for tensile and compressive strains appear in Figure 7-11.

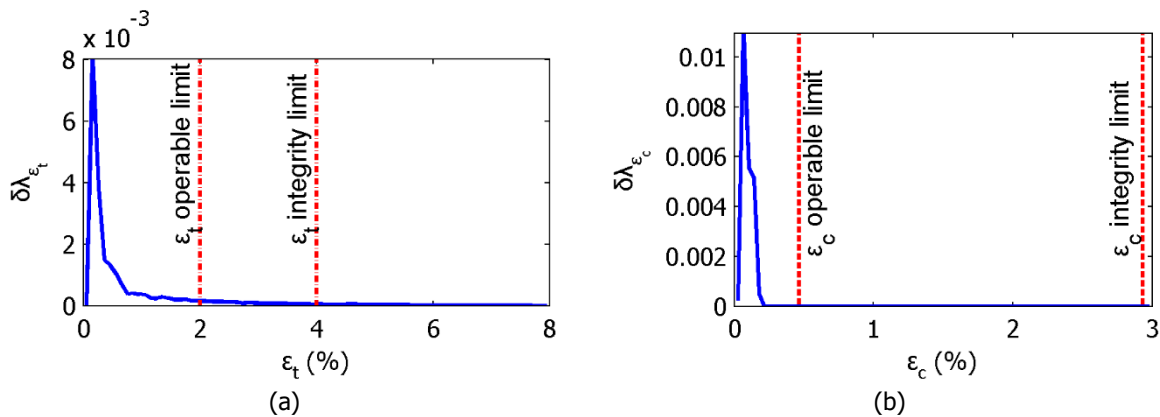


Figure 7-10: Tensile and compressive strains mean annual rate of equaling (deterministic demand and capacity)

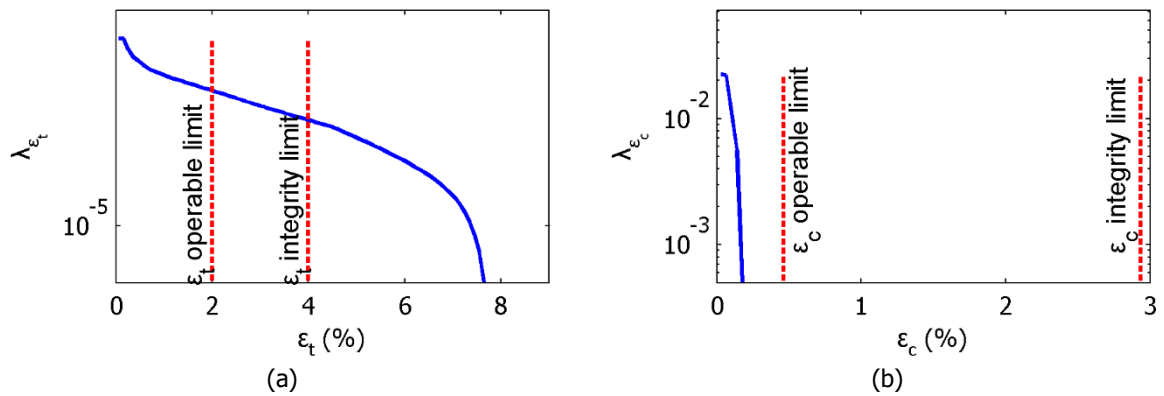


Figure 7-11: Tensile and compressive strains hazard curves (deterministic demand and capacity)

The pipeline fragility surface for tensile fracture is depicted in Figure 7-12, where the probability of strain demand exceeding strain capacity after Eq. (7-40) is plotted versus the selected vector intensity measure, i.e. the independent fault displacement components Δ_1 and Δ_3 . On the other hand, the local buckling probability has been shown to be very low and the corresponding fragility curves cannot provide useful information. It is noted that in general local buckling is an essential pipeline failure mode. However, the pipe response in the examined case is mainly tensional due to the following facts: (i) the considered fault dip angle is $\psi=70^\circ$ that is often found in nature (Abers 2009); this angle leads to increased pipe tension rather than bending, in contrast to the case of $\psi=90^\circ$, where pipe is subjected mainly to bending, (ii) the considered pipe – fault crossing angle is $\beta=80^\circ$, which indicates that the pipe is subjected to tension apart from bending and (iii) the fault investigated is of normal type but there is also fault movement along the fault plane, i.e. the fault-parallel horizontal component (Figure 2-1) is not zero.

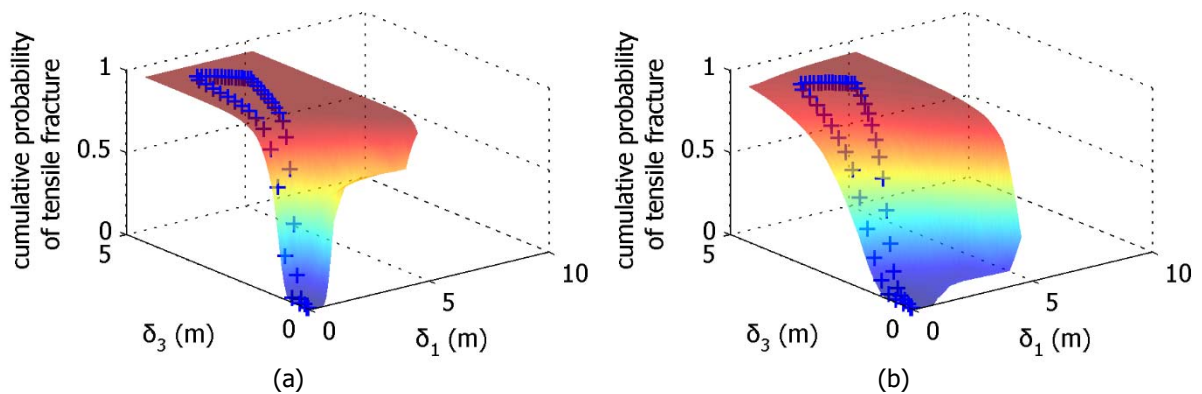


Figure 7-12: Cumulative probability of tensile fracture (random demand and capacity) for (a) operable limits and (b) pressure integrity limits, the crosses indicate the physical possible combinations for given pipeline – fault geometry

7.5.4 Deterministic versus probabilistic approach

Pipeline design against tectonic fault rupture is usually carried out in a deterministic way. It is thus essential to demonstrate the differences between the common analysis procedure (deterministic) and the probabilistic approach that is presented in the present study. In order to obtain qualitative and quantitative understanding of the way that each method handles the pipe assessment, the three step procedure followed in the probabilistic approach will be considered also in the deterministic one. Therefore, the first step is the estimation of the seismic load, i.e. the fault offset magnitude. The usual procedure employs empirical expressions using geometrical characteristics of the fault. Herein, the fault

rupture length equals 40km and the fault offset for normal faulting is estimated after Wells and Coppersmith (1994):

$$\log(\hat{\Delta}_{\text{average}}) = -1.99 + 1.24 \log(\text{SRL}) \quad (7-42)$$

which is the median estimate of the average fault displacement, which is selected based on the suggestions of Wells and Coppersmith (1994) based on the fact that the location of the maximum fault displacement is improbable to occur at the pipe crossing. SRL is assumed to be equal to the entire fault length as only a single scenario of fault rupture is considered. Therefore, the median estimate of the average fault displacement according to Eq. (7-42) yields 0.99m. For additional safety, the 84% estimate of 2.33m may be used (Cornell 1993). Proceeding to the second step, namely the pipe structural analysis, the principal fault displacement component Δ_3 is assumed to equal the corresponding upper bound of Table 7-5 with respect to fault offset magnitude, while the other two components are estimated via Eqs. (2-1) and (2-2). Thus, the obtained fault displacement components are $\Delta_1=1.51\text{m}$, $\Delta_2=0.76\text{m}$ and $\Delta_3=2.09\text{m}$. The maximum longitudinal tensile strain obtained from structural analysis is 3.39% and the compressive one is 0.13%. Without introducing any additional safety factors to add conservatism, it is easily concluded that the pipe will fail as $3.39\% > 2\%$ by considering the operable limit and will not fail as $3.39\% < 4\%$ by considering the pressure integrity limit (Table 7-7). Perhaps this result could be considered as a useful check for design purposes, yet it will surely lead to a highly conservative and expensive design. In other cases, it would be the exact opposite, as unknown level of safety is offered. On the other hand, the probabilistic approach, when done correctly, offers the desired compromise between cost and reliability.

7.6 CASE STUDY 2

The second case study aims at illustrating the performance assessment methodology for pipelines at fault crossings as an engineering decision making tool. A simplified version of the methodology is used by considering a buried pipeline being subjected to strike-slip fault rupture, where slip occurs along the vertical fault plane and consequently it states that $\Delta=\Delta_1$ and $\Delta_2=\Delta_3=0$ (Figure 2-1). A continuous pipeline (abbreviated as CP), a pipeline with two (abbreviated as 2PFJ) and a pipeline with four flexible joints (abbreviated as 4PFJ) are investigated (Figure 7-13). It noted that the flexible joints in 2PFJ are located at distance L_j and in 4PFJ at distances L_j and $L_j/2$ on each side of the fault, according to the procedure presented in section 6.3.1. Pipeline characteristics are presented in section 7.5.

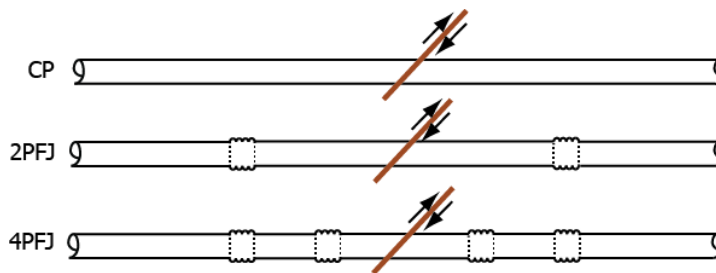


Figure 7-13: Continuous pipeline (CP), pipeline with two (2PFJ) and pipeline with four flexible joints (4PFJ) considered in case study 2

A pipeline – strike-slip fault crossing is considered with fault trace length $LF=40\text{km}$ and fault dip angle $\psi=70^\circ$, while the pipeline intercepts the fault trace in distance $L_p=10\text{km}$ with crossing angle $\beta=90^\circ$ (Figure 2-1). The seismological and uncertainty parameters considered in this case study are summarized in Table 7-9, while the minimum earthquake magnitude under consideration is $M_{\text{min}}=4.50$.

Table 7-9: Seismological and seismic hazard uncertainty parameters considered in case study 2

parameter	weight factor	parameter	weight factor	parameter	weight factor
$v_1=1.10$	$wv_1=0.30$	$M_{\max,1}=7.1$	$wM_1=0.20$	AD approach	$wD_1=0.50$
$v_2=1.20$	$wv_2=0.40$	$M_{\max,2}=7.2$	$wM_2=0.60$	MD approach	$wD_2=0.50$
$v_3=1.30$	$wv_3=0.30$	$M_{\max,3}=7.3$	$wM_3=0.20$		

7.6.1 Seismic hazard analysis

The mean fault displacement hazard curve is shown in Figure 7-14, where the descending curve shape is predictable, as the lower the fault displacement is, the higher is the mean annual rate of exceedance. It is noted that for the purpose of this case study, seismic hazard results are represented by their mean values accounting also for all pertinent uncertainties.

However, for a pure strike-slip fault, fault displacement Δ equals the principal fault displacement component Δ_1 ($\Delta=\Delta_1$) and consequently their MAR of exceedance are equal:

$$\lambda_{\Delta}(\delta) = \lambda_{\Delta_1}(\delta_1) \quad (7-43)$$

Therefore, for the considered case, the calculation of the fault displacement component hazard surface (section 7.2.4) is not applicable.

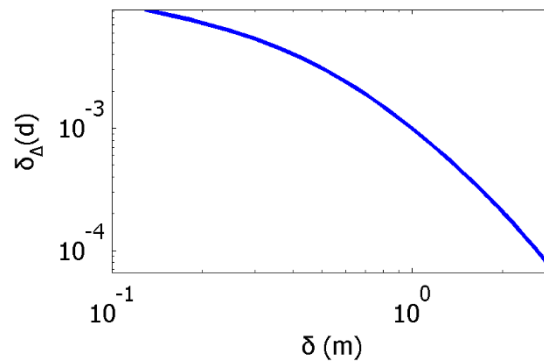


Figure 7-14: Mean fault displacement hazard curve on pipeline crossing site

7.6.2 Pipeline structural analysis

The pipeline structural analysis is carried out by employing the finite element model presented in section 6.2, using the finite element software ADINA (ADINA R&D 2006). The flexible joints are integrated in the pipelines in locations according to the procedure of section 6.3.1. The strain limits after American Lifelines Alliance (2005) for the pipelines under investigation are $\epsilon_{t,cap}=2\%$ and $\epsilon_{c,cap}=0.39\%$, corresponding to operable conditions (section 2.2.2). Numerical results regarding the developing strains from a single analysis, where the pipe is subjected to 1.83m of fault offset, are presented as an indicative example. The continuous pipeline (CP) is compared against the pipelines with flexible joints (2PFJ and 4PFJ). The pipeline displacements are illustrated in Figure 7-15, indicating a smooth curved shape for CP, while 2PFJ and 4PFJ follow a piece-wise linear shape.

The effectiveness of joints in terms of drastically decreasing bending moments is shown in Figure 7-16a where the bending moment distributions are plotted. On the other hand, from the axial force distributions (Figure 7-16b), a minor increase in axial force is reported.

The distributions of longitudinal tensile and compressive strains are presented in Figure 7-17, revealing a significant decrease achieved by the introduction of flexible joints. The strains are concentrated at the joints, so that much lower strains are developed along the pipe steel parts, reducing the overall risk of failure.

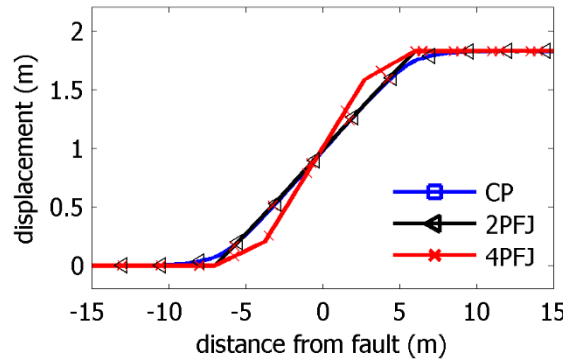


Figure 7-15: Deformation of continuous pipeline (CP) and pipelines with two (2PFJ) or four (4PFJ) flexible joints subjected to 1.83m fault offset

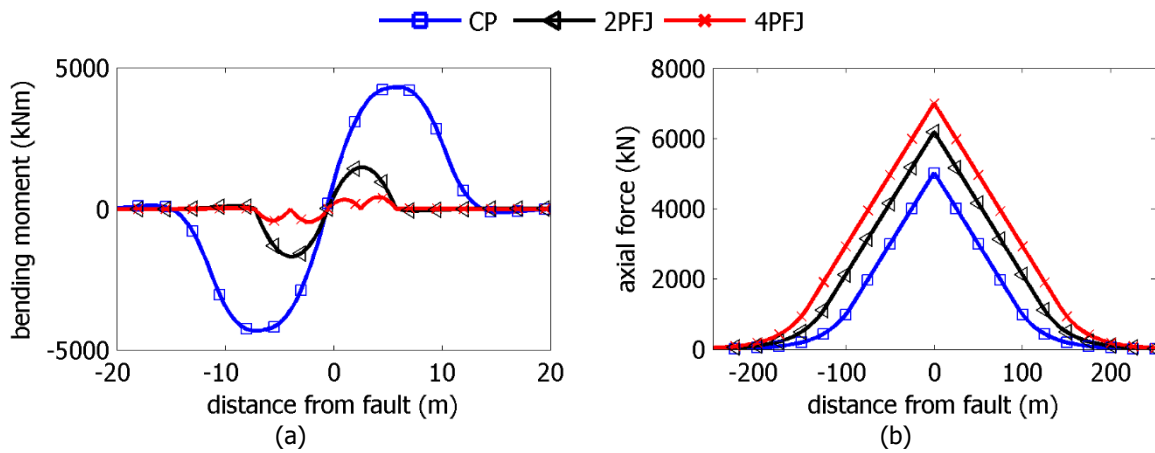


Figure 7-16: (a) Bending moment and (b) axial force distributions of continuous pipeline (CP) and pipelines with two (2PFJ) or four (4PFJ) flexible joints subjected to 1.83m fault offset

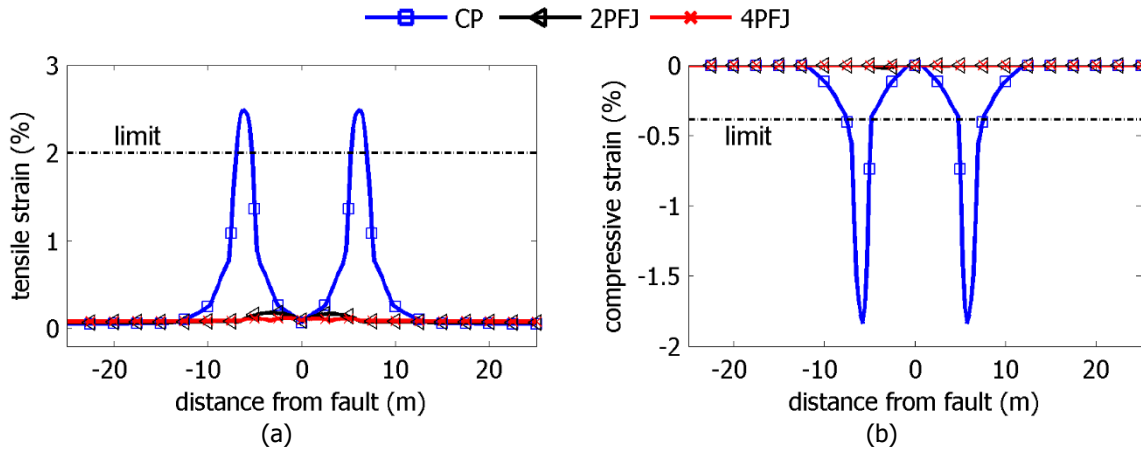


Figure 7-17: Longitudinal (a) tensile and (b) compressive strain distributions of continuous pipeline (CP) and pipelines with two (2PFJ) or four (4PFJ) flexible joints subjected to 1.83m fault offset

7.6.3 Strain hazard analysis

The mean annual rate of exceeding the tensile and compressive limit states is estimated using the general Eq. (7-34). For the case of strike-slip faulting it applies that $\Delta=\Delta_1$ and therefore, considering that tensile rupture and local buckling are not correlated failure modes, Eq. (7-31) is simplified to:

$$\lambda_{LS,t} = \sum_{\epsilon_c, \epsilon_t} P(\epsilon_{dem} > \epsilon_{t, cap}) \Delta \lambda_{\epsilon}(\epsilon_c, \epsilon_t) \tag{7-44}$$

$$\lambda_{LS,c} = \sum_{\varepsilon_c, \varepsilon_t} P(\varepsilon_{dem} > \varepsilon_{c, cap}) \Delta \lambda_{\varepsilon}(\varepsilon_c, \varepsilon_t) \quad (7-45)$$

Additionally, for the two limit states of tensile and compressive failure, respectively, the strain hazard analysis is carried out considering strain demand and capacity as non-random variables. So, the strain results of structural analysis are formalized as deterministic function of fault displacement Δ , i.e. $\varepsilon_t = h(\Delta)$ and $\varepsilon_c = h(\Delta)$, then Eqs. (7-44) and (7-45) can be simplified to:

$$\lambda_{LS,t} = \lambda_{\Delta} (h^{-1}(\varepsilon_{t, cap})) \quad (7-46)$$

$$\lambda_{LS,c} = \lambda_{\Delta} (h^{-1}(\varepsilon_{c, cap})) \quad (7-47)$$

Strain hazard analysis yields the tensile and compressive strain hazard curves of Figure 7-18a and Figure 7-18b, respectively. The hazard curves indicate that developing strains of CP exceed the code-based tensile limit of 2% and the compressive limit of 0.39%. The mean annual rate of exceeding compressive and tensile limit states for CP is $\lambda_{LS,t} = 8.46 \times 10^{-4}$ and $\lambda_{LS,c} = 40.94 \times 10^{-4}$, respectively. These may be compared against a 10% probability of failure in 50 years, or equivalently a mean annual rate of exceedance equal to $\lambda = 21 \times 10^{-4}$. Tensile failure is expected to occur less frequently, which is acceptable at this desired level of safety (operable limits), while compressive failure will occur about twice more often than allowed. Obviously, a more stringent safety requirement, e.g. 2% in 50 years would make the design more conservative for both failure modes. On the other hand, the corresponding tensile and compressive strains of pipelines with either two or four flexible joints are much lower than the code-based limits, and thus the corresponding MAR of exceeding limit states are negligible. In general, strain curves demonstrate the significant reduction of strains due to the introduction of flexible joints, as the developing strains on pipe steel parts are substantially decreased.

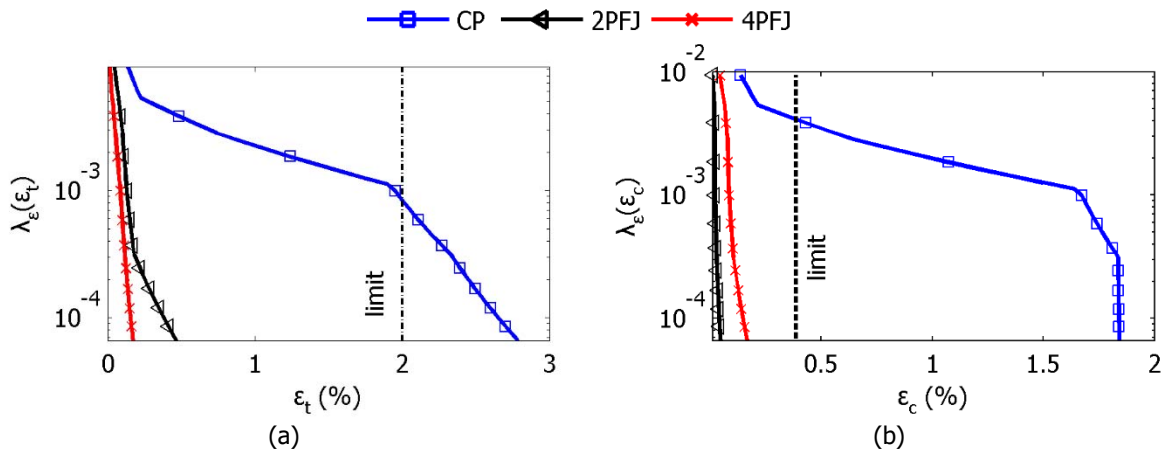


Figure 7-18: (a) Tensile and (b) compressive strain hazard curves for the three pipeline models (CP: continuous pipe, 2PFJ and 4PFJ: pipes with flexible joints)

7.7 CONCLUSIONS

A methodology for performance assessment of buried pipelines at fault crossings is presented. The seismic hazard analysis is performed at first through an indirect method to quantify the probabilistic nature of fault movement by implementing the Probabilistic Fault Displacement Hazard Analysis (PFDHA). The PFDHA conceptual algorithm for pipeline – fault crossing accounts for all pertinent seismological parameters and includes the probability of the fault rupture intercepting the pipeline. Epistemic uncertainties are handled through a typical logic tree formulation. The fault displacement is

then decomposed to the corresponding components in the three-dimensional space. Fault components are selected as the vector intensity measure to consider the impact of components displacement on the pipeline mechanical behavior. The fault offset decomposition is a dominant aspect of the process as it allows the engineer to incorporate a wide range of spatial fault movement values in the seismic hazard analysis, which is crucial to assess the pipeline behavior due to faulting in light of the uncertain fault movement in nature. A simple and approximate procedure is also introduced to estimate the principal fault displacement component with respect to the fault type being strike-slip, normal or reverse. Pipeline structural analysis is then performed to account for the effect of fault displacement components on the pipeline and estimate the model demand in terms of maximum developing tensile and compressive strains. Structural analysis can be performed either analytically or numerically. Finally, the convolution of seismic hazard and structural response yields the joint hazard surfaces of tensile and compressive strains. Strain hazard surfaces provide all the necessary information regarding the potential of failure due to local buckling or tensile rupture. Furthermore, expressions are presented for estimating the corresponding rates of failure limit state, considering accordingly demand and capacity uncertainty.

Finally, two case studies are presented to illustrate the application of the proposed methodology. In the first case study, a complete application of the methodology is presented by dealing with a continuous pipeline subjected to normal faulting, where slip occurs in three dimensions. The results of the seismic hazard analysis are discussed at first regarding (i) the dispersion around the fault displacement mean hazard curve, (ii) the effect of the average versus the maximum displacement option of PFDHA on the fault displacement hazard curve and (iii) disaggregation results on the earthquake magnitude in Eurocode 8 limit states. Thereafter, the pipeline structural response is shown in terms of tensile and compressive strain demand. Finally, strain hazard analysis results are examined by considering strain demand and capacity as non-random or random variables. In each case the tensile rupture and local buckling rates of failure are presented, indicating the effect of demand and/or capacity uncertainty on the corresponding rates of failure. In the second case study, a simplified version of the methodology is used by considering a strike-slip fault, where the principal fault displacement component equals the fault displacement. The response of a continuous pipe is compared to those of two pipes with flexible joints. The strain hazard analysis does not consider demand and capacity uncertainty. The scope of the case study is to demonstrate the performance assessment methodology as an engineering decision making tool. For that purpose, strain hazard curves for tensile and compressive strains are constructed. They are useful visual tools, used by the engineers to assess the effectiveness of flexible joints in mitigating the consequences of faulting on buried pipelines by comparing the rate of a potential failure for every case. It is noted that failure modes associated with the flexible joints themselves were not considered in the analysis.

Part of the work presented in this chapter has been submitted for publication (Melissianos et al. 2016c).

8 SUMMARY AND CONCLUSIONS

8.1 EXTENDED SUMMARY

Objective of the present doctoral thesis is the investigation of the behavior and the formulation of practical guidelines for the design of onshore, buried steel pipelines transmitting oil and gas, subjected to seismic fault rupture and equipped with flexible joints as innovative mitigating measure against the consequences of faulting. To that effect, a combined experimental and numerical approach is adopted and a performance assessment methodology for pipelines at fault crossings is developed.

Buried steel pipelines transporting oil and oil products are among the most vital links of the energy supply chain and their contribution to the economy is significant. Pipelines extend over long distances, connecting oil rigs and oil consumers, and they transverse territories with various geological conditions. Thus, crossing seismic areas that are prone to large ground displacements, such as due to landslides, tectonic fault ruptures and ground settlements, may be unavoidable. Reports after major past earthquake events have demonstrated that the dominant geohazard causing severe damage to pipelines is fault rupture. If a tectonic fault is activated, a buried pipeline crossing the fault is forced to follow the ground movement, thus developing deformations and stresses, having bending, shear and axial components, depending on the relative orientation of the pipeline with respect to the fault plane and the fault dip angle. In such cases, the most common failure modes of the pipeline are local buckling of the pipeline wall caused by significant compression and tensile weld fracture due to developing tension. The pipeline design against fault rupture is carried out in strain terms, given that the problem is displacement-controlled. Hence, pertinent design codes provide expressions of allowable upper bounds for the compressive and the tensile strains. The safety evaluation of buried pipes is thus carried out by ensuring that the developing strains remain below the code-based limits, in order to avoid local buckling and/or tensile failure.

Analysis and design of buried pipelines at fault crossings is a highly nonlinear problem that is governed by the pipe – soil interaction. Pipe response to ground movement differs from that of common civil engineering structures. The latter are founded in the soil and in case of an earthquake event, their foundation follows the ground motion and their superstructure is excited due to inertia. Buried pipes, on the other hand, are embedded in a trench, a few meters below the ground surface, and consequently, when a fault is activated, the pipe is forced to follow the ground movement, thus developing excessive deformation. Research on the assessment of buried pipeline response due to fault rupture through experimental, analytical and numerical studies is extensive.

Even though the grave environmental, social and economic losses (e.g. environment rehabilitation, human injuries, fuel flow interruption, pipe repair, etc.) of a pipe rupture necessitate the implementation

of appropriate seismic countermeasures in order to minimize the consequences of fault activation and the potential of pipe failure, pertinent research on mitigating measures is relatively limited. In engineering practice, a variety of measures is used nowadays, whose primary aim is the reduction of the developing friction on the pipe – soil interface (e.g. trench backfilling with loose granular soil, pipe wrapping with friction-reducing geotextile, use of concrete culverts), or the increase of the pipe strength (e.g. steel grade upgrade, pipe wall thickness increase). However, the range of application of these measures is not broad (e.g. maximum allowable fault offset magnitude with respect to pipe diameter), while their efficiency has not been fully quantified considering also that reliable estimation of soil properties is inherently difficult.

Flexible joints are proposed as an innovative mitigating measure and are introduced along the pipeline in the fault vicinity, aiming at absorbing the developing deformation through relative rotation between adjacent pipeline parts, which then remain relatively undeformed and consequently unstressed. This concept introduces a different design approach for reducing the risk of local buckling and/or tensile failure, by transforming the pipeline structural system from continuous to segmented, thus concentrating strains at the joints, instead of reducing the soil-induced friction. Flexible joints are mechanical products used in industrial piping networks to absorb thermal expansion, machinery vibration and thrust and also as connecting devices between the adjacent parts of segmented pipelines. The main type of commercially available flexible joints are the expansion joints, the ball joints and the bellows. The first two types, namely expansion and ball joints have been studied by numerous researchers as possible mitigating measures for low pressure water and sewer pipelines, while their behavior in segmented pipes subjected to ground movement has been also investigated. However, all pertinent research carried out until now has not considered the case of high-pressure oil and gas pipes subjected to fault rupture, while bellow-type joints have not been examined. Following a study on the properties of commercial flexible joints, it was concluded that the appropriate type of joint for buried high-pressure pipes under faulting applications is the metallic bellow-type and in particular the single or the hinged bellow, with the latter being suggested for pipes under very high pressure. It is noted that for application of bellow-type joints in buried oil and gas pipes, formulation of specifications regarding, among others, the pipe – joint welding, joint protection against corrosion and external damage and joint contribution to pipeline operability is necessary.

Various methodologies, mainly analytical, have been proposed for the analysis and seismic evaluation of segmented pipelines subjected to seismic fault rupture. However, these approaches have been developed for pipes, in which the adjacent segments are connected with flexible joints that are not of bellow-type and do not ensure the pipe continuity. The assumptions used in these approaches on the one hand are suitable for preliminary design only and not for final design, and on the other hand are not applicable for bellow-type joints. Aiming at contributing towards filling this gap, the behavior of buried pipelines with flexible joints has been addressed numerically in the context of the present thesis.

In this thesis, the design and execution of a series of experimental tests of four circular hollow section beams, three continuous and one with flexible joints (single bellow-type), are initially presented. The specimens were clamped at their ends and subjected to transverse displacement applied at the middle, in three-point displacement-controlled bending tests. The test layout was selected so that the deformed shape of each half resembles the s-shaped deformation exhibited by a pipe subjected to strike-slip fault rupture. The effect of the surrounding soil was not considered, which is also the case in pertinent experimental studies published in the literature for the strength evaluation of pipes. The test results for the continuous specimens and the specimen with flexible joints are presented by means of photographs at various displacement levels, as well as load – displacement and strain – displacement curves. The continuous specimen's behavior was found to be initially elastic, up to the formation of plastic hinges at the locations of maximum bending moment and the post-yielding response was governed by material nonlinearity. The global response of the continuous specimen was that of a fixed beam under

transverse displacement at the middle and the deformation was in the form of an s-shaped curve. On the contrary, the response of the specimen with flexible joints was fully elastic and the deformation was segmented, characterized by large rotations at the joints. Based on the comparison of experimental results, the effectiveness of flexible joints in reducing the developing longitudinal strains by three orders of magnitude and thus efficiently protecting the pipe against failure has been convincingly demonstrated.

Next, numerical modeling of the experimental tests with the finite element method is presented, aiming at predicting the specimens' behavior and extracting useful remarks for the subsequent stages of the research. The continuous specimens were meshed with both beam and shell elements, while their boundary conditions were assumed to be rigid, following an investigation on the effect of stiffness of the specimen – testing frame connection to the specimen's behavior. Additionally, the effect of longitudinal residual stresses due to seam-welding of the specimen at the manufacturing stage, adopting stress distributions published in the literature, was incorporated in the shell models by discretizing the section into appropriate zones, each of which had different initial stress. It was concluded that if geometrical and material nonlinearity, as well as longitudinal residual stresses due to seam-welding, are included in the analysis, a satisfactory agreement between numerical and experimental results is observed, in terms of strength, deformation and developing strains. Then, the specimen with flexible joints was modeled with beam-type finite elements and the flexible joints with nonlinear rotational and translation springs, whose properties were evaluated by individual experimental tests. Comparison of numerical and experimental results indicated a good match.

As explained above, the integration of flexible joints between adjacent pipe parts aims at protecting the pipe against local buckling and/or tensile fracture. However, in case of reverse faulting the pipeline is subjected to high compressive forces, and the reduction of overall stiffness induced by the flexible joints may lead to a third possible failure mode, namely flexural buckling, also known as upheaval buckling, as the pipe may then deform heavily within the trench or even outside of it. To investigate this potential, a Winkler beam with internal flexible joints (hinged bellow-type) was created as the appropriate numerical model. An internal hinge, modelling flexible joints, modifies the beam global stiffness and consequently affects the corresponding buckling and post-buckling behavior. The extent of this effect depends on the relative pipe – joint – soil stiffness and has to be taken into account in case flexible joints are applied to mitigate the aftereffects of faulting. In order to acquire qualitative understanding, from a structural design point-of-view, of the interaction between the hinge and the soil stiffness for different cases, the beam under investigation is considered as either simply-supported or clamped and with one or two equally-spaced internal flexible joints. The analysis model parameters were chosen to be representative of the case of a buried pipe subjected to tectonic fault rupture. Firstly, elastic critical buckling loads and the corresponding eigenmodes are numerically obtained via linearized buckling analysis. Eigenmode cross-over is also investigated by considering the interaction of soil and hinge rotational stiffness. Then, geometrically nonlinear analyses with imperfections are performed, indicating for most cases descending post-buckling paths, thus unstable post-buckling behavior, with the exception of cases of very soft soil. The response sensitivity to initial geometrical imperfections is also addressed, indicating insignificant effect of the imperfection shape but, on the contrary, significant impact of the imperfection magnitude on the post-buckling behavior and ultimate load. Moreover, the beam has been considered to be embedded in soil exhibiting different stiffness in the upward and the downward direction. Corresponding results show that such soil nonlinearity has to be considered in the analysis in order to obtain reliable results of the beam's buckling behavior. The results are compared for each case to the corresponding ones of a continuous beam, in order to highlight the impact of internal hinges on the beam overall buckling behavior.

Next, the effectiveness of flexible joints in buried pipelines subjected to strike-slip fault rupture has been numerically evaluated. Firstly, the proposed numerical model for the analysis of buried pipelines with

flexible joints, based on the model of beam resting on soil springs, is described in detail. Then, the optimization of the flexible joints' configuration in terms of number and location is outlined. The behavior of pipes with flexible joints subjected to strike-slip fault rupture is presented and the essential differences compared to the continuous pipe in terms of deformation, developing stress-state, stress and strain distributions and surrounding soil response are highlighted. Consequently, extensive parametric studies are carried out to determine the effect of pipeline – fault crossing angle, fault offset magnitude, joint angular capacity, burial depth and diameter over thickness ratio on the joint efficiency. Crossing angle and fault offset magnitude dominate the relationship of the bending and axial forces developing along the pipe and thus affect the behavior of pipes with flexible joints. On the contrary, burial depth and diameter over thickness ratio have insignificant influence. The uncertainty regarding the exact fault trace location is addressed, indicating the need for integrating joints along the pipe length, where fault trace might appear on the ground surface, as is also the case for other mitigating measures. The effectiveness of flexible joints is eventually compared to other commonly used mitigating measures in terms of developing strains, highlighting their competitiveness. In general, the efficiency of flexible joints in protecting the pipe against local buckling and/or tensile failure is demonstrated convincingly. The results are used to formulate preliminary design guidelines for the practical use of flexible joints in buried pipelines crossing active faults.

Finally, a performance assessment methodology for buried steel pipelines at fault crossings is presented. The uncertainty associated with earthquakes and fault displacements generates the need to determine the distribution of fault displacement that has to be taken into account for the seismic risk assessment of a pipeline and thus a probabilistic approach is selected. The proposed methodology is based on the framework of Performance-Based Earthquake Engineering and consists of three interrelated steps: seismic hazard assessment, pipe structural analysis and pipe strain hazard assessment. At first, Probabilistic Fault Displacement Hazard Analysis is performed to quantify the probabilistic nature of the fault offset, while the magnitude of the three fault displacement components in space is determined. Decomposing the fault offset in three components leads to the introduction of a vector to serve as the measure of intensity, instead of the typical scalar (e.g. peak ground acceleration or displacement). Additionally, aleatory and epistemic uncertainties are considered in the seismic hazard analysis through sampling and logic trees, respectively. Then, three-dimensional structural analysis of the pipe is performed, using the nonlinear beam-type finite element model. Finally, the convolution of seismic hazard and structural response results in joint hazard surfaces of compressive and tensile strains leads to the estimation of the mean annual rate of exceeding any limit-state of interest. Strain demand and capacity uncertainty are incorporated in the analysis and their effect on the mean annual rate of exceeding local buckling or tensile fracture is evaluated. To demonstrate also the proposed methodology as an engineering decision making tool, it is implemented to compare the failure probability of a continuous pipe and the corresponding pipe with flexible joints.

In conclusion, flexible joints are highlighted as a very promising alternative for the protection of buried steel pipelines against seismic fault activation.

8.2 CONCLUDING REMARKS

In this section the main conclusions derived from the several parts of the thesis are summarized. In the first stages of this investigation, evaluation of the properties of commercially available flexible joints revealed that the appropriate type of joints for application as a mitigating measure to onshore buried oil and gas high-pressure pipelines subjected to seismic fault rupture are the bellows, which can withstand high pressure and ensure pipe structural continuity. Thus, this type of joint was considered for subsequent investigation.

The experimental investigation of continuous beams and beams with flexible joints under transverse displacement, modeling buried pipes under strike-slip fault rupture and without considering the effect of the surrounding soil, highlighted the following aspects:

- Continuous specimens behaved elastically until yielding took place at the locations where the maximum bending moment develops. Post-yielding behavior was dominated by the material nonlinearity.
- Specimen with flexible joints behaved totally elastically.
- Comparison of experimental results confirmed that the integration of flexible joints leads to the modification of the structural system from continuous to segmented, thus achieving strain reduction in the order of three times and load reduction in the order of two times.
- Good agreement between numerical models consisting of shell elements and experimental results was observed for the continuous specimens at both global (specimen deformation) and local (strain) level. Considering longitudinal residual stresses due to seam-welding at the specimen manufacturing stage led to relative improvement of the numerical results, depending on the location of the seam-weld on each specimen, the considered simplified distribution of longitudinal residual stresses and the developing stress-state of the specimens.
- Numerical modeling of the specimen with flexible joints with beam-type finite elements for the pipe and translational and rotational springs for the flexible joint proved sufficient, exhibiting sufficient agreement with experimental results

The conclusions from geometrically nonlinear analyses of the simplified numerical model created to investigate the overall buckling behavior of beams with internal flexible joints resting on foundation and subjected to compressive load, can be summarized as follows:

- Internal hinges modify the beam global stiffness and affect the overall buckling behavior, reducing the linear and nonlinear buckling loads. The extent of this effect depends on the relative pipeline – joint – soil stiffness and has to be taken into account in case flexible joints are used as mitigating measures.
- Increasing rotational stiffness progressively restores beam continuity. Increasing soil stiffness leads to eigenmode cross-over, provided that hinge rotational stiffness is sufficiently high.
- Antisymmetric eigenmode shapes are dominated by the hinges' location on the beam, while symmetric shapes are not affected.
- Geometrically nonlinear analysis with imperfections revealed that hinged beams have descending post-buckling equilibrium paths in the majority of the cases under investigation, with the exception of very low soil stiffness, which leads to stable post-buckling response, same as in laterally free beams.
- The imperfection magnitude was found to highly influence the beam ultimate load, highlighting the need of conservative design assumptions and adoption of appropriately high safety factors. On the contrary, the imperfection shape was shown to play a relatively minor role compared to imperfection magnitude for the overall buckling behavior, at least among considered imperfection shapes.
- Considering soil to exhibit lower stiffness in the upward than in the downward direction, was found to have significant effect on the beam overall buckling response in terms of deformation shape as well as ultimate load.

The numerical investigation of the behavior of pipelines with hinged bellow-type flexible joints under strike-slip fault rupture led to the following conclusions:

- Flexible joints integrated in the pipeline in the fault vicinity succeed in concentrating developing strains and retaining the pipe adjacent segments virtually undeformed and consequently unstressed. Strain concentration is achieved through significant rotation of the adjacent pipe segments.

- The optimum configuration of joints can be derived based on the bending moment distribution of the continuous pipeline, considering that joints act in the pipeline structural system as internal hinges.
- Flexible joints have significant contribution to developing bending moment reduction, while they may lead to minor axial force increase.
- Developing longitudinal strains are drastically decreased due to the introduction of joints, thus efficient protection of pipeline against local buckling and tensile fracture is achieved.
- The response of the surrounding soil is not affected.
- Fault offset magnitude and pipe – fault crossing angle play a significant role on the effectiveness of joints in terms of strain reduction, in case of strike-slip fault rupture. The efficiency of joints is maximized for pipe – fault crossing angles close to 90° , where bending moment dominates the pipeline behavior. Joints significantly contribute to strain reduction for larger crossing angles than 90° , in which case the pipe is subjected to significant compression, provided that precautions are taken regarding the considerable pipe deformation within the trench. For crossing angles lower than 90° , the pipe is also subjected to tension and hinged bellows should be used for higher angles than 70° . In the last case it would be desirable for the bellows to be capable of accommodating some axial deformation in order to expand their efficiency to lower crossing angles.
- Pipe burial depth and diameter over thickness ratio have nearly negligible affect the behavior of pipes with flexible joints.
- The introduction of flexible joints is a competitive mitigation approach compared to the usual approaches in terms of strain reduction for the range of pipeline – fault crossing angle mentioned above.
- Integration of joints is necessary along the entire pipe length where the appearance of fault trace on the ground surface is likely, considering the inherent uncertainty in the exact location, akin to engineering practice for the usual mitigation approaches. Joints should be integrated in the pipeline at constant distances L_j when pipe – fault crossing angle is close to 90° , while for lower angles the optimum distance is $L_j/2$. If there is uncertainty regarding the angle β , then distance $L_j/2$ should be selected. Length L_j is defined as the distance between the location of the maximum moment and the fault trace of the corresponding continuous pipe.

The performance assessment methodology of pipelines at fault crossings allows estimating the tensile or compressive failure probability by considering the fault offset and corresponding epistemic and aleatory uncertainties, as well as strain demand and capacity uncertainties through the framework of Performance-Based Seismic Engineering framework.

8.3 RESEARCH CONTRIBUTION AND INNOVATION

An investigation of the behavior of buried pipelines with flexible joints subjected to seismic fault rupture has been presented, aiming at the formulation of practical design guidelines. Flexible joints of bellow-type have been proposed as innovative mitigating measures to minimize the potential of pipe failure. Both experimental and numerical research has been undertaken to evaluate the response of pipelines with flexible joints, while a probabilistic seismic engineering framework has been adopted to assess their performance at fault crossings. Contributions to the state-of-art in engineering science as well as engineering practice have been made, as outlined in more detail next. The numerical and experimental investigation have validated this new method of seismic protection for pipelines, while the performance assessment framework has delivered a robust and uncertainty-proof approach to support their use in practice. At the same time any new or existing pipeline crossing active faults can be now assessed at the highest standards. The achieved innovation of the thesis, both scientific and practical, is presented subsequently.

8.3.1 Contribution to the advancement of engineering science

The innovations that contribute to the advancement of engineering science can be summarized as follows:

- Commercial bellow-type flexible joints have been proposed as a mitigating measure to protect buried pipes subjected to fault rupture. This approach differs significantly from the commonly used measures that aim at reducing the developing pipe – soil friction. The flexible joints are part of the structural system and actually transform the pipeline from continuous to segmented (Melissianos and Gantes 2014c, 2015b). Flexible joints have not been investigated until now for buried high-pressure pipes under faulting applications.
- Original experimental tests of circular hollow section beams, continuous and with flexible joints, under transverse displacement have been conducted to demonstrate the effectiveness of flexible joints in reducing the developing strains and to verify the transformation of the structural system from continuous to segmented. Experimental results included both deformation (in global and local scale) and strain measurements to provide adequate and sufficient understanding of the mechanical response of pipes with flexible joints in comparison to continuous ones (Melissianos et al. 2016b). Testing procedure followed the common approach published in the literature regarding the strength evaluation of pipes without considering the effects of surrounding soil. Geometrically and materially nonlinear analyses were performed to reproduce the experimental results. The effect of longitudinal residual stresses due to seam-welding of the specimen were included in the analysis of continuous specimens. Flexible joints were modeled with nonlinear springs, whose properties were obtained from individual tests of the flexible joints. Comparison of experimental and numerical results showed a good match (Melissianos et al. 2016b).
- A simplified numerical model was established to investigate the overall buckling behavior of internally hinged Winkler beams resting on foundation and subjected to compressive load, modeling buried pipes with bellow-type flexible joints under reverse faulting. Model parameters have been chosen to be representative of the case of buried pipes under fault rupture. The investigation revealed that soil and hinge rotational stiffness interact, thus creating a double parameter problem. The internal hinges affect significantly the beam critical buckling load, eigenmode cross-over, ultimate load and the post-buckling behavior compared to the corresponding continuous beams (Gantes and Melissianos 2014; Melissianos and Gantes 2014a; b, 2016), while special attention was given on the behavior sensitivity on geometrical imperfections.
- A finite element model was established to evaluate the mechanical response of buried pipes with flexible joints at strike-slip fault crossings (Melissianos and Gantes 2015a). The performed numerical studies revealed the basic aspects of the behavior of pipes with flexible joints, in terms of deformation, developing stress-state and surrounding soil response. Extensive parametric studies of pipes with flexible joints at strike-slip fault crossing were carried out to investigate the effect of pipe – fault crossing angle, fault offset magnitude, burial depth, diameter over thickness ratio and fault trace uncertainty, while the effectiveness of joints was compared to commonly used seismic countermeasures. Results provided evidence on the efficiency of the proposed measure (Melissianos et al. 2016a).
- A methodology for performance assessment of buried pipes at fault crossing was developed. The first step of the proposed methodology is the standard approach of Probabilistic Fault Displacement Hazard Analysis, considering that the site of interest is located on the fault. This was further improved and extended by decomposing the fault displacement into its three spatial components, to account for the three-dimensional fault movement in nature with respect to the fault type. In the second step structural analysis is carried out, while in the third seismic hazard results are convolved with structural results to conduct the performance assessment. The proposed methodology fills a research gap in

the performance assessment of pipes at fault crossings by introducing the decomposition of fault displacement into individual components acknowledging the different pipe response to different fault deformations and providing a simplified approach for the quantification of the probabilistic nature of fault offset (Melissianos et al. 2014b, 2015b, 2016c).

8.3.2 Contribution to the advancement of engineering practice

It is often necessary to use seismic countermeasures in buried pipelines under fault rupture, whose effectiveness is either limited or not fully known, and is related many times to high capital and replacement costs. Flexible joints are herein proposed as an innovative mitigating measure to reduce the risk of pipe local buckling and/or tensile rupture in such cases. The main contributions of the present doctoral thesis to engineering practice can be summarized as follows:

- The efficiency of bellow-type flexible joints as mitigating measures in buried pipe – fault crossing has been qualitatively and quantitatively demonstrated convincingly.
- Joints should be introduced along the entire pipe length over which the fault trace may be encountered, at constant distances derived from the bending moment distribution of the corresponding continuous pipeline. Thus, fault trace uncertainty is addressed, in a similar manner as in other mitigating methods.
- The effectiveness of joints is much better for pipeline – fault crossing angle around 90° , in which case they can successfully handle fault offset of high magnitude, regardless of pipe burial depth and wall thickness over diameter ratio.
- In such cases, flexible joints offer much better performance than most other commonly used mitigating measures, providing engineers and pipeline operators with a reliable mitigating measure, especially for high fault offsets.
- The proposed methodology for performance assessment of buried pipes at fault crossings can be used by design engineers as a reliable engineering decision making tool, e.g. throughout the route selection procedure or to evaluate the efficiency of alternative mitigating measures. The main advantages are: (i) low computational effort, (ii) incorporation of seismic hazard uncertainty, (iii) robust pipeline numerical models available to analysis by any commercial software, (iv) incorporation of any strain-related limit state, (v) incorporation of demand and capacity uncertainty and (vi) expandable to loss assessment.

8.4 SUGGESTIONS FOR FUTURE RESEARCH

The topic of buried pipelines with flexible joints under seismic fault rupture is broad and cannot be fully covered in the context of a doctoral thesis. Some suggestions for future research are summarized below:

- Experimental investigation of the efficiency of joints in reducing the pipe developing longitudinal strains by considering the effects of the surrounding soil, using an appropriate experimental set-up, such as a shear box or a centrifuge.
- The simplified numerical model established to investigate the overall buckling behavior of Winkler beams with internal hinges under compression resting on elastic foundation, can be readily extended to issues that are commonly encountered in practice, such as non-straight pipeline route, inhomogeneous soil conditions, varying axial force distribution along the pipeline accompanied by bending moments, etc.
- The established numerical model for the evaluation of the mechanical behavior of buried pipelines with flexible joints under strike-slip fault rupture can be extended for pipes subjected to normal and reverse faulting, taking into account the fault dip angle.

- A study is suggested on determining the appropriate axial stiffness and other characteristics of joints that elastically restrain axial movement, thus also contributing to axial force reduction apart from bending moment reduction, which may be beneficial in cases of pipeline – fault crossing angles deviating significantly from 90°.
- The presented performance assessment methodology for buried pipelines at fault crossings includes the first three steps of the PEER framework, i.e. seismic hazard, structural and damage analysis. The fourth and final step of the PEER framework equation, namely the loss assessment, can be also incorporated by defining additional limit states related to leakage, rupture and probably explosion effects and their associated monetary/human/environmental costs.

9 REFERENCES

- Abdoun, T. H., Ha, D., O'Rourke, M. J., Symans, M. D., O'Rourke, T. D., Palmer, M. C., and Stewart, H. E. (2009). "Factors influencing the behavior of buried pipelines subjected to earthquake faulting." *Soil Dynamics and Earthquake Engineering*, 29(3), 415–427.
- Abers, G. A. (2009). "Slip on shallow-dipping normal faults." *Geology*, 37(8), 767–768.
- Abrahamson, N. A., and Bommer, J. J. (2005). "Probability and uncertainty in seismic hazard analysis." *Earthquake Spectra*, 21(2), 603–607.
- ADINA R&D. (2006). "Theory and modeling guide Volume: I ADINA, Report AED 06-7." Watertown, MA, USA.
- "Afoi Valasi & Sons O.E." (2015). </www.valasis.gr>.
- Agüero, A., Pallarés, L., and Pallarés, F. J. (2015). "Equivalent geometric imperfection definition in steel structures sensitive to flexural and / or torsional buckling due to compression." 96, 160–177.
- AISC. (1994). *Manual of steel construction. Load & resistance factor design connections*. (American Institute of Steel Construction, ed.), Chicago, IL, USA.
- AISI. (2007). *Welded steel pipe - design manual*. American Iron and Steel Institute, Washington, DC, USA.
- Amazigo, J. C., Budiansky, B., and Garrier, G. F. (1970). "Asymptotic analysis of the buckling of imperfect columns on nonlinear elastic foundations." *International Journal of Solids and Structures*, 6, 1341–1356.
- American Lifelines Alliance. (2005). *Guidelines for the design of buried steel pipe*.
- American Petroleum Institute. (2002). *API Recommended Practice 1102: Steel pipelines crossing railroads and highways*.
- American Petroleum Institute. (2005). *API Standard 1104: Welding of pipelines and related facilities*.
- American Petroleum Institute. (2012). *ANSI/API Specification 5L for Line Pipe, Forty-fifth Edition*.
- American Society of Mechanical Engineers (ASME). (2012). *ASME B31.8 - 2012 - Gas transmission and distribution piping systems*.
- Angell, M., Hanson, K., Swan, F., Youngs, R. R., and Abramson, H. (2003). "Probabilistic fault displacement hazard assessment for flowlines and export pipelines, mad dog and Atlantis field developments, deepwater gulf of Mexico." *Proceedings of Offshore Technology Conference*, Houston, TX, USA, OTC 15402.

- Ariman, T., and Lee, B. J. (1992). "Tension/bending behaviour of buried pipelines subject to fault movements in earthquakes." *Proceeding of Earthquake Engineering, Tenth World Conference*, Rotterdam, The Netherlands, 5423–5426.
- Aristizabal-Ochoa, J. D. (2013). "Stability of slender columns on an elastic foundation with generalised end conditions Estabilidad de columnas esbeltas sobre fundación elástica con." *Ingeniería e Investigación*, 33(3), 34–40.
- ASCE. (1984). *Guidelines for the seismic design of oil and gas pipeline systems*. American Association of Civil Engineers, New York, NY, USA.
- Ballantyne, D. B. (1992). "Thoughts on a pipeline design standard incorporating countermeasures for permanent ground deformation." *Proceedings of the Fourth Japan-U.S. Workshop on Earthquake Resistant Design of Lifeline Facilities and Countermeasures for Soil Liquefaction*, Honolulu, HI, USA.
- Bathe. (1995). *Finite element procedures*. Prentice-Hall, Inc., New Jersey, NJ, USA.
- Bathe, K. J., and Dvorkin, E. N. (1983). "On the automatic solution of nonlinear finite element equations." *Computers & Structures*, 17(5-6), 871–879.
- Bazzurro, P., and Cornell, C. A. (2002). "Vector-valued probabilistic seismic hazard analysis (VPSHA)." *Proceedings of the 7th U.S. National Conference on Earthquake Engineering*, EERI, Boston, MA, USA.
- Bekki, H., Kobayashi, K., Tanaka, Y., and Asada, T. (2002). "Dynamic behavior of buried pipe with flexible joints in liquefied ground." *Journal of Japan Sewage Association*, 39, 201–208.
- Benjamin, J., and Cornell, C. A. (1970). *Probability, statistics, and decisions for civil engineers*. McGraw-Hill, Inc.
- Besstrashnov, V. M., and Strom, A. L. (2011). "Active faults crossing trunk pipeline routes: Some important steps to avoid disaster." *Natural Hazards and Earth System Science*, 11(5), 1433–1436.
- "BOA Group." (2016). <www.boagroup.com>.
- Bommer, J. J. (2002). "Deterministic vs. probabilistic seismic hazard assessment: an exaggerated and obstructive dichotomy." *Journal of Earthquake Engineering*, 6, 43–73.
- Bommer, J. J., and Scherbaum, F. (2008). "The use and misuse of logic trees in probabilistic seismic hazard analysis." *Earthquake Spectra*, 24(4), 997–1009.
- Bouckovalas, G. D., Valsamis, A., Gantes, C. J., Triantafyllou, A., Kalocheiretis, K. E., Asteriou, P., Vernardos, S., and Tsadilis, A. (2015). *Parametric analyses for the evaluation of the response of underground pipes with flexible joints (W.P. 12) - Project 4916-ENSSTRAM, ARISTEIA II*. Athens, Greece.
- Brendel, B., and Ramm, E. (1980). "Linear and nonlinear stability analysis of cylindrical shells." *Computers & Structures*, 12(1), 549–558.
- British Standards Institution. (1993). *BS 8010: Code of practice for pipeline - Part 3. Pipelines subsea: design, construction and installation, with amendment*. London, UK.
- Canadian Energy Pipeline Association. (2016). "About pipelines." <www.cepa.com> (Jan. 5, 2016).
- Canadian Standards Association. (2007). *Z662-07 Oil and Gas Pipeline Systems*.
- Casella, G., and Berger, R. L. (2002). *Statistical Inference*. Duxbury Thomson Learning, Pacific Grove.
- Chaudhary, V., Dilip, V., Pasupuleti, K., and Ramancharla, P. K. (2013). "Finite element analysis of buried continuous pipeline subjected to fault motion subjected to fault motion." *International Journal of Structural Engineering*, 4(4), 314–331.

- Chen, H., Ji, L., Huang, C., Wang, H., and Li, Y. (2012). "Analysis of bending test of 40-in X70 line pipe." *Proceedings of the Twenty-second (2012) International Offshore and Polar Engineering Conference*, The International Society of Offshore and Polar Engineers, ed., Rhodes, Greece, 571–576.
- Cheng, L. (2001). "Seismic design of water pipelines at fault crossings." *Proceedings of the 2nd Japan and U.S. Workshop on Seismic Measures for Water Supply*, AWWA, Tokyo, Japan.
- Choo, Y. W., Abdoun, T. H., O'Rourke, M. J., and Ha, D. (2007). "Remediation for buried pipeline systems under permanent ground deformation." *Soil Dynamics and Earthquake Engineering*, 27(12), 1043–1055.
- Constitution Pipeline. (2016). "Pipeline construction." <<http://constitutionpipeline.com/construction/>> (May 9, 2016).
- "ConstructionWeekOnline.com." (2016). <www.constructionweekonline.com> (Apr. 15, 2016).
- Coppersmith, K. J., and Youngs, R. R. (1993). "Likelihood of surface rupture as a function of magnitude." *Seismological Research Letters*, 4(1), 54.
- Coppersmith, K. J., and Youngs, R. R. (2000). "Data needs for probabilistic fault displacement hazard analysis." *Journal of Geodynamics*, 29, 329–343.
- Cornell, C. A. (1968). "Engineering seismic risk analysis." *Bulletin of the Seismological Society of America*, 58(5), 1583–1606.
- Cornell, C. A. (1993). "Which 84th percentile do you mean?" *Proceedings of the Fourth DOE Natural Phenomena Hazards Mitigation Conference*, Lawrence Livermore National Laboratory, Atlanta, GA, USA, 152–159.
- Cornell, C. A., and Krawinkler, H. (2000). "Progress and Challenges in Seismic Performance Assessment." *PEER Center News*, 3(2), 1–4.
- Dama, E., Karamanos, S. A., and Gresnigt, A. M. (2007). "Failure of locally buckled pipelines." *ASME Journal of Pressure Vessel Technology*, 129(2), 272–279.
- DePolo, C. M. (1994). "The maximum background earthquake in the basin and range." *Bulletin of the Seismological Society of America*, 84, 466–472.
- Desmod, T. P., Power, M. S., Taylor, C. L., and Lau, R. W. (1995). "Behavior of large-diameter pipeline at fault crossings." *ASCE Journal Technical Council*, 6, 296–303.
- Det Norske Veritas. (2006). *DNV-RP-F106: Factory applied external pipeline coatings for corrosion control*. Høvik, Norway.
- Det Norske Veritas. (2007). *DNV-RP-F110: Global buckling of submarine pipelines structural design due to high temperature / high pressure*. Høvik, Norway.
- Det Norske Veritas. (2008). *DNV-RP-D101: Structural analysis of piping systems*. Høvik, Norway.
- Det Norske Veritas. (2010a). *DNV-RP-C204: Design against accidental loads*. Høvik, Norway.
- Det Norske Veritas. (2010b). *DNV-RP-F101: Corroded pipelines*. Høvik, Norway.
- Det Norske Veritas. (2011). *DNV-RP-B401: Cathodic protection design*. Høvik, Norway.
- Det Norske Veritas. (2012a). *DNV-OSS-300: Risk based verification*. Høvik, Norway.
- Det Norske Veritas. (2012b). *DNV-OS-F101: Submarine pipeline systems - offshore standard*. Høvik, Norway.
- Dimopoulos, C. A., and Gantes, C. J. (2012). "Comparison of alternative algorithms for buckling analysis of slender steel structures." *Structural Engineering and Mechanics*, 44(2), 219–238.

- Dorey, B., Murray, D. W., and Cheng, J. J. R. (2000). "An experimental evaluation of critical buckling strain criteria." *Proceedings of the 2000 International Pipeline Conference*, John R. Ellwood, ed., ASME, Calgary, Alberta, Canada, 71–80.
- Earthquake Engineering Research Institute. (1999). *Kocaeli, Turkey Earthquake of August 17*. Pasadena, CA, USA.
- "EBBA Iron Sales, Inc." (2016). <www.ebba.com> (Apr. 15, 2016).
- EJMA. (2008). *Standards of the expansion joint manufacturers association, Inc.* EJMA, New York, NY, USA.
- Elchalakani, M., Zhao, X. L., and Grzebieta, R. (2002). "Bending tests to determine slenderness limits for cold-formed circular hollow sections." *Journal of Constructional Steel Research*, 58(11), 1407–1430.
- Elhmedi, K., and O'Rourke, M. J. (1990). "Seismic damage to segmented buried pipelines." *Earthquake Engineering and Structural Dynamics*, 19(1990), 529–539.
- "European Commission, Energy - Infrastructure." (2008). <ec.europa.eu/energy/en/topics/infrastructure> (Jan. 5, 2016).
- European Committee for Standardization. (2006). *Eurocode 8: Design of structures for earthquake resistance - Part 4: Silos, tanks and pipelines*. Brussels, Belgium.
- European Committee for Standardization. (2007). *Eurocode 3: Design of steel structures - Part 4-3: Pipelines*. Brussels, Belgium.
- European Committee for Standardization. (2013). *EN 1594: Gas infrastructure - Pipelines for maximum operating pressure over 16baar - functional requirements*. Brussels, Belgium.
- Ferino, J., Fonzo, A., Porta, R., and Spinelli, C. M. (2013). "Analytical formulation for line pipe bending strain capacity evaluation developed through experimental - numerical approach." *ISOPE*, 9(4), 531–538.
- Foeken, R. J., and Gresnigt, A. M. (1988). *Buckling and collapse of UOE manufactured steel pipes*. Arlington, TX, USA.
- Ford, D. B. (1983). "Joint design for pipelines subjected to large ground deformations." *Proceedings of the ASME 1983 Pressure Vessels and Piping Division Conference*, ASME, New York, NY, USA, 160–165.
- Fowler, J. R. (1990). "Recommended design procedures for offshore pipelines." *Seminar Proceeding of Offshore Pipelines*.
- Furchtgott-roth, D. (2013). "Pipelines are safest for transportation of oil and gas." *Manhattan Institute for Policy Research*, Issue Brief.
- Gantes, C. J., and Bouckovalas, G. D. (2013). "Seismic verification of the high pressure natural gas pipeline Komotini–Alexandroupoulis–Kipi in areas of active fault crossings." *Structural Engineering International*, 23(2), 204–208.
- Gantes, C. J., Bouckovalas, G. D., Melissianos, V. E., and Valsamis, A. (2015). "Pipeline – fault crossing: structural considerations on the use of flexible joints for mitigating a potential failure." *Jubilee Volume of Andreas Anagnostopoulos*, National Technical University of Athens, ed., Athens, Greece.
- Gantes, C. J., and Fragkopoulos, K. A. (2010). "Strategy for numerical verification of steel structures at the ultimate limit state." *Structure and Infrastructure Engineering*, 6(1-2), 225–255.
- Gantes, C. J., and Melissianos, V. E. (2013). "Numerical analysis of buried steel pipelines." *Proceedings of the 2nd International Balkans Conference on Challenges of Civil Engineering*, BCCCE, EPOKA University, Tirana, Albania.

- Gantes, C. J., and Melissianos, V. E. (2014). "Buckling and post-buckling behavior of beams on elastic foundation modeling buried pipelines." *Proceedings of Civil Engineering for Sustainability and Resilience International Conference*, Amman, Jordan, 70–77.
- Gao, S., Usami, T., and Ge, H. (1998). "Ductility of steel short cylinder in compression and bending." *ASCE Journal of Engineering Mechanics*, 124(2), 176–183.
- "Georg Fischer Harvel LLC." (2016). <www.harvel.com> (Jan. 5, 2016).
- Gresnigt, A. M. (1986). *Plastic design of buried pipelines*. HERON, Delft, The Netherlands.
- Gresnigt, A. M., and van Foeken, R. J. (2001). "Local Buckling of UOE and Seamless Steel Pipes." *International Offshore and Polar Engineering Conference*, I, 131–142.
- Gresnigt, A. M., and Karamanos, S. A. (2009). "Local buckling strength and deformation capacity of pipes." *Proceedings of the Nineteenth (2009) International Offshore and Polar Engineering Conference*, The International Society of Offshore and Polar Engineers (ISOPE), ed., Osaka, Japan, 212–224.
- Gutenberg, B., and Richter, C. F. (1944). "Frequency of earthquakes in California." *Bulletin of the Seismological Society of America*, 34(4), 185.
- Ha, D., Abdoun, T. H., O'Rourke, M. J., Symans, M. D., O'Rourke, T. D., Palmer, M. C., and Stewart, H. E. (2010). "Earthquake faulting effects on buried pipelines – case history and centrifuge study." *Journal of Earthquake Engineering*, 14(5), 646–669.
- Hall, W. J., Nyman, D. J., Johnson, E. R., Symans, M. D., O'Rourke, T. D., Palmer, M. C., and Stewart, H. E. (2003). "Performance of the Trans-Alaska pipeline in the November 3, 2002 Denali Fault earthquake." *Proceedings of the 6th U.S. Conference and Workshop on Lifeline Earthquake Engineering*, ASCE, ed., Long Beach, CA, USA.
- Hamada, M., and O'Rourke, T. D. (1992). "Large ground deformations and their effects on lifelines." *Japanese Case Studies of Liquefaction and Lifeline Performance During Past Earthquakes*, Buffalo, NY, USA.
- Hanks, T. C., and Kanamori, H. (1979). "A moment magnitude scale." *Journal of Geophysical Research*, 84(B5), 2348–2350.
- Hansen, W. R. (1971). *Effects at Anchorage, The Great Alaska earthquake of 1964*. Washington, DC, USA.
- Hart, J. D., Lee, C., Kelson, K. I., Zulfigaar, N., Dauby, F., and Hitchcock, C. (2004). "A unique pipeline fault crossing design for a highly focused fault." *Proceeding of the IPC2004 International Pipeline Conference*, ASCE, Calgary, Alberta, Canada.
- Hegde, A. M., and Sitharam, T. G. (2015). "Experimental and numerical studies on protection of buried pipelines and underground utilities using geocells." *Geotextiles and Geomembranes*, Elsevier Ltd, 43(5), 372–381.
- Hetenyi, H. (1946). *Beams on elastic foundation theory with applications in the fields of civil and mechanical engineering*. (T. U. of Michigan, ed.), The University of Michigan Press, Ann Arbor.
- Hunt, G. W., and Blackmore, A. (1996). "Principles of localized buckling for a strut on an elastoplastic foundation." *ASME Journal of Applied Mechanics*, 63, 234–239.
- Hunt, G. W., and Wadee, M. K. (1991). "Comparative lagrangian formulations for localized buckling." *Proceeding of the Royal Society A*, 434, 485–502.
- Hunt, G. W., Wadee, M. K., and Schiocolas, N. (1993). "Localized elasticae for the strut on the linear foundation." *ASME Journal of Applied Mechanics*, 60, 1033–1038.
- "Impact Solutions." (2016). <www.impact-solutions.co.uk> (Apr. 19, 2015).

- Indian Institute of Technology Kanpur, and Gujarat State Disaster Management Authority. (2007). *Guidelines for seismic design of buried pipelines*. National Information Center of Earthquake Engineering, Kanpur, India.
- International Organization for Standardization. (2010). *EN ISO 6892.01 - Metallic materials - Tensile testing - Part 1: Method of test at room temperature*. Geneva, Switzerland.
- Isenber, J., and Escalante, L. E. (1984). *Damages to lifelines*. EERI, Pasadena, CA, USA.
- Isenberg, J., and Richardson, E. (1989). "Countermeasures to mitigate damage to pipelines." *Proceedings of the Second U.S.-Japan Workshop on Liquefaction, Large Ground Deformation and Their Effects on Lifelines*, New York, USA, 468–482.
- "J. Bellos & Co." (2015). <www.tekesyp.gr> (Jan. 5, 2016).
- Japan Gas Association. (2000). *Seismic Design for Gas Pipelines*.
- Joshi, S., Prashant, A., Deb, A., and Jain, S. K. (2011). "Analysis of buried pipelines subjected to reverse fault motion." *Soil Dynamics and Earthquake Engineering*, Elsevier, 31(7), 930–940.
- Ju, G. T., and Kyriakides, S. (1992). "Bifurcation and localization instabilities in cylindrical shells under bending—II. Predictions." *International Journal of Solids and Structures*, 29(9), 1143–1171.
- Kalochairetis, K. E., Gantes, C. J., and Lignos, X. A. (2014). "Experimental and numerical investigation of eccentrically loaded laced built-up steel columns." *Journal of Constructional Steel Research*, Elsevier Ltd, 101, 66–81.
- Kaneko, S., Miyajima, M., and Erami, M. H. (2013). "Study on behavior of ductile iron pipelines with earthquake resistant joints buried across a fault." *Proceedings of the International Efforts in Lifeline Earthquake Engineering*, ASCE, 221–228.
- Karamanos, S. A., Keil, B., and Card, R. J. (2014). "Seismic design of buried steel water pipelines." *Proceedings of the Pipelines 2014: From Underground to the Forefront of Innovation and Sustainability*, ASCE, Portland, OR, USA, 1005–1019.
- Karamitros, D. K., Bouckovalas, G. D., and Kouretzis, G. P. (2007). "Stress analysis of buried steel pipelines at strike-slip fault crossings." *Soil Dynamics and Earthquake Engineering*, 27(3), 200–211.
- Karamitros, D. K., Bouckovalas, G. D., Kouretzis, G. P., and Gkesouli, V. (2011). "An analytical method for strength verification of buried steel pipelines at normal fault crossings." *Soil Dynamics and Earthquake Engineering*, Elsevier, 31(11), 1452–1464.
- Keener, J. P. (1974). "Buckling imperfection sensitivity of columns and spherical caps." *Quarterly of Applied Mathematics*, 32(2), 173–188.
- Kennedy, R. P., Chow, A. W., and Williamson, R. A. (1977). "Fault movement effects of buried oil pipeline." *ASCE Journal of Transportation Engineering*, 103, 617–633.
- Kennedy, R. P., and Kincaid, R. H. (1983). "Fault crossing design for buried gas oil pipeline." *Proceedings of the ASME 1983 Pressure Vessels and Piping Division Conference*, ASME.
- Kim, J., Lynch, J. P., Michalowski, R. L., Green, R. A., Pour-Ghaz, M., Weiss, W. J., and Bradshaw, A. (2009). "Experimental study on the behavior of segmented buried concrete pipelines subject to ground movements." *Proceedings of Nondestructive Characterization for Composite Materials, Aerospace Engineering, Civil Infrastructure, and Homeland Security 2009*, (734), 729419–729419–10.
- Klamflex Pipe Couplings Ltd. (2016). "VARIplus-DC Dedicated Couplings." <<http://www.klamflex.com/>> (May 28, 2016).
- Kojic, M., and Bathe, K. J. (2004). *Inelastic analysis of solid and structures, Computational fluid and soil mechanics series*. Springer Verlag, Berlin, Germany.

- Kokavassiss, N. K., and Anagnostidis, G. S. (2006). "Finite element modeling of buried pipelines subjected to seismic loads: soil structure interaction using contact elements." *Proceedings of the ASME 2006 Pressure Vessels and Piping Division Conference*, ASME, Vancouver, Canada.
- Kounadis, A. N., Mallis, J., and Sbarounis, A. (2006). "Postbuckling analysis of columns resting on an elastic foundation." *Archive of Applied Mechanics*, 75(6-7), 395–404.
- Kramer, S. L. (1996). *Geotechnical earthquake engineering*. Prentice-Hall, Inc., New Jersey, NJ, USA.
- Kristoffersen, M., Borvik, T., Langseth, M., and Hopperstad, O. S. (2015). "X65 steel pipes subjected to combined stretching and bending." *Proceedings of the VI International Conference on Computational Methods in Marine Engineering*, Rome, Italy.
- Kyriakides, S., and Shaw, P. K. (1987). "Inelastic buckling of tubes under cyclic bending." *ASME Journal of Pressure Vessel Technology*, 109(2), 169–178.
- Lee, M.-Z. (2013). "A primer on pipe supports." <www.machinedesign.com> (Jun. 1, 2016).
- Li, S., and Batra, R. C. (2007). "Thermal buckling and postbuckling of Euler-Bernoulli beams supported on nonlinear elastic foundations." *AIAA Journal*, 45(3), 712–720.
- Liu, A. W., He, Q. M., and Jia, X. H. (2013). "Fault displacement hazard analysis for the seismic design of oil and gas pipeline." *Proceedings of the Sixth China-Japan-U.S. Trilateral Symposium on Lifeline Earthquake Engineering*, ASCE, Chengdu, China, 229–236.
- Liu, B., Liu, X. L., and Zhang, H. (2009). "Strain-based design criteria of pipelines." *Journal of Loss Prevention in the Process Industries*, Elsevier Ltd, 22(6), 884–888.
- Liu, X., Zhang, H., Han, Y., Xia, M., and Zheng, W. (2016). "A semi-empirical model for peak strain prediction of buried X80 steel pipelines under compression and bending at strike-slip fault crossings." *Journal of Natural Gas Science and Engineering*, Elsevier Ltd, doi: 10.1016/j.jngse.2016.04.054.
- Manson, M. (1908). *Report on an auxiliary water supply system for fire protection for San Francisco, California*. San Francisco, CA, USA.
- Marlow, R. S. (1988). *Effects of external hydrostatic pressure on tubular beam-columns*. San Antonio, TX, USA.
- Mason, J. A., O'Rourke, T. D., and Jung, J. K. (2010). "Direct tension performance of steel pipelines with welded slip joints." *Journal of Pipeline Systems Engineering and Practice*, 1(4), 133–140.
- Massalas, C. V., and Tzivanidis, G. I. (1979). "Equilibrium paths of a beam resting on a non-linear elastic foundation." *Revue Roumaine des Sciences Techniques - Serie de Mecanique Applique*, 24(2), 257–62.
- Massalas, C. V., Tzivanidis, G. I., and Katsikadelis, J. T. (1978). "Buckling of a continuous beam resting on a tensionless elastic foundation." *Journal of the Franklin Institute*, 306(6), 449–455.
- McCaffrey, M. A., and O'Rourke, T. D. (1983). "Buried pipeline response to reverse faulting during the 1971 San Fernando earthquake." *Earthquake Behavior and Safety of Oil and Gas Storage Facilities, Buried Pipelines and Equipment, PVP-77*, ASME, ed., New York, 151–159.
- Medeiros, J., da C. Veiga, J. L. B., and Veiga, J. C. C. (2009). "Analysis of FCC expansion joints movement test." *Proceedings of the ASME 2009 Pressure Vessels and Piping Division Conference*, Prague, Czech Republic.
- Melissianos, V. E., and Gantes, C. J. (2014a). "Earthquake induced upheaval buckling of buried pipelines with flexible joints." *Proceedings of the Second European Conference on Earthquake Engineering and Seismology*, A. Ansal and M. Nurlu, eds., Istanbul, Turkey.

- Melissianos, V. E., and Gantes, C. J. (2014b). "Upheaval buckling of onshore buried steel pipelines with flexible joints." *Proceedings of the IASS-SLTE 2014 Symposium "Shells, Membranes and Spatial Structures: Footprints*, M. L. R. F. Brasil and R. M. O. Pauletti, eds., International Association of Shell and Spatial Structures, Brasilia, Brazil.
- Melissianos, V. E., and Gantes, C. J. (2014c). "On the efficiency of flexible joints in mitigating the consequences of seismic fault activation on buried pipelines." *Proceedings of the Qatar Foundation Annual Research Conference ARC'14*, Qatar Foundation, Doha, Qatar, EOP0052.
- Melissianos, V. E., and Gantes, C. J. (2015a). "Numerical modeling aspects of buried pipeline – fault crossing." *Computational Methods in Earthquake Engineering*, M. Papadimitriou, M. Fragiadakis, and V. Plevris, eds., Springer Verlag.
- Melissianos, V. E., and Gantes, C. J. (2015b). "Failure mitigation of buried steel pipeline under strike-slip fault offset using flexible joints." *Proceedings of SECED 2015 Conference: Earthquake Risk and Engineering towards a Resilient World*, Cambridge, UK.
- Melissianos, V. E., and Gantes, C. J. (2016). "Buckling and post-buckling behavior of beams with internal flexible joints resting on elastic foundation modeling buried pipelines." *Structures*, 7, 138–152.
- Melissianos, V. E., Gantes, C. J., and Kalfantis, P. P. (2014a). "Upheaval buckling risk assessment of buried steel pipelines due to reverse seismic fault activation." *Proceedings of the 8th National Conference on Steel Structures*, Steel Structures Research Society, Tripoli, Greece.
- Melissianos, V. E., Korakitis, G. P., Gantes, C. J., and Bouckovalas, G. D. (2016a). "Numerical evaluation of the effectiveness of flexible joints in buried pipelines subjected to strike-slip fault rupture." *Soil Dynamics and Earthquake Engineering*, (under review).
- Melissianos, V. E., Lignos, X. A., Bachas, K. K., and Gantes, C. J. (2016b). "Experimental investigation of CHS beams with flexible joints under transverse loading." *Journal of Constructional Steel Research*, (under review).
- Melissianos, V. E., Vamvatsikos, D., and Gantes, C. J. (2014b). "Seismic risk assessment of buried pipelines at active fault crossings." *Proceedings of the Second European Conference on Earthquake Engineering and Seismology*, M. A. Ansal and M. Nurlu, eds., Istanbul, Turkey.
- Melissianos, V. E., Vamvatsikos, D., and Gantes, C. J. (2015a). "Probabilistic assessment of innovative mitigating measures for buried steel pipeline - fault crossing." *Proceedings of the ASME 2015 Pressure Vessels & Piping Conference PVP2015*, ASME, Boston, MA, USA.
- Melissianos, V. E., Vamvatsikos, D., and Gantes, C. J. (2015b). "Performance assessment of pipeline - fault crossing." *Proceedings of the 5th ECCOMAS Thematic Conference on Computational Methods in Structural Dynamics and Earthquake Engineering COMPDYN 2015*, M. Papadrakakis, V. Papadopoulos, and V. Plevris, eds., Crete Island, Greece, 2044–2060.
- Melissianos, V. E., Vamvatsikos, D., and Gantes, C. J. (2016c). "Performance assessment of buried pipelines at fault crossings." *Earthquake Spectra*, (under review).
- Meslem, A., Vamvatsikos, D., Porter, K., and Rossetto, T. (2015). *Guidelines for analytical vulnerability assessment - Low/mid-rise buildings*.
- Miranda, E., and Aslani, H. (2003). *Probabilistic response assessment for building-specific loss estimation*. Berkely, CA, USA.
- Mohr, W. (2003). *Strain-based design of pipelines - Project No. 45892GTH*. Columbus, OH, USA.
- Mokhtari, M., and Alavi Nia, a. (2015). "The influence of using CFRP wraps on performance of buried steel pipelines under permanent ground deformations." *Soil Dynamics and Earthquake Engineering*, Elsevier, 73, 29–41.
- Monroy-Concha, M. (2013). "Soil restraints on steel buried pipelines crossing active seismic faults." The University of British Columbia.

- Moore, R. L., and Clark, J. W. (1952). *Torsion, compression, and bending tests of tubular sections machined from 75S-T6 rolled round rod*. Washington, DC, USA.
- Moradi, M., Rojhan, M., Galandazadeh, A., and Takada, S. (2013). "Centrifuge modeling of buried continuous pipelines subjected to normal faulting." *Journal of Earthquake Engineering and Engineering Vibration*, 12(1), 155–164.
- Moss, R. E. S., and Ross, Z. E. (2011). "Probabilistic fault displacement hazard analysis for reverse faults." *Bulletin of the Seismological Society of America*, 101(4), 1542–1553.
- Murphy, C., and Langner, C. (1985). "Ultimate pipe strength under bending, collapse and fatigue." *Proceedings of the 4th International Conference on Offshore Mechanics and Arctic Engineering OMAE*, Dallas, TX, USA.
- Murray, D. W. (1997). "Local buckling, strain localization, wrinkling and postbuckling response of line pipe." *Engineering Structures*, 19(5), 360–371.
- Nakata, T., and Hasuda, K. (1995). "Active fault I 1995 Hyogoken Nanbu earthquake." *Kagaku*, 65, 127–142.
- "National Snow & Ice Data Center." (2016). <nsidc.org> (Jan. 5, 2016).
- Newmark, N. M., and Hall, W. J. (1975). "Pipeline design to resist large fault displacement." *Proceedings of the US National Conference on Earthquake Engineering*, 416–425.
- Nilsson, K.-F., and Giannakopoulos, A. (1995). "A finite element analysis of configurational stability and finite growth of buckling driven delamination." *Journal of Mechanics and Physics of Soils*, 43(12), 1983–2021.
- Nobuhiro, H., Hiroshi, N., and Toshio, I. (2013). "Development of 'Steel Pipe for Crossing Fault (SPF)' using buckling pattern for water pipelines." *JFE GIHO*, (31), 61–65.
- Noguchi, H., and Hisada, T. (1993). "Sensitivity analysis in post-buckling problems of shell structures." *Computers*, 47(4/5), 699–710.
- O'Rourke, M. J. (2009). "Analytical fragility relation for buried segmented pipe." *Proceedings of the 2009 TCLEE Conference: Lifeline Earthquake Engineering in a Multihazard Environment*, ASCE, Oakland, CA, USA, 771–780.
- O'Rourke, M. J., and Ballantyne, D. (1992). *Observations on water system and pipeline performance in the Limon area of Costa Rica due to the April 22, 1991 earthquake*. (Multidisciplinary Center for Earthquake Engineering Research, ed.), Buffalo, NY, USA.
- O'Rourke, M. J., and Liu, X. (1999). *Response of buried pipelines subject to earthquake effects*. Multidisciplinary Center for Earthquake Engineering Research, Buffalo, NY, USA.
- O'Rourke, M. J., and Liu, X. (2012). *Seismic design of buried and offshore pipelines*. Multidisciplinary Center for Earthquake Engineering Research, Buffalo, NY, USA.
- O'Rourke, M. J., Liu, X., and Flores-Berrones, R. (1995). "Steel Pipe Wrinkling due to Longitudinal Permanent Ground Deformation." *Journal of Transportation Engineering*, 121(5), 443–451.
- O'Rourke, M. J., and Liu, X. L. (1994). "Failure criterion for buried pipe subject to longitudinal PGD: Benchmark case history." *Proceedings of the 5th U.S.-Japan Workshop on Earthquake Resistant Design for Lifeline Facilities and Countermeasures Against Soil Liquefaction*, Buffalo, NY, USA.
- O'Rourke, M. J., and Norberg, C. (1991). "Analysis procedures for buried pipelines subject to longitudinal and transverse permanent ground deformation." *Proceedings of the Third Japan-U.S. Workshop on Earthquake Resistant Design of Lifelines and Countermeasures for Soil Liquefaction*, San Francisco, CA, USA, 439–453.

- O'Rourke, T. D., and Palmer, M. C. (1994). "Earthquake performance of gas transmission pipelines." *Proceedings of the Fifth U.S.-Japan Workshop on Earthquake Resistant Design of Lifeline Facilities and Countermeasures Against Soil Liquefaction*, Multidisciplinary Center for Earthquake Engineering Research, Snowbird, UT, USA, 679–702.
- O'Rourke, T. D., and Trautmann, C. H. (1981). "Earthquake ground rupture effects on jointed pipe." *Proceedings of the Second Speciality Conference of the Technical Council on Lifeline Earthquake Engineering*, ASCE, 65–80.
- Odina, L., and Tan, R. (2009). "Seismic fault displacement of buried pipeline using continuum finite element methods." *Proceedings of the ASME 28th International Conference on Ocean, Offshore and Arctic Engineering*, ASME, Honolulu, HI, USA.
- Ogawa, Y., Yanou, Y., Kawakami, M., and Kurakake, T. (2004). "Numerical study for rupture behavior of buried gas pipeline subjected to seismic fault displacement." *Proceedings of the 13th World Conference on Earthquake Engineering*, Vancouver, Canada.
- Peng, L.-C., and Peng, T.-L. (2009). *Pipe stress engineering*. ASME, New York, USA.
- Petersen, M. D., Dawson, T. E., Chen, R., Cao, T., Wills, C. J., Schwartz, D. P., and Frankel, A. D. (2011). "Fault displacement hazard for strike-slip faults." *Bulletin of the Seismological Society of America*, 101(2), 805–825.
- Pezzopane, S. K., and Dawson, T. E. (1996). "Fault displacement hazard: a summary of issues and information." *Seismotectonic framework and characterization of faulting at Yucca mountain, Nevada*, U.S. Geological Survey.
- Plate tectonic & northern Pacific. (2016). "No planar fault." <<http://plate-tectonic.narod.ru/>> (May 28, 2015).
- Prion, H. D. L., and Birkemoe, P. C. (1992). "Beam-column behavior of fabricated steel tubular members." *Journal of Structural Engineering*, 118(5), 1213–1232.
- Rahman, M. A., and Taniyama, H. (2015). "Analysis of a buried pipeline subjected to fault displacement: A DEM and FEM study." *Soil Dynamics and Earthquake Engineering*, Elsevier, 71, 49–62.
- Rao, V. G., and Neetha, R. (2002). "Methodology to evaluate first transition foundation stiffness for columns on Winkler foundation." *Journal of Structural Engineering*, 128(7), 956–959.
- Reddy, B. D. (1979). "An experimental study of the plastic buckling of circular cylinders in pure bending." *International Journal of Solids and Structures*, 15(9), 669–683.
- Rofooei, F. R., Jalali, H. H., Attari, N. K. A., and Alavi, M. (2012). "Full-scale laboratory testing of buried pipelines subjected to permanent ground displacement caused by reverse faulting." *Proceedings of the 15th World Conference on Earthquake Engineering*, Lisbon, Portugal.
- Ross, D. A., and Chen, W. F. (1976). "Tests of fabricated tubular columns, January 1976." *Proceedings of the ASCE National Water Resources Conference*, Paper 447.
- Roy, G., Braid, M., and Shen, G. (2003). "Application of ADINA and hole drilling method to residual stress determination in weldments." *Computers & Structures*, 81, 929–935.
- Sanghal, A. C. (1980). "Strength characteristics of buried jointed pipelines." *Report to the Engineering Foundation and ASCE, Grant No. RC-A-77-6A*, USA.
- Schneider, W., and Brede, A. (2005). "Consistent equivalent geometric imperfections for the numerical buckling strength verification of cylindrical shells under uniform external pressure." *Thin-Walled Structures*, 43, 175–188.
- Schneider, W., Timmel, I., and Ho, K. (2005). "The conception of quasi-collapse-affine imperfections: A new approach to unfavourable imperfections of thin-walled shell structures." *Thin-Walled Structures*, 43, 1202–1224.
- Shantz, T. (2013). *Caltrans procedures for calculation of fault rupture hazard*.

- Sherman, D. R. (1976). "Test of circular steel tubes in bending." *ASCE Journal of Structural Division*, 102(11), 2181–2195.
- Sherman, D. R. (1983). "Flexural tests of fabricated pipe beams." *Proceedings of the Third International Colloquium Stability of Metal Structures*, Toronto, Canada.
- Sim, W. W., Towhata, I., Yamada, S., and Moinet, G. J. M. (2012). "Shaking table tests modelling small diameter pipes crossing a vertical fault." *Soil Dynamics and Earthquake Engineering*, Elsevier, 35, 59–71.
- Song, X., and Li, S. R. (2007). "Thermal buckling and post-buckling of pinned-fixed Euler-Bernoulli beams on an elastic foundation." *Mechanics Research Communications*, 34(2), 164–171.
- Steinbrugge, K. V., and Moran, D. F. (1954). "An engineering study of the Southern California earthquake of July 21, 1952 and its aftershocks." *Bulletin of the Seismological Society of America*, 44, 199–462.
- Steinman, S. L., and Vojta, J. F. (1989). *Hydrostatic beam column tests phase II - CBI Contract number C92731I*.
- Strom, A., Ivaschenko, A., and Kozhurin, A. (2011). "Assessment of the design displacement values at seismic fault crossings and of their excess probability." *Journal of Mountain Science*, 8(2), 228–233.
- Sun, S., and Shien, L. (1983). "Analysis of seismic damage to buried pipelines in Tangshan earthquake." *Earthquake Behavior and Safety of Oil and Gas Storage Facilities, Buried Pipelines and Equipment, PVP-77*, American Society of Mechanical Engineers (ASME), ed., New York, 365–369.
- Suzuki, H. (1988). "Damage to buried pipes caused by large ground displacement." *Proceedings of the First Japan-U.S. Workshop on Liquefaction, Large Control Deformation and Their Effects on Lifeline Facilities*, Tokyo, Japan, 127–132.
- Takada, S. (1984). "Model analysis and experimental study on mechanical behavior of buried ductile iron pipelines subjected to large ground deformations." *Proceedings of the Eighth World Conference on Earthquake Engineering*, San Francisco, CA, USA, 255–262.
- Takada, S., Hassani, N., and Fukuda, K. (2001). "A new proposal for simplified design of buried steel pipes crossing active faults." *Earthquake Engineering and Structural Dynamics*, 30(8), 1243–1257.
- Takada, S., Liang, J.-W., and Li, T. (1998). "Shell-mode response of buried pipelines to ground movements." *Journal of Structural Engineering*, 44(A), 1637–1646.
- Takada, S., Nakayama, M., Ueno, J., and Tajima, C. (1999). *Report on Taiwan Earthquake*. Kobe, Japan.
- Thinwongpituk, C., Poonaya, S., Choksawadee, S., and Lee, M. (2008). "The ovalisation of thin-walled circular tubes subjected to bending." *Proceedings of the World Congress on Engineering*.
- Timoshenko, S. P., and Gere, J. M. (1961). *Theory of elastic stability*. McGraw-Hill, Inc., New York, NY, USA.
- Trautmann, C. H., and O'Rourke, T. D. (1983). "Behavior of pipe in dry sand under lateral and uplift loading." *Geotechnical Engineering Report 83-7*, C. University, ed., Ithaca, NY, USA.
- Trifonov, O. V. (2015). "Numerical stress-strain analysis of buried steel pipelines crossing active strike-slip faults with an emphasis on fault modeling aspects." *ASCE Journal of Pipeline Systems Engineering and Practice*, 6(1), 1–10.
- Trifonov, O. V., and Cherniy, V. P. (2010). "A semi-analytical approach to a nonlinear stress-strain analysis of buried steel pipelines crossing active faults." *Soil Dynamics and Earthquake Engineering*, Elsevier, 30(11), 1298–1308.
- Trifonov, O. V., and Cherniy, V. P. (2012). "Elastoplastic stress-strain analysis of buried steel pipelines subjected to fault displacements with account for service loads." *Soil Dynamics and Earthquake Engineering*, Elsevier, 33(1), 54–62.

- Tugcu, P., and Schroeder, J. (1979). "Plastic deformation and stability of pipes." *International Journal of Solids and Structures*, 15, 643–658.
- "U.S. Bellows." (2016). <www.usbellows.com> (Apr. 15, 2015).
- Uckan, E., Akbas, B., Shen, J., Rou, W., Paolacci, F., and O'Rourke, M. J. (2015). "A simplified analysis model for determining the seismic response of buried steel pipes at strike-slip fault crossings." *Soil Dynamics and Earthquake Engineering*, Elsevier, 75, 55–65.
- Vamvatsikos, D., and Cornell, C. A. (2002). "Incremental dynamic analysis." *Earthquake Engineering & Structural Dynamics*, 31(3), 491–514.
- Vazouras, P., Dakoulas, P., and Karamanos, S. A. (2015). "Pipe–soil interaction and pipeline performance under strike–slip fault movements." *Soil Dynamics and Earthquake Engineering*, Elsevier, 72, 48–65.
- Vazouras, P., Karamanos, S. A., and Dakoulas, P. (2010). "Finite element analysis of buried steel pipelines under strike-slip fault displacements." *Soil Dynamics and Earthquake Engineering*, Elsevier, 30(11), 1361–1376.
- Vazouras, P., Karamanos, S. A., and Dakoulas, P. (2012). "Mechanical behavior of buried steel pipes crossing active strike-slip faults." *Soil Dynamics and Earthquake Engineering*, Elsevier, 41, 164–180.
- Veiga, C., Kavanagh, N., Sousa, A. M. F., and Veiga, J. L. (2016). "Determination of Gimbal and Hinged expansion joints reaction moments." *ASME Journal of Pressure Vessel Technology*, 135, 055001.
- Vougioukas, E. A., Theodossis, C., and Carydis, P. G. (1979). "Seismic analysis of buried pipelines subjected to vertical fault movement." *ASCE Journal Technical Council*, 105, 432–441.
- Wadee, M. K., Hunt, G. W., and Whiting, A. I. M. (1997). "Asymptotic and Rayleigh – Ritz routes to localized buckling solutions in an elastic instability problem Asymptotic and Rayleigh – Ritz routes to localized buckling solutions in an elastic." *Proceeding of the Royal Society A*, 453, 2085–2107.
- Wakamatsu, K., and Yoshida, N. (1994). "Ground deformations and their effects on structures in Midorigaoka district, Kushiro City, during the Kushiro-Oki earthquake on January 15, 1993." *Proceedings of the Fifth U.S.-Japan Workshop on Earthquake Resistant Design of Lifeline Facilities and Countermeasures Against Soil Liquefaction*, Multidisciplinary Center for Earthquake Engineering Research, Snowbird, UT, USA, 41–62.
- Waller, R., and Ramanathan, M. (1980). "Site visit report on earthquake damages to water and sewage facilities El Centro, California, November 15, 1979." *Reconnaissance Report, Imperial Valley, California Earthquake, November 15, 1979*, EERI, ed., 97–106.
- Wang, C. Y. (1992). "Stability of a column with two interior hinges." *Mechanics Research Communications*, 19(5), 483–488.
- Wang, C. Y. (2002). "Buckling of an internally hinged column with an elastic support." *Engineering Structures*, 24(10), 1357–1360.
- Wang, C. Y. (2008). "Optimum location of an internal hinged column with an elastic support." *Journal of Applied Mechanics*, 75(3), 034501.
- Wang, C. Y. (2010). "Buckling of a weakened infinite beam on an elastic foundation." *ASCE Journal of Engineering Mechanics*, 136(4), 534–537.
- Wang, L. R. L. (1990). "Performance of water pipeline systems from 1987 Whittier Narrows, California earthquake." *Proceedings of the Fourth U.S. National Conference on Earthquake Engineering*, 965–974.
- Wang, L. R. L. (1996). "Some aspects of prioritization for rehabilitation of buried lifelines." *Proceedings of the Eleventh World Conference on Earthquake Engineering*, Acapulco, Mexico, Paper No. 1902.

- Wang, L. R. L., and Wang, L. J. (1995). "Parametric study of buried pipelines due to large fault movement." *Proceedings of ASCE, TCLEE*, 152–159.
- Wang, L. R. L., and Yeh, Y. A. (1985). "A refined seismic analysis and design of buried pipelines subjected to vertical fault movement." *Earthquake Engineering & Structural Dynamics*, 13(1984), 75–96.
- Wang, X., Kibey, S., Tang, H., Cheng, W., Minnaar, K., Macia, M. L., Kan, W. C., Ford, S. J., and Newbury, B. (2010). "Strain-based design - advantages in prediction methods of tensile strain capacity." *Proceedings of the Twentieth International Offshore and Polar Engineering Conference, ISOPE 2010*, Beijing, China.
- Wang, Y. Y., Horsley, D., and Liu, M. (2007). "Strain based design of pipelines." *Proceedings of the 16th Joint Technical Meeting*, Australian Pipeline Association, Canberra, Australia.
- Wells, D. L., and Coppersmith, K. J. (1994). "New Empirical Relationships among Magnitude, Rupture Length, Rupture Width, Rupture Area, and Surface Displacement." *Bulletin of the Seismological Society of America*, 84(4), 974–1002.
- Wells, D. L., and Kulkarni, V. S. (2014). "Probabilistic fault displacement hazard analysis - sensitivity analyses and recommended practices for developing design fault displacement." *Proceedings of the 10th National Conference on Earthquake Engineering2*, EERI, Anchorage, Alaska, USA.
- Wijewickreme, D., Karimian, H., and Honegger, D. (2009). "Response of buried steel pipelines subjected to relative axial soil movement." *Canadian Geotechnical Journal*, 46(7), 735–752.
- Wilson, J. F. (1984). "Mechanics of bellows: a critical survey." *International Journal of Mechanical Sciences*, 26(11/12), 593–605.
- "Witzenmann GmbH." (2016). <www.witzenmann.de> (Apr. 19, 2016).
- Wood, H. O. (1933). "Preliminary report on the Long Beach Earthquake." *Bulletin of the Seismological Society of America*, 73(3), 863–877.
- Wu, B., and Zhong, H. (1999). "Postbuckling and imperfection sensitivity of fixed-end and free-end struts on elastic foundation." *Archive of Applied Mechanics*, 69(69), 491–498.
- Xinxing Pipes International Development Co. Ltd. (2016). "Push-on Joint (T-type Joint)." <<http://www.xinxingpipes.com.cn/>> (Jun. 1, 2016).
- Yaffe, R., and Abramovich, H. (2003). "Dynamic buckling of cylindrical stringer stiffened shells." *Computers & Structures*, 81, 1031–1039.
- Yamashita, T., and Shiro, K. (2001). "Elastic buckling characteristics of two-way grid shells of single layer and its application in design to evaluate the non-linear behavior and ultimate strength." *Journal of Constructional Steel Research*, 57, 1289–1308.
- Yang, G., and Bradford, M. A. (2015). "Antisymmetric post-buckling localization of an infinite column on a nonlinear foundation with softening." *International Journal of Structural Stability and Dynamics*, 15(8), 1540028.
- Yokel, F. Y., and Mathey, R. G. (1992). *FEMA-233: Earthquake resistant construction of gas and liquid fuel pipeline systems serving, or regulated by, the Federal Government*. Washington, DC, USA.
- Yoo, H., and Choi, D. (2008). "New method of inelastic buckling analysis for steel frames." 64, 1152–1164.
- Yoshizaki, K., O'Rourke, T. D., and Hamada, M. (2003). "Large scale experiments of buried steel pipelines with elbows subjected to permanent ground deformation." *Structural Engineering / Earthquake Engineering*.

- Youngs, R. R., Arabasz, W. J., Anderson, R. E., Ramelli, A. R., Ake, J. P., Slemmons, D. B., McCalpin, J. P., Doser, D. I., Fridrich, C. J., Swan, F. H., Rogers, A. M., Yount, J. C., Anderson, L. W., Smith, K. D., Bruhn, R. L., Knuepfer, P. L. K., Smith, R. B., DePolo, C. M., O'Leary, D. W., Coppersmith, K. J., Pezzopane, S. K., Schwartz, D. P., Whitney, J. W., Olig, S. S., and Toro, G. R. (2003). "A methodology for probabilistic fault displacement hazard analysis (PFDHA)." *Earthquake Spectra*, 19(1), 191–219.
- Yun, H., and Kyriakides, S. (1990). "On the beam and shell modes of buckling of buried pipelines." *Soil Dynamics and Earthquake Engineering*, 9(4), 179–193.
- Zhang, C., Guo, Q., and Zhang, X. (2015a). "Determination of the strain-free configuration of multispan cable." *Shock and Vibration*, Article ID 890474.
- Zhang, J., Liang, Z., and Han, C. (2015b). "Failure Analysis and Numerical Simulation of the Buried Steel Pipeline in Rock Layer Under Strike-Slip Fault." *Journal of Failure Analysis and Prevention*, Springer US, 15(6), 853–859.
- Zhang, J., Liang, Z., and Han, C. J. (2014). "Buckling behavior analysis of buried gas pipeline under strike-slip fault displacement." *Journal of Natural Gas Science and Engineering*, Elsevier B.V, 21, 921–928.

10 APPENDIX – BASIC ASPECTS OF STATISTICS AND PROBABILITY THEORY

A brief introduction to statistics and probability theory is hereinafter presented after Casella and Berger (2002) to provide the basic mathematical aspects that are used in the performance assessment methodology. The probability density function, the cumulative density function and the total probability theorem are firstly outlined and then the commonly used statistical distributions and their properties are presented.

10.1 PROBABILITY DENSITY FUNCTION

A random variable X is considered to be continuous under the conditions: (i) the possible values of variable X comprise either a single interval, e.g. for $A < B$ on the number line, any number x between A and B is a possible value, or a union of disjoint intervals, (ii) the probability for any number that is a possible value of X is $P(X=c)=0$. Then, the Probability Density Function (PDF) of the continuous random variable X is a function $f(x)$ that describes the relative likelihood for this random variable to take on a given value (Benjamin and Cornell 1970). The probability of a random variable X falling within a particular range of values (e.g. for numbers a and b with $a \leq b$) is given by the area between the horizontal axis and the density function as depicted in Figure 10-1, or by the integral over the range:

$$P(a \leq X \leq b) = \int_a^b f(x) dx \quad (10-1)$$

The basic properties of a PDF are:

– $f(x) \geq 0, \forall x \in \mathbb{R};$

– $\int_{-\infty}^{+\infty} f(x) dx = 1.$

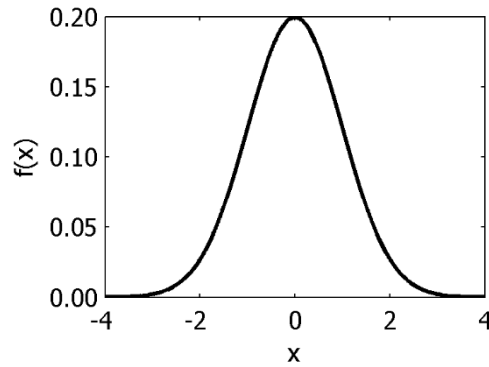


Figure 10-1: Example of a probability density function (standard normal distribution)

10.2 CUMMULATIVE DISTRIBUTION FUNCTION

The Cumulative Distribution Function (CDF) of a real-valued continuous variable X , denoted as $F_X(x)$, is given by the function:

$$F_X(x) = P(X \leq x) = \int_{-\infty}^x f_X(t) dt \quad (10-2)$$

CDF describes the probability that variable X with a given probability distribution will be less than or equal to x , corresponding to the area between the horizontal axis and the PDF from minus infinity to x . An example of CDF for a standard normal distribution is illustrated in Figure 10-2. Then, the probability that X lies within space $(a, b]$ is defined by the expression:

$$P(a < X \leq x) = F_X(b) - F_X(a) = \int_a^b f_X(x) dx \quad (10-3)$$

The properties of a cumulative distribution function are:

- non-decreasing monotone;
- right continuous;
- $\lim_{x \rightarrow -\infty} F_X(x) = 0$;
- $\lim_{x \rightarrow +\infty} F_X(x) = 1$.

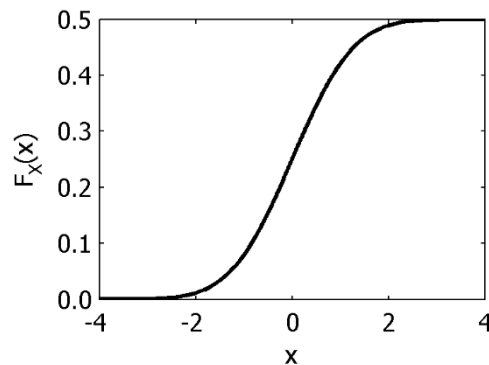


Figure 10-2: Example of a cumulative distribution function (standard normal distribution)

10.3 UNIFORM DISTRIBUTION

The continuous uniform distribution is a symmetric probability distribution where all the intervals of the same length on the distribution's support are equiprobable. The support range is defined between a minimum value a and a maximum value b . For a random variable X it is the maximum entropy probability distribution without any constraint other than the constraints of its support range. The uniform distribution parameters are listed in Table 10-1.

Table 10-1: Uniform distribution parameters

notation		$X \sim U(a,b)$	
support	$x \in [a,b]$ with $a < b$ and $x \in \mathbb{R}$	mean value	$\frac{1}{2}(a+b)$
variance	$\frac{1}{12}(b-a)^2$	median	$\frac{1}{2}(a+b)$
PDF	$f(x) = \begin{cases} \frac{1}{b-a}, x \in [a,b] \\ 0, \text{otherwise} \end{cases}$	CDF	$F_x(x) = \begin{cases} 0 & x < a \\ \frac{x-a}{b-a} & x \in [a,b] \\ 1 & x > b \end{cases}$

Examples of a PDF and a CDF of a uniform distribution are provided in Figure 10-3, where PDF and CDF are straight lines for $a=1$ and $b=5$.

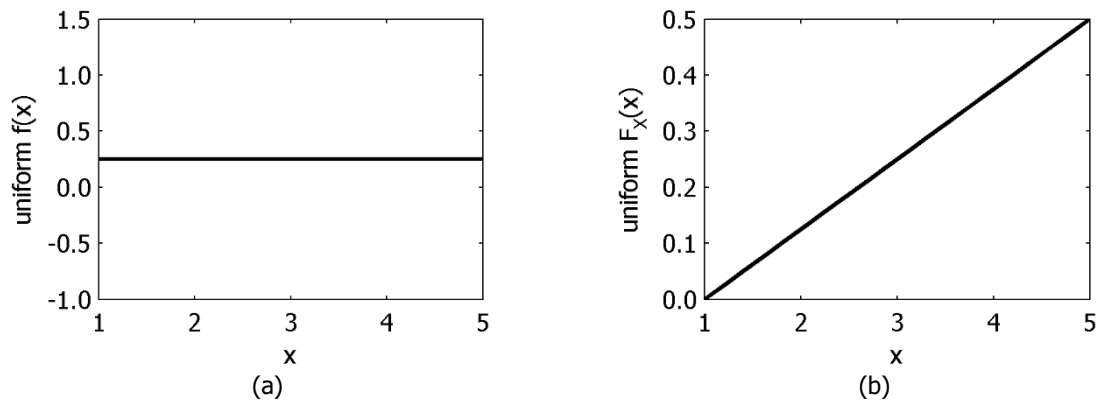


Figure 10-3: Examples of uniform distribution (a) PDF and (b) CDF with parameters $a=1$ and $b=5$

10.4 NORMAL DISTRIBUTION

The normal or Gaussian distribution is a very common and widely used continuous PDF. The normal distribution has a wide scope of applications and is important in statistics as it often appears in nature. The normal distribution is useful because of the central limit theorem, which states that the mean of many random variables independently drawn from the same distribution are distributed approximately normally, irrespective from the form of the original distribution. The Gaussian distribution is also referred in practice as the "bell curve", whose characteristics are listed in Table 10-2.

Table 10-2: Normal distribution parameters

notation		$X \sim N(\mu, \sigma^2)$	
support	$x \in \mathbb{R}$	mean	μ
variance	σ^2	value	μ
		median	μ
PDF	$f(x) = \frac{1}{\sqrt{2\pi\sigma^2}} e^{-\frac{(x-\mu)^2}{2\sigma^2}}$	CDF	$F_x(x) = \frac{1}{\sqrt{2\pi\sigma^2}} \int_{-\infty}^x e^{-\frac{(t-\mu)^2}{2\sigma^2}} dt$

Examples of PDF and CDF of normal distribution are depicted in Figure 10-4 for constant mean value and in Figure 10-5 for constant standard deviation. In case the mean value is constant, the peak value of PDF decreases for higher standard deviation and the CDF curve “rotates” around a constant point. On the other hand, for constant standard deviation, the PDF and CDF curves are shifted with increasing mean value, while their shape is unchanged.

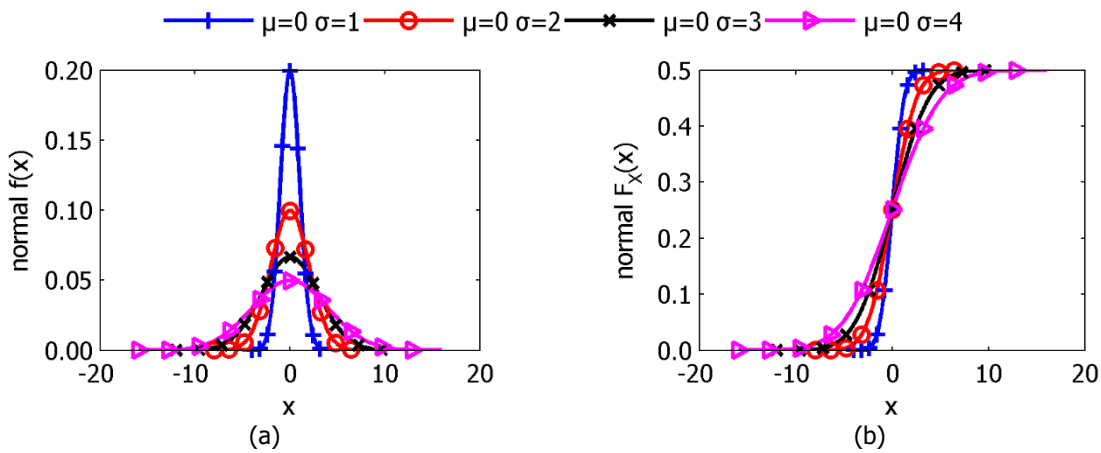


Figure 10-4: Examples of normal distribution (a) PDF and (b) CDF with constant mean value

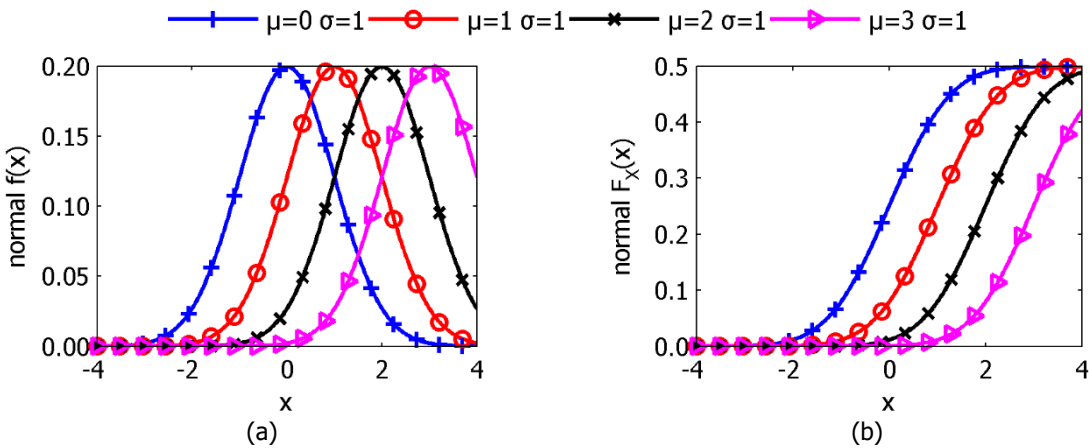


Figure 10-5: Examples of normal distribution (a) PDF and (b) CDF with constant standard deviation

The general properties of the Gaussian distribution are:

- it is symmetric around $x=\mu$;
- its first derivative is negative for $x<\mu$, positive for $x>\mu$ and zero only at $x=\mu$;
- its second derivative is zero and changes sign only at points $x=\mu-\sigma$ and $x=\mu+\sigma$;
- it is infinitely differentiable.

10.5 LOGNORMAL DISTRIBUTION

The lognormal distribution is a continuous probability distribution of a random variable whose logarithm is normally distributed. Thus, if the random variable Y is lognormally distributed, then variable X=logY is normally distributed. A random variable that is lognormally distributed takes only positive values. A variable might be modeled as lognormal if it can be thought as the multiplicative product of many independent random variables each of which is positive by considering the central limit theorem in the log-domain. Lognormal distribution characteristics are listed in Table 10-3.

Table 10-3: Lognormal distribution parameters

	notation	$X \sim \text{LN}(\mu, \sigma^2)$	
support	$x \in (0, +\infty)$	mean value	$e^{\mu+\sigma^2/2}$
variance	$(e^{\sigma^2} - 1)e^{2\mu+\sigma^2}$	median	$e^{\mu+\sigma^2/2}$
PDF	$f(x) = \frac{1}{x\sqrt{2\pi\sigma^2}} \times e^{-\frac{(\ln x - \mu)^2}{2\sigma^2}}$	CDF	$F_x(x) = \int_0^x \frac{1}{t\sqrt{2\pi\sigma^2}} \times e^{-\frac{(\ln t - \mu)^2}{2\sigma^2}} dt$

Examples of lognormal PDF and CDF are illustrated in Figure 10-6 for constant mean value ($\mu=0$) and in Figure 10-7 for constant standard deviation ($\sigma=1$).

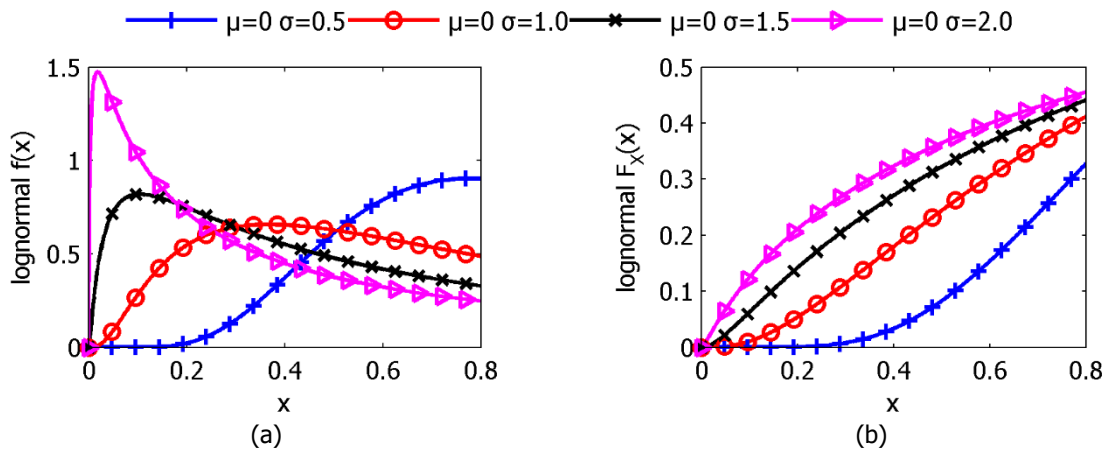


Figure 10-6: Examples of lognormal distribution (a) PDF and (b) CDF with constant mean value

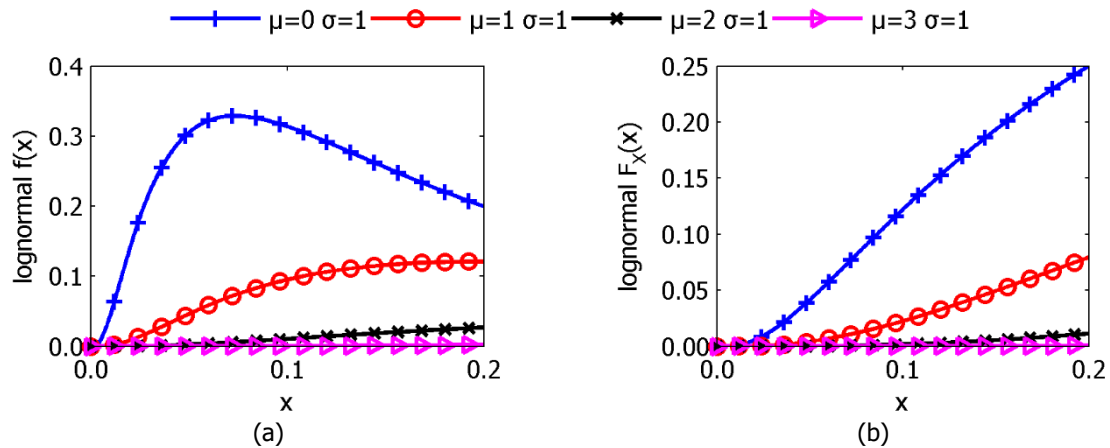


Figure 10-7: Examples of lognormal distribution (a) PDF and (b) CDF with constant standard deviation

10.6 GAMMA DISTRIBUTION

The gamma distribution in probability theory and statistics is a two-parameter family of continuous probability distributions. The two parameters are the shape parameter α and the inverse scale parameter β or rate parameter, which are positive real numbers. Gamma distributions parameters are listed in Table 10-4. Characteristic examples of gamma distribution PDF and CDF are provided in Figure 10-8.

Table 10-4: Gamma distribution parameters

	notation	$X \sim \Gamma(\alpha, \beta) \equiv \text{Gamma}(\alpha, \beta)$	
support	$x \in (0, +\infty)$	mean value	α / β
variance	α / β^2	median	not closed form
PDF	$g(x; \alpha, \beta) = \frac{\beta^\alpha x^{\alpha-1} e^{-\beta x}}{\Gamma(\alpha)}, x \geq 0$	CDF	$F(x) = \int_0^x f(u; \alpha, \beta) du = \frac{\gamma(\alpha, \beta x)}{\Gamma(\alpha)}$ $\gamma(\alpha, \beta x) = 0$ is the lower incomplete gamma function

Characteristic examples of gamma distribution PDF and CDF are provided in Figure 10-8 by varying the parameters α and β .

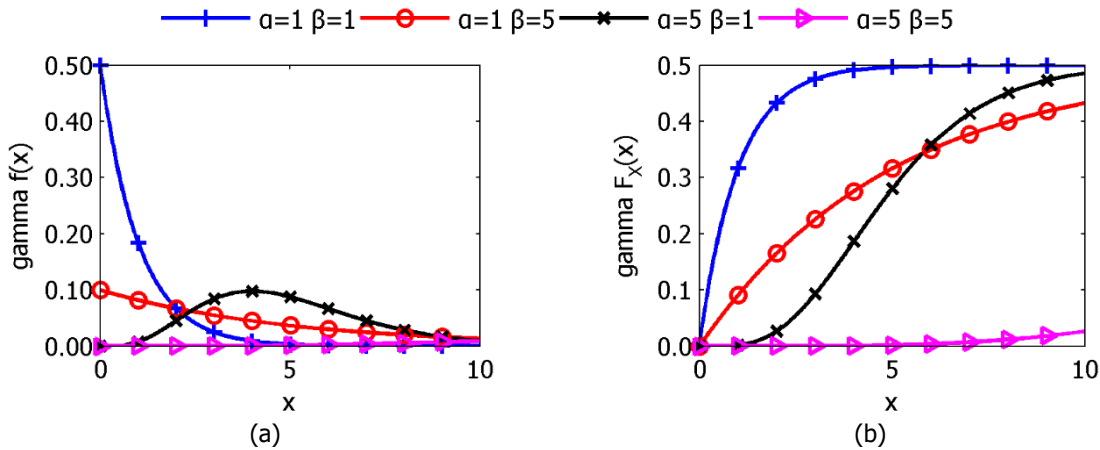


Figure 10-8: Examples of gamma distribution (a) PDF and (b) CDF

10.7 WEIBULL DISTRIBUTION

The Weibull distribution in probability theory and statistics is a continuous probability distribution. The distribution is parameterized by the shape parameter k and the scale parameter λ , which are positive number. The Weibull distribution is related to a number of other probability distributions and in particular interpolated between the exponential distribution ($k=1$) and the Rayleigh distribution ($k=2$ and $\lambda=\sqrt{2}\sigma$). The characteristics of Weibull distribution are listed in Table 10-5.

Table 10-5: Weibull distribution parameters

notation		$X \sim \text{Wei}(k, \lambda)$	
support	$x \in [0, +\infty)$	mean value	$\lambda \Gamma(1 + 1/k)$, where Γ is the gamma function
variance	$\lambda^2 \left[\Gamma\left(1 + \frac{2}{k}\right) - \left(\Gamma\left(1 + \frac{1}{k}\right)\right)^2 \right]$, where Γ is the gamma function	median	$\lambda (\ln(2))^{1/k}$
PDF	$f(x; k, \lambda) = \begin{cases} \frac{k}{\lambda} \left(\frac{x}{\lambda}\right)^{k-1} e^{-(x/\lambda)^k} & x \geq 0 \\ f(x; k, \lambda) = 0 & x < 0 \end{cases}$	CDF	$F(x; k, \lambda) = \begin{cases} 1 - e^{-(x/\lambda)^k} & x \geq 0 \\ F(x; k, \lambda) = 0 & x < 0 \end{cases}$

Indicative examples of Weibull distribution PDF and CDF are provided in Figure 10-9 by considering the scale parameter λ as constant and the shape parameter k as a variable.

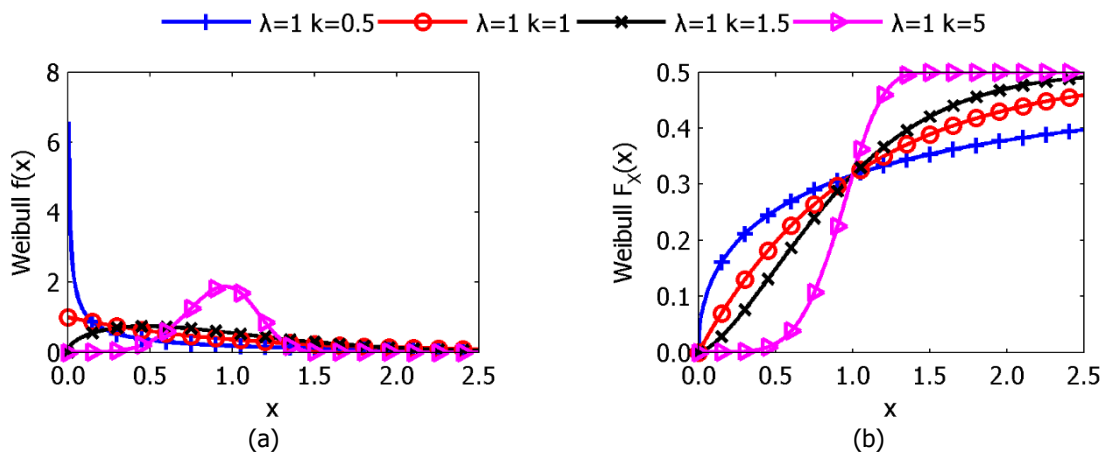


Figure 10-9: Examples of Weibull distribution (a) PDF and (b) CDF with constant scale parameter ($\lambda=1$)

10.8 BETA DISTRIBUTION

The beta distribution in probability theory and statistics is a family of continuous probability distributions defined in the interval $[0,1]$ and parameterized by two positive shape parameters, denoted by α and β , which control the distribution shape and appear as exponents of the random variable. The beta distribution is applied in modeling the behavior of random variables limited to intervals of finite length. The characteristics of beta distribution are listed in Table 10-6.

Table 10-6: Beta distribution parameters

notation		$X \sim \text{Beta}(\alpha, \beta)$	
support	$x \in [0, 1]$	mean value	$\alpha / (\alpha + \beta)$
variance	$\frac{\alpha\beta}{(\alpha + \beta)^2 (\alpha + \beta + 1)}$	median	$\frac{\alpha - 1/3}{\alpha + \beta - 2/3}$
PF	$b(x; \alpha, \beta) = \frac{x^{\alpha-1} (1-x)^{\beta-1}}{B(\alpha, \beta)}, x \geq 0$	CDF	$F(x) = \int_0^x b(u; \alpha, \beta) du = \frac{B(x; \alpha, \beta)}{B(\alpha, \beta)}$ $B(x; \alpha, \beta)$ is the lower incomplete beta function

Characteristic examples of beta distribution PDF and CDF are illustrated in Figure 10-10 for various combinations of shape parameters α and β .

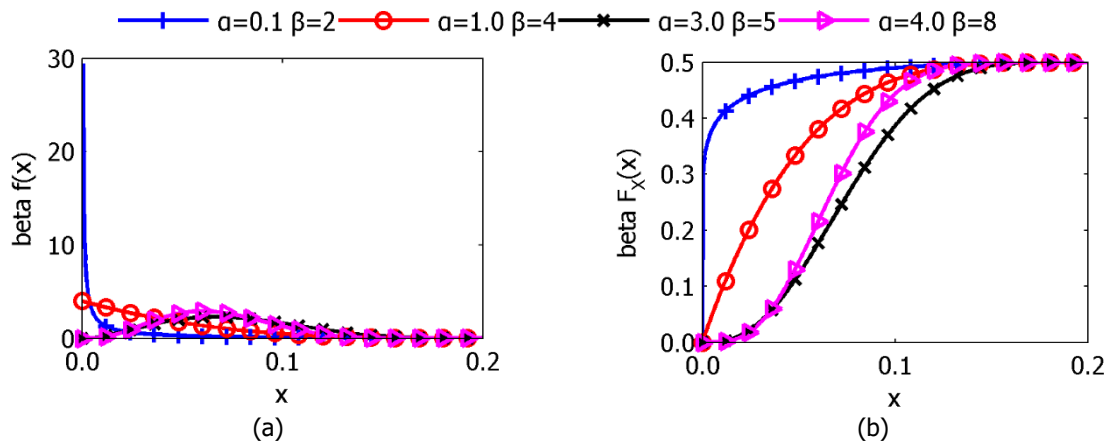


Figure 10-10: Examples of beta distribution (a) PDF and (b) CDF

10.9 TOTAL PROBABILITY THEOREM

Assuming that Ω is a sampling space and $B_n, n=1,2,3,\dots$ is a finite and countable partition of space Ω with B_n being pairwise disjoint events and additionally each event B_n is measurable, then for every event A in the sampling area Ω , its probability is calculated from the total probability theorem:

$$P(A) = \sum_n P(A \cap B_n) = \sum_n P(A | B_n)P(B_n) \quad (10-4)$$